

Laser-assisted Modification of Metals and Metal Oxide Semiconductors as Photoactive Materials

Inaugural-Dissertation
zur Erlangung des Doktorgrades
der Mathematisch-Naturwissenschaftlichen Fakultät
der Universität zu Köln



vorgelegt von
Danny Bialuschewski
aus Arolsen, jetzt Bad Arolsen

Köln, 2019

Berichterstatter: Prof. Dr. Dr. (h.c.) Sanjay Mathur
Prof. Dr. Klas Lindfors
Vorsitzender: Prof. Dr. Ines Neundorf
Beisitzer: Dr. Thomas Fischer
Tag der Promotion: 25.11.2019

Dedicated to my family

Engineering is not quite as important as imagination.

Satoru Iwata

Acknowledgement

First and foremost, I would like to thank Prof. Dr. Sanjay Mathur for allowing me to work on this very interesting and interdisciplinary topic while always taking time out of his busy schedule for me. His connections allowed me to visit many conferences and present my research to an international audience, including research visits to both Montréal, Canada and Melbourne, Australia, which further increased the scope and reach of my work. I give my thanks to Prof. Dr. Klas Lindfors for taking the position as second examiner, and the DFG in frame of the SPP 1839 "Tailored Disorder" for financial support.

Special thanks must be given to my cooperation partners in Bochum, Prof. Dr. Evgeny Gurevich and Mr. Jan Hoppius, for making the whole project possible. Their expertise was necessary to develop new laser treatment processes, and allowed to investigate even more complex systems.

I would like to thank the many different operators in our research groups, highlighting the XRD-Team with Alexander Möllmann, Myeongwhun Pyeon, Michael Haiduk and others, especially with more complex measurements due to rough substrates and thin films, the AFM-Team with Christoph Bohr, Matthias Grosch and Daniel Stadler for the difficult measurements and analysis, and the XPS-Team with Robert Frohnhoven, Tim Ludwig, Michael Wilhelm and others, who analyzed many samples and always supported me, even with fitting the more complex data.

For the support from the other subgroups I would like to give special thanks to Vanessa Nahrstedt, Peter Tutacz, Markus Schütz and Fabian Hartl, for always being helpful, even with their own full workday.

While all members of the plasma group deserve to be mentioned here, I would like to specifically mention Dr. Yakup Gönüllü, who was the leading postdoc during the start of my PhD, and helped our research group becoming what it is today. His positive attitude has rubbed off on even the most pessimistic members, and kept some of us going even after he left. The other long term members, Myeongwhun Pyeon and Alexander Möllmann, supported everyone by repairing and maintaining many machines we still use today, and became close friends. Of the many great short term members of our plasma group, I would like to thank Dr. Meng Wang for his expertise in PEC water splitting, Dr. Meenal Deo, who supported me on both scientific and technical level, and Dr. Mehmet Gürsoy as an expert in PE-CVD processes.

Additional thanks to everyone not mentioned here for the many fruitful discussions, the fun social activities and many cultural insights, ranging from Kölsch to korea.

Lastly, my thanks go to my family for their continued support, and my fiance Lisa Kreh, who makes everything much more worthwhile.

Abstract

Laser-induced order and disorder on both chemical and structural level through absorption of femtosecond (fs) laser pulse was investigated on different metal (e.g. Al or Ti) and metal oxide systems (e.g. Fe_xO_y or TiO_x) in order to modulate their surface chemistry and topography. For example, semiconductor materials were engineered towards their optical, electrical and electronic properties by femtosecond laser treatment to improve their water splitting properties. Thin metal and metal oxide films with tunable photophysical properties can be used for new solar harvesting systems, which might fulfill the demand for renewable energy and reduce CO_2 emission, which poses one of the biggest challenges in the current era. The combination of chemistry (precursor synthesis), material science (thin film fabrication and device engineering) and physics (femtosecond laser treatment) is rarely performed due to the sheer complexity of the different subjects, but has been proven to be invaluable in this work to develop a fundamental understanding of the relationship of the surface treatment and the functional properties.

The first step was to standardize the laser structuring parameters to enable reproducible processes. In order to reduce random absorption and scattering of the laser beam on interfaces like grain boundaries, metal films were introduced to efficiently absorb the photon energy due to their high free electron density. For this reason, either metal substrate (Al or Ti) or a sputtered metal film (Al) were used. The metal oxide thin films were grown by plasma-enhanced chemical vapor deposition (PE-CVD) techniques.

With reproducible laser processing more complex systems could be investigated, for example the effects of gradual changes in laser fluence on films of titanium oxide in combination with iron oxide, or bimetallic oxides (MAI_2O_4 , $\text{M} = \text{Ni}, \text{Co}$) were studied. Possible structures ranging from shallow to deep ripples to particle formation were observed. Surface roughness, ripple depth, hydrophobicity and absorption was found to improve with increasing laser power. Additionally, laser treated titanium oxide layers revealed a gas sensing response towards reductive gas (H_2) at room temperature. Through precise parameter tuning, the titanium oxide thin films could be crystallized by laser-assisted patterning.

Laser-induced texturing of metal substrates has shown to improve two-fold, the photoelectrochemical performance of titanium oxide (from 0.031 to 0.061 mA/cm^2) and iron oxide absorber films (from 0.028 to 0.057 mA/cm^2) due to increased light trapping, and availability of a higher number of surface states. The photoelectrodes patterned by fs laser

pulses were investigated towards their light absorption, conversion efficiency, morphology, crystallographic structure and composition, to further improve the understanding of periodically patterned materials by laser treatment.

Moreover, transition metal spinel films (MA_2O_4 , $M = Ni, Co$) were decomposed by laser treatment with the intention of embedding transition metal clusters into an aluminum oxide matrix, forming so called CERMETS (ceramic-metal composite materials). These show unique optical and catalytic properties as supported by photocatalytic degradation of methylene blue. It could be observed that laser treated $NiAl_2O_4$ samples showed photocatalytic performance, while compositional studies have shown that laser treatment reduce the divalent transition metal centers to elemental state producing Ni/ or Co/ Al_2O_3 nanocomposites.

In summary, this research improved the understanding and possibilities of ultrashort laser pulses to structurally and compositionally modify metal and metal oxides systems, and enhance their properties for many different applications, like photoelectrochemical water splitting, gas sensing or photocatalysis.

Kurzzusammenfassung

Laser-induzierte Ordnung und Unordnung sowohl auf chemischer als auch struktureller Ebene wurde durch die Absorption von Femtosekunden (fs) Laserpulsen untersucht, um verschiedene Metall- (z. B. Al oder Ti) und Metalloxid-Systeme (z. B. Fe_xO_y oder TiO_x) bezüglich ihrer Oberflächenchemie und Topography zu modulieren. So wurden zum Beispiel Halbleitermaterialien durch Femtosekundenlaser-Behandlung auf ihre optischen, elektrischen und elektronischen Eigenschaften hin entwickelt, um ihre wasserspaltenden Eigenschaften zu verbessern.

Dünnschichten aus Metall- und Metalloxiden mit abstimmbaren photophysikalischen Eigenschaften können für neue Solaranlagen verwendet werden, die den Bedarf an erneuerbarer Energie decken und den CO_2 -Ausstoß reduzieren könnten, eine der größten Herausforderungen der heutigen Zeit. Die Kombination aus Chemie (Präkursorsynthese), Materialwissenschaft (Dünnschichtabscheidungen und Geräteanwendung) und Physik (Femtosekundenlaser-Behandlung) wird aufgrund der schiereren Komplexität der verschiedenen Themengebiete selten durchgeführt, hat sich aber in dieser Arbeit als unschätzbar erwiesen, um ein grundlegendes Verständnis der Beziehung zwischen der Oberflächenbehandlung und der funktionellen Eigenschaften zu entwickeln.

Der erste Schritt war die Standardisierung der Laserstrukturierungsparameter, um reproduzierbare Prozesse zu ermöglichen. Um die zufällige Absorption und Streuung des Laserstrahls an Grenzflächen wie zum Beispiel Korngrenzen zu reduzieren, wurden Metallschichten eingeführt, die aufgrund ihrer hohen freien Elektronendichte die Photonenenergie effizient absorbieren. Aus diesem Grund wurde entweder ein metallisches Substrat (Al oder Ti) oder eine gesputterte Metallschicht (Al) verwendet. Die dünnen Metalloxidschichten wurden mittels der plasmaunterstützten chemischen Gasphasenabscheidung (PE-CVD) abgeschieden.

Mit reproduzierbarer Laserprozessen konnten komplexere Systeme untersucht werden, z. B. die Auswirkungen graduellen Änderungen der Laserfluenz auf eine Kombination aus Titanoxid und Eisenoxid, oder auf Schichten aus bimetalloxyden (MAl_2O_4 , $\text{M} = \text{Ni}, \text{Co}$). Mögliche Strukturen, die von flachen über tiefe Wellen bis hin zur Partikelbildung reichen, wurden beobachtet. Es wurde festgestellt, dass sich Oberflächenrauigkeit, Welligkeit, Hydrophobie und Absorption mit zunehmender Laserleistung verbessern. Zusätzlich zeigten laserbehandelte Titanoxidschichten eine höhere Gassensorik gegenüber reduzierendem Gas (H_2) bei

Raumtemperatur. Durch präzise Parametereinstellung konnten die dünnen Titanoxidschichten durch lasergestützte Strukturierung kristallisiert werden.

Die laserinduzierte Strukturierung von Metallsubstraten hat zu einer Verdopplung geführt, die photoelektrochemische Leistung von Titanoxid- (von 0,031 bis 0,061 mA/cm²) und Eisenoxid-Absorberschichten (von 0,028 bis 0,057 mA/cm²) wurden aufgrund ihrer erhöhten Lichtfangleistung und der Verfügbarkeit einer höheren Anzahl von Oberflächenzuständen verbessert. Die durch fs-Laserpulse strukturierten Photoelektroden wurden auf ihre Lichtabsorption, Umwandlungseffizienz, Morphologie, kristallografische Struktur und Zusammensetzung hin untersucht, um das Verständnis von periodisch strukturierten Materialien durch Laserbehandlung weiter zu verbessern.

Darüber hinaus wurden Übergangsmetall-Spinellschichten (MAl₂O₄, M = Ni, Co) durch Laserbehandlung mit der Absicht zersetzt, Übergangsmetallcluster in eine Aluminiumoxidmatrix einzubetten und so genannte CERMETS (engl. für *ceramic-metal composite materials*, Keramik-Metall-Verbundwerkstoffe) zu bilden. Diese zeigen einzigartige optische und katalytische Eigenschaften, die durch den photokatalytischen Abbau von Methylenblau unterstützt werden. Es konnte beobachtet werden, dass laserbehandelte NiAl₂O₄-Proben eine photokatalytische Leistung zeigten, während Kompositionsstudien gezeigt haben, dass die Laserbehandlung die zweiwertigen Übergangsmetallzentren in den elementaren Zustand reduziert und Ni/ oder Co/Al₂O₃-Nanokomposite produziert.

Zusammenfassend lässt sich sagen, dass diese Forschung das Verständnis und die Möglichkeiten ultrakurzer Laserpulse verbessert hat, um Metall- und Metalloxidsysteme strukturell und kompositorisch zu modifizieren und ihre Eigenschaften für viele verschiedene Anwendungen, wie zum Beispiel die photoelektrochemische Wasserspaltung, die Gassensorik oder die Photokatalyse, zu verbessern.

Table of Content

1	Introduction.....	1
2	Theoretical Background: Thin Film Synthesis and Modification.....	3
2.1	Materials and Modifications.....	3
2.1.1	Material Challenges for Energy Harvesting.....	3
2.1.2	State of the Art Materials.....	3
2.2	Fabrication Methods of Multi-Dimensional Materials.....	9
2.2.1	Effects of Different Deposition Methods on Metal Oxides.....	9
2.2.2	Vapor Deposition Methods.....	10
2.2.3	Sputter Deposition Methods.....	10
2.2.4	Plasma Enhanced Deposition Methods.....	11
2.2.5	Post-Synthesis Modification.....	12
2.3	Physical and Chemical Modification of Materials.....	13
2.3.1	State of the Art Structures and Enhanced Properties.....	13
2.3.2	Heterojunction.....	18
2.4	Photoactive Applications.....	20
2.4.1	Principle of Photoelectrochemical Water Splitting.....	20
2.4.2	Basic Photoelectrochemical Cells and Performance Analysis.....	21
2.4.3	Photocatalytic Degradation.....	23
2.5	Gas Sensing.....	25
2.6	Laser-assisted Structuring Methods.....	27
2.6.1	Laser Patterning.....	27
2.6.2	Different Laser Systems.....	28
2.6.3	Influence of Structuring Parameters on Metals and Metal Oxides.....	28
2.6.4	Laser Processing Techniques.....	29
2.7	Other Strategies for Surface Modifications.....	31
2.7.1	Physical Surface Modification Methods.....	31
2.7.2	Chemical Surface Modification Methods.....	31
3	Results and Discussion.....	33
3.1	Establishment of Laser Treatment Parameters.....	33
3.1.1	Laser Patterning of Metal Systems.....	33
3.1.2	Laser Processing of Quartz Systems.....	45
3.2	Laser Treatment of Metal Oxide Thin Films.....	51
3.2.1	Scope and Overview.....	51

3.2.2	Metal Substrate Systems	52
3.2.3	Metal Interlayer System	55
3.3	Water Splitting Properties of Laser-Textured Metal Substrates.....	62
3.3.1	Scope and Overview.....	62
3.3.2	Influence of Annealing on PEC Performance	63
3.3.3	PEC Performance of Laser-Textured Systems.....	74
3.4	Laser Treatment of MA ₂ O ₄ (M = Ni ²⁺ , Co ²⁺) Films.....	83
3.4.1	Scope and Overview.....	83
3.4.2	Analysis of M[Al(O ⁱ Pr) ₄] ₂ (M = Ni ²⁺ , Co ²⁺) Precursor.....	83
3.4.3	Deposition and Analysis of MA ₂ O ₄ (M = Ni ²⁺ , Co ²⁺) Layers	85
3.4.4	Photocatalytic Degradation of Methylene Blue	90
4	Experimental Part.....	101
4.1	Substrates and Annealing	101
4.2	Deposition Methods.....	101
4.3	Laser Treatment Experiments.....	102
4.4	Characterization Methods.....	103
4.5	Precursor Synthesis.....	107
5	Summary and Outlook	109
6	References	113
7	Appendix	i
7.1	Erklärung	i
7.2	Publikationsliste.....	ii
7.3	Curriculum Vitae	iii

Abbreviations

AFM	atomic force microscopy
CA	contact angle
CERMET	ceramic-metal composite material
CIER	chlorine evolution reaction
CSP	concentrated solar power
DI	deionized
DTA	differential thermal analysis
EBSD	electron backscatter diffraction
EDX	energy dispersive X-ray spectroscopy
EI-MS	electron ionization mass spectroscopy
FIB	focused ion beam
FTO	fluorine doped tin oxide
HER	hydrogen evolution reaction
LASER	light amplified by stimulated emission of radiation
LIPSS	laser-induced periodic surface structures
LP-CVD	low pressure chemical vapor deposition
MB	methylene blue
ME-CVD	microwave enhanced chemical vapor deposition
MO	methyl orange
MOF	metal-organic framework
Nd:YAG	neodymium-doped yttrium aluminum garnet
Nd:YLF	neodymium-doped yttrium lithium fluorid
OER	oxygen evolution reaction
PE-CVD	plasma-enhanced chemical vapor deposition
PEC	photoelectrochemical water splitting
POM	polyoxometalates
RF	radio frequency
RhB	rhodamine B
SEM	scanning electron microscopy
STEM	scanning transmission electron microscopy
TGA	thermogravimetry analysis
THT	tetrahydrothiophene
w/o	without
XPS	X-ray photoelectron spectroscopy
XRD	X-ray diffraction

1 Introduction

The need for renewable energy sources and the transition away from fossil fuels is an important avenue, which is accompanied by research in many different energy conversion technologies, including for example^[1] geo- and hydrothermal (including tidal and wave power),^[2] wind power, biomass produced power (biomass/-gas/-fuel) and solar, for example as concentrated solar power (CSP), photovoltaics and photocatalysis.^[3] The conversion can be either directly into electricity, which is the case for CSP and photovoltaics, or into a chemical energy carrier, like hydrogen or hydrocarbons.^[4] These are promising choices, usually converted via electrolysis or fuel cells^[5] due to their easy handling.^[6] Using harvested solar energy to split water into oxygen and hydrogen is possible through photoelectrochemical water splitting (PEC), which allows a one-step conversion, minimizing transformation losses. While this is a viable way to produce hydrogen in lab scale, it still underperforms at industrial large scale application because of the interfacial losses and high overpotentials, which reduces the overall efficiency. This needs to be addressed by feasible large-scale cell designs and new photocatalyst materials. These can be ceramics, especially metal oxide semiconductors, which function as absorber and charge transport layers with tunable optical, electrical and electronic properties.^[7, 8] Other ways to utilize the solar energy is the photocatalytic degradation of pollutants, where catalysts are used to decompose organic components under illumination.

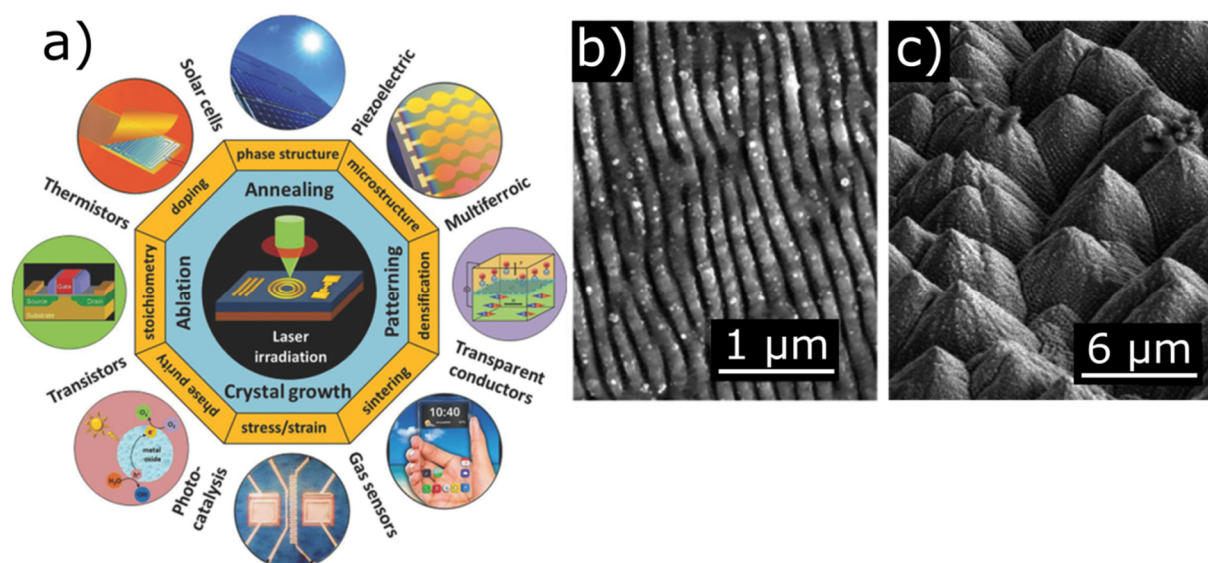


Figure 1: Overview of the many capabilities of laser irradiation of metal oxides and their possible applications (a), reprinted with permission from ^[9], copyright WILEY 2018, SEM image of femtosecond laser-induced periodic surface structures on stainless steel with low (b) and high overlap (c), reprinted with permission from ^[10], copyright Royal Society of Chemistry 2018.

Enhancing the fundamental properties of these materials is a vital part of today's research, and can either be done on a physical level, like using multi-dimensional systems and nanostructuring, or a chemical level, by introduction of foreign atoms (doping) and changing the oxidation state. These modifications, and even a combination of both, is possible using a variety of methods, with laser pulse treatment enabling precise changes through its many tunable parameters. While continuous beams and long pulses have their own application, the unique possibilities of ultra-short pulses in the femtosecond region is undeniable, as the time frame for reordering of atoms, carrier and thermal diffusion, and the evaporation processes are in the pico- to nanoseconds regimes. By providing short energy burst below this, non-thermal melting and multi-photon interaction is possible area through the use of the femtosecond laser setups, allowing many enhancements without damaging the surrounding.

2 Theoretical Background: Thin Film Synthesis and Modification

2.1 Materials and Modifications

2.1.1 Material Challenges for Energy Harvesting

Fundamental for energy harvesting applications is the solar energy absorption, which can be improved by structural and compositional modification,^[11] while other requirements include the charge separation of the photogenerated electron-hole pairs, carrier mobility and lifetimes, and the surface electrochemistry to efficiently split water.^[12] The band gap edges must fit the water splitting potential while compensating for losses in the system. Generally, the gap should be around 1.8 - 2.2 V to absorb most of the visible light. Stability against both the chemical environment and photo corrosion is desired, which is a problem with long time measurements. Additionally, the materials should be cheap and abundant, to increase the industrial viability, and make the processing environmentally friendly.^[13]

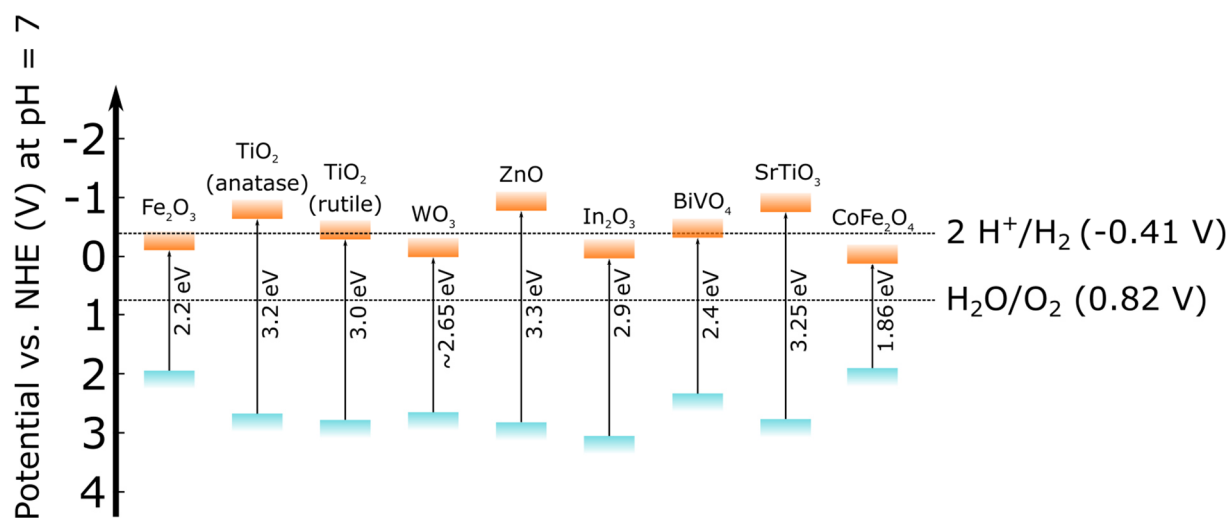


Figure 2: Band edge energies of different n-type semiconductor materials compared to the water splitting potential. Adapted from ^[14].

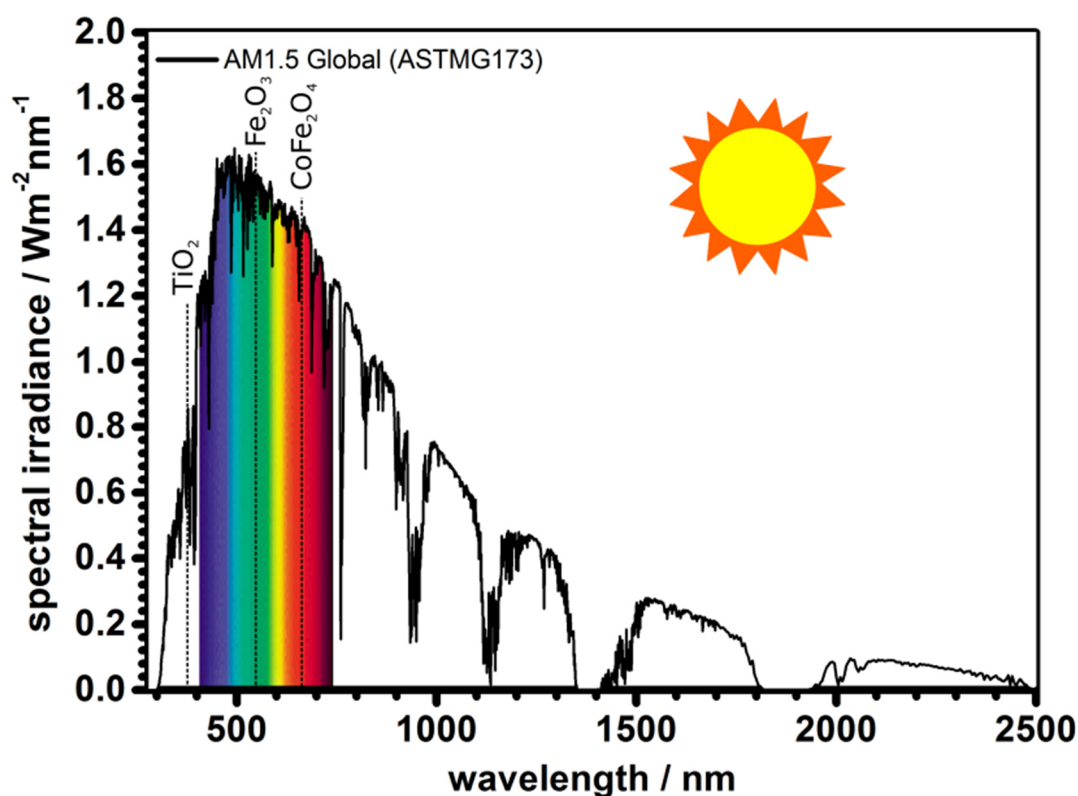
2.1.2 State of the Art Materials

A short overview of commonly used n-type semiconductor materials, including multi-layer and doped metal oxide systems, is given in Table 1. The account below focuses on the most prominent materials, iron(III) oxide in the hematite phase (Fe_2O_3) and titanium(IV) oxide (TiO_2) in the anatase phase, with their effect on the water splitting performance, while less common n-type materials will only be mentioned briefly.^[13]

Table 1: Most common materials for photoelectrochemical water splitting, including exemplary multi-layer and doped systems, with their photocurrent density (calculated vs. RHE).

Material	System	Photocurrent Density in mA/cm ²	References
α -Fe ₂ O ₃	single crystalline nanorods	4.32 (1.23 V vs RHE)	[15]
Si: α -Fe ₂ O ₃	1 wt.% Si doped thin film	0.7 (1.23 V vs RHE)	[16]
α -Fe ₂ O ₃ /TiO ₂	thin film with TiO ₂ underlayer	0.68 (1.5 V vs RHE)	[17]
TiO ₂	nanorods	0.8 (1.23 V vs RHE)	[18]
H: Au/TiO ₂	hydrogenated gold nanoparticles in nanorods	3 (0.8 V vs RHE)*	[19]
TiO ₂ /SnO ₂	3D hierarchically branched nanowires	1.0 (1.2 V vs RHE)*	[20]
WO ₃	thin film	4.2 (1.23 V vs RHE)	[21]
Gd:WO ₃	4 wt.% Gd in tungsten oxide nanoplates	2.28 (1.2 V vs RHE)*	[22]
WO ₃ /BiVO ₄	tungsten oxide nanorods covered with BiVO ₄	2.3 (1.23 V vs RHE)	[23]
ZnO	nanowires	0.057 (0.2 V vs RHE)*	[24]
ZnO/S:ZnO	8 wt.% S in zinc oxide core-shell nanocomposite	1.08 (0.3 V vs RHE)	[25]
In ₂ O ₃	nanowires	1.2 (0.42 V vs RHE)*	[26]
In ₂ O ₃ /In ₂ S ₃	core-shell nanocubes	6.19 (0.2 V vs RHE)*	[27]

*Recalculated to RHE


 Figure 3: Standard solar irradiation spectrum (AM 1.5G)^[28] with the main absorption bands of TiO₂, Fe₂O₃ and CoFe₂O₄.

Iron(III) oxide

The hematite phase of iron(III) oxide (Fe_2O_3) is the thermodynamically most stable^[29] and usually crystallizes around 600°C .^[30] It is one of the most promising materials for photoelectrochemical water splitting due to its stability and abundance in nature.^[15] Hematite is stable under PEC conditions^[31] and has a band gap of around 2.2 eV, that imparts high visible absorption and a maximum theoretical solar-to-hydrogen efficiency of around 13%^[32] to 15%^[33] (AM1.5 global). However, it has a rather low absorption coefficient, low carrier mobility^[34] and a short intrinsic hole diffusion length of only around 2 - 4 nm, which leads to significant recombination losses.^[31] This can possibly be compensated by electronic doping, using for example silicon,^[16] titanium^[35] or tin,^[36, 37] which increases charge carrier diffusion.^[38] Gold modification leads to changes in morphology and structures due to local reactions of Au^{3+} with Fe^0 , which was deposited before subsequently annealed to form hematite (Fe_2O_3).^[34] This enhances both the absorption and charge separation through the localized metal/oxide contacts. By adding titanium to the iron/gold system, the performance was found to increase even further, a result of improved optical properties, with both higher bulk and surface charge injection efficiency.^[34] Hematite in multi-material systems also leads to boosted photoelectrochemical performance, for example as top layer on titanium oxide, leading to enhanced absorption^[17] or nanorods surrounding single crystalline SnO_2 nanobelts, where an increased electrical conductivity through self-doping was observed.^[39] A TiO_2 underlayer limited the electron back injection from FTO into hematite and hole injection from hematite into FTO, while a TiO_2 top layer increases charge transfer from hematite to the electrolyte. Both processes improve the charge carrier dynamics.^[40] This multi-layer system can be further improved with patterning^[41, 42] or by using core-shell structures.^[43] Other electron-blocking layers can be added on top of the hematite to prevent contact with the electrolyte, for example with ultra-thin ZnO , which ultimately results in a $\text{Fe}_2\text{O}_3/\text{ZnFe}_2\text{O}_4/\text{ZnO}$ system that blocks electrons and allows hole diffusion through surface states instead of the valence band.^[44]

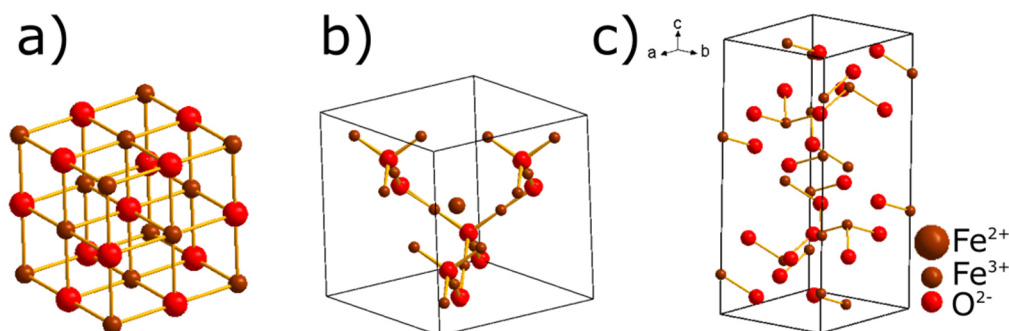


Figure 4: Crystal structures of wustite (FeO , a)^[45], magnetite (Fe_3O_4 , b)^[46] and hematite (Fe_2O_3 , c)^[47] from iron oxide.

Titanium(IV) oxide

Titanium oxide (TiO_2), another prominent photoabsorber material, has low cost and high stability in both acid and alkaline conditions.^[48] It absorbs in the UV region, which is only around ~4 - 5% of the solar spectrum. Among the two commonly used TiO_2 phases, rutile is thermodynamically more stable and, while strongly depending on the synthesis route, can crystallize around 600°C .^[49] It exhibits a band gap of ~3.0 eV, with a maximum theoretical solar-to-hydrogen efficiency of 2.2% (AM 1.5 global)^[32] due to the very low charge carrier lifetime, which is only a few tens of nanoseconds.^[50] The metastable anatase phase is formed around 500°C , depending on the processing method.^[51] It exhibits a band gap of ~3.2 eV, with a maximum theoretical solar-to-hydrogen efficiency of 1%^[33] to 1.3%^[32] (AM1.5 global). The electron lifetime of anatase of several microseconds is much higher than those of rutile, while the holes decay after a few nanoseconds.^[50] Doping allows to increase the visible light absorption without decreasing the stability, and has been investigated with several metal cations^[52-55] and non-metal anions,^[56, 57] like tin,^[58] hydrogen^[59] or nitrogen.^[60] This often results in the formation of midgap states, causing band gap narrowing. By incorporating hydrogen in the TiO_2 lattice, for example through hydrogen plasma treatment,^[61, 62] the Ti^{4+} centers are locally reduced to Ti^{3+} , accompanied by the darkening of the material, resulting in so called "black titania". This material exhibits an increased level of defects and increased light absorption. Plasma treatment can etch lattice oxygen atoms, creating electron traps and scattering centers for free charge carriers.^[59] The incorporation of nitrogen adds additional energy levels above the valence band, narrowing the band gap further. Increasing doping level can turn N: TiO_2 into a p-type semiconductor, depending on whether nearby oxygen atoms occupy the surface sites.^[63] Co-doping of nanowires with hydrogen and nitrogen, by annealing them in H_2/Ar and NH_3 atmosphere, results in synergistic effects between the reduced Ti^{3+} and nitrogen, shifting the absorption maxima from ~420 nm (TiO_2 without annealing) over ~550 nm (N: TiO_2) to ~570 nm (H/N: TiO_2).^[64] Co-doping of tungsten and nitrogen also results in increased photoabsorption,^[65] with time-dependent and normal density functional theory (TD-DFT and DFT) calculations revealing interstitial nitrogen next to titanium vacancies adding an energy level around ~1.9 eV above the valence band maximum, acting as a trap state that promotes recombination. Substituting titanium with tungsten, in addition to the substitution of a nearby oxygen by nitrogen, adds shallow in-gap levels near conduction band minimum and valence band maximum. This band gap narrowing again increases the photoactivity.^[66] With a multi-material system, for example titanium oxide nanorods on tin oxide nanowires, enhanced performance because of higher surface area, improved light absorption and better charge

collection, has been seen.^[20] Gold nanoparticles, used to create surface disorder by increasing the amount of Ti^{3+} and oxygen vacancies, increase the PEC performance. This effect is even further enhanced by hydrogenation.^[19]

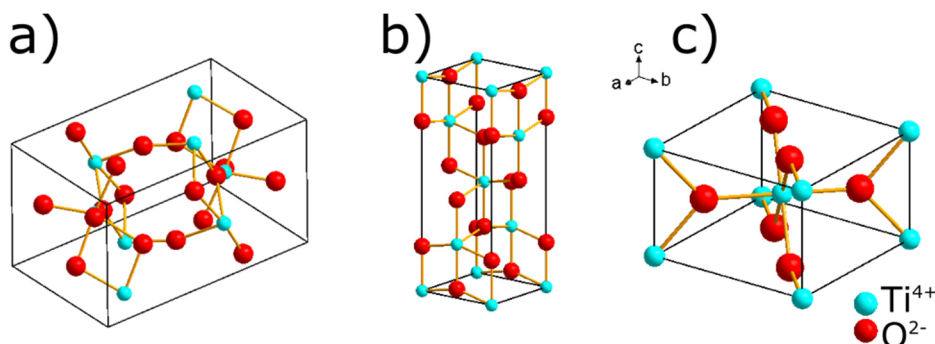


Figure 5: Crystal structures of brookite (TiO_2 , a),^[67] anatase (TiO_2 , b)^[68] and rutile (TiO_2 , c)^[69] from titanium oxide.

Tungsten(VI) oxide

Tungsten oxide (WO_3) is stable under acidic conditions and to photocorrosion, but dissolves in strongly alkaline solutions.^[21] It has a band gap around $\sim 2.5 - 2.8 \text{ eV}$ ^[70] and absorbs in the visible region of the solar light. The bare material exhibits slow charge transfer at the semiconductor/electrolyte interface in addition to rapid electron-hole recombination.^[71] The maximum theoretical solar-to-hydrogen efficiency ranges from 4.8%^[32] to 6%^[33] (AM1.5 global). By combining it with BiVO_4 , the performance can be increased, attributed to faster charge separation and reduced recombination.^[23] This can be further improved by adding Co-Pi as co-catalyst.^[72] Tungsten(VI) oxide is also used as gas sensor^[73] and electrochromic material.^[74] While it is usually not doped due to the high intrinsic electron mobility there is a wide variation in PEC performance, depending on the deposition methods and surface structures.^[75]

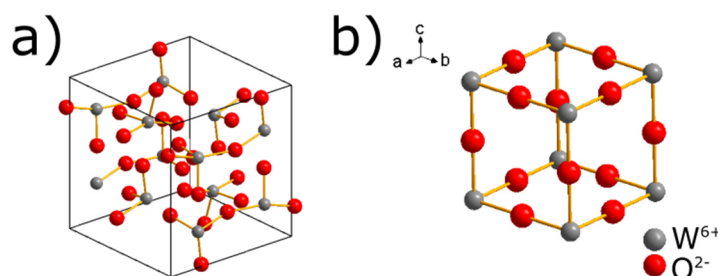


Figure 6: Crystal structures of monoclinic (WO_3 , a)^[76] and cubic (WO_3 , b)^[77] from tungsten oxide.

Zinc(II) oxide

Zinc oxide (ZnO) has a band gap of around ~ 3.3 eV with in very weak visible light absorption,^[78] but exhibits high electron mobility, optical transparency and can be produced in bulk at low cost.^[79] It is chemically stable in water, but not resistant to acidic or basic environments, which leads to its common use in photocatalytic degradation^[80] or gas sensing reactions.^[81] The combination of core-shell structures with sulfur doping, which leads to substitution of oxygen sites, introduces mid-gap states in ZnO while also functioning as protective layer, which enhances the PEC activity.^[25] Adding silver nanoparticles as co-catalyst enhances light absorption and charge separation through the localized surface plasmon resonance effect.^[82] A three component system of zinc oxide for the UV absorption and cadmium sulfide for the visible light absorption, in addition to nickel oxide as co-catalyst, improves the charge separation compared to a reference system, while using only nickel oxide on zinc oxide results in an inactive material.^[83]

Indium(III) oxide

Indium oxide (In_2O_3), which is very stable in aqueous environments, has a high conductivity^[84] and a favorable band edge structure for PEC water splitting.^[85] It exhibits a wide band gap of around ~ 3.5 eV, and solely absorbs UV light.^[86] It can be narrowed to around ~ 2.9 eV through carbon doping^[87] or by applying different structures such as cubes,^[88] nanowalls or nanotowers,^[89] which also increase the PEC performance. This is further improved by combining the band gap narrowing with a multi-layer system of $\text{In}_2\text{O}_3@ \text{In}_2\text{S}_3$ core-shell nanocubes, which increase the charge transport due to improved band alignment of the two semiconductors.^[27] Nitrogen doping shows positive effects for the interstitial sites, leading to singly ionized oxygen vacancies.^[90] Other uses include high performance gas sensor with nanobelt structures,^[91] UV laser or in light emitting diodes.^[92]

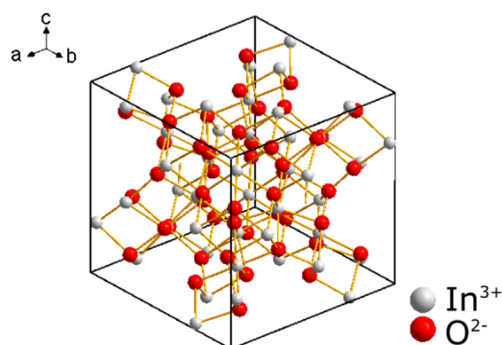


Figure 7: Crystal structure of cubic (In_2O_3) from indium oxide.^[93]

As seen above, by changing the dimension of materials, disadvantages can be suppressed and improved properties can be achieved. A vital role in designing multi-dimensional materials, like thin films, mesoporous or anisotropic structures, is the fabrication method, which will be discussed in the following section.

2.2 Fabrication Methods of Multi-Dimensional Materials

The deposition methods are categorized into physical (e.g., evaporation, sputtering),^[94] solution, or gas phase chemical processes (e.g., sol-gel, hydrothermal, atomic layer or chemical vapor deposition),^[95] with some using a combination of physical and chemical phenomena (e.g., ball-milling, reactive sputtering, etc.).^[13, 96]

2.2.1 Effects of Different Deposition Methods on Metal Oxides

Different structures can be reached by using a variation of deposition method, which have their own effects on the photoelectrochemical water splitting performance, and can be seen on Fe₂O₃ as example in the Table 2. The most established deposition methods for the fabrication of thin film PEC electrodes is discussed in this section.

Table 2: Structural and chemical effect on the photocurrent densities of Fe₂O₃ through deposition techniques and modifications.

Fe ₂ O ₃ Photoanodes	Structure	Methods	Photocurrent Density in mA/cm ²	Reference
Si:Fe ₂ O ₃	mesoporous thin film	atmospheric pressure CVD	2.2 (1.23 V vs RHE)	[97]
Co-Pi/Fe ₂ O ₃	nanorods	hydrothermal	0.27 (1.23 V vs RHE)	[98]
Fe ₂ O ₃	nanoflake	hydrothermal	2 (2.2 V vs RHE)	[99]
Ti:Fe ₂ O ₃	nanorods	hydrothermal	0.72 (0.43 V vs RHE)*	[100]
Ru:Fe ₂ O ₃	nanoporous nanorods	hydrothermal, doctorblading	5.7 (1.23 V vs RHE)	[101]
Fe ₂ O ₃	thin film	pulsed plasma deposition	0.09 (1.23 V vs RHE)	[102]
Fe ₂ O ₃	wormlike	solution-based	1.26 (1.23 V vs RHE)	[15]
Pt:Fe ₂ O ₃	doped, wormlike	solution-based	2.19 (1.23 V vs RHE)	[15]
Pt:Fe ₂ O ₃ /Co-Pi	doped, wormlike	solution-based	4.32 (1.23 V vs RHE)	[15]
Fe ₂ O ₃	nanotubes	sonoelectrochemical anodization	1.41 (0.7 V vs RHE)	[103]
Fe ₂ O ₃ /TiO ₂	thin film with TiO ₂ underlayer	spin coating	0.68 (1.5 V vs RHE)	[17]
Fe ₂ O ₃ /Sb:SnO ₂	nanorods	thermal evaporation, chemical bath	0.88 (1.23 V vs RHE)	[39]
Si:Fe ₂ O ₃	1 wt-% doping, thin film	ultrasonic spray pyrolysis	0.7 (1.23 V vs RHE)	[16]

*Recalculated to RHE

2.2.2 Vapor Deposition Methods

Gas phase deposition methods, for example microwave-enhanced (ME-) or low-pressure (LP-) chemical vapor deposition methods (CVD),^[104] produce a film by thermally decomposing an evaporated precursor on heated substrates.^[105] Most of the chemical reactions take place on the surface, as the molecular concentration in the gas phase is very low, where nucleation would lead to a powdery coating. The deposition can also be performed on complex surfaces or masked substrates, while a high range of materials is available. The resulting film can be either amorphous or crystalline, depending on substrate temperature, which also influences the purity of the film, as higher temperatures will burn the carbon contaminations from the incorporated precursor in the lattice. Disadvantages include the high temperature needed to decompose the precursor, which means substrates with low thermal stability can't be used, and the sometimes expensive equipment required. Additionally, the precursors can be expensive, difficult to produce, unstable or hazardous.

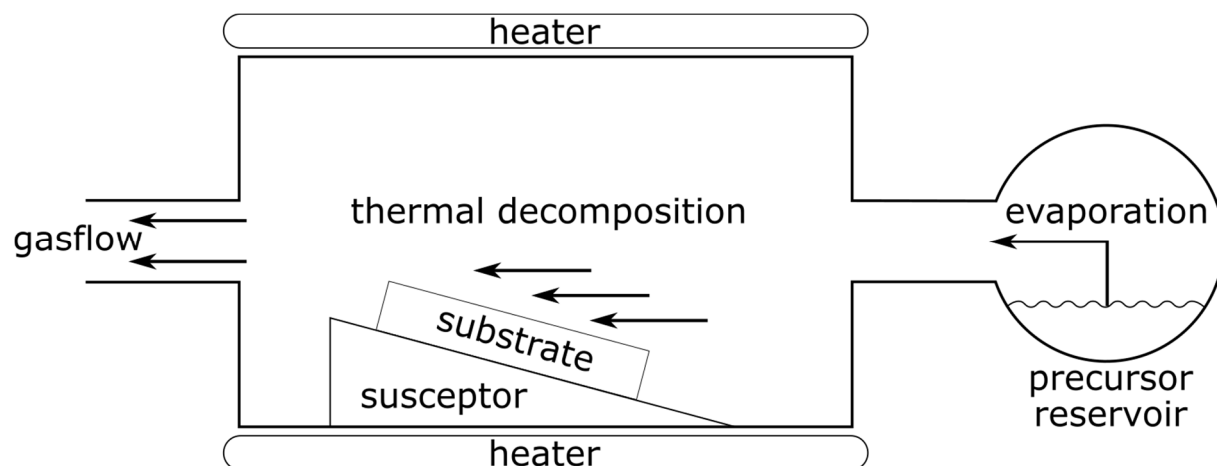


Figure 8: Schematics of the CVD process. Adapted from ^[106].

2.2.3 Sputter Deposition Methods

Sputtering is a physical method based on glow-discharge between the working and counter electrode.^[107] After ionizing the reaction gas, for example argon, the highly energetic plasma is accelerated towards the target material, which is etched by this ion bombardment. This liberates atoms and ions, which deposit onto the substrate. The layers are of high purity, and the low process temperature allows the use of heat sensitive substrates. Many solid materials can be used as target, and some are not usable with other deposition methods. The reaction of the etched particles with the surface leads to a good adhesion, and masks can be used to produce structures. Metal nanoparticles can be grown through sputtering onto ionic liquids, followed by

thermodynamically driven self-assembly,^[108] which in the case of gold can perform as catalyst, or even template for *vapor liquid solid* (VLS) growth.^[109] This mechanism involves growth of one dimensional structures (nanowires or fibers). Some limitations of this process include the low deposition rate, sometimes expensive targets and low yield on the substrate, as the whole chamber is deposited during a process.

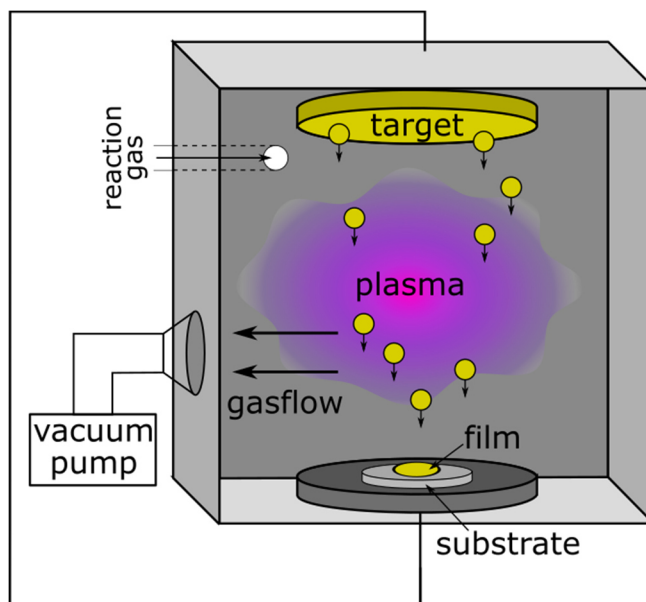


Figure 9: Schematics of a sputter deposition process.

2.2.4 Plasma Enhanced Deposition Methods

Plasma enhanced processes such as the plasma enhanced (PE-) chemical vapor deposition (CVD),^[110] are hybrid methods that use plasma to split the precursors through collisions with kinetically agitated electrons, which are produced by ionisation of the reaction gas. It is ignited by electrical power, resulting in electrons, ions and neutral particles, which oscillate between the electrodes.^[111] These particles fragment the precursor molecules through collision, which then deposit onto the substrate (see Figure 10), which can also be masked to deposit a pattern. A wide variety of plasma gases can be used, ranging from argon and nitrogen to oxygen and hydrogen and even mixtures. Depending on the desired material, the plasma gas can also be used as precursor, like acetylene for carbon thin films.^[112] As the substrate does not need to be heated during the deposition, the use of thermally sensitive substrates like polymers is possible, but in turn only amorphous films with high carbon content can be deposited. Additionally, 1D materials can be grown at elevated temperatures.

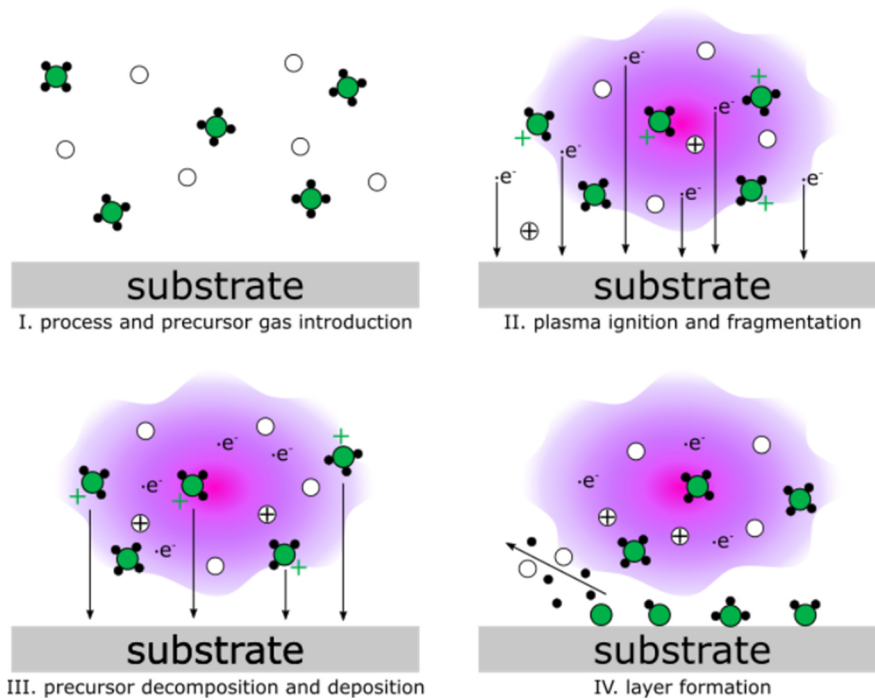


Figure 10: Schematics of the different steps during a plasma enhanced chemical vapor deposition process.

2.2.5 Post-Synthesis Modification

The methods mentioned above can also be used to induce changes post-synthesis, for example plasma sputtering processes also allow to etch the material, and is used to clean surface, create patterns or even change the surface chemistry by using different gases. Better accuracy and control over the etched structure results from the use of self-limiting Atomic Layer Etching (ALE). In most cases, plasma is used,^[113] which overcomes the limitations of continuous and isotropic etching by alternating cycles of gas flux and ion bombardment, removing material layer-by-layer with very little damage. Thermal ALE processes also exist, using the thermal-drive of the reaction.^[114]

The fabrication method of a materials plays an integral role in its performance for different applications, yet the modification on a physical or chemical level is necessary to improve them even further, and current methods are discussed in the following section.

2.3 Physical and Chemical Modification of Materials

2.3.1 State of the Art Structures and Enhanced Properties

Changing a material on physical and/or chemical level can result in new and unique properties, for instance, hydrogen treated titania ($\text{H}:\text{TiO}_2$) exhibits a substantial improvement in photocatalytic activity through induced disorder, and is also known as black titania.^[61] Highly disordered materials (e.g. amorphous) exhibit very low absorption and many surface states, while highly ordered materials (e.g. single crystalline) inherit very high absorption, yet fewer surface states (see Figure 11). By inducing order and disorder, these properties can be tuned, and even materials with alternating crystalline and amorphous areas can be achieved. The amorphous domains improve the absorption cross-section with more dangling bonds and improved electron diffusion processes. The crystalline stripes on the other hand enhance the charge transport properties through additional mid-gap states, as shown in latest simulations.^[13, 115]

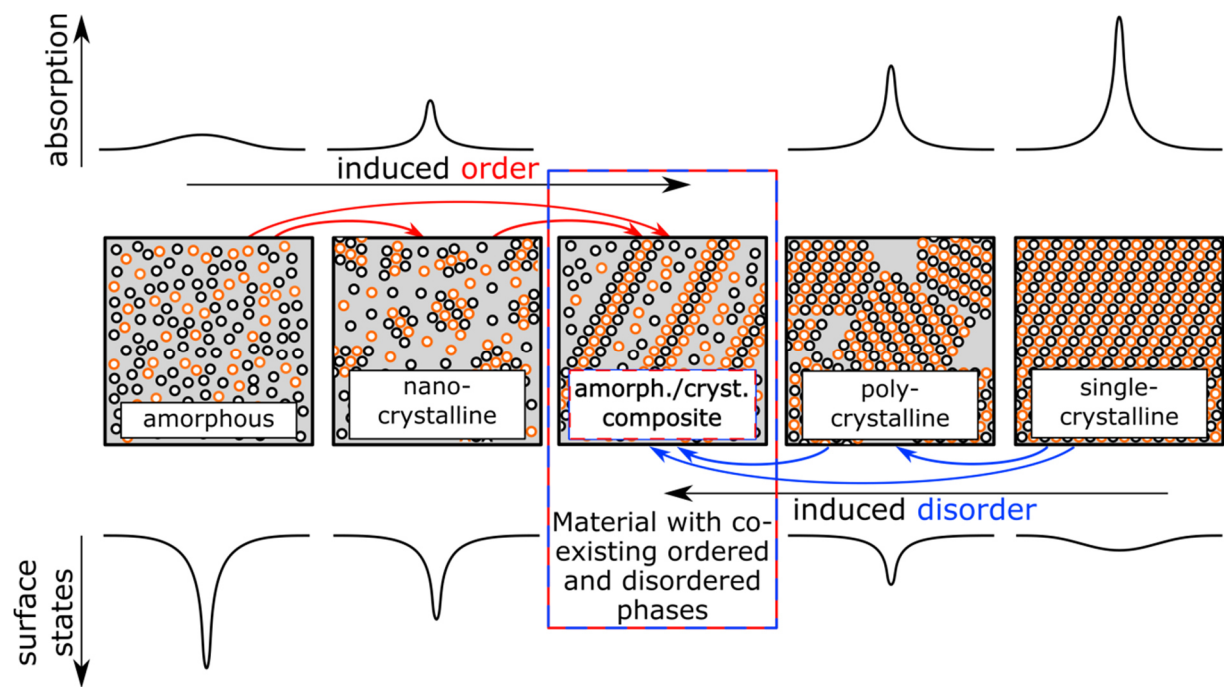


Figure 11: Schematics of induced order and disorder with their changes in absorption and surface states.

Many different types of modifications will be briefly discussed in this section, ranging from 1D or 2D structures, a combination of different phases, controlled doping, and layer by layer configuration of different materials in stacks (see Figure 12). In order perform at peak efficiency, an optimal combination of these method is often employed, with some example also discussed.

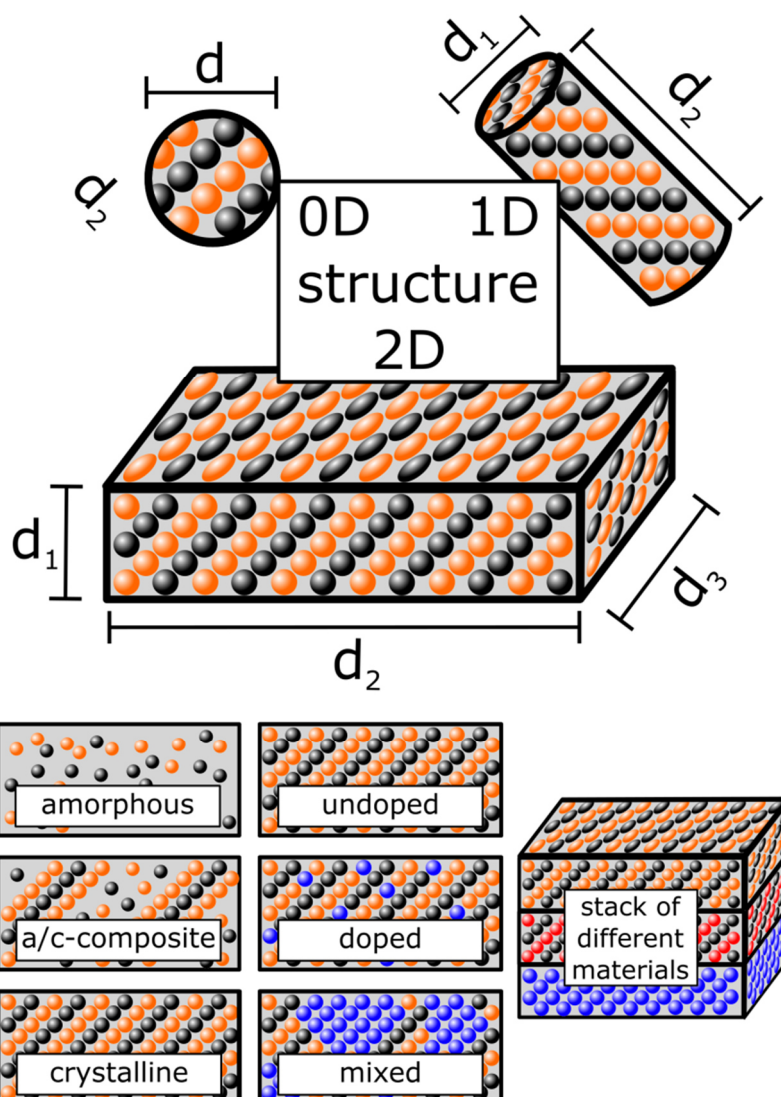


Figure 12: Schematics of the different dimensions of a material with their diffusion distances, and physical/chemical modifications, either through changes in crystallinity (amorphous, crystalline or a composite), introduction of foreign atoms (doping) or the combination of different materials in stacks.

Structural Modification of Electrodes

2D structures for photoelectrochemical water splitting are in most cases thin films (see Figure 13c and f), often made of TiO_2 ,^[116] $\alpha\text{-Fe}_2\text{O}_3$,^[117] or WO_3 ,^[118] or nanosheets made of MoS_2 ^[119] or In_2S_3 .^[120] Increasing the thickness of the layers, next to the increase in absorption, result in longer charge carriers diffusion distances. Even with the increased light harvesting, the overall PEC performance is found to decrease because of the higher recombination rates, depending on the charge carrier lifetime.^[121] A way to circumvent this is using 1D electrodes (see Figure 13b and e), which allow decoupling the direction of light absorption and the charge carriers diffusion.^[122] A long axis can absorb light while a shorter axis allows a smaller shorter distance for the carriers (see Figure 13g).^[123]

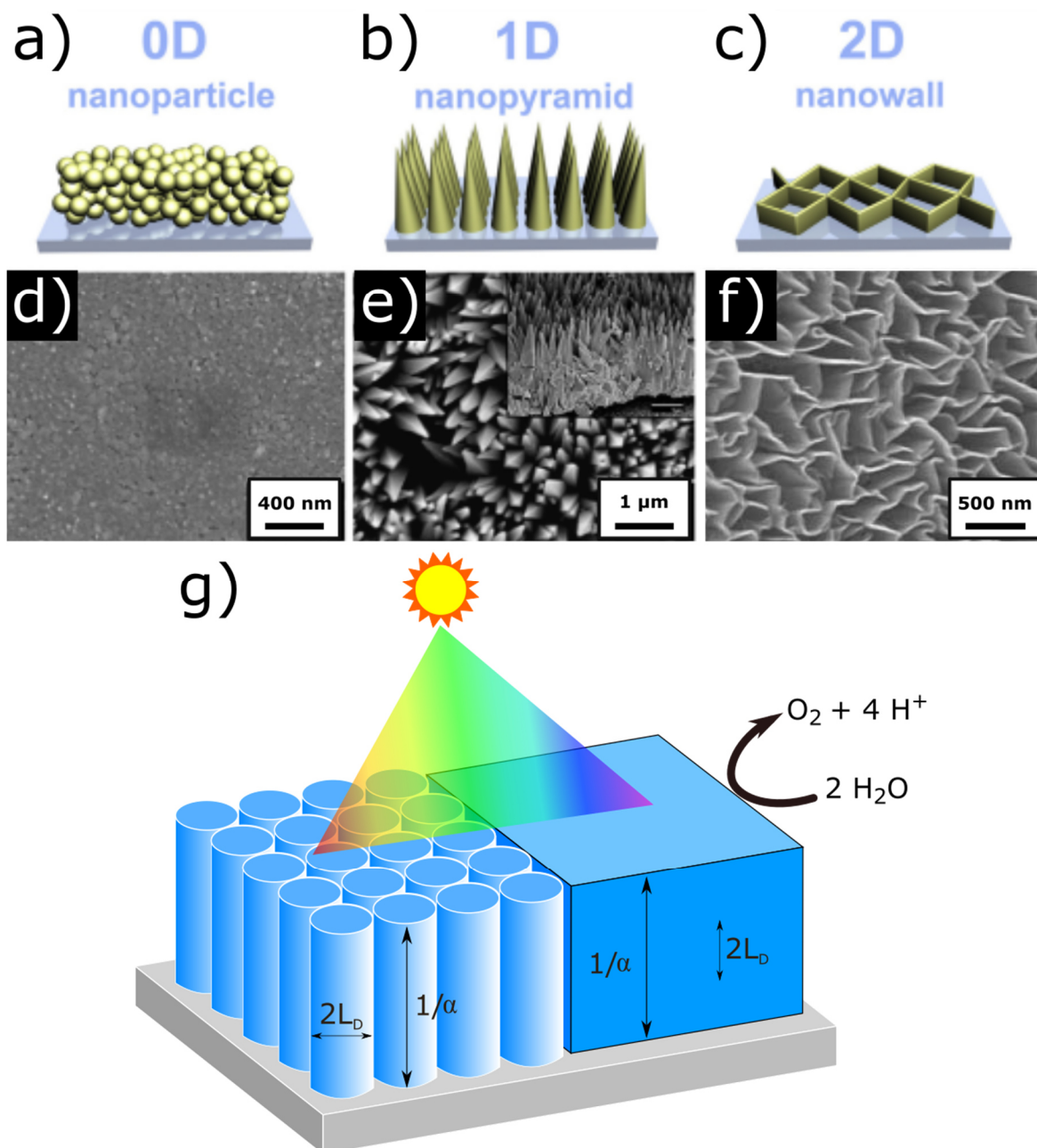


Figure 13: Overview of 0D (a), 1D (b) and 2D (c) nanostructures, reprinted with permission from ^[121], copyright Elsevier 2013, and corresponding SEM images, with (d) reprinted with permission from ^[121], copyright Elsevier 2013, (e) reprinted with permission from ^[124], copyright American Chemical Society 2010 and (f) reprinted with permission from ^[125], copyright Royal Society of Chemistry 2003, as scheme and as SEM image. The influence of nanostructures on the diffusion path distances L_D is compared to bulk materials (g). Adapted from ^[126].

This increases the active electrode-electrolyte interface area, further improving the PEC properties, and can be even higher when using hollow materials.^[127] State of the art 1D structures are typically nanorods made out of materials like TiO_2 ,^[128] ZnO ^[129] or WO_3 ,^[130] nanotubes of TiO_2 ,^[131] carbon^[132] or Ta_3N_5 ^[133] or nanowires of $\alpha\text{-Fe}_2\text{O}_3$,^[134] ZnO ^[135] or In_2O_3 .^[26] Other structures, like spikes or pyramids, are also observed, but they are less common compared to nanoparticle or quantum dots (see Figure 13a and d).^[133] These structural modifications allow a tunable band gap and thus visible light absorption by size variation, and are generally used as sensitizer on base structures.^[136] For instance, the morphology of hematite

can be modified by increasing the Si doping content in order to obtain a large range of structures, manifesting in hollow, ellipsoids particles to 1D nanowires.^[137] Other examples are discussed in section 2.2.1, with reference to the structural effects on the PEC performance summarized in Table 2.

Mixed Cation Phases

The fabrication of a defined junction between two modifications of one material, like amorphous/crystalline, or different phases, like rutile/anatase in TiO_2 ,^[138] is achievable through fabrication methods,^[138] ratios,^[139] additives^[140] or post processing steps like local annealing^[141] or simply adding a different layer.^[142] This allows to tailor properties like absorption, conductivity and photoexcitation, which commonly increase from amorphous to crystalline phases in semiconductor materials, due to a defined band gap and fewer surface and trapping states, especially at the grain boundaries. On the other hand, the defects in the crystal structure can be modified and lead to improved optical and electrical properties through added mid gap states, which for example can be a result from oxygen vacancies in the TiO_2 lattice.^[143] Hematite/magnetite films have boosted PEC performance due to their improved electron transport to the charge collectors, increasing with magnetite content, while hematite only resides on the surface. Additionally, the charge separation and overall electrical conductivity is increased by using the different chemical constitution and energy levels of the Fe^{+2} and Fe^{3+} ions.^[144]

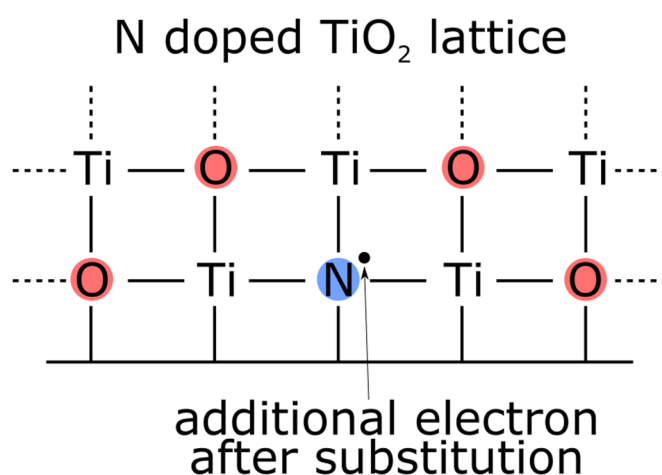


Figure 14: Schematic of a nitrogen doped TiO_2 lattice, showing the additional electron after substitution.

Adding impurities to a semiconductor material below a certain amount is called doping. For example, substituting silicon with an element owning fewer electrons, like boron, a positive charge remains in the lattice. This is known as positive (p-) type doping. Alternatively, adding

phosphorus with an additional electron results in a negative charge, known as negative (n-) type doping. They generally add additional energy levels, changing the band gap levels, and by variation of the dopant and its concentration, the optical, electrical and structural properties can be tuned. Examples for doped materials and the effect on PEC electrode materials can be found in section 2.1.2, Table 1, and include hydrogenation of hematite and gold nanoparticles on TiO_2 or silicon doping.

Charge Carrier Blocking Layers

Blocking layers are often used to prevent charge carriers from diffusing in undesired directions, which can be achieved by using a material with specific band gaps. An example is the FTO/ WO_3 / SnO_2 / BiVO_4 system, where the generated holes in the BiVO_4 layer are prevented from traversing towards the FTO because of the much lower valence band of the SnO_2 , while the photoelectrons can freely move towards the conductive layer, as seen in Figure 15.^[145] This increases the PEC performance if the thickness stays below approximately ~ 6 nm, corresponding to the Debye length.^[146] In a FTO/ TiO_2 / α - Fe_2O_3 systems, the amorphous TiO_2 underlayer prevents electron diffusion from FTO into the hematite absorption layer in addition to stopping the hole transfer from hematite to FTO, as discussed in section 2.1.2.^[40] For ZnO nanowires, a TiO_2 in anatase phase as underlayer decreases the overall PEC performance, while a ZnO as a top layer on TiO_2 increase both open-circuit voltage and fill factor.^[142]

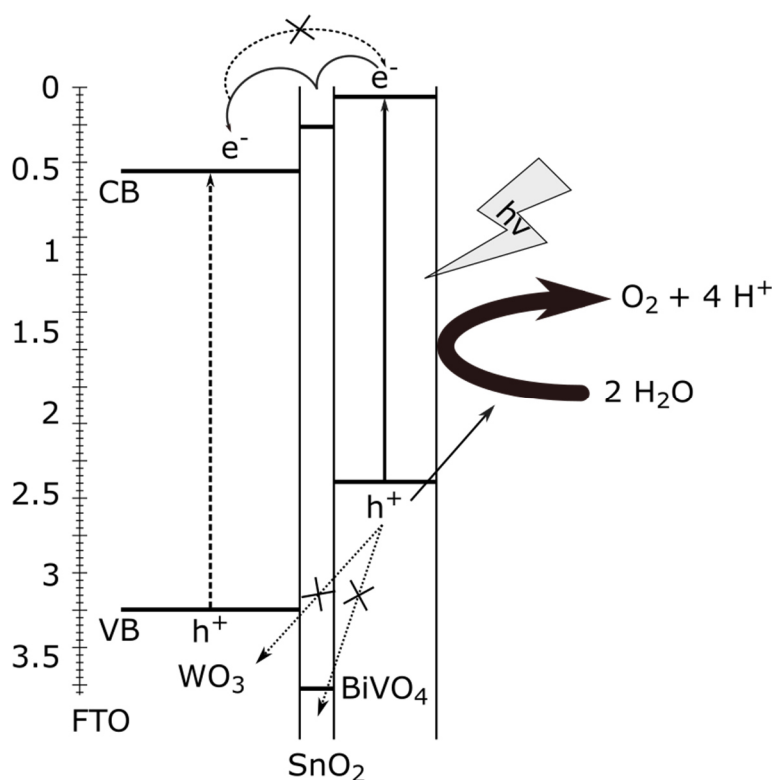


Figure 15: Energy diagram of a multi-layer PEC system with SnO_2 blocking layer. Adapted from ^[145].

Mixed Metal Oxides

A combination of compositionally and structurally different metal oxides may lead to enhanced properties, especially the charge transport and separation through synergistic effects. However, due to the increased complexity and lack of established models to fully understand the functional behaviour and electronic properties of these systems, the research on mixed metal oxides is limited. By combining structural components with amorphous and crystalline phases, like an amorphous NaTaO_3 network decorated with crystalline NaTaO_3 nanoparticles, the surface area is increased while also improving the charge separation through the structurally heterogeneous amorphous-crystalline junction.^[140] Another example is a crystalline/amorphous TiO_2 core/shell systems increasing visible light absorption by narrowing the band gap through increased oxygen vacancies, while also improving the charge separation.^[147] The combination of nitrogen doped titania ($\text{N}:\text{TiO}_2$) in anatase phase as nanotubes covered with thin amorphous tantalum oxy-nitride (TaO_xN_y) exhibits higher absorption, charge carrier separation and diffusion because of surface-doping in addition to the heterojunction. The amorphous thin film possibly has two different effects, as it increases charge carrier dynamics through the interface while also passivating the trap states of the doped bulk.^[148] Other amorphous and crystalline core-shell structures included crystalline ZnO with an amorphous Al_2O_3 shell, which works as barrier layer and improved the open-circuit voltage while having reduced the recombination rate, yet also decreasing the overall efficiency because of lower electron injection.^[142] 1D structures like TiO_2 in rutile phase can also be decorated with amorphous sensitizer, like phosphates nickel-chromium hydroxide, inhibiting the oxygen reduction.^[149] The effect on the energy bands by using different materials, during contact and under illumination, are discussed in the following section.

2.3.2 Heterojunction

To overcome the limitations of a single material, tremendous research is dedicated to the investigation of bi-/ and multilayer systems. These are designed to combine different work functions and band gap energies, while their interface forms the heterojunction, which enhances the overall optical activity through additional absorption.^[150] Metal oxide semiconductors with small band gaps are the main absorber of visible light and inject electrons into the adjacent semiconductor layers. The other material need larger band gaps with optimal edge alignments for the water splitting reaction.^[151, 152] An improvement of the chemical stability can be reached by adding a protective coating,^[153] which can also enhance the charge separation,^[154] which is

driven by the internal electrical field, a result from the electron and hole reordering during the equilibration of the Fermi levels.^[155]

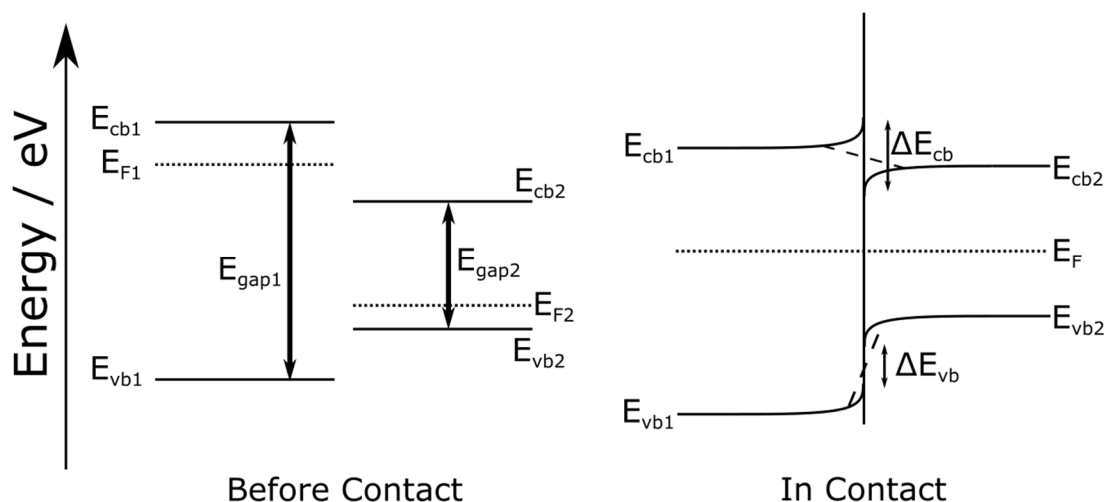


Figure 16: Heterojunction of n- and p-type material before (a) and after being in contact (b). Adapted from ^[156].

The synergy of multiple materials can enhance several properties, but they also need to fulfil additional requirements, for example the band structures should be similar, with the edges partially overlapping to drive the charge separation. This is important as the reductive and oxidative power of the charge carriers decreases with each diffusion step. If the energy difference is too high, the electron will be below H^+ -reduction level and can't participate in the water splitting reaction, which also applies for holes.^[157] This means that an increased charge separation does not automatically lead to increased PEC performance, as misaligned band edges will cause high energy loss and the accumulated charge will dominantly recombine.

Band Bending in Metal Oxide Semiconductors

When a semiconductor electrode comes into contact with aqueous electrolyte, their Fermi level, which is the energy level with 50% probability of being occupied by an electron, will equilibrate with the electrochemical potential of the H^+/H_2 and O_2/H_2O redox pair. This is done through charge carrier diffusion towards the surface, which results in band bending,^[158] which additionally leads to a depletion region at the interface, causing an internal electric field, also promoting charge separation.^[159]

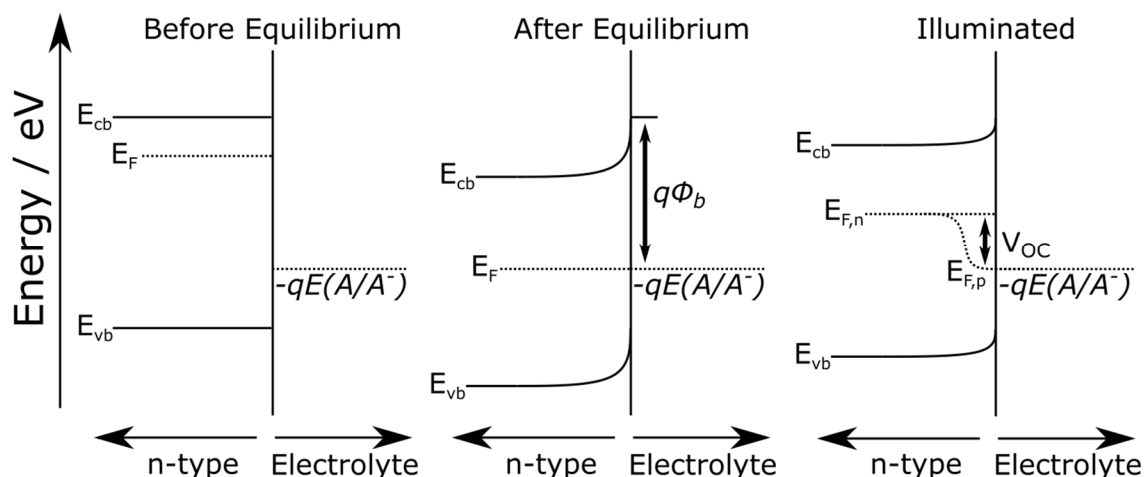


Figure 17: Energy bands of semiconductor-electrolyte interface before/after equilibrium, and during illumination. Adapted from [122].

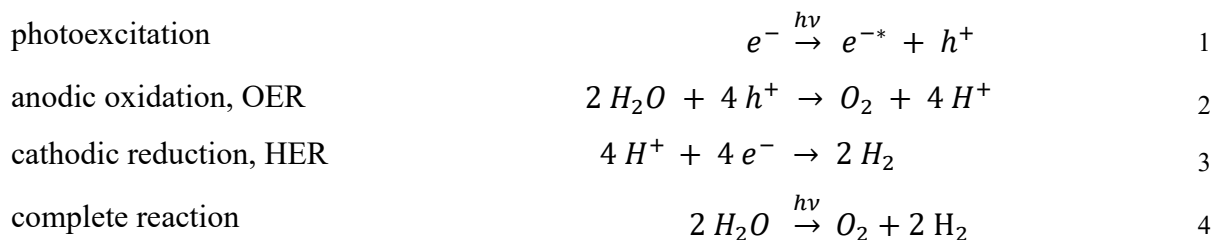
During illumination additional electrons are excited into the conduction band which causes a non-equilibrium state and split Fermi levels. The resulting quasi-Fermi level are from the holes, which remains in equilibrium with the redox potential of the electrolyte, and from the electron. Their energy difference is the open circuit voltage.^[122]

All these methods can be used to enhance fabricated materials for a multitude of applications, for example as photocatalyst for water splitting or the degradation of organic pollutants, or the sensing of different gases, which will be discussed in the following section.

2.4 Photoactive Applications

2.4.1 Principle of Photoelectrochemical Water Splitting

The basic principle of photoelectrochemical (PEC) water splitting is to use harvested sunlight to convert water into hydrogen and oxygen, using a suitable photocatalytic material, immersed in an aqueous electrolyte, while often applying an external bias potential. This process can be separated into the following main steps: (I) Sunlight is absorbed by the photoanode, which excites electrons into a higher energy state and generate an electron-hole pair (equation 1). (II) The holes diffuse towards the photoanode-electrolyte interface when using n-type materials, and react by oxidizing water molecules to oxygen (oxygen evolution reaction, OER) and protons. The electrons meanwhile diffuse from the photoanode through the conductive substrate and wire towards the cathode (equation 2). (III) The protons diffuse through the electrolyte to the cathode, being reduced to hydrogen (hydrogen evolution reaction, HER) (equation 3), which results in a complete reaction (equation 4). There are several side reactions taking place, which are discussed in the section 2.4.3.^[13]



The theoretical thermodynamic potential of the full water splitting reaction is 1.23 V, which is used as the reference bias value for all following photocurrent densities.

2.4.2 Basic Photoelectrochemical Cells and Performance Analysis

The water splitting performance of photoelectrodes is commonly determined using modified electrochemical cells with a photoelectrode assembly, with either n-type or p-type metal oxide films on current collectors, like transparent conductive oxides (TCOs) or metals as working electrode and platinum as counter electrode. To ensure comparability, the three-electrode system consists of a working, a counter and a reference electrode, for example a reversible hydrogen (RHE), silver/silver chloride (Ag/AgCl) or saturated calomel electrode (SCE). The conductivity of the electrolyte can be adjusted by using either acidic or basic pH. This setup ensures stable operation conditions of the electrodes and photocatalyst.^[160] Possible performance measurements include linear sweep voltammetry, to screen the water splitting performance over an applied potential, cyclic voltammetry, to see influence of repeated measurements, or chronoamperometric measurements, to analyse the variation over time under PEC conditions. A proper detector and monochromator allows incident photon-to-current (IPCE) analysis, measuring how many photons are converted to electrons at which wavelength, and how many contribute to the water splitting reactions.

$$IPCE(\lambda) = EQE(\lambda) = \frac{\text{electrons/cm}^2/\text{s}}{\text{photons/cm}^2/\text{s}} = \frac{|j_{ph}(\text{mA/cm}^2)| \cdot 1239.8(\text{V} \cdot \text{cm})}{P_{\text{mono}}(\text{mW/cm}^2) \cdot \lambda(\text{nm})} \quad 5$$

with 1239.8 Vnm representing a multiplication of the Planck's constant h and the speed of light c , P_{mono} being the calibrated and monochromated illumination power intensity, and λ being the wavelength where this power was measured.^[161]

In standard PEC cells (see Figure 18), the evolving gases can be separated by either a membrane, or by having both half-cell reactions in different compartments, connected by a salt bridge. Another distinction for these cell types is to be either wired or not. The metallic wire serves as a connection between the anode and cathode, increasing the distance electrons have

to travel during the water splitting reaction. On the other hand, both active electrodes can be positioned close to each other, significantly reducing the travel distance of the ions produced during the reaction. For non-wired system, where the electrodes are fused together, the electron travel distance is smaller, while ion diffusion distance increases.^[162]

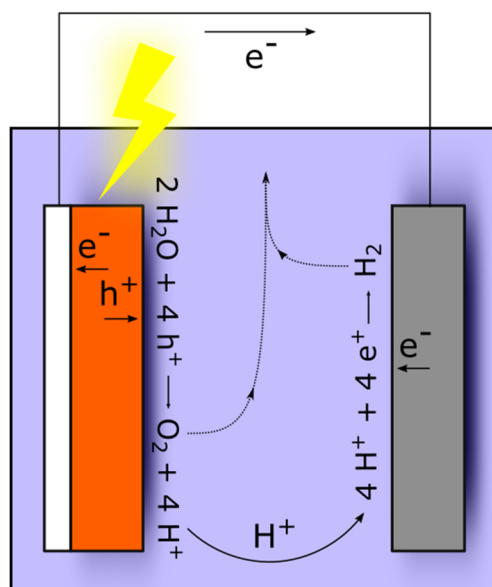


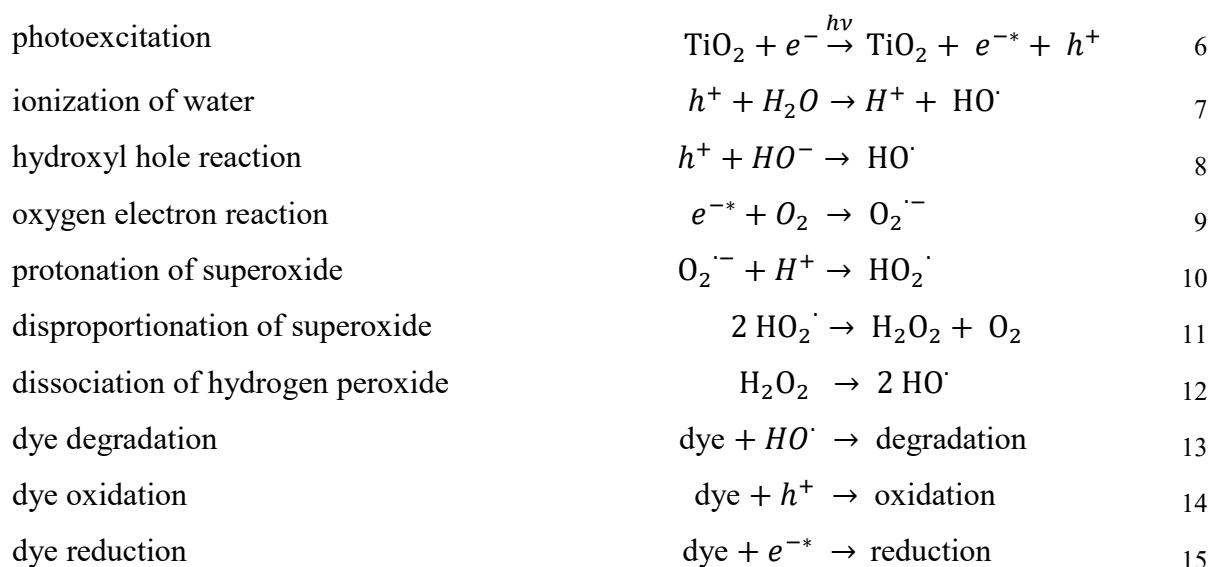
Figure 18: Standard PEC cell wired one-compartment system with the respective reactions. Adapted from ^[163].

One compartment PEC cells consist of a transparent container, like a quartz beaker, filled with electrolyte, submerged electrodes and a proper light source. Much more complex systems include in- and outlets to renew the electrolyte, a closed setup to prevent interaction with the environment, electrolyte cooling or *in situ* analysis like hydrogen/oxygen gas sensors and mass spectrometers. The main disadvantage is the mixing of the produced hydrogen and oxygen, making it difficult to precisely estimated the amount of gas produced due to increased recombination reactions near the electrodes.^[163]

Two compartment system are built to circumvent this problem by separating both electrodes. This is achieved with a semi permeable separator, for example a proton exchange membrane, which conducts protons but blocks H₂/O₂ gases.^[164] A setup like this can be a H-shaped cell, with both parts being connected by a small tube containing a separator,^[165] with either no reference electrode or one for each compartment. In the four-electrode setup, the potential between the references can be measured, which additionally allows to analyze the losses and resistance of the electrolyte. Up to this date, there is still no standardized cell or system, making the comparison of different research groups difficult.^[162]

2.4.3 Photocatalytic Degradation

Materials used purify water from organic pollutants with solar energy have similar requirements to those applied for PEC water splitting (see section 2.1.1). Dyes like methylene blue, methyl orange or methyl red, are often used in lab scale experiments as organic material. Photocatalytic degradation can be homogenous, most commonly a liquid as active material in a liquid environment, or heterogenous, often a solid catalyst in a liquid environment.^[166] While the decomposition steps are similar to the water splitting reaction (see section 2.4.1), the formation of radicals is necessary, which can either be seen in Figure 19, or with the equations using TiO₂ as exemplary photocatalyst.^[167]



The catalysts absorb light (UV in case of TiO₂), exciting an electron (e⁻) from valence to the conduction band, with a hole (h⁺) remaining (see equation 6). These can react on the surface of the semiconductor with either water (H₂O) to produce a proton (H⁺, see equation 7), or a hydroxyl ion (HO⁻, see equation 8), resulting in an hydroxyl radical (HO[·]) in both cases. This radical is a very strong oxidizing agent. The electron (e⁻) can react with oxygen (O₂) to form a superoxide (O₂^{·-}, see equation 9) while preventing electron-hole recombination. This radical further reacts with a proton (H⁺) to form a hydroperoxyl radical (HO₂[·], see equation 10), which can disproportionate into hydrogen peroxide (H₂O₂) and oxygen (O₂, see equation 11). Hydrogen peroxide can further dissociate into two hydroxyl radicals (HO[·], see equation 12).

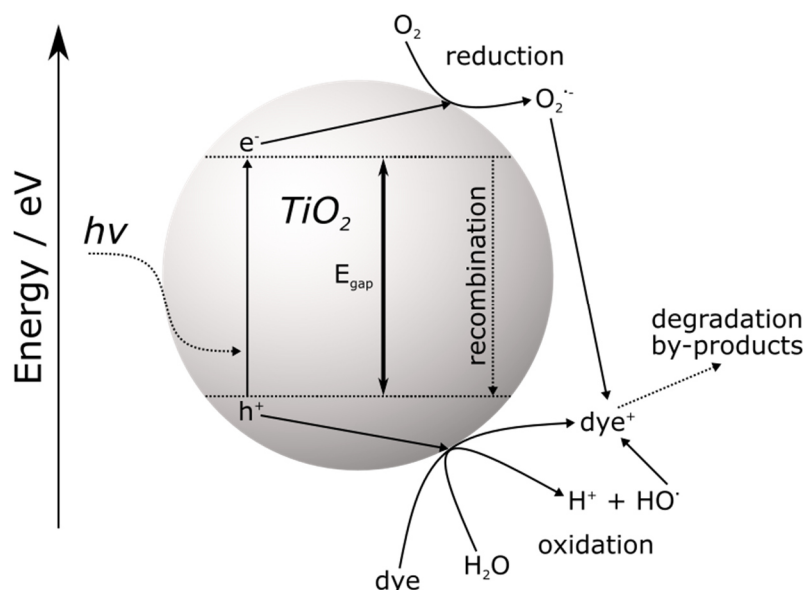


Figure 19: Photocatalytic degradation mechanism of a metal oxide in the presence of a dye. Adapted from [168].

Table 3 shows materials used for water purification with dye mimicking organic pollutants, together with a rough estimation of their degradation performance. A conventional experimental reactor system for measuring the dye decomposition in of thin films is shown in Figure 20.

Table 3: Examples of photocatalytic active materials for dye degradation.

Photocatalytic Material	Dye	Degradation	Reference
g-C ₃ N ₄	MO	~65% after 5 h	[169]
	RhB	>95% after 60 min	
B:g-C ₃ N ₄	MO	~75% after 5 h	[170]
	RhB	>95% after 40 min	
ZnO	MB	>85% after 20 min	[170]
ZnO-rGO	MB	>95% after 20 min	[171]
ZnO/TiO ₂	MO	>90% after 150 min	[171]
TiO ₂	RhB	>35% after 1 hour	[172]
N:TiO ₂	RhB	>95% after 1 hour	[172]
TiO ₂ @Fe ₃ O ₄	MO	>80% after 120 min	[173]
	MB	>75% after 120 min	
TiO ₂ /zeolite	MO	~90% after 90 min	[174]
1.5% Pt:TiO ₂ /zeolite	MO	>95% after 90 min	

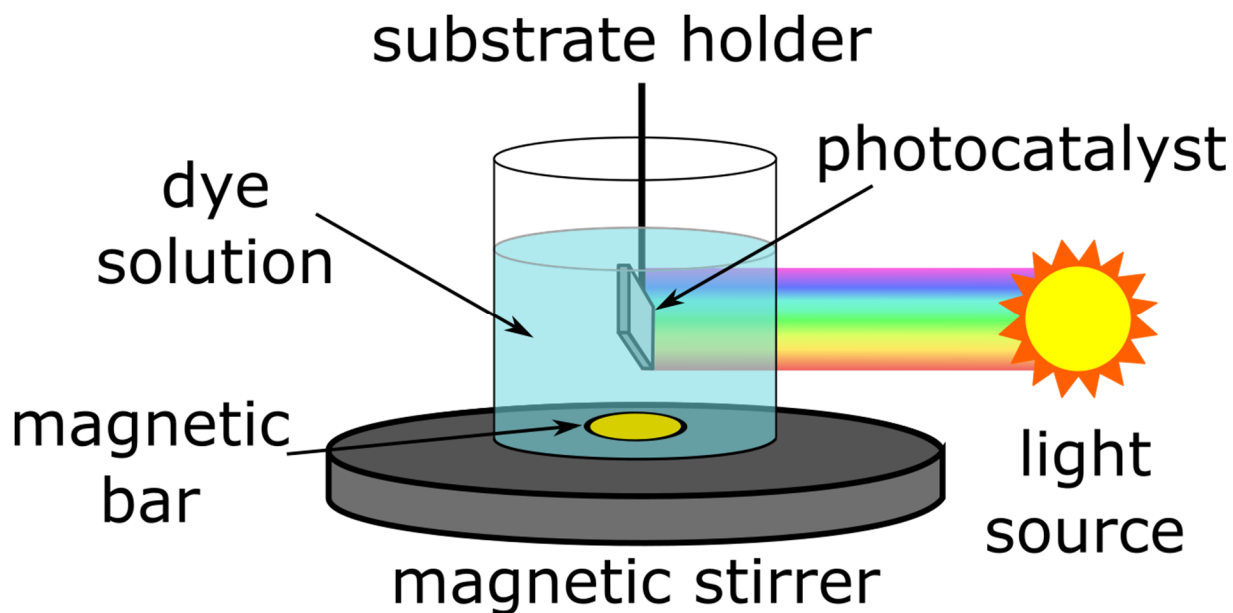


Figure 20: Schematics of a degradation reactor system with thin film photocatalyst.

2.5 Gas Sensing

The precise surface reactions during the gas sensing process is still not fully understood. As one theory suggests, the sensing is only indirectly influenced by the surface composition and lattice oxygen atoms, and instead the chemisorbed gas molecules and their added electron density result in the overall change in conductivity, while the change in resistance is measured during the analysis.^[175]

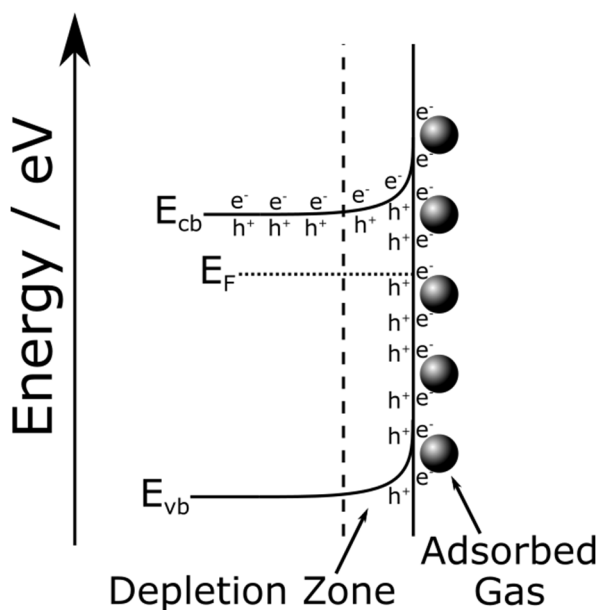


Figure 21: Scheme of band bending through chemisorbed oxygen and depicting the depletion zone. Adapted from [122].

During the interaction of the gas species with the sensor, the charge carriers diffuse as a result from either electrons being transferred from the adsorbed species to the material, or the other way around. This phenomena of two semiconductors being in contact, as discussed in section 2.3.2. It ultimately leads to an internal electric field and band bending. As the charge carrier concentration in the material decreases towards the surface, a depletion zone is formed, influencing the conductivity. This change is directly dependent on the amount of adsorbed gas molecules.^[176] Gas sensors follow similar requirements to the photoactive materials discussed before, as they need to be cheap, non-toxic and easy to produce, while performing reliable, remain small and use a low amount of power, with high selectivity and sensitivity. Semiconductor metal oxides are the most well investigated group of materials. Next to this, infrared conductivity, infrared adsorption, electro chemical or catalytic combustion gas sensors exist.^[177] The deposition and modification methods discussed before apply for the fabrication of gas sensing electrodes, and a list of common materials is depicted in Table 4.

Table 4: Common gas sensing materials.

Active Material	Gas Detected	Reference
TiO ₂	H ₂	[178]
	CO	[179]
	Ethanol	[180]
	Methane	[181]
α -Fe ₂ O ₃	Ethanol	[180]
	CO	[182]
	NH ₃	[182]
	H ₂	[182]
In ₂ O ₄	NH ₃	[183]
	NO _x	[184]
	H ₂ S	[185]
ZnO	CO ₂	[186]
	N ₂	[186]
	Ethanol	[187]

All the applications discussed above need new materials with high functional performance, low production cost and easy device integration. While the current methods for fabricating and modifying materials enable boosting the performances, each one is limited in its own way. A superior technique would involve the production and treatment in an energy and atom efficient way, minimizing material requirements while maximizing functional performance. A method like this is the use of laser systems, which will be discussed in the following section.

2.6 Laser-assisted Structuring Methods

The modulation of the topology and morphology of a metal oxide surface and the introduction of defects, vacancies or patterns, can produce unique properties^[188] compared to the bulk material.^[189] The following section focuses on laser-assisted methods due to their wide range of application, and will introduce the most important parameters and their effects on different materials.^[13]

2.6.1 Laser Patterning

Metals, dielectrics and semiconductors, when treated with lasers produce laser-induced periodic surface structures (LIPSS), firstly reported by Birnbaum in 1965.^[190] The actual physical formation mechanism is still not completely understood, with two most prominent theories. One is considering the interference of the incident light with the surface-scattered waves,^[191, 192] which presumes that the laser photons are either scattered or collectively excite the free electrons of the surface and forces them to oscillate. This would result in a nearly perfectly ordered periodic structure being imprinted on the surface. The other model considers the surface self-organization through hydrodynamical processes,^[193, 194] which would lead to periodic structures with a high degree of disorder. Neither approach can solely explain the observed properties of laser-driven patterning, yet a combined approach, under the assumption that the interference could cause weak periodic changes of the surface temperature which then supports the hydrodynamic processes, delivers a plausible explanation. The latter would result in defects in the periodic patterns, also shifting the absorption wavelength.^[195, 196] Many different laser-induced structures can be obtained, as seen in Figure 22.

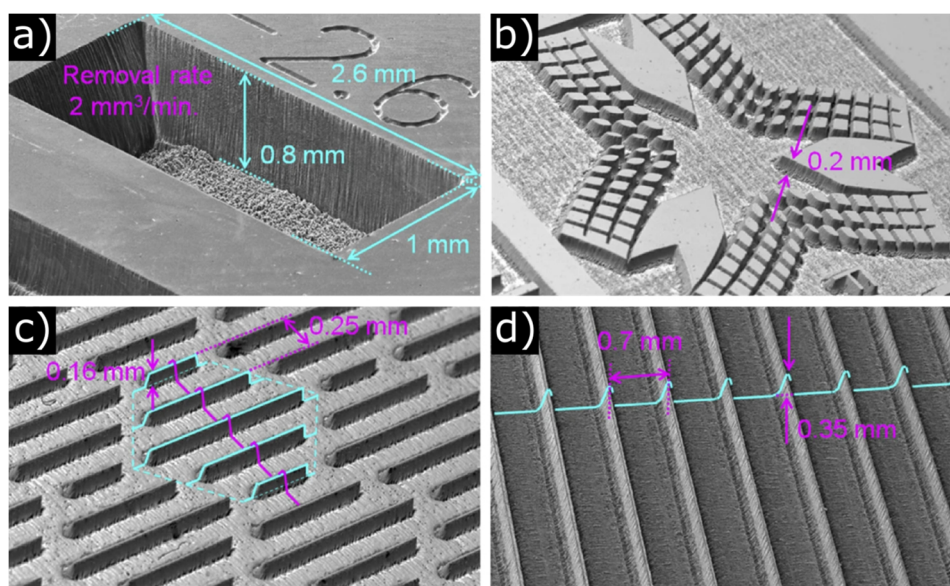


Figure 22: Examples of different laser-induced surface structures, ranging from rectangular cavity (a), the logo of the Center for Physical Sciences and Technology (b), bio-inspired shark skin-like structure (c) and drag reducing blade-riplet structure (d). Reprinted with permission from^[197], copyright Springer Nature 2018.

2.6.2 Different Laser Systems

A laser setup can be categorized into the physical state of the gain medium, for example solid-state, dye or gas systems.^[198, 199] Solid-state gain mediums include neodymium-doped yttrium aluminum garnet (Nd:YAG) or yttrium lithium fluorid (Nd:YLF) lasers, which have ~1% doping. Dye laser use organic dyes, which themselves are excited by another laser and allow a defined emission wavelength. Gas lasers, for example helium-neon, has advantages like very homogenous distribution of the gain medium, which allows for a much higher usable volume, in addition to better cooling because of better diffusion. A few examples of commercially available femtosecond laser systems can be seen in Table 5.

Table 5: Examples of commercially available ultrafast laser systems for material processing.

Laser System (Company)	Average Power	Energy per Pulse	Pulse-width	Repetition Rate	Central Wavelength	Reference
Tangerine SP (Amplitude Systems)	<50 W	<200 μ J	<150 fs to >10 ps	single shot to 40 MHz	~1030 nm	[200]
Tangor 300 (Amplitude Systems)	>300 W	>1 mJ	<500 fs to >10 ps	single shot to 40 MHz	~1030 nm	[201]
Spitfire Ace-PA-100 (Spectra Physics)	14 to 16 W	>1.4 mJ	<120 fs	1 to 10 kHz	780 to 820 nm	[202]
Solstice Ace (Spectra Physics)	5 to 8 W	>0.5 mJ	<35 fs	1 to 10 kHz	780 to 820 nm	[203]
Monaco 1035-80-60 (Coherent)	<60 W	~80 μ J	<350 fs	single shot to 50 MHz	~1035 nm	[204]
FemtoFAB (Workshop of Photonics)	<20 W	<2 mJ	200 fs to 10 ps	1 kHz to 1 MHz	~1030 nm	[205]

Note: As a laser system consists of many different parts, distinguishing it only by e.g. the gain medium results in important information missing to reach the above mentioned values.

2.6.3 Influence of Structuring Parameters on Metals and Metal Oxides

Lasers can precisely affect a small, local area due to the beam being focused on a very small spot through several optics, and can be used for different methods due to their many tunable parameters.^[206] These include structuring processes like pinpoint ablation, local laser annealing or patterning.^[207]

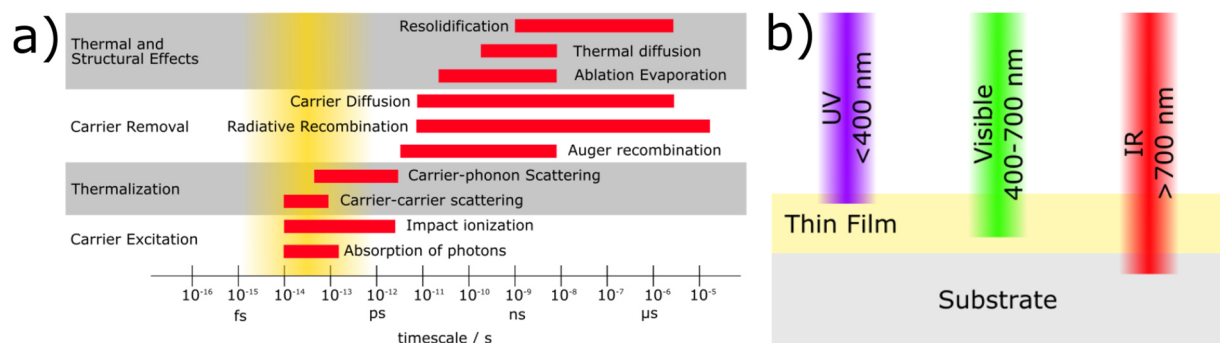


Figure 23: The timescales of energy transition during the laser excitation of a semiconductor (a), adapted from ^[208], and wavelength dependence on the penetration depth (b). Adapted from ^[209].

The treatment depth of the beam in materials is mostly depending on the laser wavelength, where the penetration depth decreases with higher energy. This is why UV lasers can be used to dominantly treat the surface of thin films, while IR lasers are able to affect the bulk. Additionally, some materials can be transparent to certain wavelengths, allowing focused treatment in multi-layer systems. The beam power determines whether the substrate is melted, vaporized or turned into a plasma, as higher intensity results in more energy absorbed. The dwell time, also called pulse length, is the energy distribution over time, with ultra-short pulses ($10^{-9} \text{ s} > t_{\text{pulse}} > 10^{-15} \text{ s}$) transferring it nearly instantly, resulting in very high peak power. Longer pulses ($10^{-2} \text{ s} > t_{\text{pulse}} > 10^{-5} \text{ s}$) have lower peak power, as the intensity is distributed over a longer window of time. Alternatively, unpulsed beams can be used in continuous wave mode,^[210] which is often used for melting or cutting, with the downside of increased power fluctuation.^[199] The diameter of a focused beam affecting the substrate, called spot size, distributes the beam over a fixed area. If the whole energy is exposed to a very small area, a high peak intensity similar to ultra-short pulses is reached. Bigger areas lead to lower peak intensity, and the energy distribution over these spots are often resembling a Gaussian curve, with the highest intensity in the center and decreasing towards the edges, depending on the laser setup, while different shapes, like squares or circles, can also be used.

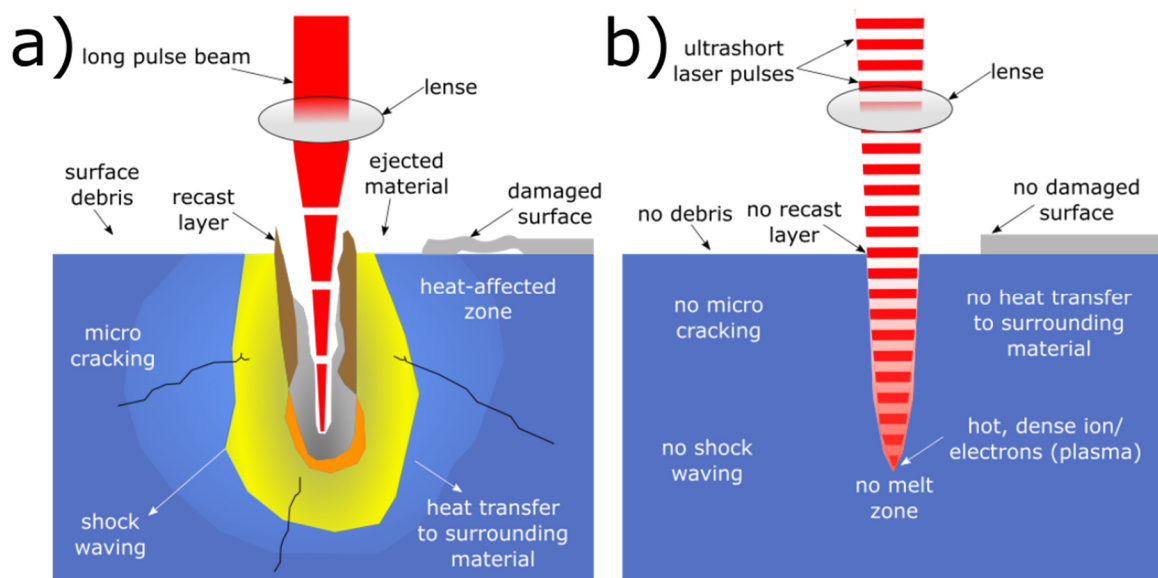


Figure 24: The comparison of long (a) and ultra-short pulses (b) on thin films and substrates. Adapted from ^[211].

2.6.4 Laser Processing Techniques

By tuning these parameters, a plethora of effects can be achieved, like the physical removal of solid materials using high intensity and ultra-short pulses. This leads to high energy distribution on a small area, which breaks the chemical bonds and results in a gas or plasma. Longer pulses or higher intensities can result in heat distribution towards the untreated area, which can be used

to etch the surface of a film, increasing its roughness and surface area, or even create 1D structures. On the other hand, longer pulses and lower intensity with repeated pulses can lead to local melting through the accumulation of heat. In this case, depending on whether the atoms are given enough time to rearrange in the lattice, amorphous materials can be crystallized through this laser treatment. Shorter pulses can prevent this and force surface restructuring through etching and without atomic rearrangement. For this, the pulse duration needs to be below the time necessary for the thermal diffusion of the atoms, which roughly starts around 10^{-10} s. Laser melting can also induce local solid-solid reactions, create new junctions in a multi-layer system, or for hardening the surface.

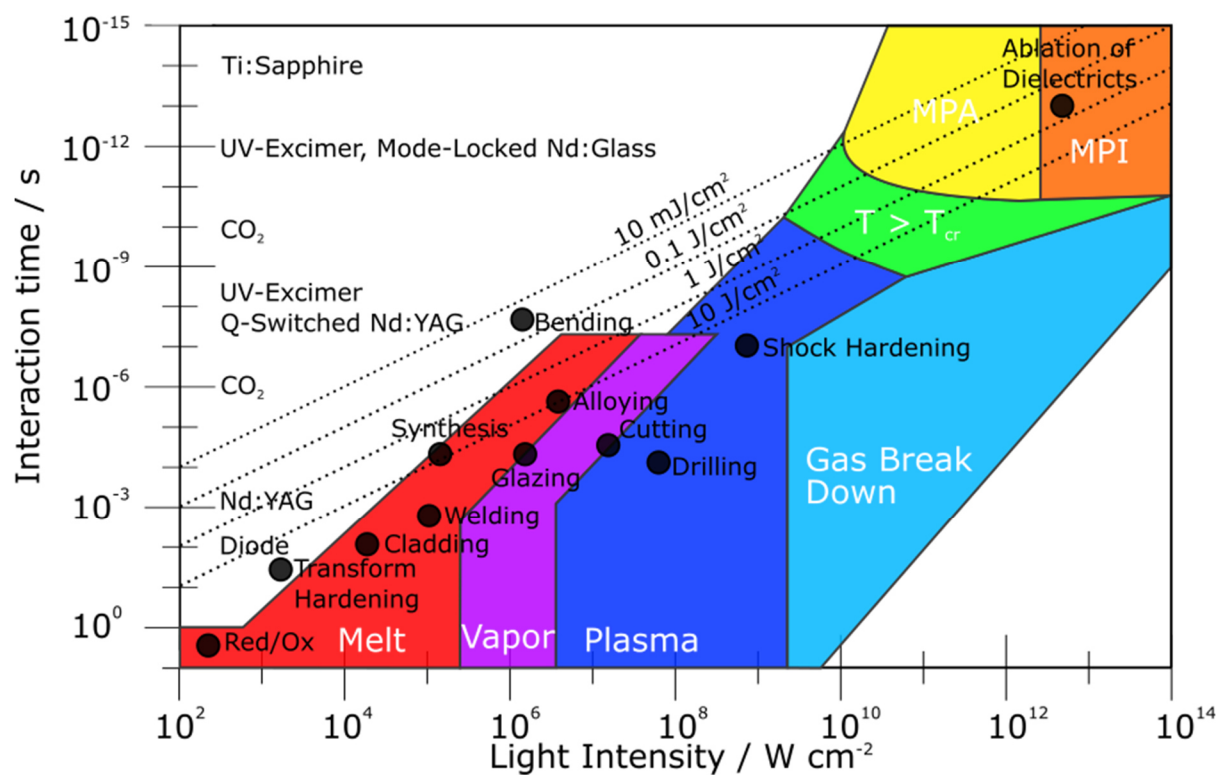


Figure 25: Overview of the different laser treatment options with different pulse lengths and light intensities. Adapted from [9].

Additionally, by laser treatment a material can be changed on a chemical level, for example by separating bimetallic oxides into two phases or by partially oxidizing/reducing them. As the process can be performed in air or with different gases, they have varying influence on the surface during the treatment. Laser systems can also be used for depositing materials, for example by laser beam etching, similar to the sputtering process.

2.7 Other Strategies for Surface Modifications

2.7.1 Physical Surface Modification Methods

The physical removal of material is usually a dry process and can be achieved through many different methods, which include mechanical methods like drilling, stamping or water jetting. They are usually of low cost and very flexible with their substrates choice, and can result in many different structures. A more precise but expensive method is the electron beam lithography,^[212] which allows precise evaporation of material with a spot size down to $\sim 1 \mu\text{m}$, without the need of masks. In contrast, plasma etching, where ionized gas collides with the substrate to partially remove atoms, affects the whole substrate area, resulting in random disorder. Masks and templates can be used to limit the treated areas, which allows to produce order/disorder junctions. Nevertheless, these methods lead to gaseous etch products, which are commonly removed by a vacuum system.

2.7.2 Chemical Surface Modification Methods

Chemical processes are often processes involving liquids that can react with the film or substrate material, and can be much more material selective with a higher etching rate than physical etching. Yet it is less precise, with increased removal of material under masks. The process itself uses strong bases (e. g. ammonium hydroxide) or strong acids (e. g. hydrochloric, hydrofluoric or phosphoric acid), which react selectively with the target material to dissolve it. This leads to a significant amount of waste, as the dissolved material reduces the effectiveness of the chemicals during prolonged processes, increasing the cost compared to physical etching. On the other hand, the equipment is simple and cheap when compared to vacuum methods. A common example for chemical etching is the removal of fluorine doped tin oxide (FTO), a transparent conductive substrate common for solar harvesting application. In this process, zinc paste and hydrochloric acid, in which FTO is stable, are used as chemicals.^[213] The etching process occurs in several steps, with zinc negatively charging the FTO surface, attracting H_3O^+ molecules, which react with the zinc to form ZnCl_2 and H_2 . The hydrogen gas diffuses into the FTO lattice and reduce the Sn^{4+} of FTO to metallic tin, which is dissolved in the hydrochloric acid, completing the etching process.^[214]

3 Results and Discussion

3.1 Establishment of Laser Treatment Parameters

The development of a reproducible laser treatment process was a mandatory first step to allow the investigation of surface patterning systems discussed in later sections. Through systematic screening of processing properties correlation, the optimal regimes (e.g. for laser fluence or pulse duration) were determined. Additionally, two different laser structuring setups (Spitfire and Tangerine) were investigated, and the necessity of metal absorber films were shown to show the advantages of a laser beam absorbing thin film.

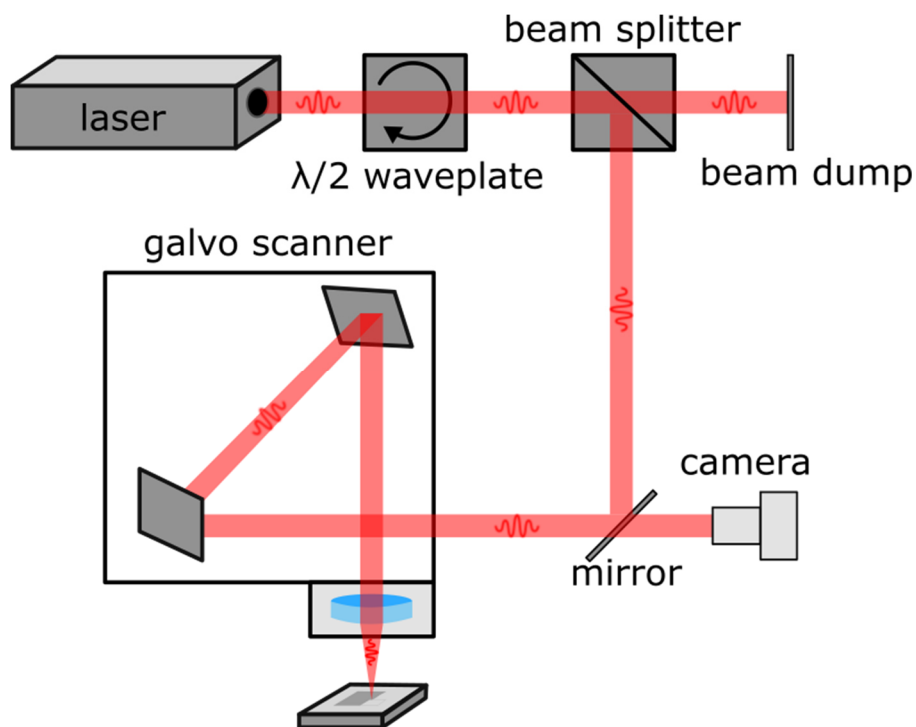


Figure 26: Experimental setup for laser treatment processes. Adapted from ^[141].

It has to be noted that only a few of the most relevant optimization steps were discussed, while the corresponding parameters for each optimized and further analyzed system were part of their respective sections.

3.1.1 Laser Patterning of Metal Systems

The first investigation was performed on metal systems consisting of either aluminum or titanium coated with a metal oxide film of either TiO_x or Fe_xO_y by PE-CVD. These were either amorphous or annealed through an additional heat treatment step after deposition, and then laser treated.

3.1.1.1 Influence of Different Laser Setups on TiO_x on Al

Two different laser treatment setups, the Tangerine and Spitfire systems, were used. Their parameter were different in pulse length, optical systems, repetition rate and wavelength (Tangerine $\tau_p \approx 280$ fs, $f = 2000$ kHz, $\lambda = 1030$ nm, $d_{spot} = 33$ μm and Spitfire $\tau_p \approx 100$ fs, $f = 5$ kHz, $\lambda = 800$ nm, $d_{spot} = 10$ μm , more details in section 4.3).

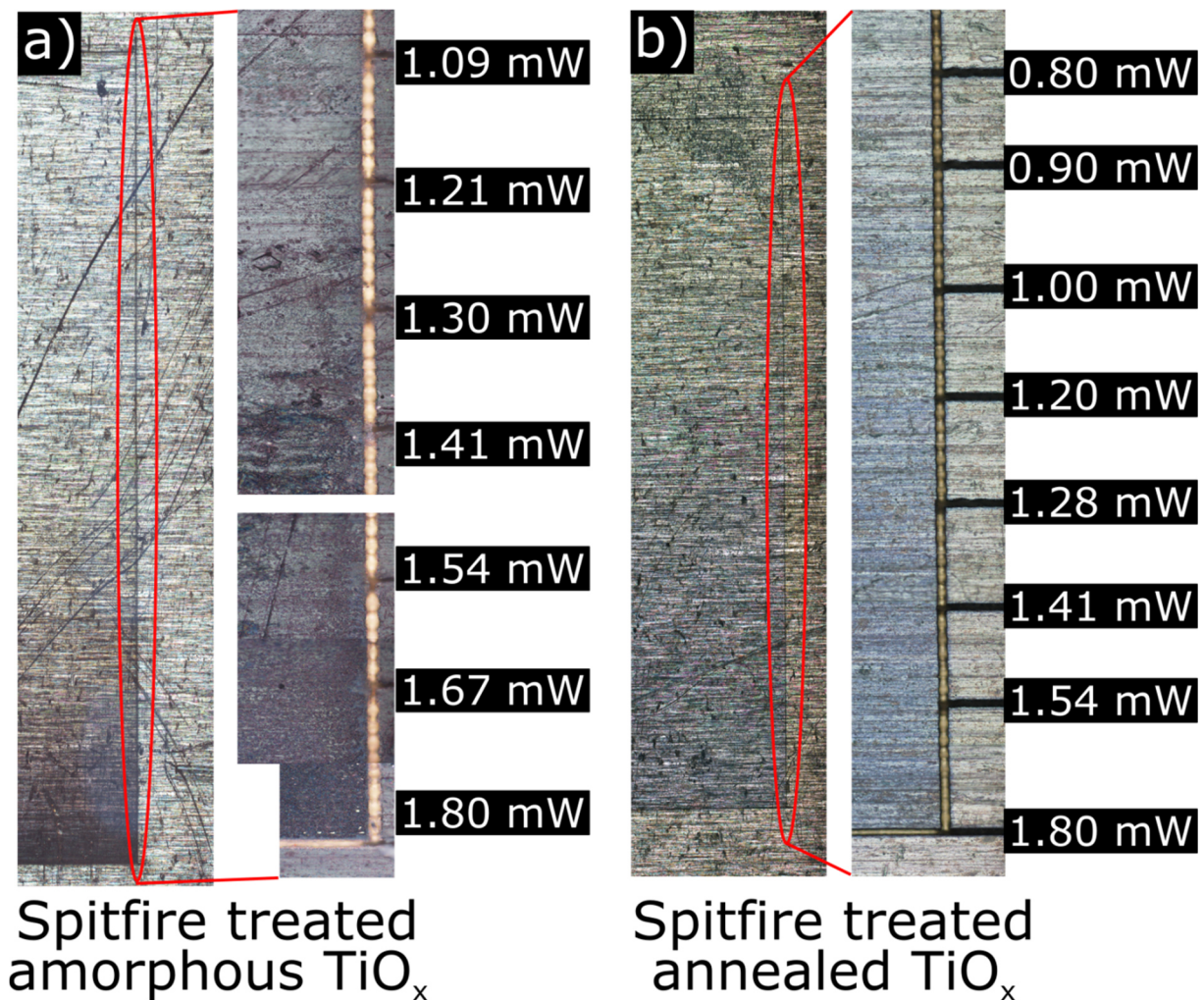


Figure 27: In plane images of the amorphous (a) and annealed laser treatment with the Spitfire system of TiO_x on Al (b) with their respective pulse power.

Each was used on TiO_x systems, and the color shift resulting from the periodic structures was investigated by optical microscope. In this first step, the possible ablation of the coating did not matter, as further optimization steps on preventing this were performed later. The treatment with the Spitfire setup on the annealed TiO_x system (see Figure 27a) showed a color shift towards higher wavelengths from violet and dark blue towards light blue, until reaching ~ 1.00 mW. Below this, no structures impacting the optical properties could be observed, as the color was identical to the untreated area, which was a result from impurities. These were very common in PE-CVD processes with alkoxide precursors, where the as-grown film contained a

high amount of carbon impurities, often $M\text{-CH}_3$.^[215-218] The amorphous samples (see Figure 27b) exhibited a darker color until ~ 1.54 mW, which could be a result from light interference in the periodic structure,^[219] as the amorphous layer was around ~ 1.3 μm thick. Below this, dark blue changed to light blue until ~ 1.30 mW, and no observable change with lower power. This sample revealed a bigger color gradient compared to the annealed sample, even though the treatment power was roughly the same. This could be due to the higher carbon content and thicker amorphous film, as annealing would both reduce embedded carbon and produce a denser, crystalline film.

Using the Tangerine setup on the annealed TiO_x system (see Figure 27c) revealed, next to a dark stripe with a too high starting intensity, a color shift towards higher wavelengths from dark green towards light green around ~ 264 mW, and the same color as the untreated area below ~ 224 mW, which would mean a lack of structures that affect absorption and reflection. The amorphous system (see Figure 27d) showed inhomogeneous structural effects on the surface at around ~ 400 mW, with several bright green stripes and randomly distributed particles, which partially appear until ~ 350 mW. This showed the increased power fluctuation of the beam, a major problem with higher intensity treatment. The color ranged from violet in some areas and green in others, with no observable change below ~ 224 mW. There was no clear color gradient which could be a result from increased fluctuations, and was not seen with the Spitfire system or annealed sample. The amorphous film possibly contained increased dangling bonds due to higher disorder and more voids,^[220] preventing high controllability.

It has to be noted that while a much higher pulse power in the order of two magnitudes was used with the Tangerine setup, its higher repetition rate reduced the average laser power to around one order of magnitude. When including the different focusing optics and incident beam diameters (Tangerine $f_{\text{optic}} \approx 63$ mm, $d_{\text{beam}} = 2.6$ mm; Spitfire $f_{\text{optic}} \approx 100$ mm, $d_{\text{beam}} = 10$ mm, more details in section 4.3), the resulting focal spot of the Tangerine setup ($d_{\text{spot}} = 33$ μm) was roughly three times larger than the Spitfire ($d_{\text{spot}} = 10$ μm). Together with the laser energy distribution over an area (laser fluence), both systems remained comparable, yet the much higher repetition rates still resulted in problematic heat accumulation.

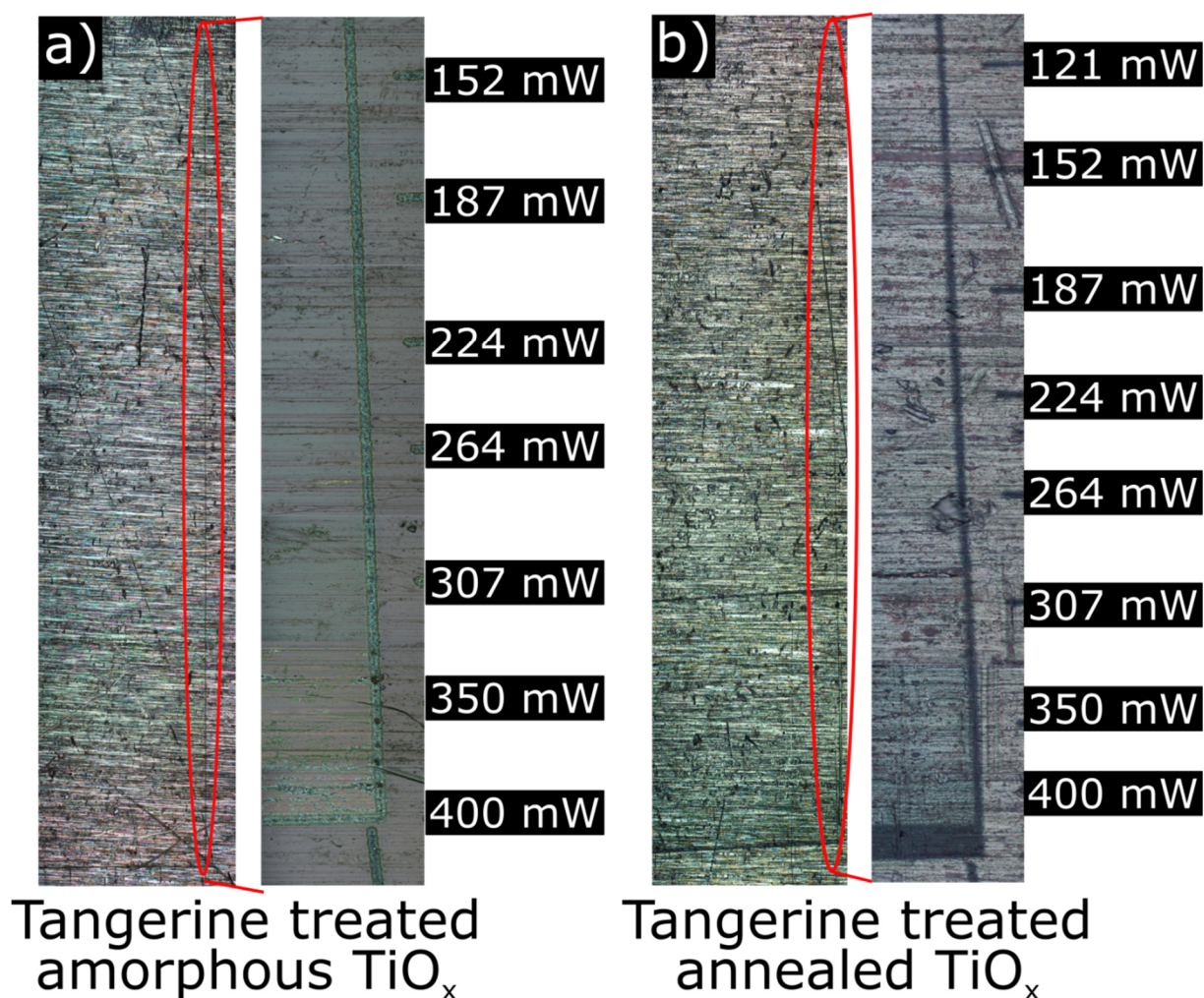


Figure 28: In plane images of the amorphous (a) and annealed laser treatment with the Tangerine system of TiO_x on Al (b) with their respective pulse power.

Unless otherwise specified, the Spitfire setup was used to perform the laser treatment in this thesis because of its lower pulse duration resulting in higher photon densities for constant pulse energies, with higher chance of nonlinear modification while keeping heat accumulation minimal. Nevertheless, other materials not investigated in this work, with different linear and nonlinear absorption coefficients, could need higher repetition rates for the desired modifications.

3.1.1.2 Influence of Focal Point Position on TiO_x on Al

In order to investigate the effect of the focal point position in comparison to the laser treatment power, amorphous TiO_x was used (see Figure 29a). The power was reduced as the x coordinate increased, starting at 1.98 mW with $x = 0$ cm and ending at 0.11 mW with $x = 10$ cm. The focal point, starting above the film with $y = 0$ cm, was positioned directly on the surface at $y = 0.5$ cm, and went below the film as the y coordinate further increased to $y = 10$ cm. The sample picture revealed full ablation of the top layer and oxidation of the substrate at high laser

powers (>1.15 mW) and a focal point close to the surface, with focusing above the surface having a more prominent effect than below, as the white areas were most likely consisting of Al_xO_y (see Figure 29a). The physical modification of the surface by power variation and fixing the focal point directly on the surface was investigated by SEM (see Figure 29b). This revealed a full ablation above ~ 1.15 mW, with a highly structured yet damaged surface, as seen with the increased amount of recast layers. This observation corresponded to the white color of the sample, indicating an oxidized substrate. Below this energy level, where the color changed from white to black, a partially ablated top layer could be observed, with both the partially exposed substrate and metal oxide film being highly structured. The damage was reduced around ~ 0.90 mW and below, with fewer structures until ~ 0.39 mW, which was the minimum threshold to observe any kind of surface structuring effect.

The effect of the focal point position with a fixed laser power of ~ 1.98 mW was also investigated by SEM (see Figure 30). By positioning the focal point above the film, the results were similar to a lower power of ~ 1.15 mW, with focus on the surface, where the top layer partially ablated while both, it and the exposed substrate, became highly structured. When the focal point came closer to the film, full ablation and substrate oxidation could be observed, with a high degree of structures, and a damaged surface with recast layer. Further below the surface, the metal oxide remained fully intact while containing laser induced patterns, similar to ~ 0.56 up to ~ 0.90 mW with the beam focused on the surface. If the focal point was even further below the surface, no structural effect could be observed.

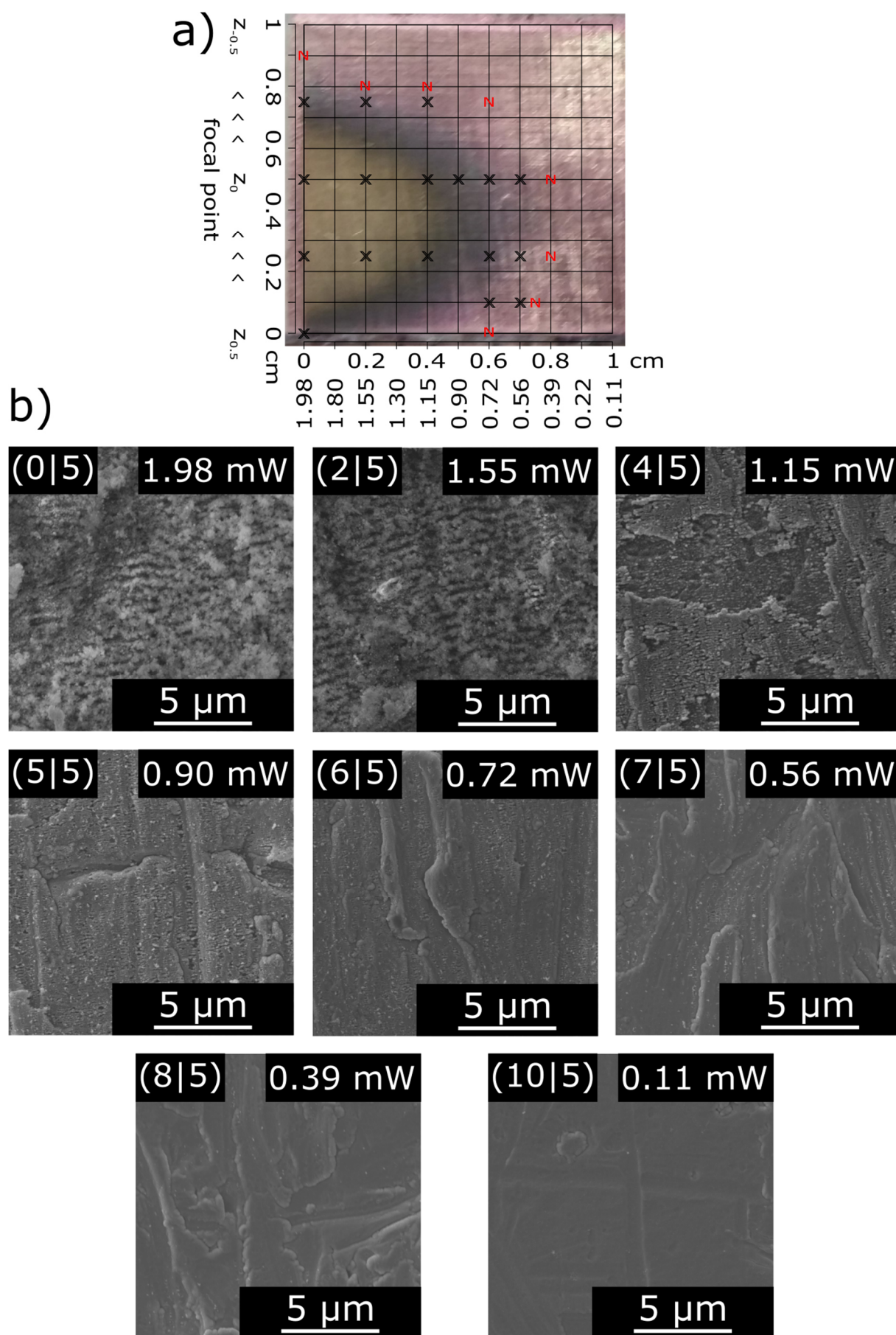


Figure 29: The measurement grid of amorphous laser treated TiO_x on Al (a), with X is marking periodic structures, while N marks no structures, and their respective SEM images with fixed focal point and varying laser power (b).

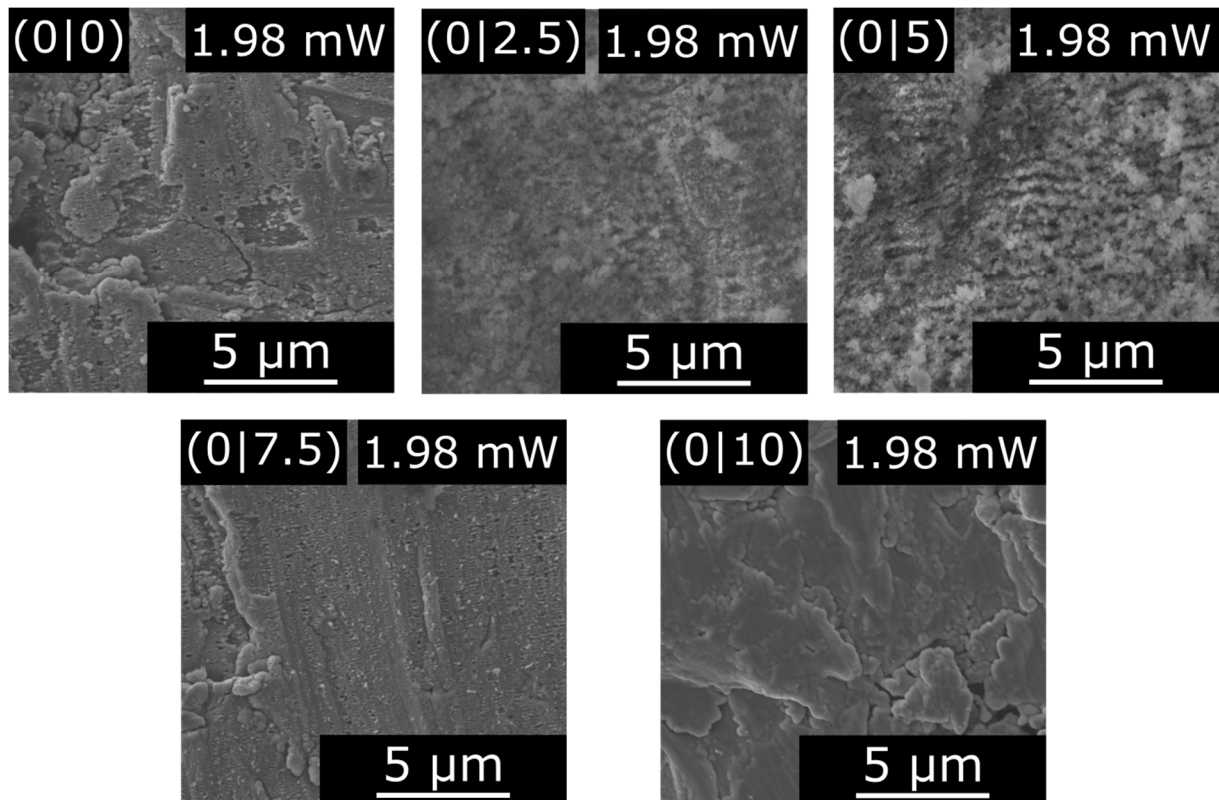


Figure 30: In plane SEM images of amorphous laser treated TiO_x on Al with fixed laser power and varying focal point, including their coordinates from the previous figure.

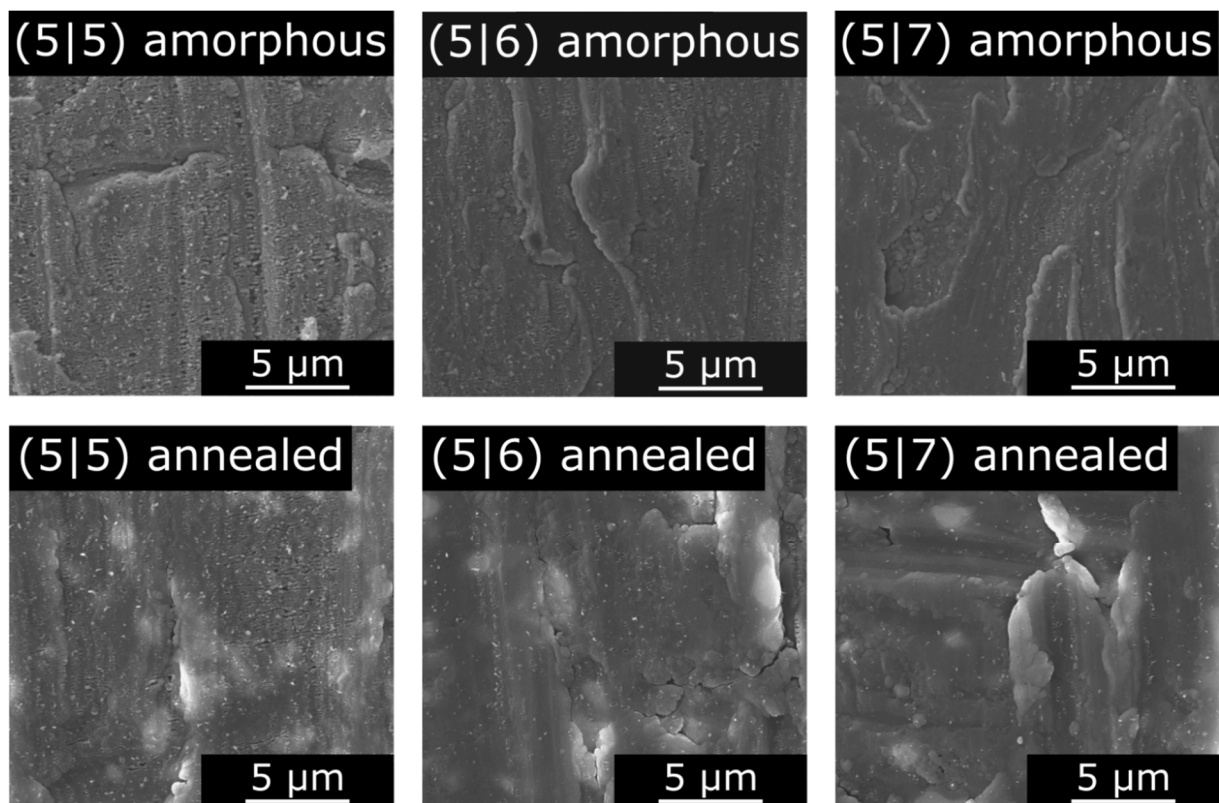


Figure 31: In plane SEM images of laser treated TiO_x on Al before and after annealing at 550°C for 2 hours.

As the physical effect on the surface from the focal point position could be compensated with variation of laser power, it was fixed to focus directly on the surface, keeping the beam energy as main parameter to influence surface structures, further boosting reproducibility.

The effect of post annealing on laser induced structures was investigated using the TiO_x system (see Figure 29a) and comparing it before and after heat treatment. The energy regime between ~ 0.56 to ~ 0.9 mW was observed, while the focal point position remained on the surface. These areas had structured metal oxide films with no ablation, making them useful for comparing the influence of the heat treatment. Post annealing had no influence on the induced patterns, while still allowing crystallization. This was important for processes involving an annealing step after laser induced structuring, necessary for PEC electrodes.

The variation of laser parameters showed a similar trend with structural changes, largely depending on laser focal point and fluence. For comparable analysis, amorphous titanium and iron oxides (TiO_x , Fe_xO_y) depositions on metal and quartz substrates were studied in detail in later sections. Titanium substrates covered with titanium oxide was further investigated in section 3.2.2, where the results of an optimized process are discussed.

3.1.1.3 Influence of Laser Spot Sizes on Fe_xO_y on Ti Systems

The effect of different spot sizes with $d \gtrsim 10 \mu\text{m}$ (see Figure 32) and $d \gtrsim 100 \mu\text{m}$ (see Figure 33), was investigated in the case of amorphous iron oxide (Fe_xO_y) deposited on Ti substrates by PE-CVD. The substrate was changed to titanium to enable water splitting reactions in later experiments, as they need annealing steps. In case of aluminum, this would result in a blocking layer consisting of Al_2O_3 . Titanium oxide on the other hand, either anatase or rutile, would create an additional photoactive layer. Fe_xO_y was used as coating to easily distinguish between fully ablated and periodically patterned metal oxide using EDX analysis.

With a laser treatment power ranging between ~ 1.80 and ~ 1.55 mW (see Figure 32, position (0|5) and (2|5)), the top layer was fully ablated, as there was no red iron oxide film visible. While this could be an effect of the highly patterned iron oxide, EDX measurements (see Table 6) revealed iron content far too low to be from the coating. Instead, it resulted from substrate impurities, which could be up to 0.5-wt% according to the vendor (see section 4.1). The ablation also led to the ablated layer being partially recasted onto the surface, also observable in the SEM images. By reducing the laser power to ~ 1.50 mW (see Figure 32, position (3|5)), the Fe_xO_y layer remained partially intact, yet with many cracks and craters.

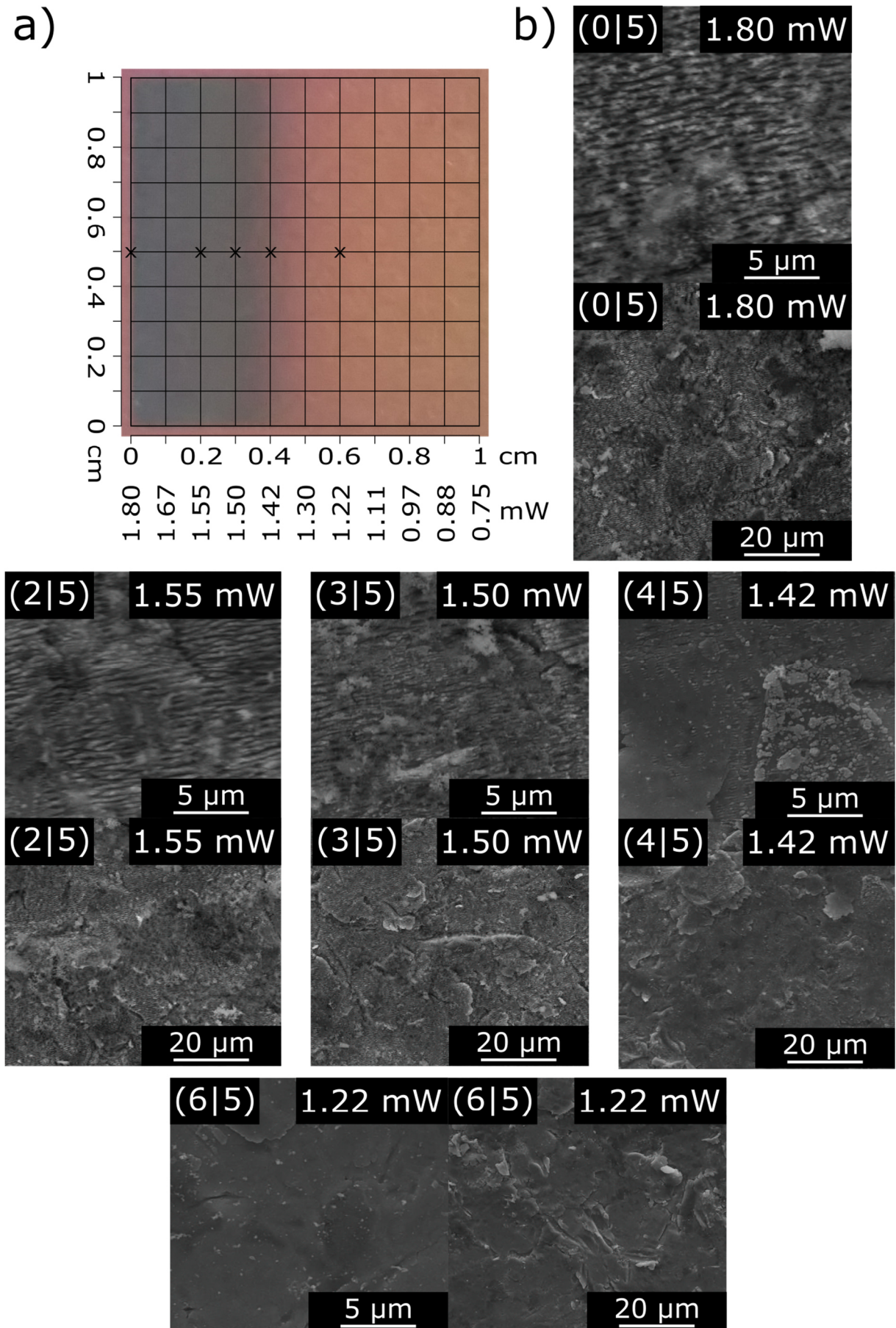


Figure 32: The measurement 1 x 1 cm² grid of annealed laser treated Fe_xO_y on Ti with a spot size of 10 μm (a), with X marking measured positions, and their respective in plane SEM images (b).

Table 6: EDX compositions of annealed laser treated Fe_xO_y on Ti at different laser powers, spot size of 10 μm .

Laser Power	Composition (EDX)				SEM Images
	Ti (%)	O (%)	Si (%)	Fe (%)	
~1.80 mW	55.11	40.69	3.44	0.75	Figure 32 (0 5)
~1.55 mW	49.36	45.21	3.29	2.16	Figure 32 (2 5)
~1.50 mW	46.54	46.84	2.67	3.96	Figure 32 (3 5)
~1.42 mW	37.24	53.14	4.85	4.67	Figure 32 (4 5)
~1.22 mW	36.47	54.27	4.04	5.22	Figure 32 (6 5)

An increased spot size would lead to lower total time needed for a full laser treatment experiment. Additionally, the screening was performed with a higher starting energy, as the previous analysis on the same system showed barely any structural effect below ~1.22 mW (see Figure 32, position (6|5)). While the top layer would definitely be ablated, the effect of high power treatment on the substrate could still be investigated. The treatment between ~2.18 and ~2.99 mW (see Figure 33b and c) showed this effect. The substrate surface turned into highly structured islands, separated by deep craters, which shrank with decreased beam power. The iron signal (see Table 7) in the EDX measurement resulted from substrate impurities (up to 0.5-wt% according to the vendor, see section 4.1), while the dark color resulted from improved scattering and absorption. By laser structuring with ~1.83 mW (see Figure 33d), which caused full ablation when a smaller spot was applied (see Figure 32b), instead led to a highly damaged and partially ablated top layer with deep cracks, supported by the increased iron signal. The substrate color turned towards red. By further decreasing the energy towards ~1.58 mW (see Figure 33e), homogenous ripples could be obtained. The degree of structuring decreased even further at ~1.41 mW (see Figure 33f) and ~1.23 mW (see Figure 33g), while the color shifted towards orange. Treating with a pulse energy of ~1.06 mW resulted in nearly no observable structures (see Figure 33h). XRD analysis could not be performed, as the iron oxide layer was too thin in addition to the rough substrate to be properly measured with a molybdenum source.^[221]

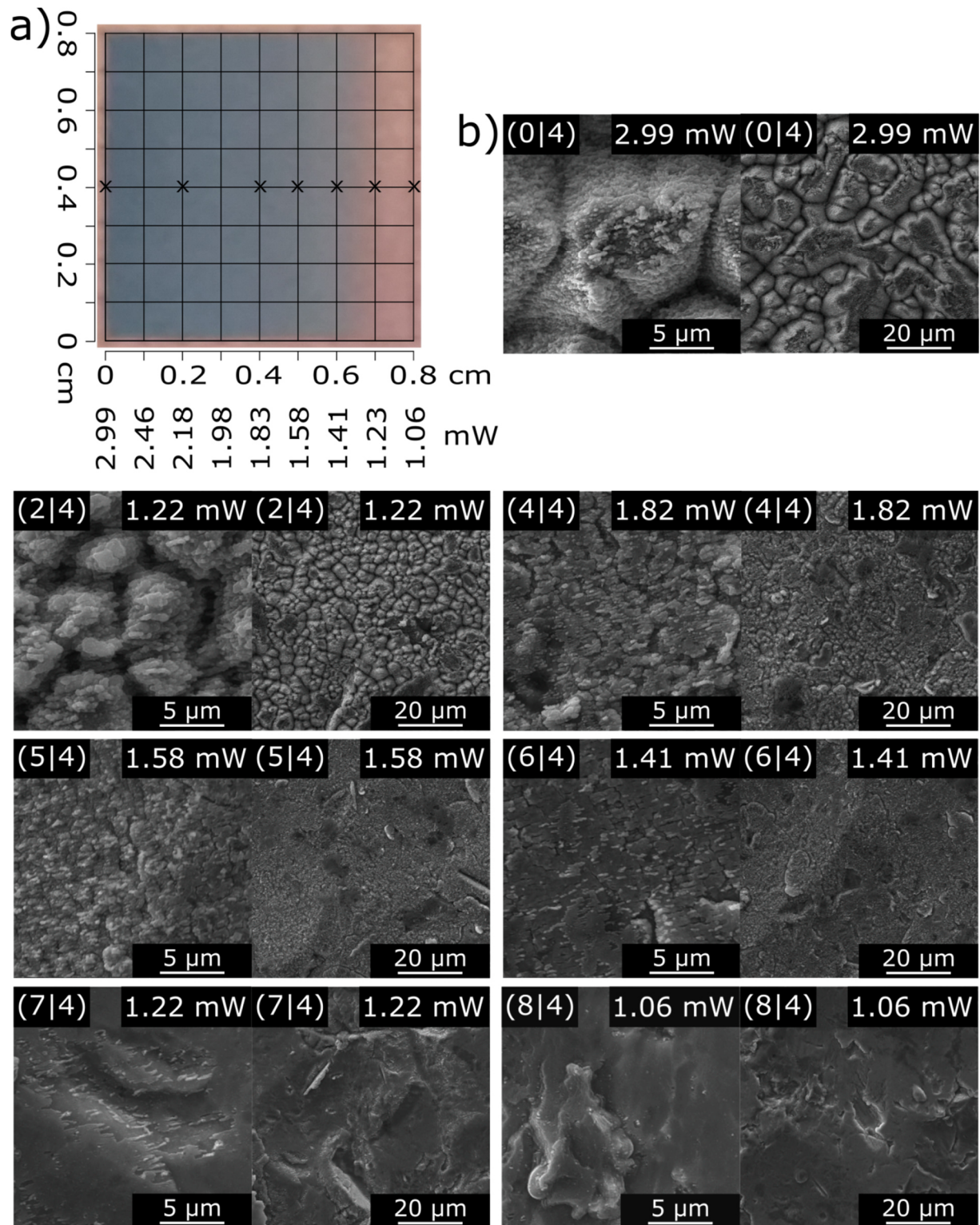


Figure 33: The measurement grid of annealed laser treated Fe_xO_y on Ti with a spot size of $100\ \mu m$ (a), with X marking SEM measured positions (b), including their coordinates.

Table 7: EDX compositions of annealed laser treated Fe_xO_y on Ti at different laser powers, spot size of $100 \mu\text{m}$.

Laser Power	Composition (EDX)				SEM Images
	Ti (%)	O (%)	Si (%)	Fe (%)	
~2.99 mW	46.15	50.05	3.03	0.76	Figure 33 (04)
~2.18 mW	47.73	48.6	2.43	1.24	Figure 33 (24)
~1.83 mW	36.23	54.65	5.62	3.51	Figure 33 (44)
~1.58 mW	34.55	55.14	5.8	4.51	Figure 33 (54)
~1.41 mW	30.43	36.23	5.62	3.51	Figure 33 (64)
~1.23 mW	39.27	54.13	1.04	5.57	Figure 33 (74)
~1.06 mW	34.96	53.01	3.43	7.8	Figure 33 (84)

Overall, the smaller spot size resulted in reduced fluctuation and higher degree of control over the surface structures, so it was exclusively used for further experiments. At higher powers the coating was fully ablated, leading to a structured substrate. The effect on the metal oxide thin films could be investigated at lower intensities. The former was further optimized and led to the development of pre-structured substrates used in PEC water splitting, as discussed in section 3.3, while the latter led to the development of processes which enhanced many properties of metal oxide thin films, as discussed in section 3.2.2.

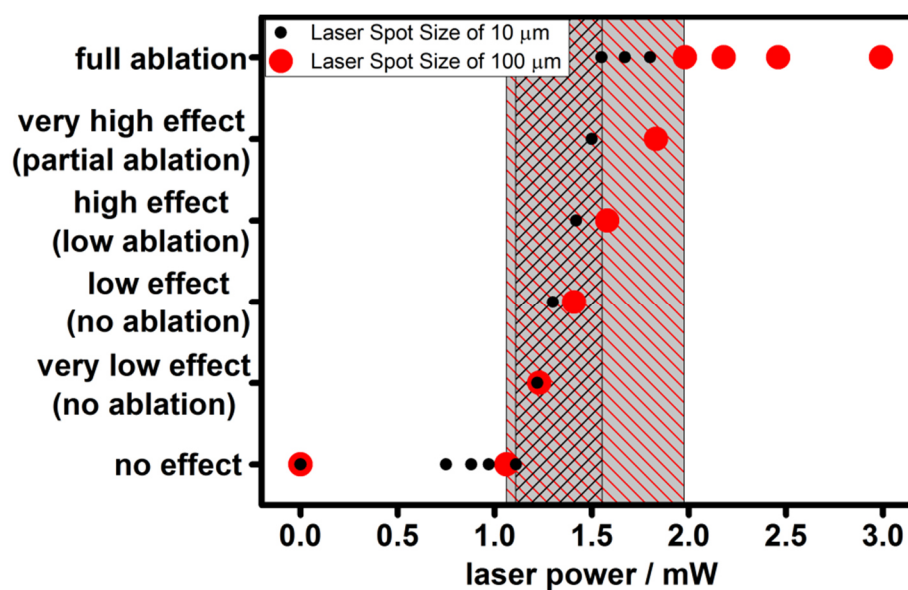


Figure 34: Correlation of laser power and structural effect using different spot sizes, with the usable regime outside of full ablation and no structural effect highlighted.

3.1.2 Laser Processing of Quartz Systems

Transparent quartz as substrate allowed the fabrication of multi-junction systems with precise interface disordering due to energy absorption focused on a sputtered metal layer. These systems were more sensitive towards power fluctuation, especially energy spikes, very thin metal film might be evaporated together with the top layer at the beginning of a laser process. While a combination of TiO_x and Fe_xO_y was used, a double stack of the same material, or other metal oxides not investigated in this research, are possible using the same procedure discussed here. None of the samples were annealed, as the sputtered metal, even when positioned between two metal oxide films, caused ablated areas during heat treatment.

3.1.2.1 Influence of Metal Interlayer on Quartz Systems

The necessity of a laser absorber layer next to the metal oxide films was investigated by comparing quartz systems covered with TiO_x and Fe_xO_y , either with or without a sputtered layer. The metal free systems was treated with a laser power between ~ 1.3 and ~ 2 mW (see Figure 35a), beginning with the higher intensities on the left side. Most of the area showed very high ablation, seen in the SEM image (see Figure 35b). Without a metal layer, nearly all of the beam power was absorbed uncontrolled as multi-photon, leading to highly chaotic and randomized ablation. Full removal of the top layer could be easily identified by SEM, as the non-conductive substrate was charged by the electron beam during the analysis, resulting in bright white areas. The area around ~ 1.7 mW (see Figure 35c) revealed highly structured TiO_x surrounded by the substrate, with no Fe_xO_y according to the EDX analysis (Fe signal: ~ 0.7 and ~ 6.4 eV). The surface structures exhibited no gradual decrease with lower laser power, and instead increased or decreased randomly. The same phenomena could be observed in the laser treatment regime of around ~ 1.3 mW (see Figure 35d), with the deviation in structure even more prominent. No Fe_xO_y layer remained in this laser treated area, according to EDX analysis.

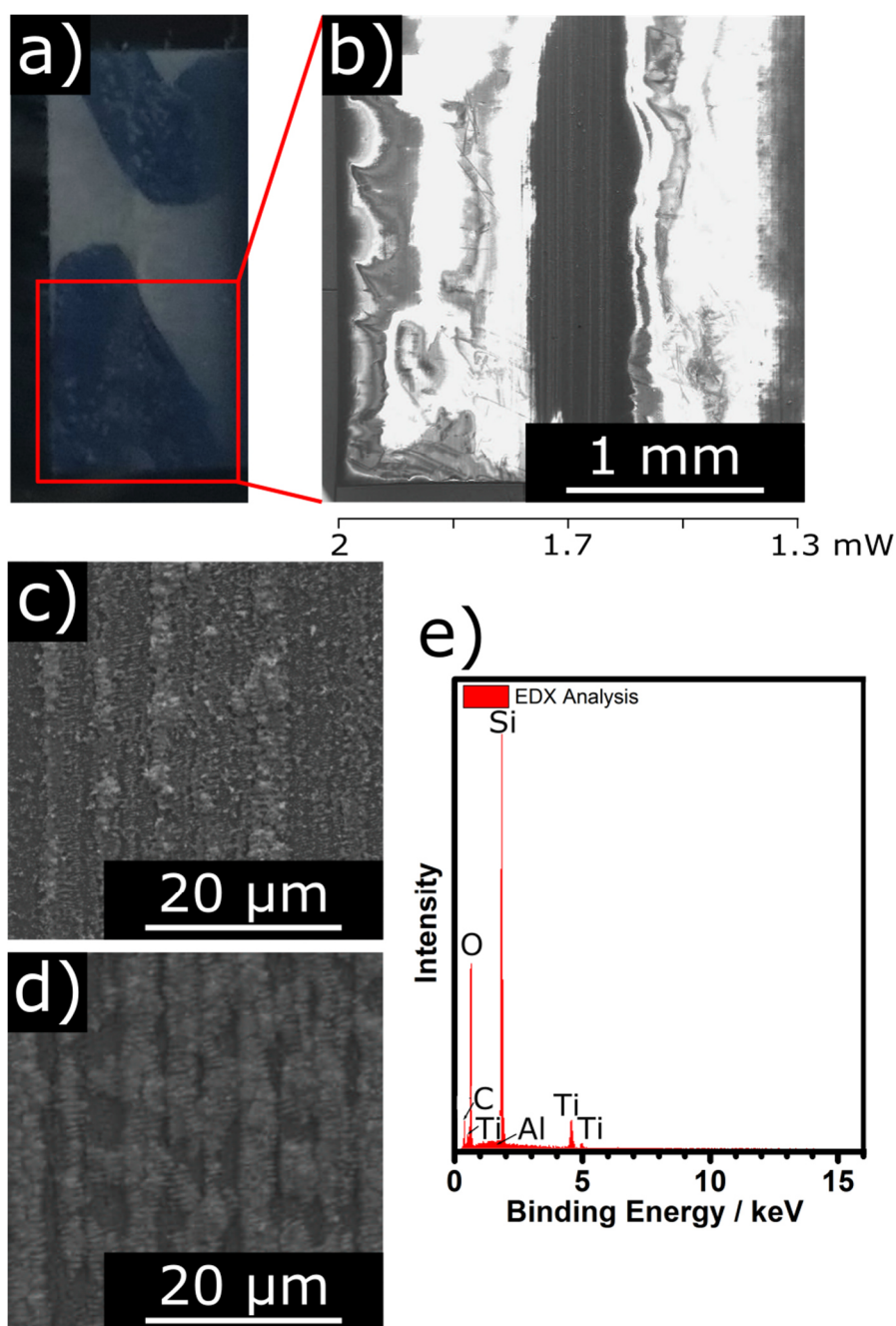


Figure 35: Picture of a metal free laser treated $\text{Fe}_x\text{O}_y/\text{TiO}_x$ on quartz (a) and the respective in plane SEM overview image, and zoomed in images of the area treated with ~ 1.7 mW (c) and ~ 1.3 mW (d), including the EDX analysis (e).

The laser treatment without a metal layer did not show any controlled absorption, and instead was based on random absorption through multi-photon processes. This also led to a lack in reproducibility, showing the necessity of either a metal as substrate or sputtered thin film.

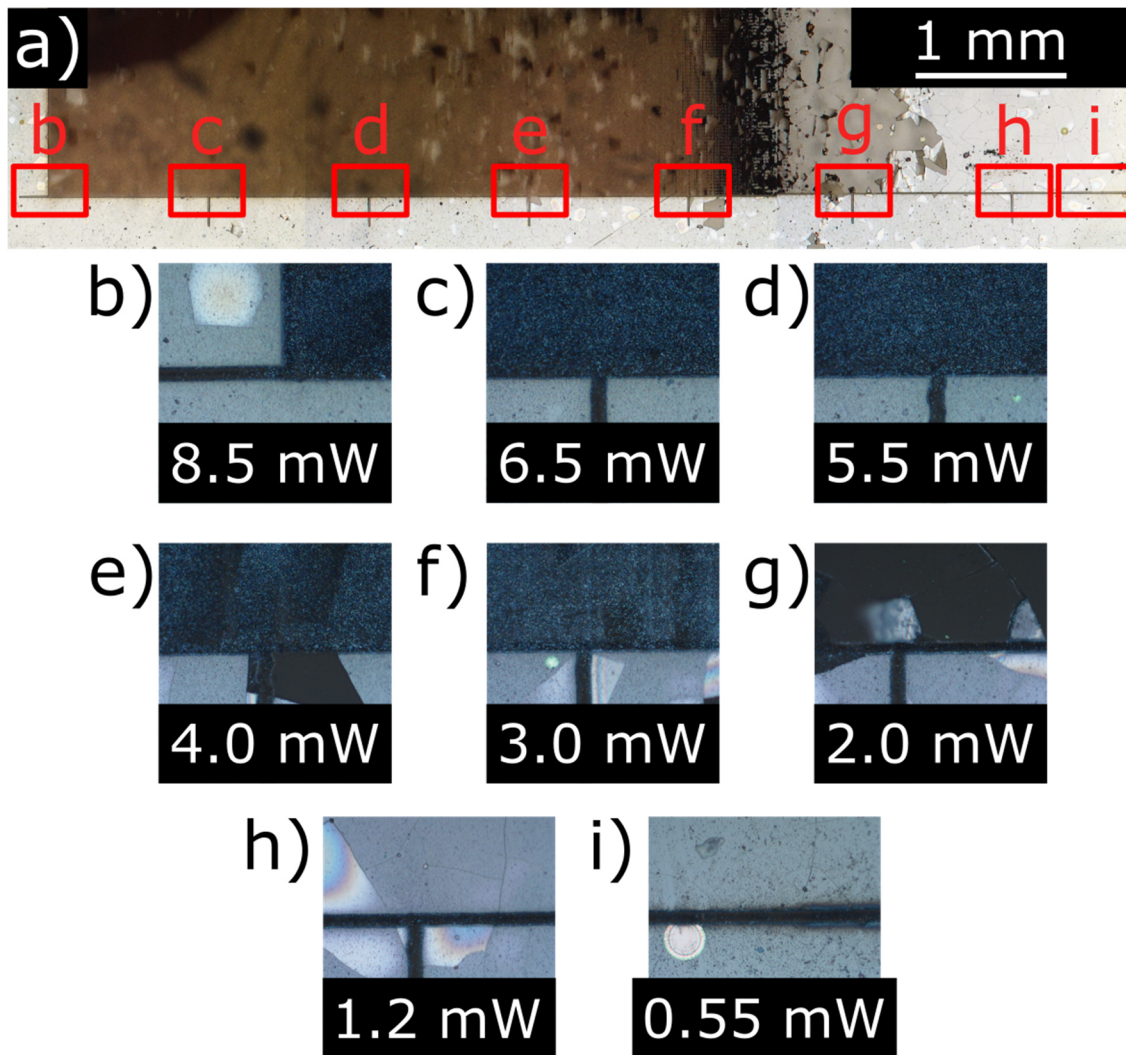


Figure 36: Optical microscopic measurements of a laser treated $\text{Fe}_x\text{O}_y/\text{Al}/\text{TiO}_x$ on quartz system (a), zoomed at different intensities (b-i).

In comparison, the variation of laser power on the $\text{Fe}_x\text{O}_y/\text{Al}/\text{TiO}_x$ system (see Figure 36) showed full ablation in the range of ~ 2.5 to ~ 8.5 mW, as indicated by transparency of the substrate. A higher power was needed to fully ablate the films compared to the metal free counterpart (see Figure 35) due to its superior energy distribution along the absorber layer. Between ~ 1.5 and ~ 2.5 mW, the top film seems to be partially ablated, forming flake like structures, an effect from the sputtered layer, often peeled off at elevated temperatures, in this case from the accumulated heat of the laser treatment. Below ~ 1.2 mW, no structuring could be observed through the optical microscope.

The effective power range for the quartz systems was further investigated and ultimately allowed precise control over morphology and enhanced properties, discussed in section 3.2.3.1.

3.1.2.2 Investigation of Quartz Systems with Inverted Metal Oxide Order

The inverted system (see Figure 37a) consisted of the quartz substrate covered with iron oxide, a sputtered Al film, and titanium oxide on top, and was investigated to see if the metal oxide layers were interchangeable, with the Fe_xO_y being much thinner than the TiO_x film.

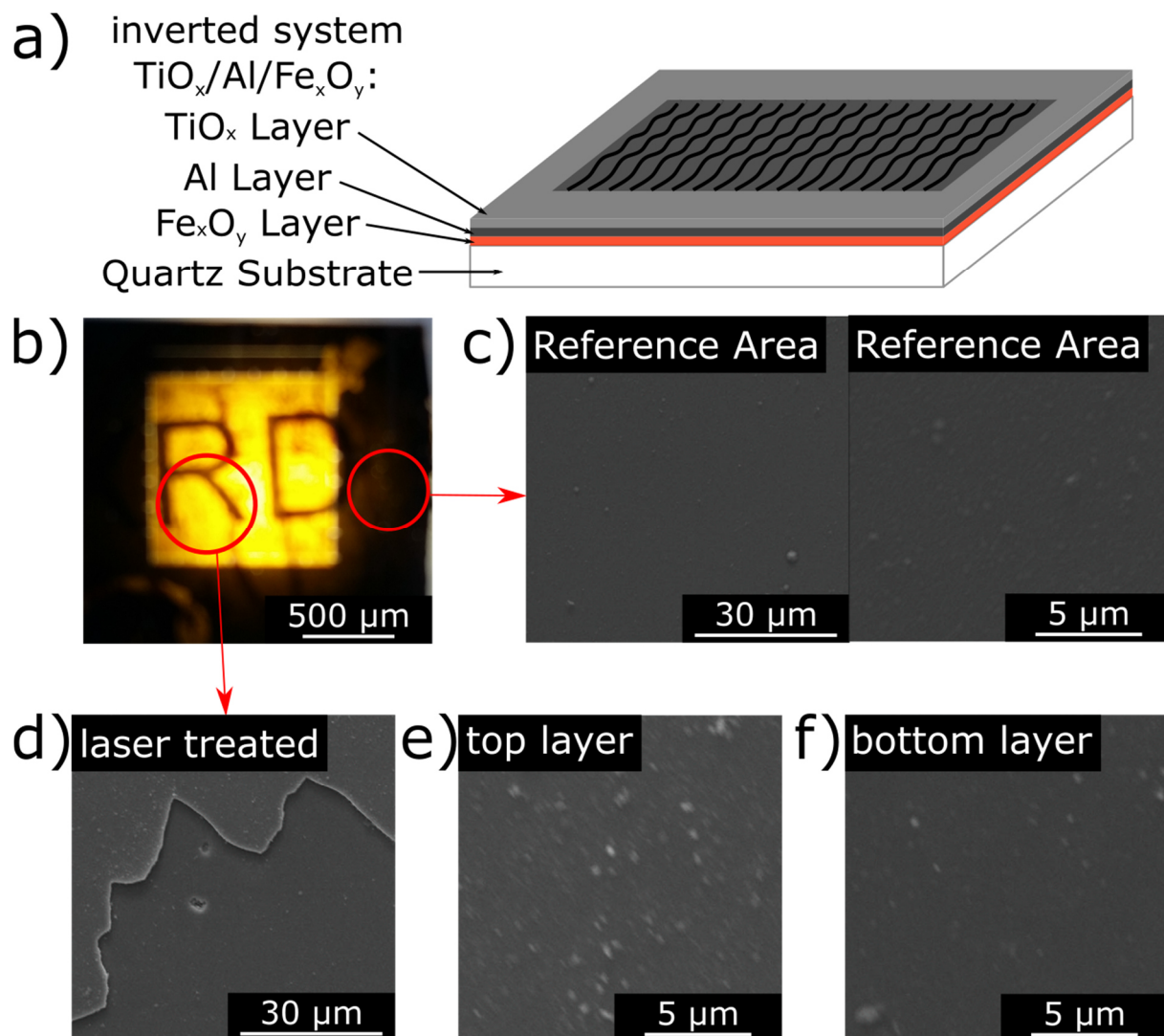


Figure 37: Schematic of the inverted stack, laser treated $\text{TiO}_x/\text{Al}/\text{Fe}_x\text{O}_y$ on quartz system (a), a backlight illuminated picture (b), in plane SEM images of the untreated reference area (c), and of the laser treated area (d), with respective focus on the top (e) and bottom layer (f).

Table 8: EDX compositions laser treated $\text{TiO}_x/\text{Al}/\text{Fe}_x\text{O}_y$ on quartz at different laser positions.

Position	Composition (EDX)					SEM Images
	Ti (%)	O (%)	Si (%)	Fe (%)	Al (%)	
Reference	38.23	61.27	0.49	/	/	Figure 37c
Top	36.83	60.69	0.64	1.09	0.46	Figure 37d and e
Bottom	22.08	52.28	10.89	12.02	2.73	Figure 37c and f

The laser treated area showed higher transparency, as seen with backlight illumination (see Figure 37b). This was a result of a thinner film through partial ablation or densification, also supported by AFM analysis (see Figure 38). Additionally, the orange color and EDX analysis indicated that the Fe_xO_y bottom layer remained (see Table 8), while the untreated reference area (see Figure 37c) exhibited no iron signal, as the thick TiO_x film blocked the X-ray beam (see Table 8). Additionally, only few particles on the otherwise homogeneous surface could be seen. The laser treated area revealed a flake like structures (see Figure 37d), similar to previous analysis (see Figure 36), with the top layer showing no significant change compared to the untreated area (see Figure 37e). The bottom layer (see Figure 37f) showed increased iron, aluminum and silicon substrate content in addition to titanium (see Table 8), revealing that only the top layer was partially ablated. This area had no periodic structures, as most of the laser energy only affected and ablated the TiO_x film through multi-phonon absorption. If the beam would have reached the Al interlayer, morphological changes would have been observed, similar to the previous experiments. The AFM analysis on the edge of the treated area showed its separation by a laser induced crater (see Figure 38a), next to the untreated reference area. This revealed an ablation depth of the fs laser beam through amorphous titanium oxide of ~ 500 nm, with a height deviation of around 40 nm in both the small (see Figure 38b) and big range measurements (see Figure 38d) for the untreated area. The laser treated area exhibited an even lower deviation in both the small (see Figure 38c) and the big range scan (see Figure 38e), of only around 25 nm. Similar to previous analysis, SEM images revealed that the top TiO_x layer was partially ablated, while the remaining film exhibited no laser induced structures (see Figure 37). As the measured area during the AFM analysis was only up to $50 \mu\text{m}$, they only revealed information on a small part of the whole sample, which had to be taken into consideration.

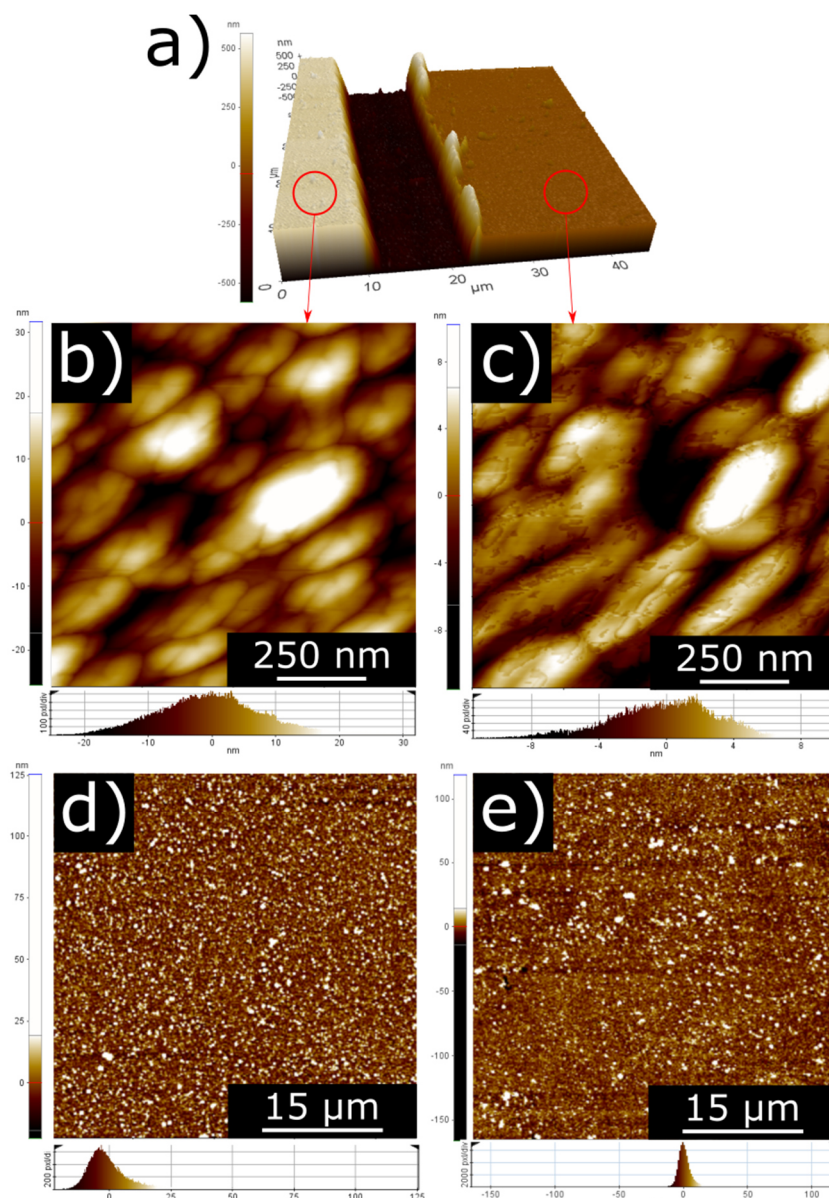


Figure 38: AFM measurements of the laser treated $\text{TiO}_x/\text{Al}/\text{Fe}_x\text{O}_y$ on quartz system on the edge in 3D (a), with the $1 \times 1 \mu\text{m}^2$ (b) and $45 \times 45 \mu\text{m}^2$ reference area (d) and with the $1 \times 1 \mu\text{m}^2$ (c) and $45 \times 45 \mu\text{m}^2$ laser treated area (e), each with their respective height histogram.

The inverted metal oxide structure $\text{TiO}_x/\text{Al}/\text{Fe}_x\text{O}_y$ on quartz system was not further investigated due to the limited effect of the laser treatment process. Instead, the processes for the normal $\text{Fe}_x\text{O}_y/\text{Al}/\text{TiO}_x$ on quartz system was further developed, resulting in many improved properties, as discussed in section 3.2.3.

3.2 Laser Treatment of Metal Oxide Thin Films

3.2.1 Scope and Overview

The effect of femtosecond laser pulses with different intensities on two different metal oxide systems (see Figure 39) were analyzed in this section, introducing order and disorder on a physical level. An aluminum metal film was added for consistent energy absorption due to its high free electron density,^[222] as discussed in section 3.1.2.1. The metal oxide layers^[223] and the quartz substrate^[224] remained mostly transparent for the applied laser wavelength ($\lambda = 800$ nm), increasing overall reproducibility. Ultra-short laser pulsing ($<ps$) allowed very precise disordering in the form of surface structures like ripples or particles. Properties like roughness and ripple depth could be tailored, while the overall light absorption was improved. Additionally, the surface hydrophobicity increased, and a gas sensing response of treated TiO_x system towards reductive gas (H_2) could be measured at room temperature. The crystallization of titanium oxide through femtosecond laser pulses was possible where conventional heat treatment would have led to ablation. All improved properties resulted from a mixture of physical and chemical disordering.^[141]

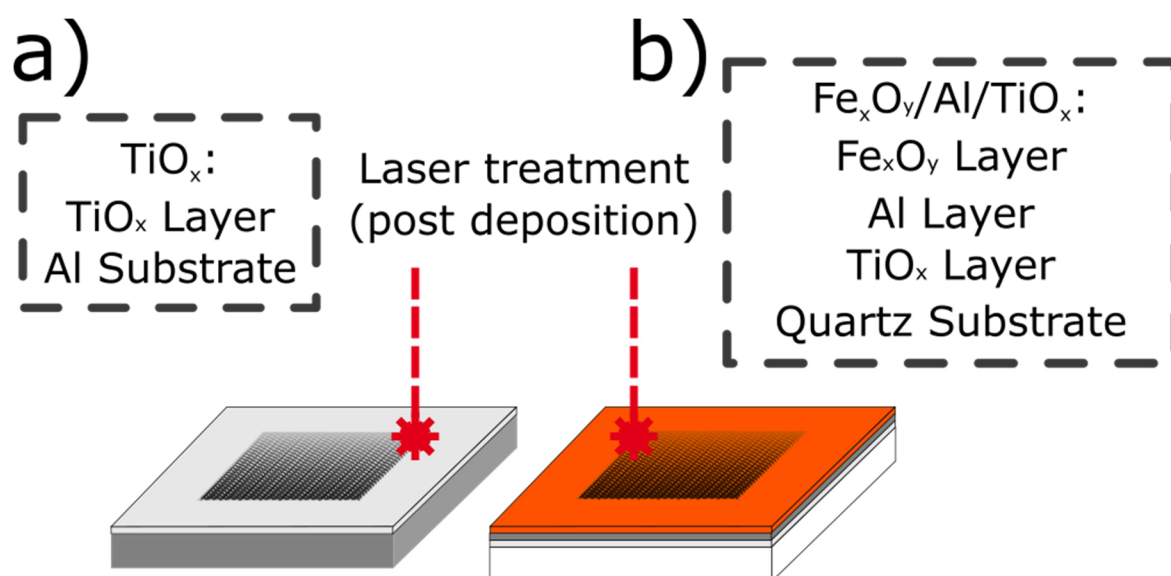


Figure 39: Overview of the two different systems investigated, either TiO_x on Al (a) or $Fe_xO_y/Al/TiO_x$ on quartz (b), both laser treated with gradually increasing intensity.

3.2.2 Metal Substrate Systems

The more simplified TiO_x systems were used to further investigate effects of femtosecond laser pulses on the TiO_x film, with the process discussed in section 3.1.1. The laser wavelength of $\lambda = 800 \text{ nm}$ resulted in a very low absorption in the amorphous TiO_x film, providing a dominantly indirect treatment effect.

3.2.2.1 Properties of Laser Treated TiO_x on Al

Contact angle measurements of TiO_x systems (see Figure 40) revealed increased hydrophobicity of samples treated with higher laser power. The high energy intake caused deep structures and a higher surface roughness which trap air, resulting in an increased contact angle of up to 96° . This is in good agreement with the Cassie Baxter model.^[225] The low structuring intensities of around $\sim 1.47 \text{ mW}$ resulted in shallow structures (see Figure 41), too small to have any effect on the hydrophobicity, so untreated and low energy laser treated systems displayed nearly identical contact angles of around 85° .

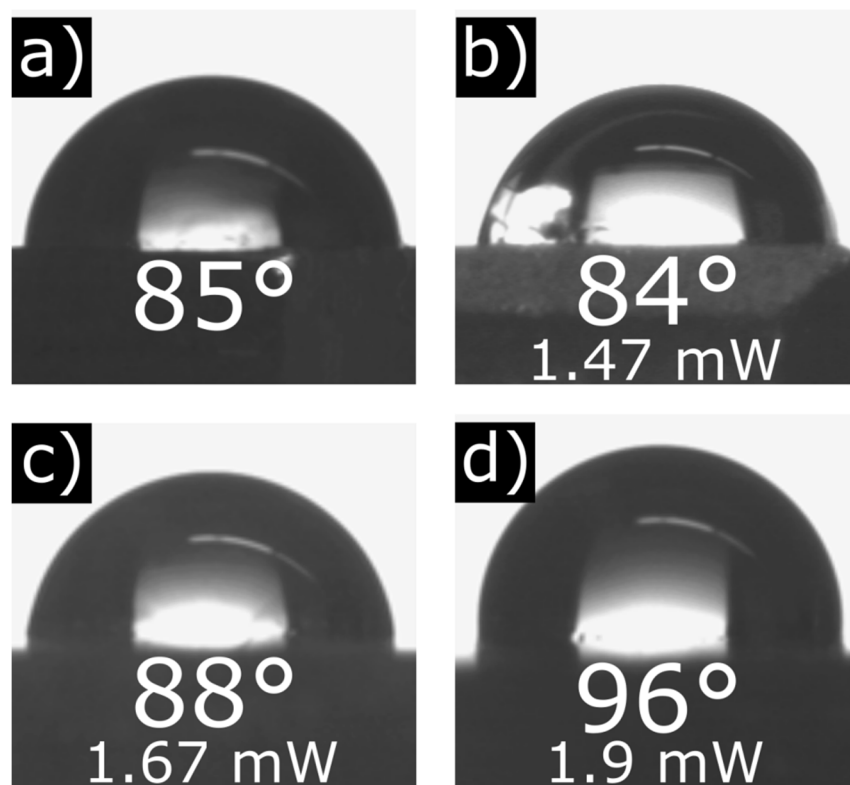


Figure 40: Contact angle measurements of the TiO_x on Al system, untreated (a) and treated with a laser power of 1.47 mW (b), 1.67 mW (c) and 1.9 mW (d).

In plane SEM images for the TiO_x system showed more and deeper structures with higher laser intensity. The untreated reference area (see Figure 41a) remained without additional structures, but retained the rough surface of the substrate. With a laser power of ~ 1.47 mW (see Figure 41b), the surface was barely structured, similar to the untreated system, as only a few random spots had ripples. With an increased power of ~ 1.67 mW (see Figure 41c) the surface was completely covered in ripples, which varied from very shallow to deep craters. This could be a result of random power fluctuations of the laser system and inhomogeneous film formation on the rough substrate. At ~ 1.9 mW (see Figure 41d) the beam intensity was high enough to form deeper craters and cracked the film through the accumulated heat.

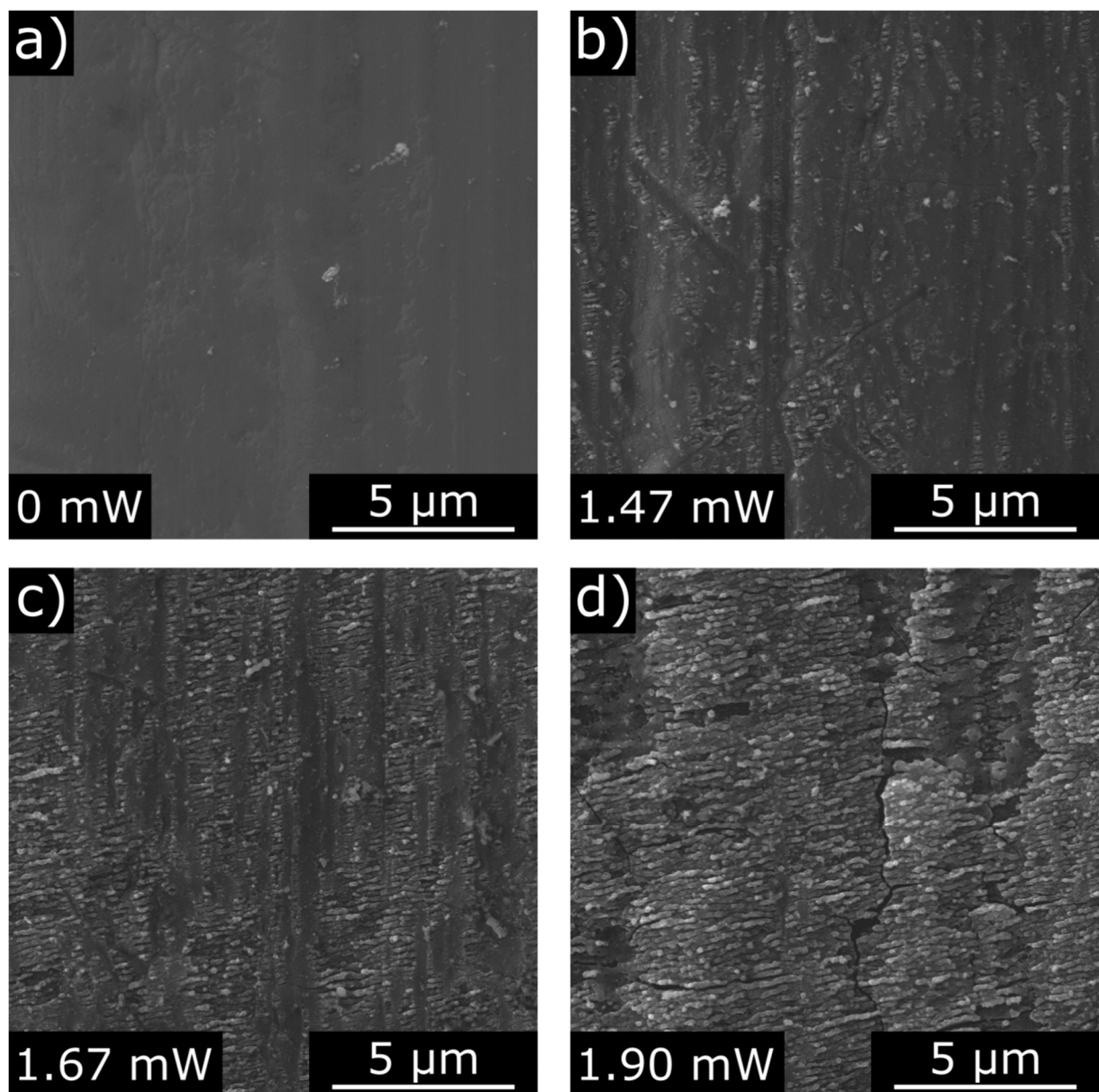


Figure 41: In plane SEM images of the TiO_x on Al system, untreated (a) and treated with a laser intensity of 1.47 mW (b), 1.67 mW (c) and 1.90 mW (d).^[141]

Electron backscatter diffraction (EBSD) measurements revealed the effect of laser treatment on TiO_x films crystallinity (see Figure 42a). Rutile became the dominant phase, with a ratio of $\sim 9:1$ rutile:anatase (see Figure 42b) and no preferred crystallization plane (see Figure 42a and c). The anatase phase only formed on the edges of the rutile sections, indicating that the decreasing energy towards these edges was not enough to fully form the more stable rutile phase, which occurred with enough energy.^[49]

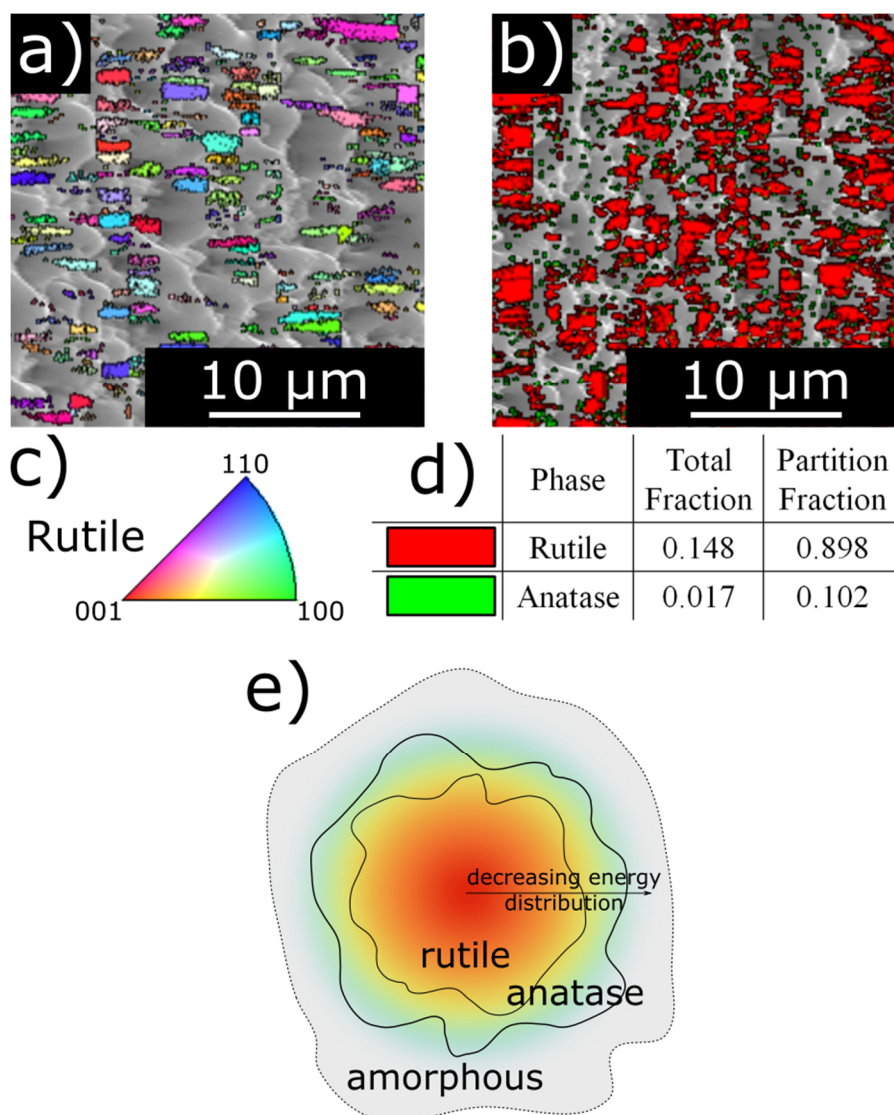


Figure 42: EBSD measurement of the TiO_x on Al system (a) including the color coded phases and fractions (b) and inverse pole figure (001) for the rutile phase (c),^[141] schematic of the energy distribution after beam absorption (d), with red representing high energy density and blue representing low energy density, and its effect on the TiO_x phase (e). Adapted from ^[226].

3.2.3 Metal Interlayer System

After investigating the substrate with one metal oxide layer in section 3.2.2, the more complex $\text{Fe}_x\text{O}_y/\text{Al}/\text{TiO}_x$ on quartz systems, where a thin Al interlayer was positioned between a TiO_x layer below and a Fe_xO_y layer on top, were investigated. This system differs from the previous one in three major aspects: First, a different material was used in addition to the former one. Second, the thin metal film itself limits the distribution of absorbed energy, and last the interaction between both oxides through the laser treatment could be investigated.

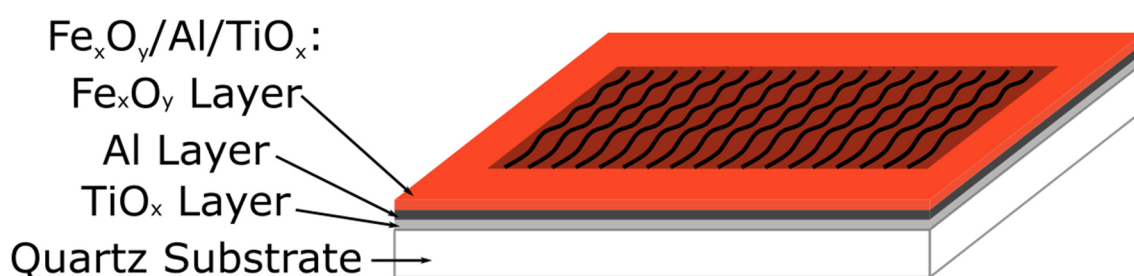


Figure 43: Metal interlayer system with quartz substrate covered with TiO_x by PE-CVD, Al by sputtering, and Fe_xO_y by PE-CVD.

3.2.3.1 Properties of Laser Treated $\text{Fe}_x\text{O}_y/\text{Al}/\text{TiO}_x$ on Quartz

SEM analysis for untreated $\text{Fe}_x\text{O}_y/\text{Al}/\text{TiO}_x$ on quartz showed no surface structures (see Figure 44a). The cross section revealed thicknesses of ~ 150 nm for Fe_xO_y top layer, ~ 30 nm for the sputtered Al layer, and ~ 1.3 μm for the TiO_x layer (see Figure 44c, with the remaining TiO_x layer cropped for increased visibility). AFM measurements revealed a roughness value of ~ 9 nm for the untreated reference area (see Figure 44b). With a low laser power of ~ 0.6 mW, long continuous ripples, ~ 700 nm apart, could be observed in both SEM and AFM images (see Figure 44d and e). The roughness value of ~ 8.5 nm was nearly identical to the reference, and a ripple depth of ~ 19.5 nm was obtained. The SEM cross section (see Figure 44f) showed formation of small bubbles due to accumulated heat at and around the metal layer. While the Fe_xO_y top layer was laser structured, the TiO_x layer remained mostly unaffected. By utilizing an increased power of ~ 1.75 mW, the ripples remained ~ 700 nm apart (see Figure 44g), which supported the literature notion that the distance of the periodic ripples was intensity independent.^[227]

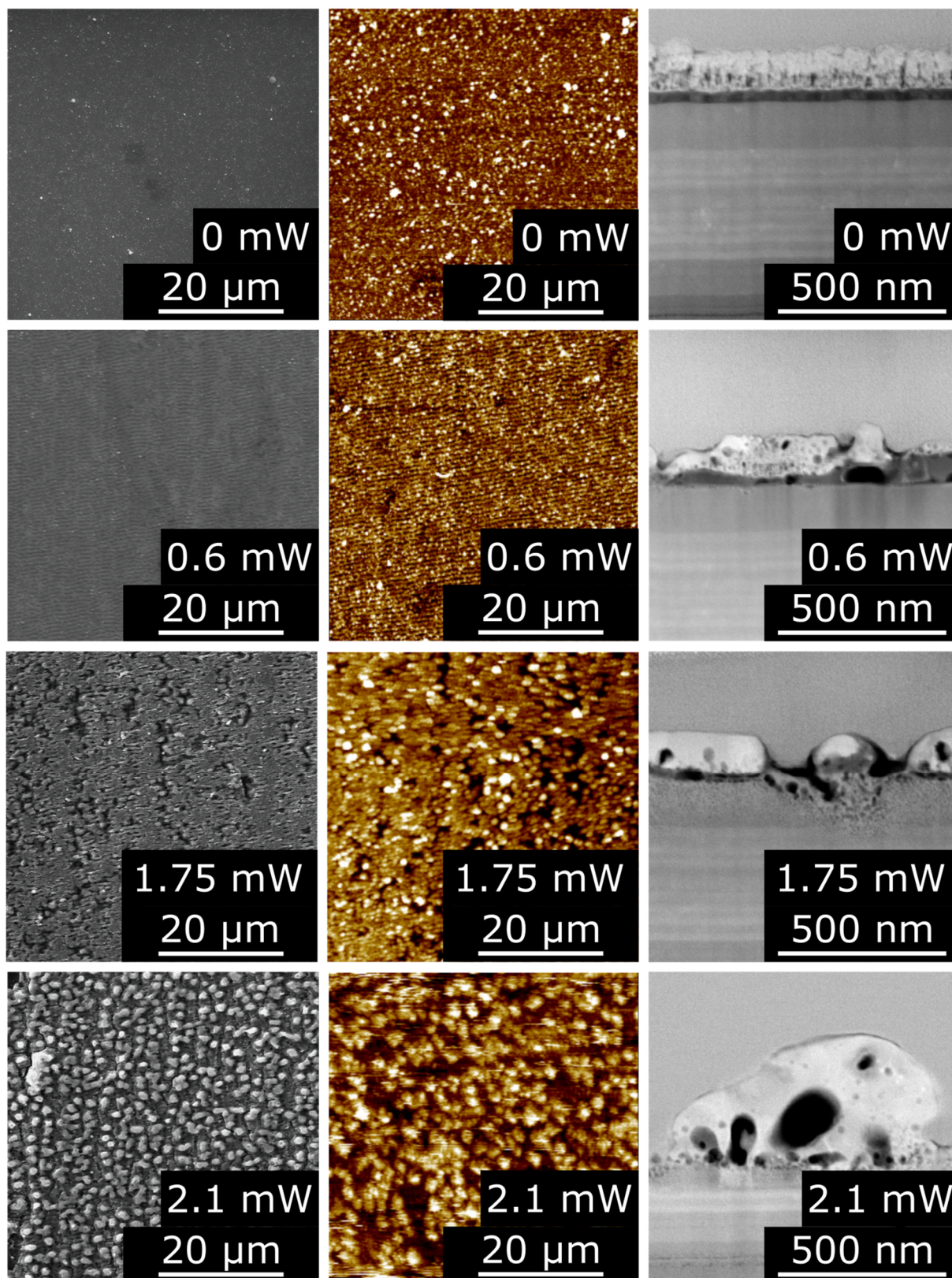


Figure 44: In plane SEM, AFM and cross section SEM images of untreated $\text{Fe}_x\text{O}_y/\text{Al}/\text{TiO}_x$ on quartz (a-c), and treated with a laser power of 0.6 mW (d-f), 1.75 mW (g-i) and 2.1 mW (j-l).

The single ripples were ~ 30 nm deep, with spikes in the laser energy output causing partial crater formation, which resulted in increased roughness of ~ 43 nm (see Figure 44h). While the ripples were bigger, the depth and periodicity was lower compared to those reported on other

metal oxides, like zinc oxide, in literature.^[228] The SEM cross section image (see Figure 44i) showed that craters resulted from evaporation of the top and metal layer due to the sudden increase in the lattice temperature. This seemed to be an extension of the bubble formation seen at lower laser power. The bottom titanium oxide layer was also affected, as seen by ripple formation. By further increasing the power to ~ 2.1 mW (see Figure 44j), the metal and top layer were molten together as big particles with a diameter of ~ 300 nm (see Figure 44l). The TiO_x layer remained structured and an overall roughness of ~ 89 nm, with an averaged ripple depth of around 69 nm was attained (see Figure 44k).

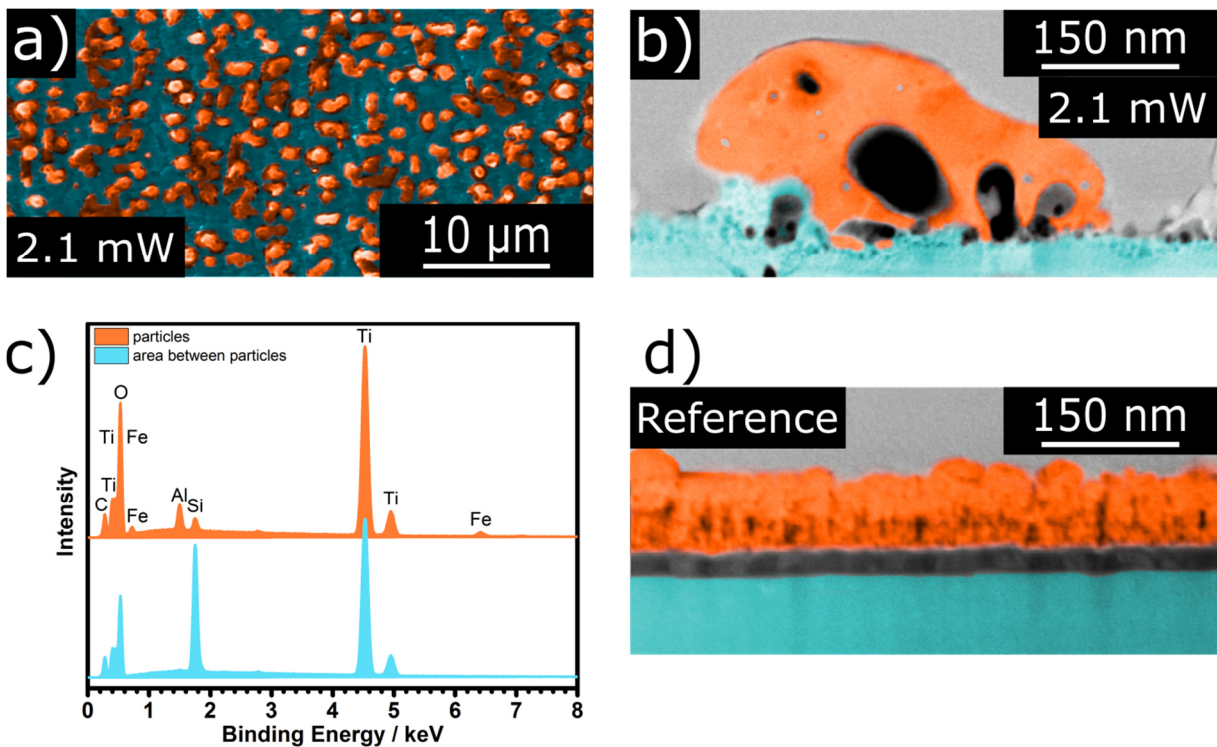


Figure 45: In plane SEM image of $\text{Fe}_x\text{O}_y/\text{Al}/\text{TiO}_x$ on quartz treated with a laser power of 2.1 mW (a), the corresponding cross section (b), the EDX of the particles and the areas between them (c) and cross section SEM image of the untreated reference (d), colored with orange representing the Fe_xO_y and blue representing the TiO_x layer.

EDX analysis proved the particles contained both iron (Fe signal: ~ 0.7 and ~ 6.4 eV) and aluminum (Al signal: 1.5 eV), while the space between them did not (see Figure 45a). These data was used to color the SEM images to containing iron (orange) and those without (blue, see Figure 45b). In literature, melting of silver films by UV laser treatment resulted in similar, but smaller particles, with a size of around 75 - 100 nm,^[229] yet they were not combined with a metal oxide top layer.

XRD measurements of $\text{Fe}_x\text{O}_y/\text{Al}/\text{TiO}_x$ on quartz (see Figure 46) revealed two dominant diffraction peaks next to the broad substrate signal between 5 and 17° , with one around 12.5° corresponding to the (110) crystallographic plane of the rutile phase, which fitted as most intense literature signal. The other diffraction peak around 11.5° (literature value: 11.7°) corresponded to the anatase phase most intense signal, which belongs to the (101) crystallographic plane. A slight shift towards lower 2θ angles were a result of anatase being forced to align to the smaller lattice parameter of the rutile phase. During laser treatment, the amorphous material crystallized in both anatase and rutile modification. The latter phase is thermodynamically more stable and thus needs more energy to crystallize, so a gradual change from the amorphous to anatase to rutile was expected during the laser treatment. When comparing the lattice parameters, the two edges of the anatase phase ($a_{\text{Anatase}} = b_{\text{Anatase}} = 3.78 \text{ \AA}$)^[230] slightly increased during the phase transition to rutile ($a_{\text{Rutile}} = b_{\text{Rutile}} = 4.59 \text{ \AA}$)^[231] while the third decreased drastically from $c_{\text{Anatase}} = 9.51 \text{ \AA}$ to $c_{\text{Rutile}} = 2.96 \text{ \AA}$. So the shift in the XRD diffractogram was a result of anatase being forced to fit the rutile lattice constants, as the decreased energy was not enough to crystallize the titanium oxide in the more stable phase. This was supported by EBSD analysis of TiO_x , which showed anatase formation at the edges of rutile crystallites (see section 3.2.2.1 Figure 42). No other characteristic diffraction peak for the TiO_2 phases could be observed due to the high background noise, and no Fe_xO_y phases were seen, even though a melting process was observed in the SEM cross section images (see Figure 44c). The particles were either too small and the signal to noise ratio too high to properly detect them with a molybdenum source,^[221] or the fast cooling resulted in amorphous particles.

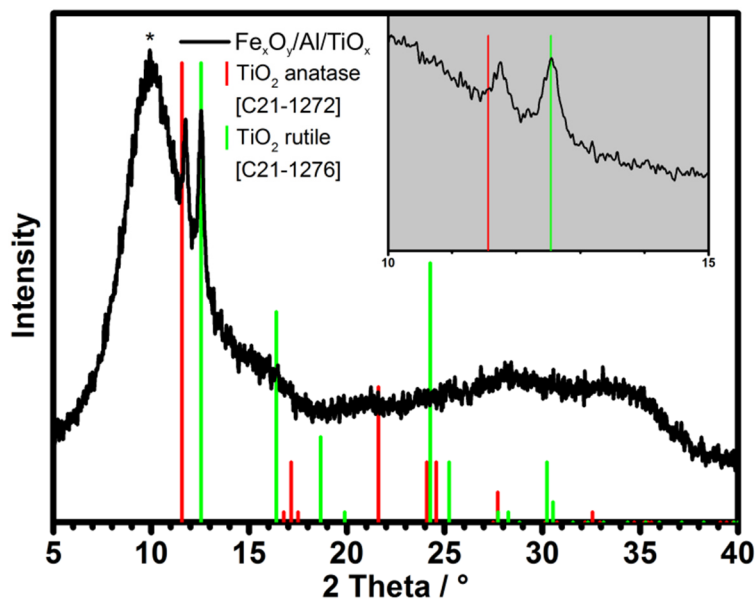


Figure 46: XRD measurement of $\text{Fe}_x\text{O}_y/\text{Al}/\text{TiO}_x$ on quartz, including anatase and rutile references. The asterisk (*) marks the broad diffraction peak of the quartz substrate.

The UV-VIS spectroscopic measurements of $\text{Fe}_x\text{O}_y/\text{Al}/\text{TiO}_x$ on quartz demonstrated enhanced absorption in the range of 400 to 800 nm after laser treatment compared to all references (see Figure 47). No distinguishable peaks could be observed in the measurement region. This could be attributed to increased light trapping from the ripple structure seen in SEM and AFM images (see Figure 44), matching previous results.^[232-234] The noisy signal resulted from interference scattering of the different structured layers, much like structural coloration in nature.^[219] The absorption of untreated references (*untreated $\text{Fe}_x\text{O}_y/\text{Al}/\text{TiO}_x$*) stems from a combination of two metal oxides,^[235] while molten particles of the laser treated system (*laser treated $\text{Fe}_x\text{O}_y/\text{Al}/\text{TiO}_x$*), caused by high energy structuring, had a much higher cross section absorption (see Figure 44c). The spectrometer could not distinguish between absorbed and reflected light, which resulted in the reference including the aluminum layer (*untreated $\text{Fe}_x\text{O}_y/\text{Al}/\text{TiO}_x$*) exhibiting an overall higher "absorption" compared to the reference without Al interlayer (*untreated $\text{Fe}_x\text{O}_y/\text{TiO}_x$*),^[236] as the Al layer could work as back reflector.

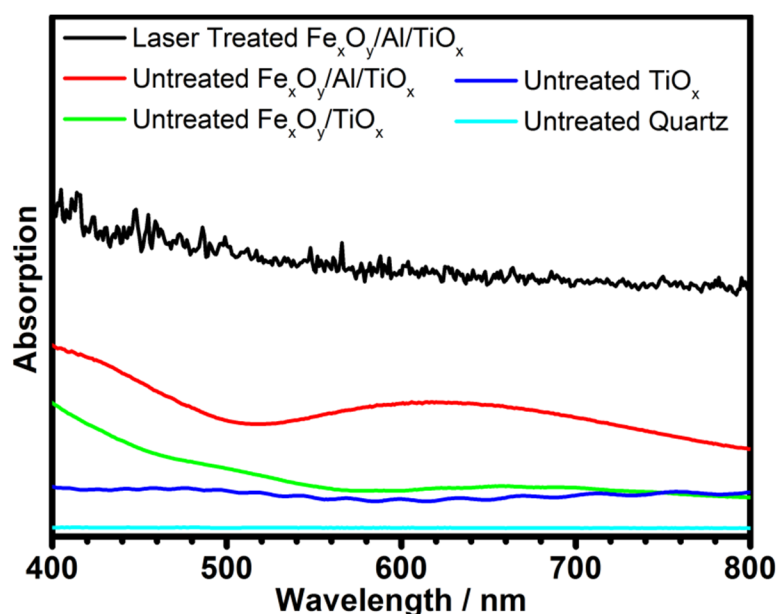


Figure 47: UV-VIS transmission spectra of $\text{Fe}_x\text{O}_y/\text{Al}/\text{TiO}_x$ on quartz, untreated and laser treated, including reference stacks with fewer layers.

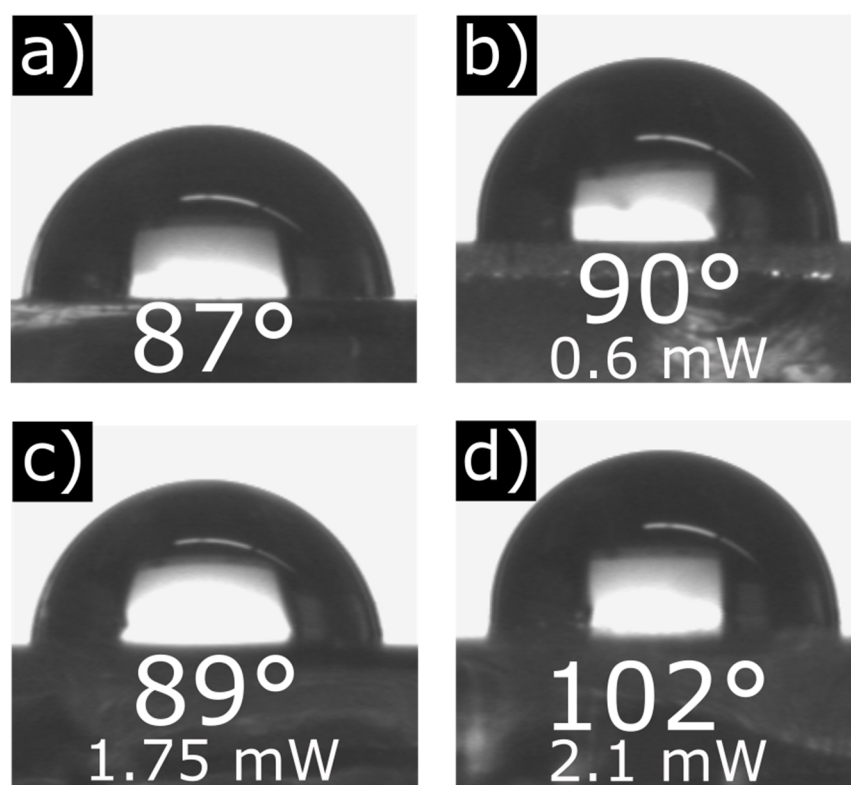
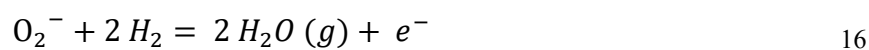


Figure 48: Contact angle measurements of $\text{Fe}_x\text{O}_y/\text{Al}/\text{TiO}_x$ on quartz, untreated (a) and treated with a laser power of 0.6 mW (b), 1.75 mW (c) and 2.1 mW (d).

To investigate a potential application as gas sensor, TiO_x on quartz were modified (see Figure 49a). Before deposition, Al stripes were sputtered on a quartz substrate and later separated through laser pulses without ablating the TiO_x film, which could be observed in SEM images (see Figure 49c and d). They also support results from previous sections, where the laser energy was absorbed by the metal layer first, and then influenced surrounding layers (see Figure 44a). This forces the current to move through a metal oxide layer, allowing to measure its changes in resistance after gas adsorption. The response of the amorphous titanium oxide towards reductive gas (H_2) showed a decrease in resistance with higher gas flow rates (from $\sim 25 \Omega$ at 25 sccm H_2 to $\sim 175 \Omega$ at 200 sccm H_2 , see Figure 49c), as hydrogen reacted with chemisorbed oxygen (O_2^- , O^- , O^{2-}) on the surface to form water molecules according to the following mechanism:^[237]



The total change in resistance remained very small ($\sim 175 \Omega$), while the background noise was very high. This may be attributed to the low substrate temperature, and could barely be observed below 25 sccm H_2 . Higher temperatures, commonly used for gas sensing analysis, were not

possible with sputtered thin films, as they would ablate. Nevertheless, the possibility of fabricating gas sensing devices on heat sensitive substrates operating at room temperature by femtosecond laser treatment was proven.

The introduction of metal films either as substrate or interlayer for laser treatment not only improved the reproducibility, like discussed in section 3.1.2.1, but allowed to produce crystalline TiO_x in both anatase and rutile phases at targeted areas, while tailoring of the morphology and roughness was also possible. The structural effect increased at higher pulse energies, which ultimately led to molten particles, as seen in the SEM images of previous samples (see Figure 44). Furthermore, improved hydrophobicity and increased optical absorption through deeper ripples and craters. Last, fabrication of a TiO_x gas sensing systems without the need of an additional heat treatment step was possible, providing a change in resistance at room temperature.

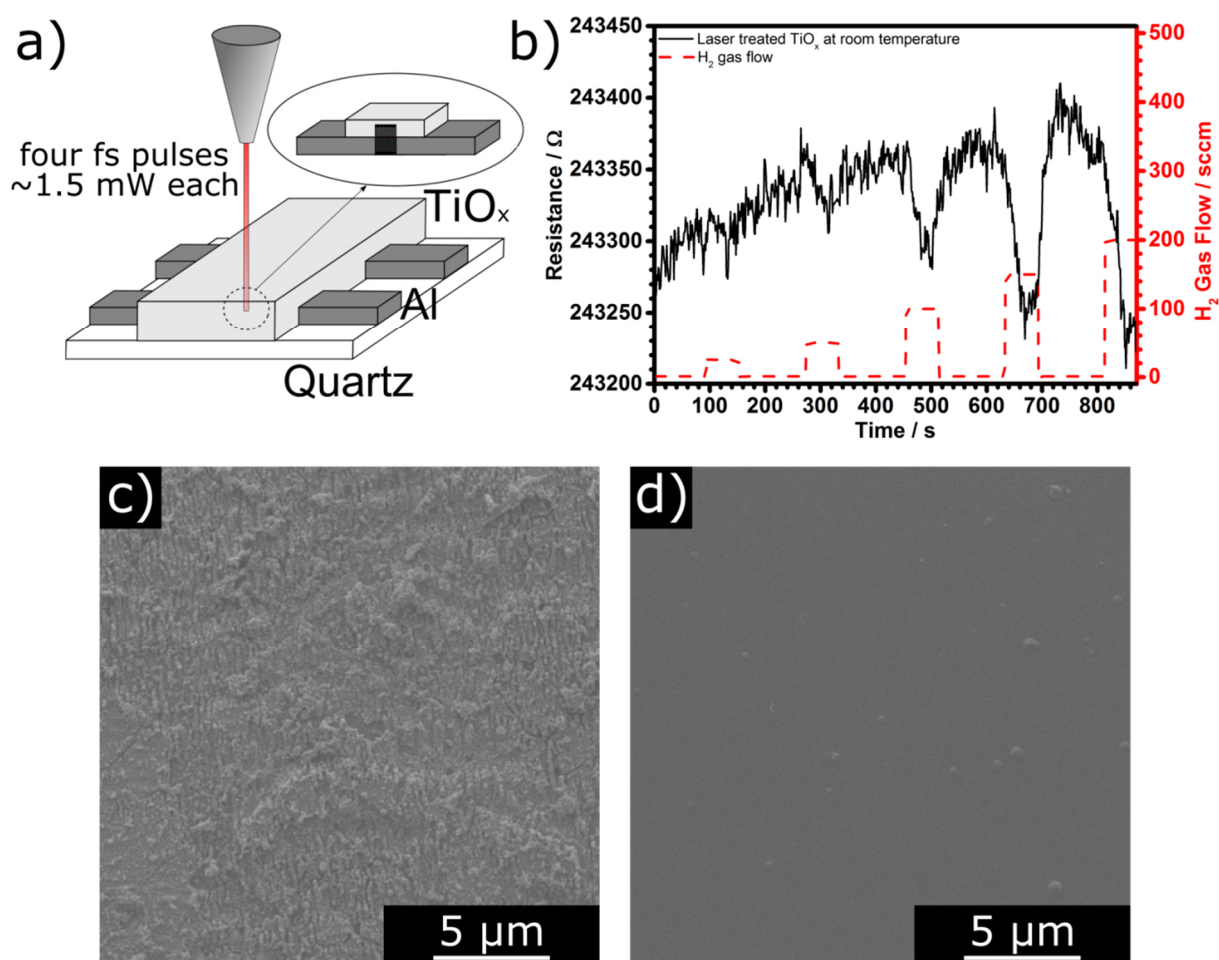


Figure 49: The system used for the gas sensing experiments (a), the changes in resistance towards different H_2 flow rates at room temperature (b) and in plane SEM images of the laser treated (c) and untreated surface (d).

3.3 Water Splitting Properties of Laser-Textured Metal Substrates

3.3.1 Scope and Overview

The physical effect of femtosecond laser treatment of titanium substrates is discussed in this section. The laser processing led to improved light absorption, photoconversion and overall photoelectrochemical water splitting performance. Supplemental investigation with additional absorber layers to boost the efficiency was performed, especially towards their spectroscopic, microscopic, crystallographic and compositional properties. The positive effect of periodic patterns was a result of an enhanced specific surface area and better in-plane light trapping compared to flat surfaces.^[238]

3.3.1.1 Development of Photoelectrochemical Water Splitting Electrodes

The investigated systems were separated into three types (see Figure 50). The first (Ti) consisted of the patterned annealed titanium substrate, while the second (TiO_x on Ti) and third (Fe_xO_y on Ti) had either additional titanium or iron oxide thin films on top, which were deposited by PE-CVD. A metal substrate was used to increase the reproducibility of the laser treatment processes, as discussed in section 3, while heat treatment was necessary to form a crystalline film. The development of an optimized annealing process was discussed in the following section 3.3.2.

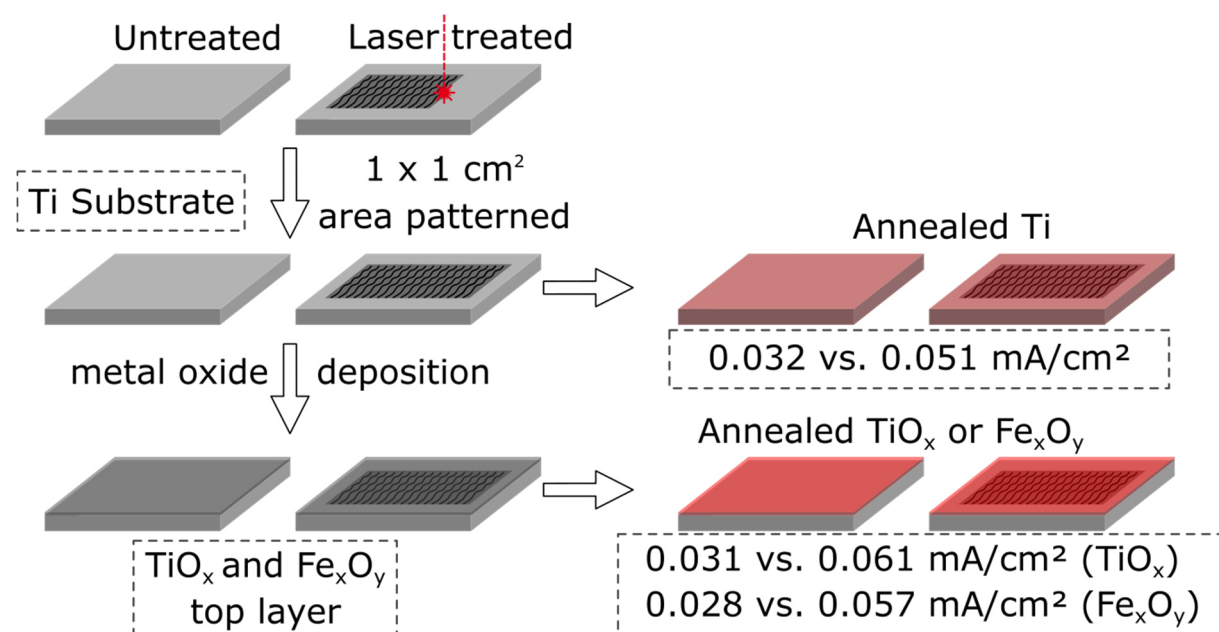


Figure 50: Overview of the different systems and their references investigated towards their optical properties and PEC performance, with their respective photocurrent densities at 1.23 eV vs. RHE.^[238]

3.3.2 Influence of Annealing on PEC Performance

In order to compare the performances of the different systems (see section 3.3.1.1), the development of an optimized annealing process was mandatory. Most importantly, the temperature T and duration t , were studied. The substrate itself could oxidize during the annealing process and form different TiO_2 phases, like anatase around 450°C ^[239] or rutile around 600°C .^[49] The latter was commonly applied in photocatalytical systems,^[240] and has a slightly smaller bandgap compared to anatase (approximately 3.0 eV vs. 3.2 eV), yet remained unsuitable for photoelectrochemical water splitting due to its much lower charge carrier lifetime of around 24 ns, compared to anatase with several microseconds.^[50] To limit rutile formation in all systems, short annealing times of either 10 or 20 minutes had been chosen. Even though longer durations would result in higher crystallinity, it would also lead to increased substrate oxidation, which would in turn reduce the overall photocurrent densities due to the additional interface, stemming from rutile formation at higher temperatures. In the case of bare Ti substrates and TiO_x on Ti sandwich structure, the annealing temperature was varied from 400 to 600°C , while 550 to 750°C were chosen for the Fe_xO_y on Ti system. This range was applied to crystallize the hematite phase, a commonly used PEC electrode material.^[241] It has to be noted that during the parameter screening, the lamp for the PE measurements was not calibrated, so while the results were comparable to each other in this section, they could not be used as reference to the laser structured systems discussed in section 3.3.3.

3.3.2.1 Ti Reference Systems

The Ti substrates did not demonstrate any photoelectrocatalytic performance, thus needed to be oxidized to TiO_2 . Annealing durations of either 10 or 20 minutes at 400°C did not change the water splitting performance of the bare substrate (see Figure 51a), while the samples shifted towards more intense yellow, most likely due to substrate impurities (see section 4.1). The in plane SEM images visualized the rough substrate surface, without any topological changes through prolonged heat treatment (see Figure 51b). No additional diffraction peaks besides the titanium substrate were seen in the XRD analysis (see Figure 51c and d), but the activity hinted towards at least partial crystallinity. The oxide layer was most too thin to be detected by XRD.

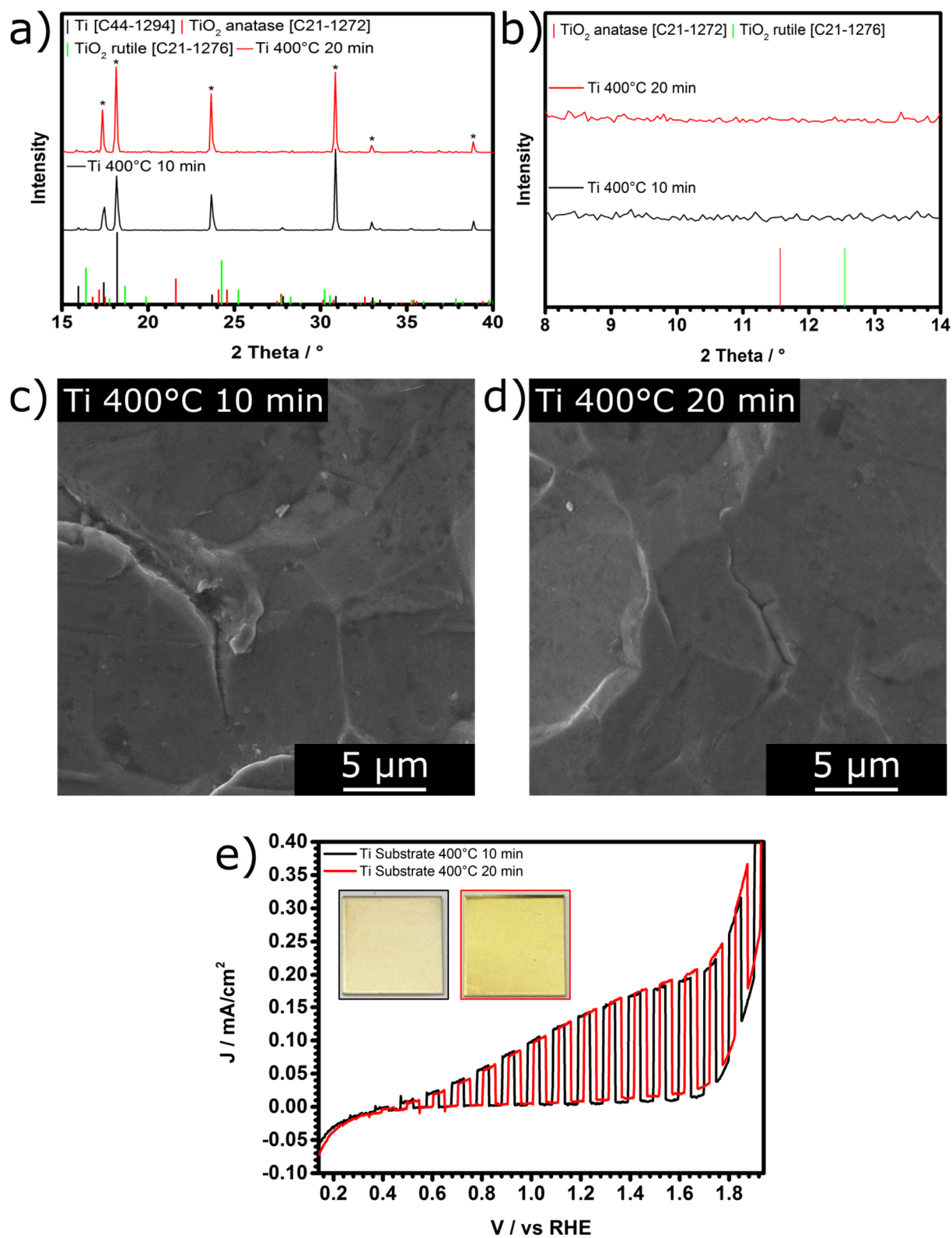


Figure 51: Overview (a) and small range XRD analysis of Ti substrates (b), annealed at 400°C for 10 or 20 minutes, their SEM images (c and d), and the corresponding photocurrent densities (e), with pictures of the samples as inset.^[238]

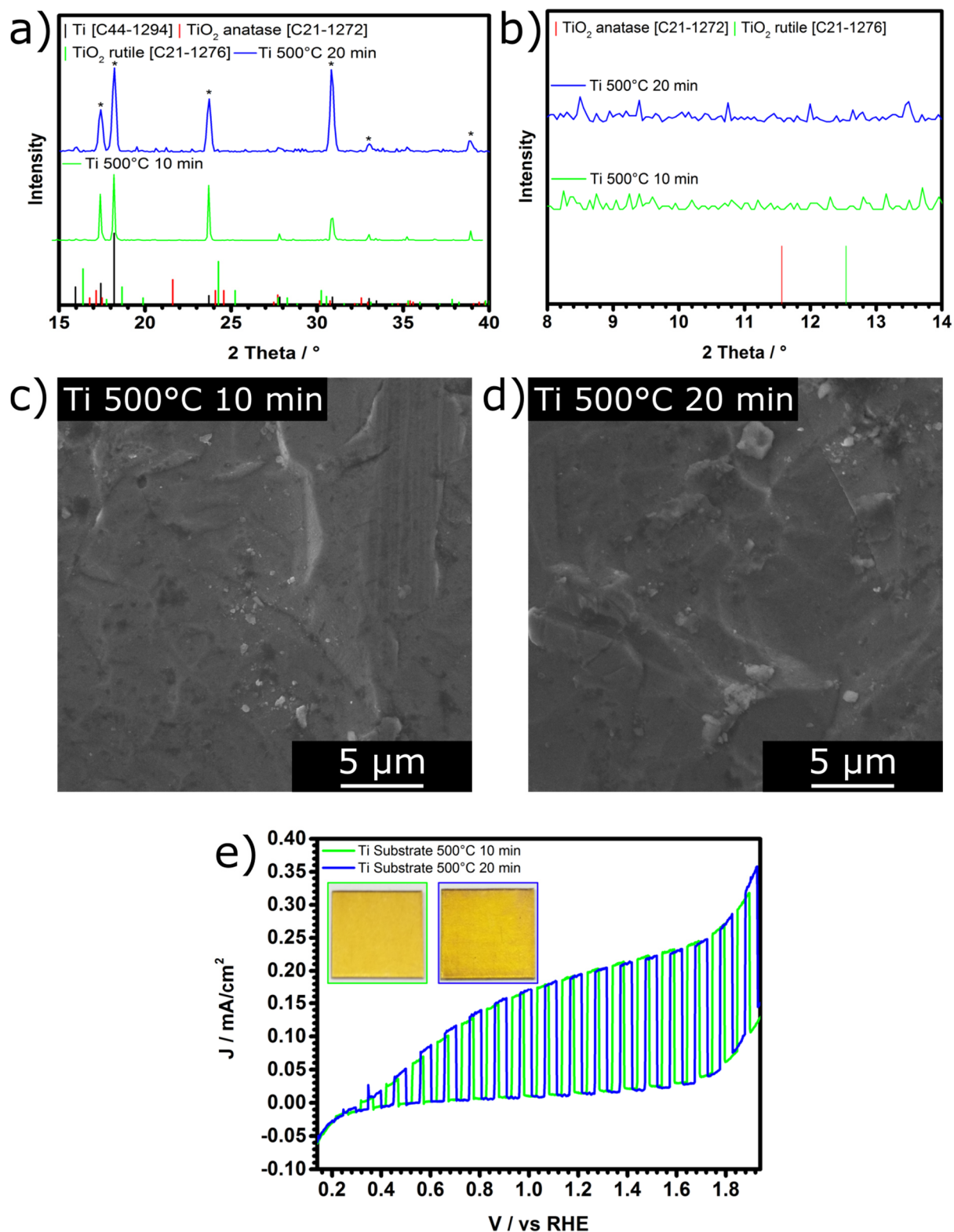


Figure 52: Overview (a) and small range XRD analysis of Ti substrates (b), annealed at 500°C for 10 or 20 minutes, their SEM images (c and d), and the corresponding photocurrent densities (e), with pictures of the samples as inset.^[238]

While there was no performance difference between 10 and 20 minutes annealing at 500°C, the overall performance improved compared to lower annealing temperatures, which would suggest a thicker and/or more crystalline film. The sample color kept the trend of becoming more yellow

with prolonged heating duration (see Figure 52a). In plane SEM analysis revealed the formation of some small particles on the rough surface (see Figure 52b), yet any phase formation was still too thin to be detected by XRD (see Figure 52c and d).

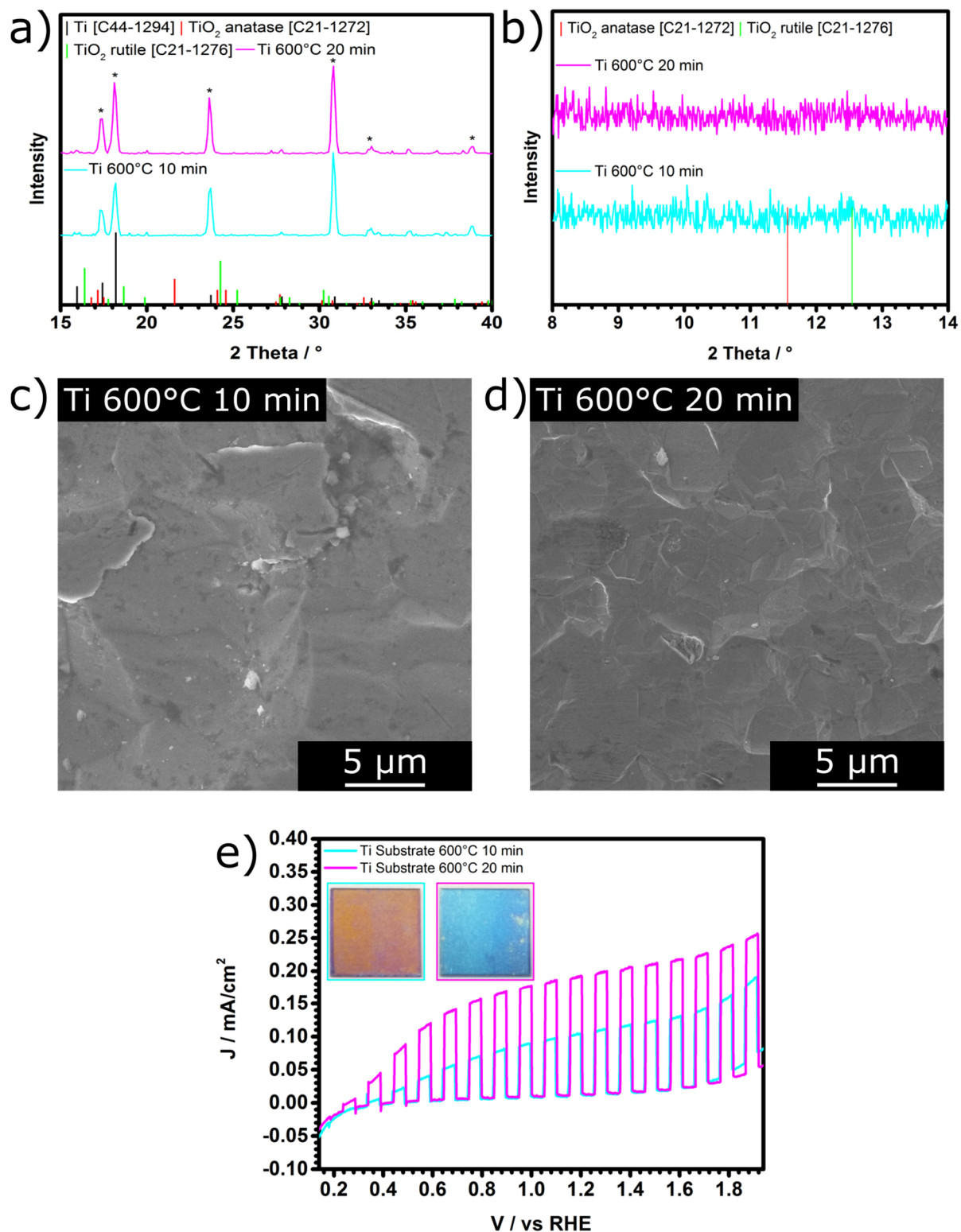


Figure 53: Overview (a) and small range XRD analysis of Ti substrates (b), annealed at 600°C for 10 or 20 minutes, their SEM images (c and d), and the corresponding photocurrent densities (e), with pictures of the samples as inset.^[238]

The performance of 20 minute annealing at 600°C was much higher than the 10 minutes sample, while the substrate color shifted from yellow to brown (10 minutes) and ultimately blue (20 minutes, see Figure 53a). Again, this color shift most likely comes from the impure substrate material (see section 4.1). In plane SEM images showed fewer, however bigger particles (see Figure 53b), while both the overview and small range XRD scan revealed no TiO₂ phase, which would indicate a very thin film or very small particles of anatase and/or rutile, which could not be detected (see Figure 53c and d).

Since high photocurrent densities were preferable to compare untreated to laser patterned systems, the annealing parameters of 20 minutes at 600°C were chosen for the experiments in section 3.3.3.

3.3.2.2 TiO_x on Ti Reference Systems

An TiO_x top layer on the already investigated substrate was produced to further improve the water splitting performance through the additional absorber. TiO₂ enhanced light absorption and both electron/hole diffusion, increasing the harvesting properties.

The overall PEC performance was nearly zero, because the TiO_x layer acted as blocking layer until further crystallization. Annealing for 20 minutes at 400°C resulted in slightly higher photocurrent density, suggesting the formation of crystalline sections of the substrate. The color of the substrate turned more intense pink (see Figure 54a), while in plane SEM images showed the TiO_x layer and particles on the rough substrate, with fewer particles after longer annealing time (see Figure 54b). No phase could be observed through the XRD measurement, as the top layer remained amorphous (see Figure 54c and d).

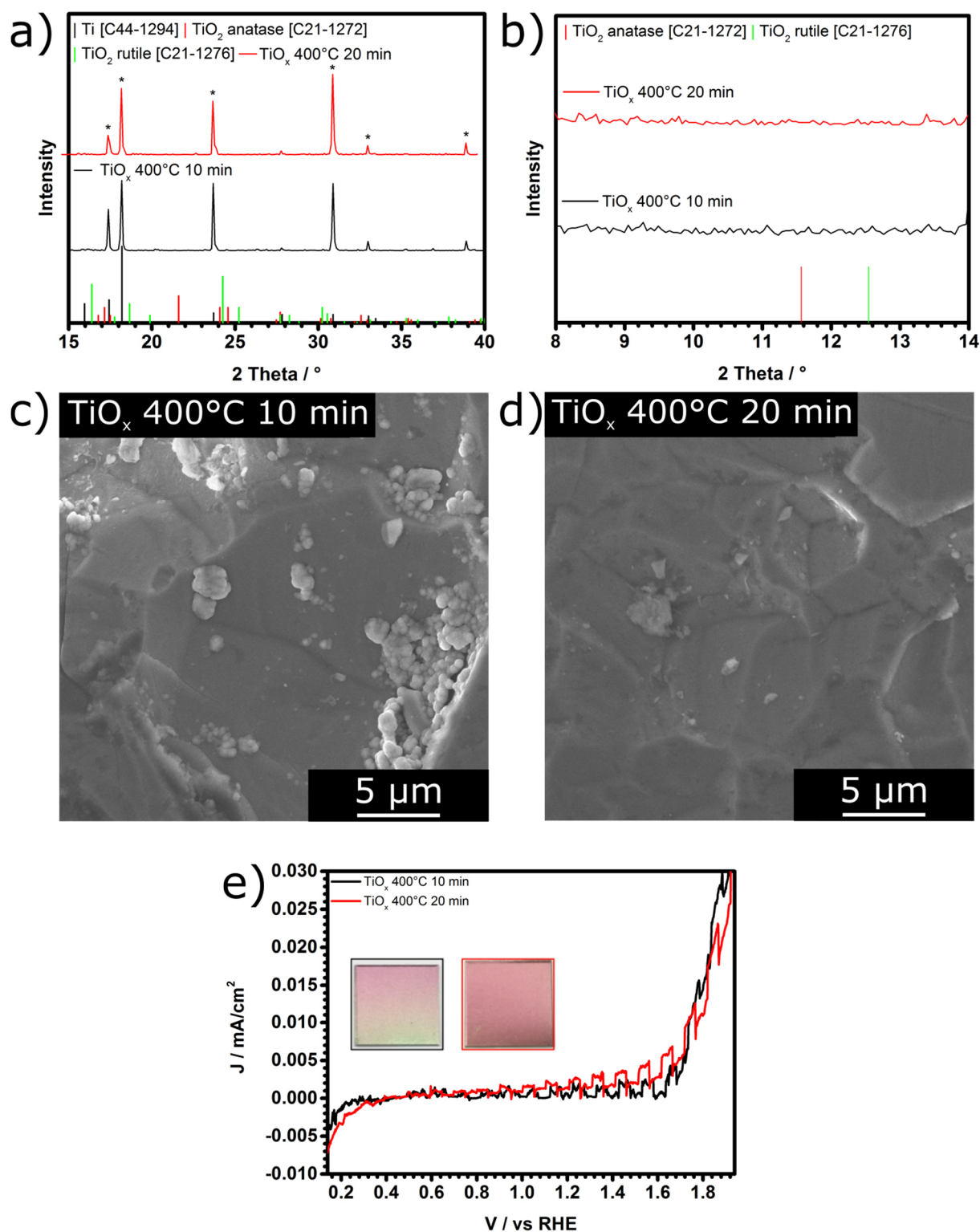


Figure 54: Overview (a) and small range XRD analysis of TiO_x on Ti (b), annealed at 400°C for 10 or 20 minutes, their SEM images (c and d), and the corresponding photocurrent densities (e), with pictures of the samples as inset.^[238]

The overall performance after annealing at 500°C was much higher for the 20-minute duration. The samples turned even more pink, with nearly no difference in photocurrent density between 10 and 20 minutes (see Figure 55a). An increased amount of particles was observed with shorter annealing time, as was the case with lower temperatures (see Figure 55b). While no phase could

be observed for the 10 minute sample, slight formation of the anatase phase, indicated by the diffraction peak around 11.6° , which could be assigned to the (101) crystallographic plane, was measurable for the 20 minute according to the XRD analysis (see Figure 55c and d).

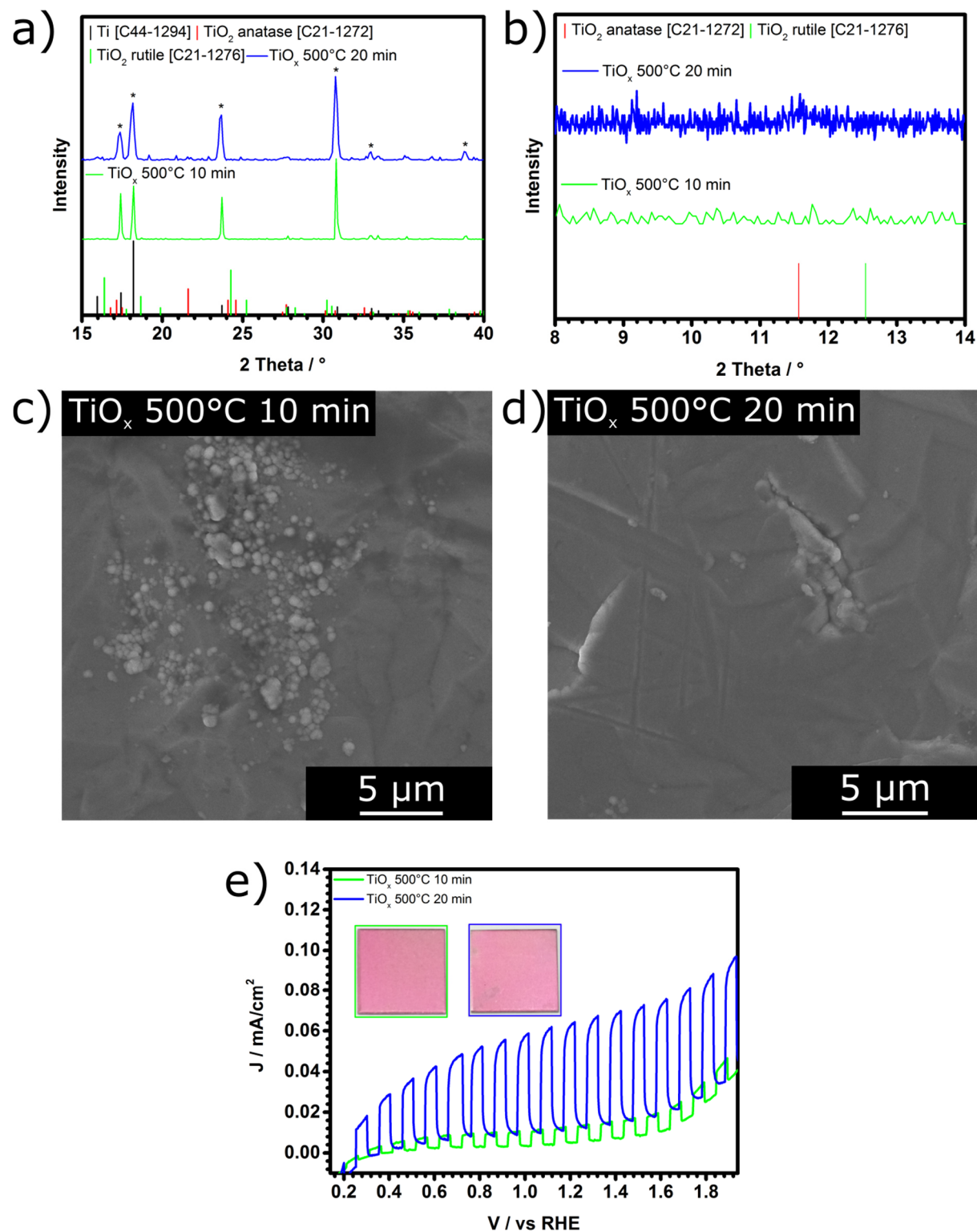


Figure 55: Overview (a) and small range XRD analysis of TiO_x on Ti (b), annealed at 500°C for 10 or 20 minutes, their SEM images (c and d), and the corresponding photocurrent densities (e), with pictures of the samples as inset.^[238]

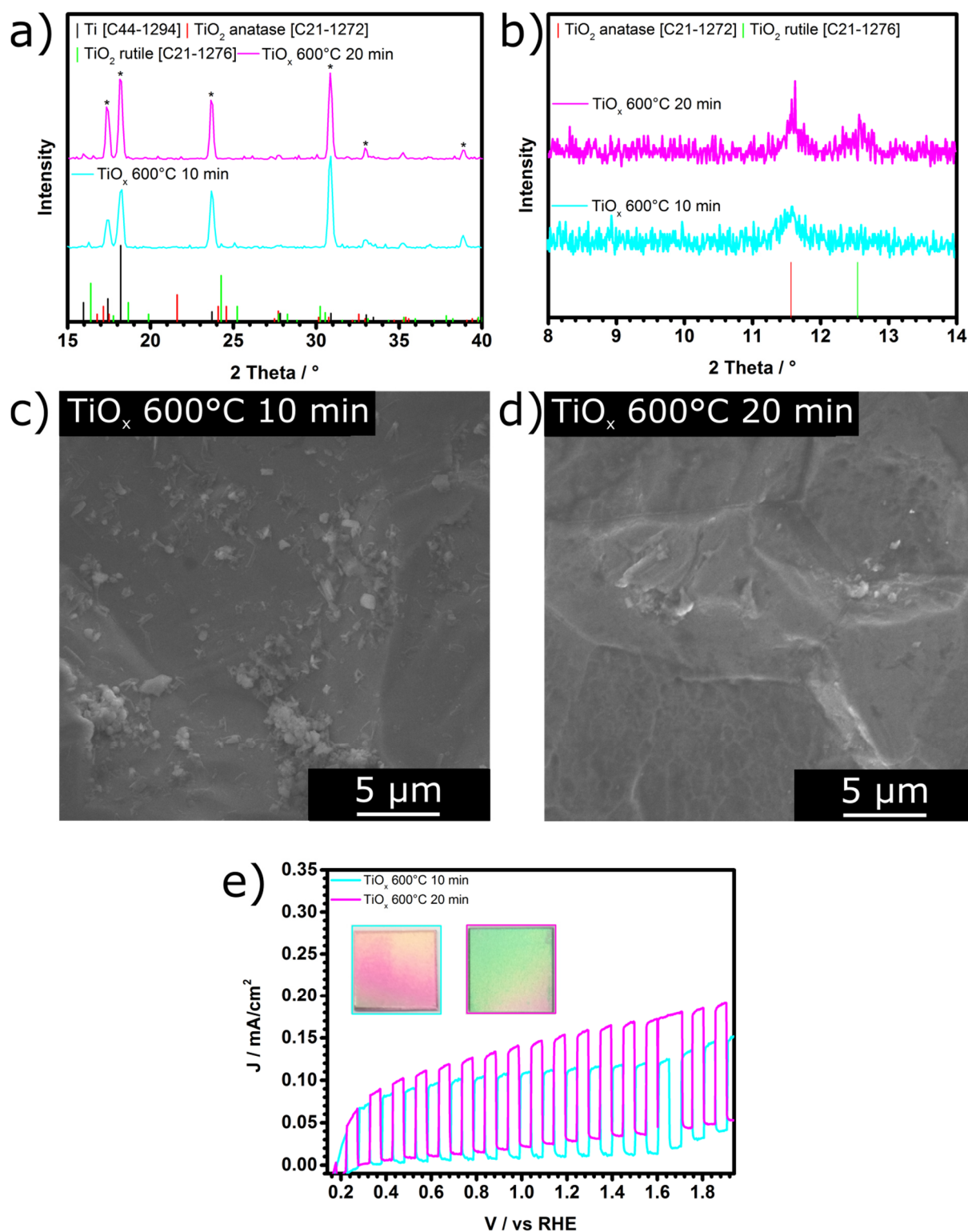


Figure 56: Overview (a) and small range XRD analysis of TiO_x on Ti (b), annealed at 600°C for 10 or 20 minutes, their SEM images (c and d), and the corresponding photocurrent densities (e), with pictures of the samples as inset.^[238]

The longer annealing time at 600°C resulted in higher PEC performance attributed to more crystalline material, while the sample color shifted from pink to green, also partially visible on the top edge of the 10 minutes system (see Figure 56a). The particles observed in SEM of the 10 minute formed a continuous film after increased annealing duration (see Figure 56b), while

XRD analysis showed that both samples consisted of the anatase phase, indicated by the diffraction peak around 11.6° which could be assigned to the (101) crystallographic plane, while 20 minute annealing time also resulted in rutile formation, indicated by the peak around 12.5° , which could be assigned to the (110) crystallographic plane (see Figure 56c and d).

Even though rutile formation already began, 20 minutes annealing at 600°C still outperformed other heat treatments and was chosen for the laser structuring experiments in section 3.3.3.

3.3.2.3 Fe_xO_y on Ti Reference Systems

An added Fe_xO_y top layer to the already investigated Ti substrate was produced, allowing to improve the PEC performance through an additional absorber layer, by additional absorption, boosting the light harvesting properties even further. Crystallized iron oxide exhibited increased visible light absorption compared to TiO_2 , but suffered from shorter carrier lifetime and diffusion length.^[242] During these measurements, the automatic shutter, which allowed to measure dark and light current densities simultaneously, broke, resulting in all PEC results depicting the dark (dotted) and light (full) measurements.

The systems showed no activity at 550°C for 10 or 20 minutes, because the iron oxide phase remained amorphous and acted as blocking layer. This meant any performance resulted from the substrate and pin holes in the Fe_xO_y film. The sample color turned blue, similar to the annealed substrates (see Figure 57a). In the in plane SEM images, small particles could be observed (see Figure 57b), while the small range XRD analysis revealed no crystalline phases (see Figure 57c). The temperature and duration were too low to form any iron oxide phase.

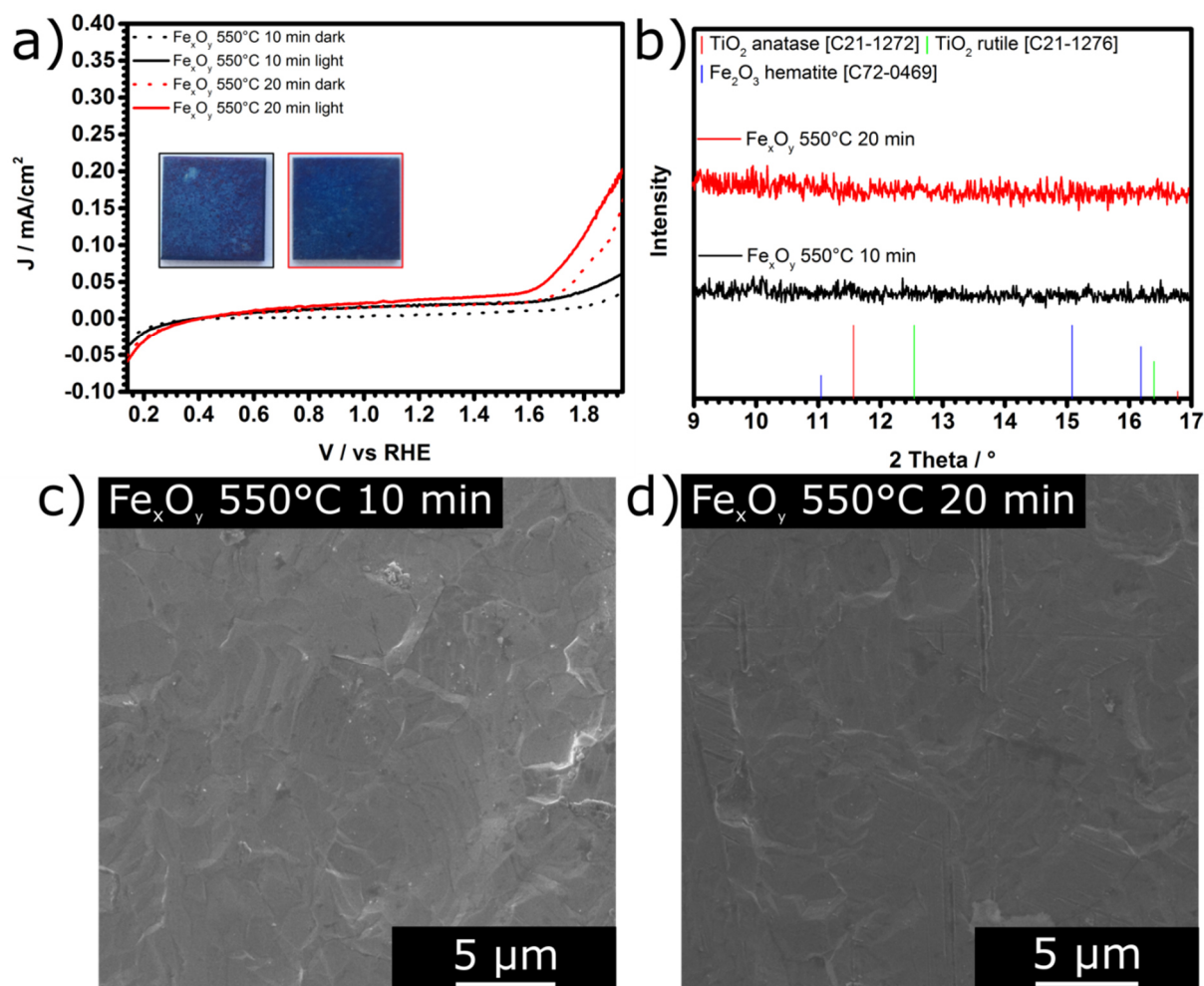


Figure 57: Photocurrent density with pictures of the samples as inset (a) and small range XRD analysis (b) of Fe_xO_y on Ti (b), annealed at 550°C for 10 or 20 minutes and their SEM images (c and d).^[238]

While there was only a marginal difference for 10 and 20-minute annealing at 650°C, it performed superior to the lower annealing temperatures. This, in addition to the high onset potential, indicated the formation of hematite, further supported by the red color of the sample, which increased with longer annealing time (see Figure 58a). SEM images showed densely packed particles, even more after prolonged treatment (see Figure 58b). XRD analysis revealed formation of hematite for the 20-minute sample, with diffraction peaks around 15.1° and 16.2°, which could be assigned to the (104) and (110) crystallographic planes. The oxidized phases of the substrate could also be observed with a diffraction peak around 11.6°, corresponding to the (101) crystallographic plane for anatase, and around 12.5° and 16.3° for the rutile phase, corresponding to the (110) and (101) crystallographic plane, respectively (see Figure 58c). This could be a result of crack formation, exposing the underlying substrate. Another explanation could be densification of the hematite layer through annealing, which could lead to the detection of the TiO_2 below it.

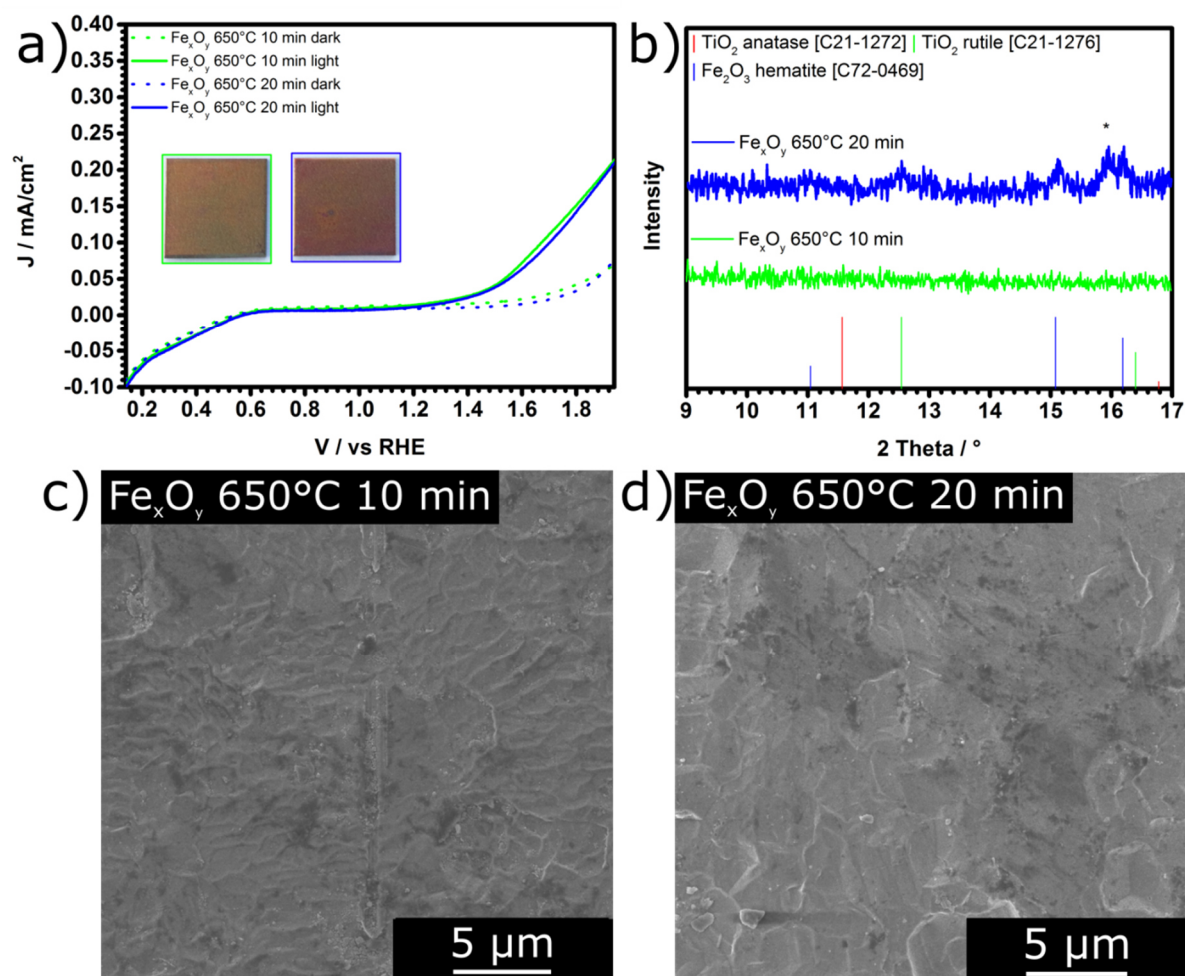


Figure 58: Photocurrent density with pictures of the samples as inset (a) and small range XRD analysis (b) of Fe_xO_y on Ti (b), annealed at 650°C for 10 or 20 minutes and their SEM images (c and d).^[238]

Longer annealing at 750°C resulted in decreasing PEC performance due to the formation of a thicker rutile layer between the substrate and the hematite film. The sample color turned darker, resulting from a combination of the blue substrate and red top layer (see Figure 59a). In the in plane SEM images, fewer separated particles and increased layer formation could be observed (see Figure 59b), while XRD analysis revealed intense hematite signal for both 10 and 20 minutes, with diffraction peaks around 15.1° and 16.2°, which could be assigned to the (104) and (110) crystallographic planes, and very intense rutile signals from the oxidized substrate around 12.5° and 16.3°, corresponding to the (110) and (101) crystallographic plane, respectively (see Figure 59c). Additionally, nearly no anatase formation was observed.

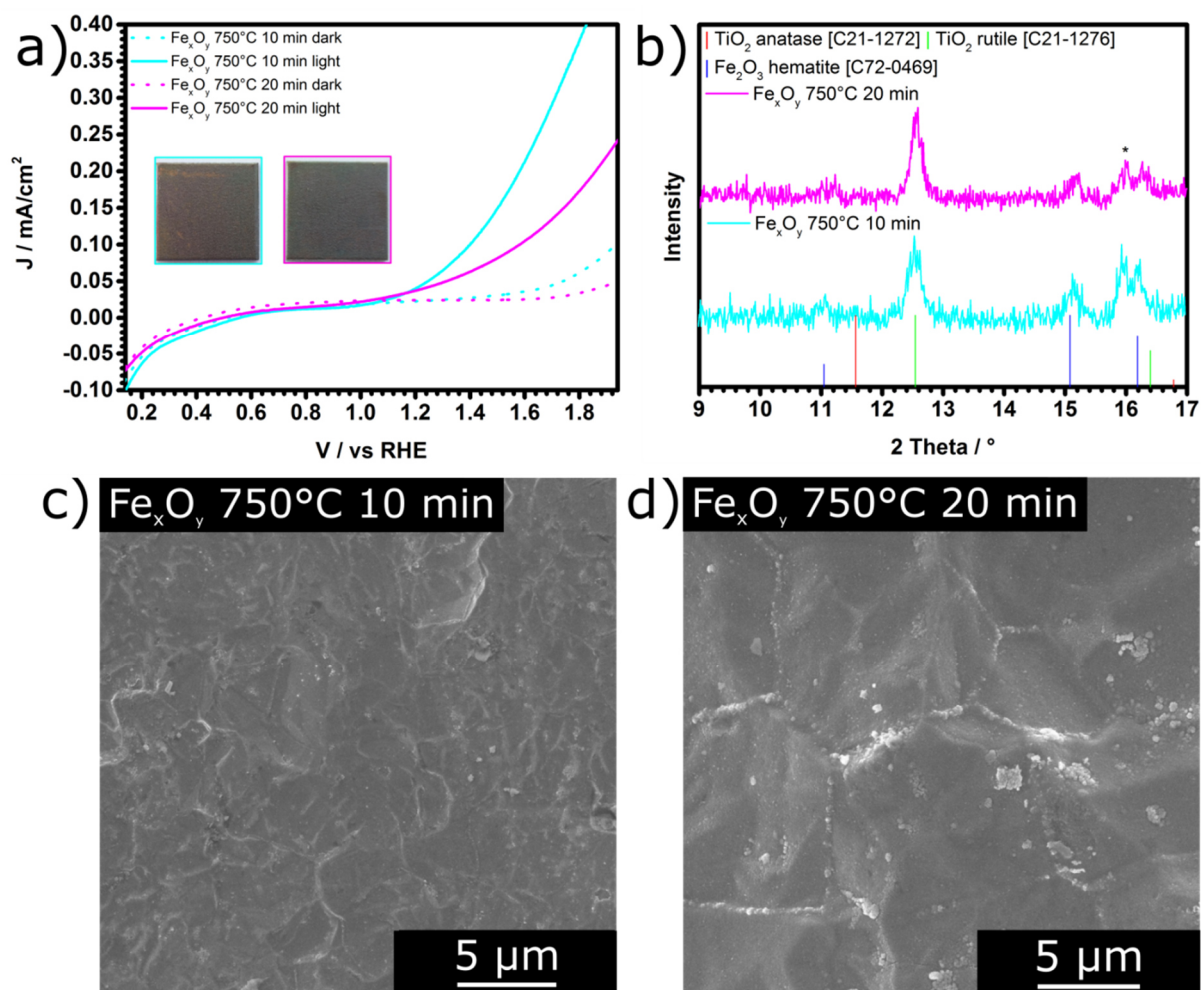


Figure 59: Photocurrent density with pictures of the samples as inset (a) and small range XRD analysis (b) of Fe_xO_y on Ti (b), annealed at 750°C for 10 or 20 minutes and their SEM images (c and d).^[238]

To reduce the loss from rutile formation while still maintaining the crystalline hematite layer, the parameters of 10 minutes annealing at 750°C were chosen for the laser structuring experiments.

3.3.3 PEC Performance of Laser-Textured Systems

The following sections discussed the effects of laser patterned metal substrates on the photoelectrochemical water splitting performance. This includes analyzing their optical properties such as absorption and photon conversion efficiency in addition to surface morphology and chemical composition in comparison to the untreated system discussed in section 3.3.2.

3.3.3.1 Patterned Ti Systems

The SEM images of the patterned substrate (see Figure 60a) showed a periodically structured patterned surface with long continuous ripples. These physical changes, known as LIPSS (laser-induced periodic surface structures), caused increased internal reflection.^[243] They remained after annealing at 600°C for 20 minutes (see Figure 60b), imparting the surface with high roughness. The long ripples were partially separated after annealing.

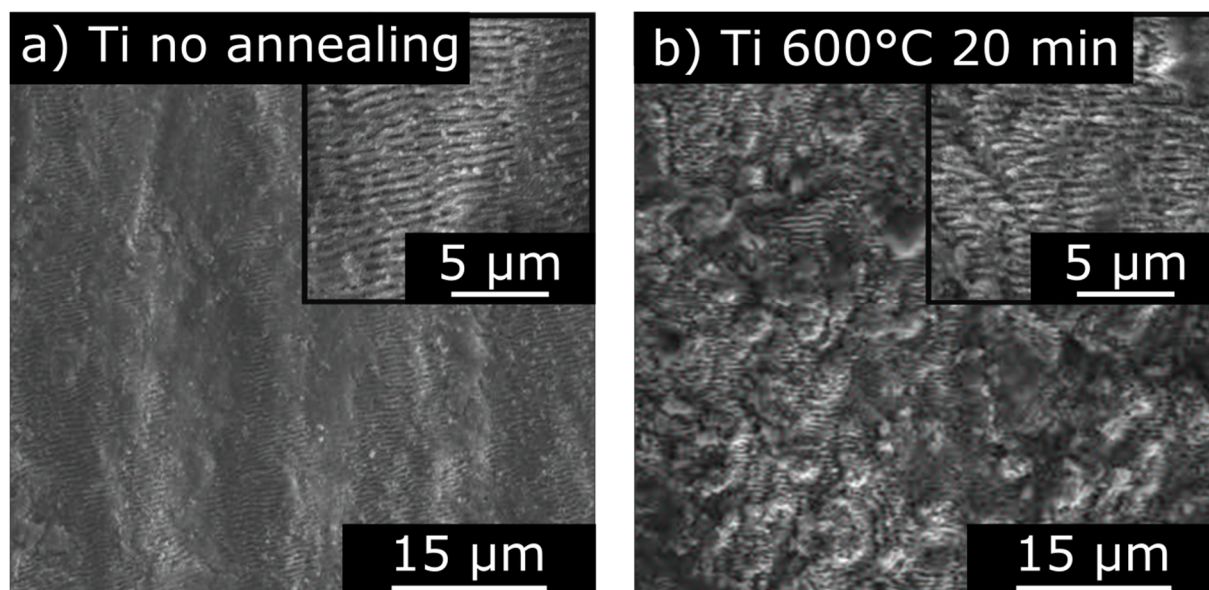


Figure 60: In plane SEM images of laser treated Ti without (a) and after annealing at 600°C for 20 minutes (b).^[238]

The untreated Ti annealed at 600° showed only a small increase photocurrent density (see Figure 61a) with longer annealing duration, which overlaps with the results presented in section 3.3.2.1. The laser treated substrate, annealed with the same process using 600°C for 20 minutes revealed a pronounced effect on the water splitting performance. The overall densities were rather low ($\sim 0.050 \text{ mA/cm}^2$) compared to other TiO_2 samples on FTO,^[244] due to the thin photoactive layer and low substrate quality. The physically modified samples performed with a significantly higher Incident Photon-to-Electron Conversion Efficiency and overall light absorption (see Figure 61b), supporting the enhanced photocurrent density. The higher absorption of the untreated samples around 550 to 750 nm came from substrate impurities, for example iron or carbon with approx. 0.5 and 0.08 wt-% respectively (see section 4.1), which also led to a coloration after annealing. No photons were converted above 500 nm, so only titanium oxide contributed to the PEC performance due to its absorption and band gap around 3.2 eV.^[245]

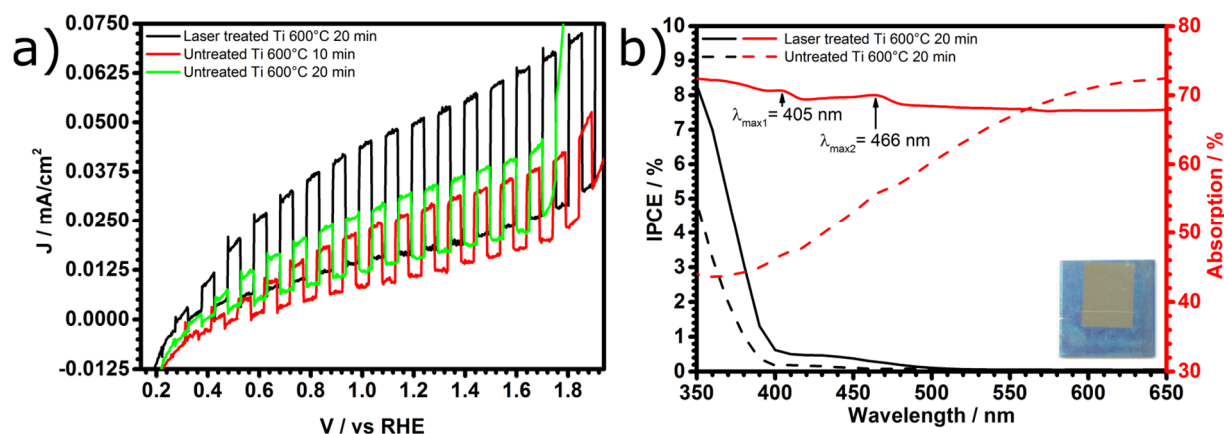


Figure 61: PEC water splitting performances of laser treated and untreated Ti (a) and their optical properties measured with IPCE (at 1.1 vs. RHE) and UV-VIS spectrometer, including an inset picture of the laser treated sample (b).^[238]

The XPS survey of the annealed system revealed remaining substrate impurities like Ca or Si (see Figure 62a), while the high resolution measurements of the Ti 2p range from both before and after annealing, untreated and laser treated samples (see Figure 62b) showed diffraction peaks from the Ti(IV) oxide, as expected. The signals centered around 459.0 eV (Ti 2p 3/2) and 464.8 eV (Ti 2p 1/2) were consistently observed for Ti 2p, according to the literature.^[246] The O 1s high resolution spectra (see Figure 62c) showed the Ti-O and Ti-OH signals around 530.0 eV and 532.0 eV, respectively.^[247] Additionally, the signal around 526.0 eV indicated a incorporated carbon-oxygen species of the substrate, most likely from the substrate production process, which was also observed in the high resolution C 1s XPS spectra (see Figure 62d) for every sample. Overall, the surface exhibited nearly identical composition, which proved that the increase in photocurrent density (see Figure 61a) must result from laser induced physical changes.

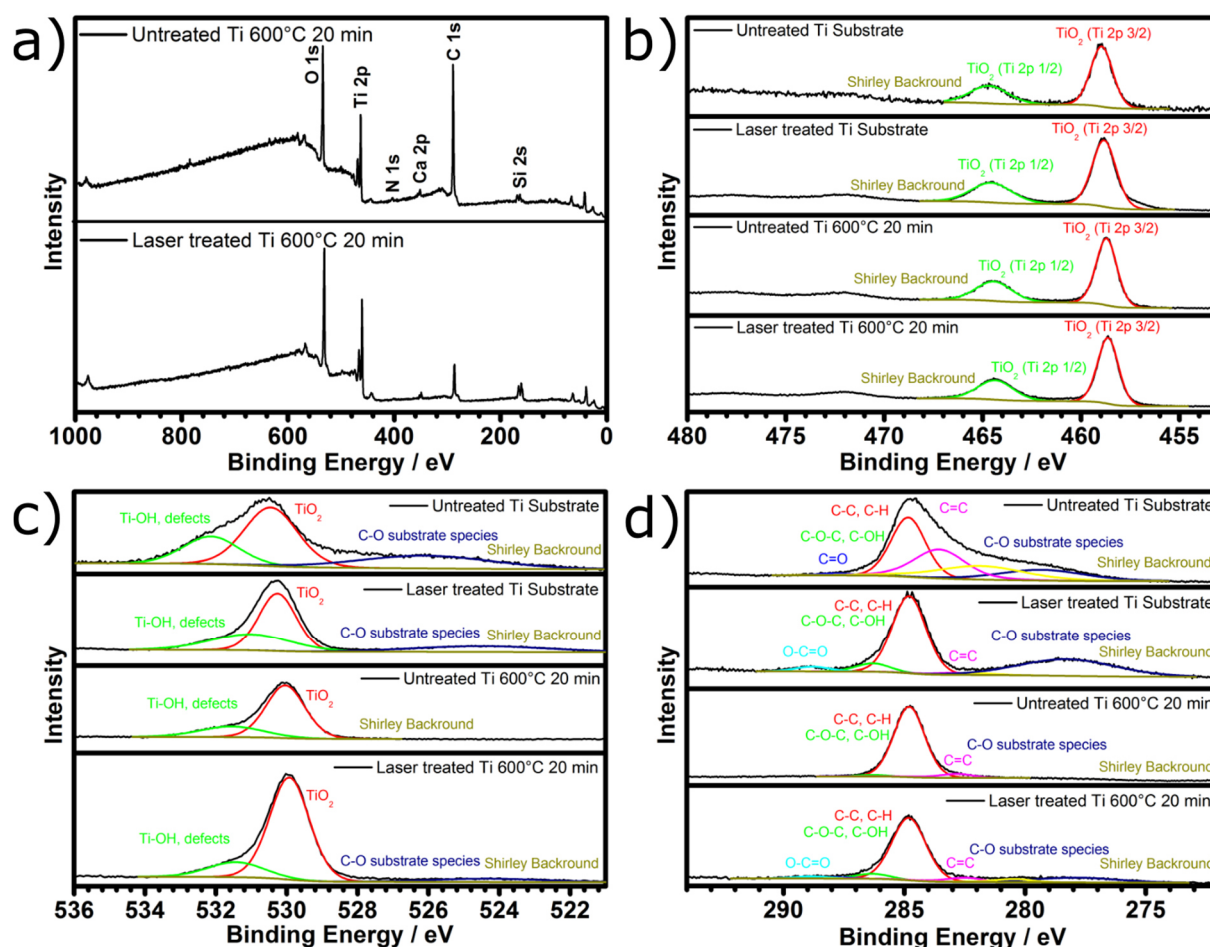


Figure 62: XPS survey of the untreated and laser treated Ti, annealed at 600°C for 20 minutes (a) and high resolution spectra of the Ti 2p (b), O 1s (c) and C 1s (d). From top to bottom, the untreated and patterned Ti before annealing, followed by both after annealing at 600°C for 20 minutes.^[238]

3.3.3.2 Patterned TiO_x on Ti Systems

The SEM images of the laser treated system after titanium oxide deposition and before annealing showed the ripple structures remaining, indicating that the titanium oxide layer was thin enough to not fill the ripples (see Figure 63a). After annealing at 600°C for 20 minutes, the film densified, producing a more homogeneous coating (see Figure 63b) through the burned carbon and increased crystallization. The laser-induced ripples were also seen after annealing.

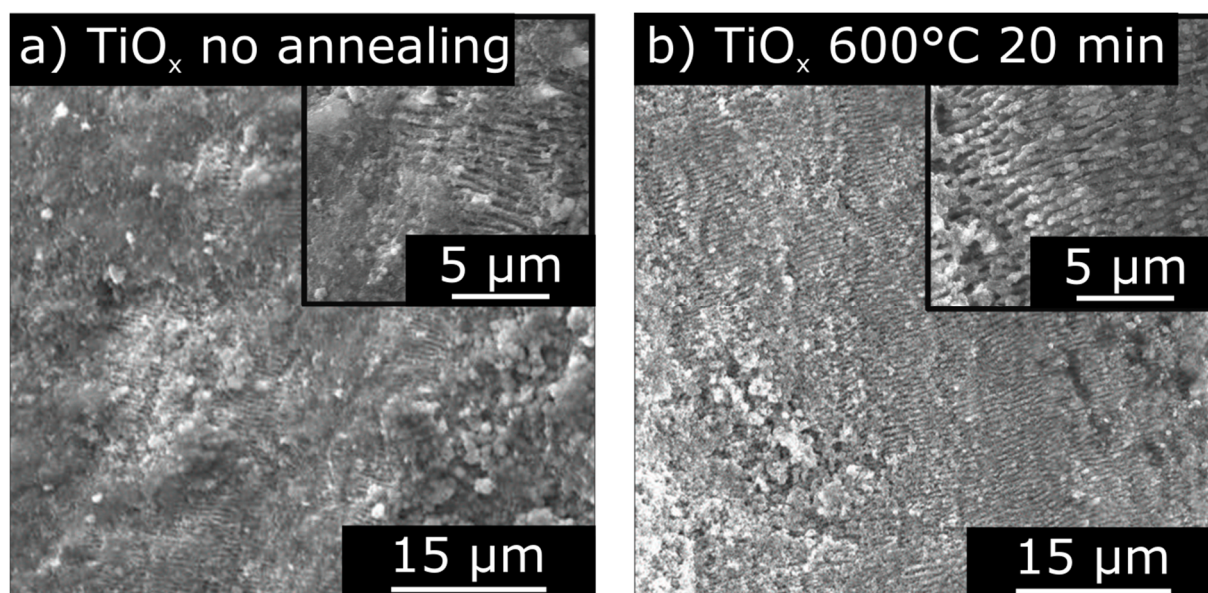


Figure 63: In plane SEM images of laser treated TiO_x on Ti without (a) and after annealing at 600°C for 20 minutes (b).^[238]

The PEC experiments revealed increased PEC performance for longer annealing duration with the untreated systems (see Figure 64a). Through the use of laser patterned substrates, it was vastly improved, with IPCE measurements revealing that most of the light absorbed above 500 nm result in nearly no photocurrent density, while most of the absorbed UV light below 400 nm participated in the reaction (see Figure 64b). The UV-VIS analysis (see Figure 64b) also showed an improvement through patterning. The annealed titanium oxide, which consisted of both anatase and rutile phases according to previous analysis (see Figure 56c and d), absorbed in the UV region,^[248] while the untreated system has additional absorption maxima due to substrate impurities, which also led to the color of the sample. These had no effect on the PEC performance according to IPCE measurements.

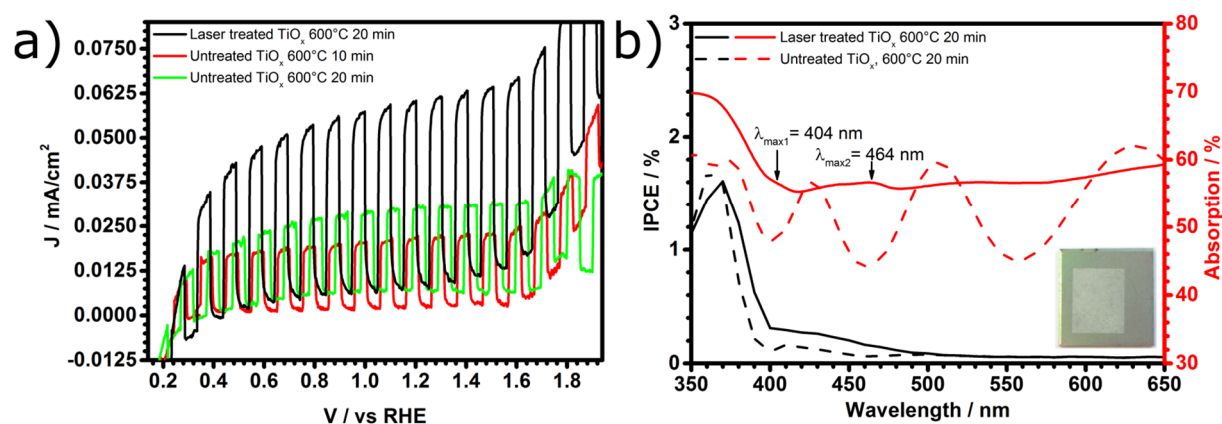


Figure 64: PEC water splitting performances of laser treated and untreated TiO_x on Ti (a) and their optical properties measured with IPCE (at 1.1 vs. RHE) and UV-VIS spectrometer, including an inset picture of the laser treated sample (b).^[238]

The XPS survey spectra of the untreated and laser treated systems were nearly identical, with some substrate impurities observable (see Figure 65a). The high resolution measurements of the Ti 2p range (see Figure 65b) showed two peaks around 459.0 eV (Ti 2p 3/2) and 464.8 eV (Ti 2p 1/2), which corresponded to Ti 2p, according to literature.^[246] In the O 1s high resolution spectra (see Figure 65c) the Ti-O and Ti-OH signals around 530.0 eV and 532.0 eV were observed.^[247] The O 1s and C 1s high resolution spectra, a slight peak shift of around 1 eV towards lower binding energies after laser treated could be observed. Additionally, an increased amount of the substrate was detected through higher roughness, while again the C-O substrate species could be measured. As expected, the surface of both untreated and laser treated samples were chemically identical, so the improved PEC performance must be a result from laser induced physical changes (see Figure 64a).

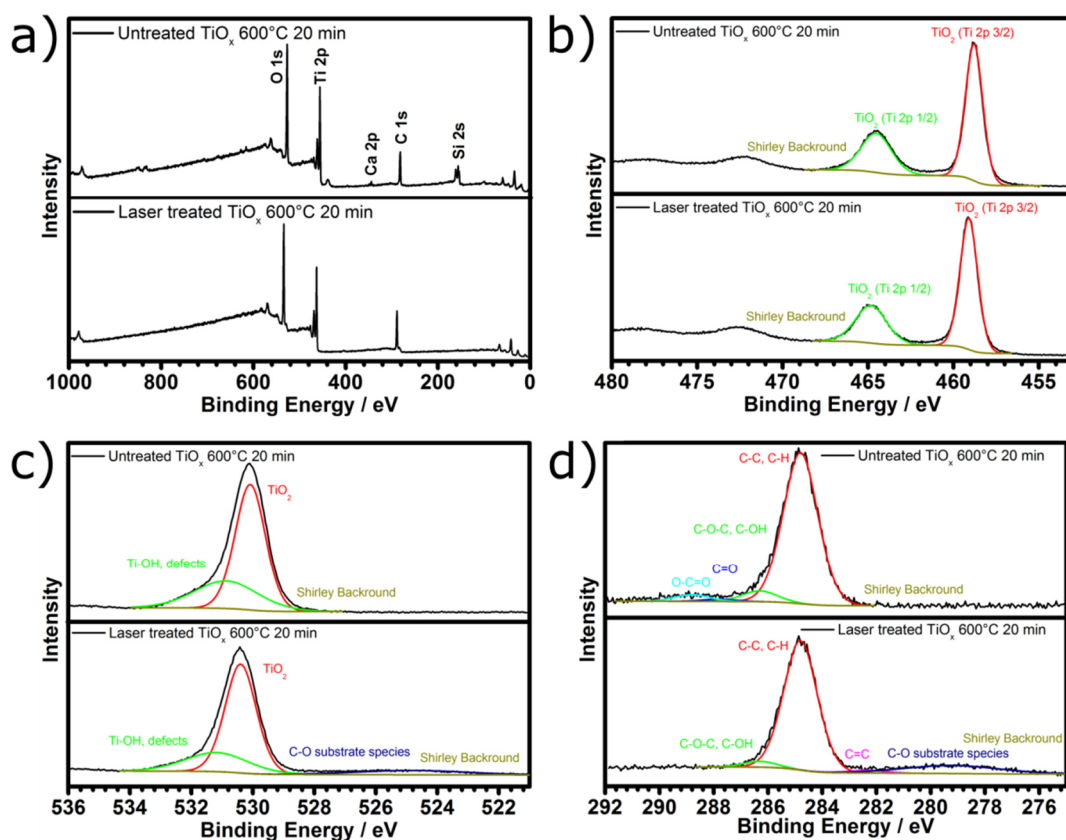


Figure 65: XPS survey (a) and high resolution spectra of the Ti 2p (b), O 1s (c) and C 1s (d), with the top as untreated TiO_x on Ti, and bottom laser treated TiO_x on Ti, both after annealing at 600°C for 20 minutes.^[238]

3.3.3.3 Patterned Fe_xO_y on Ti Systems

The SEM images of the laser treated substrate covered with amorphous iron oxide showed the LIPSS on the substrate still remained after Fe_xO_y deposition (see Figure 66a). By annealing at 750°C for 10 minutes, the layer became more dense and packed particles formed with the patterning still visible (see Figure 66b).

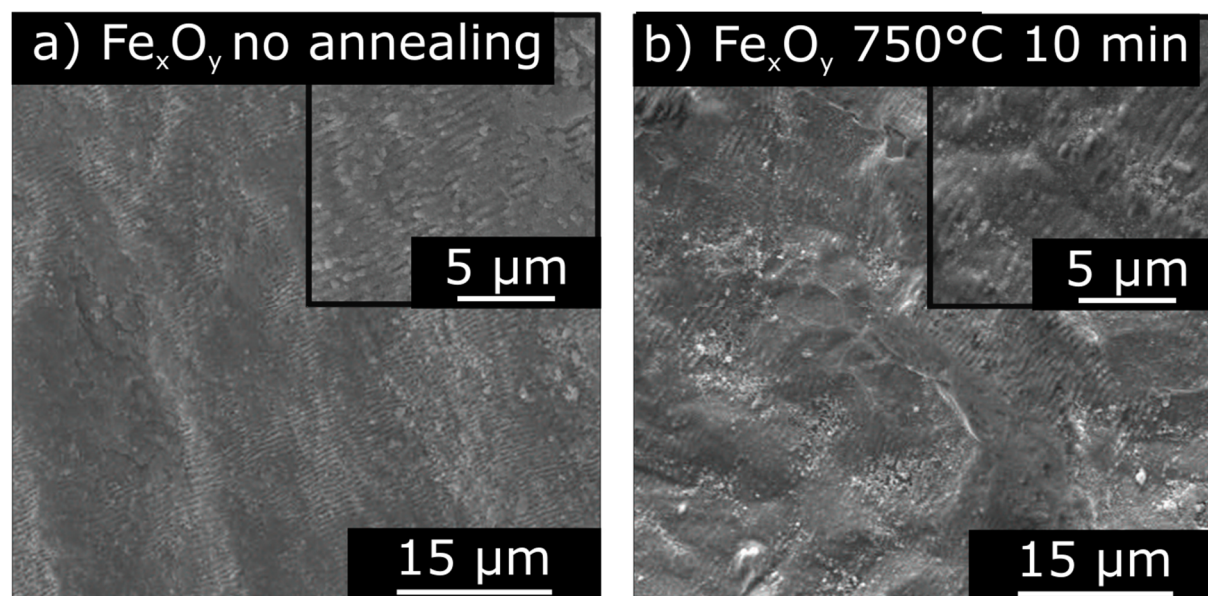


Figure 66: In plane SEM images of laser treated Fe_xO_y on Ti without (a) and after annealing at 750°C for 10 minutes (b).^[238]

The PEC measurements of the untreated samples (see Figure 67a) showed a slight increase in photocurrent density when annealed longer, as the better PEC performance from the hematite formation was counteracted by the thicker rutile blocking layer of the oxidized substrate. While this trend was different from the previous experiments (see section 3.3.2.3), the total change was legibly low, so the shorter heating duration was still used. The laser treated systems after annealing at 750°C for 10 minutes resulted in an overall PEC performance nearly doubled compared to the untreated sample, with higher photon conversion and absorption (see Figure 67b). While hematite increased the visible light absorption, the IPCE analysis revealed that its contribution was very low, most likely due to limited electron extraction through the rutile blocking layer underneath.

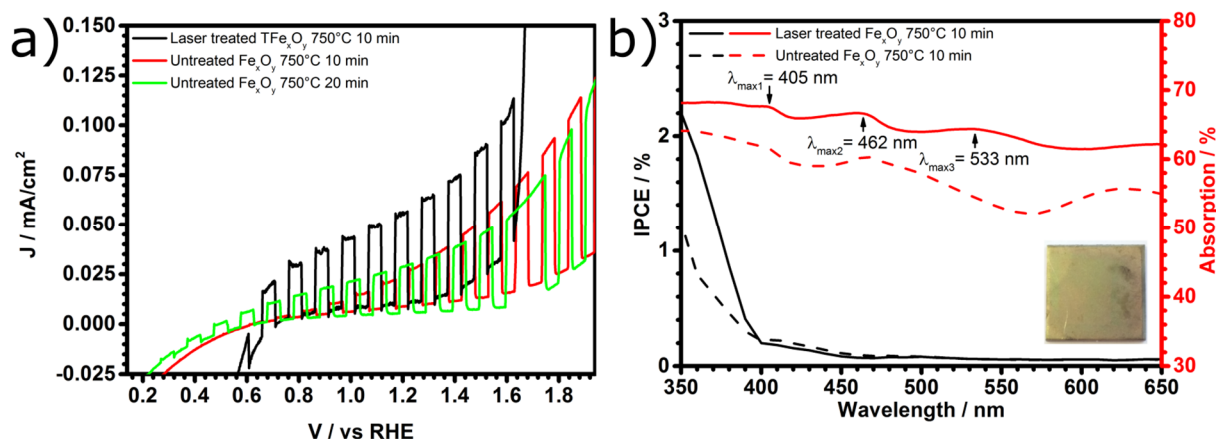


Figure 67: PEC water splitting performances of laser treated and untreated Fe_xO_y on Ti (a) and their optical properties measured with IPCE (at 1.1 vs. RHE) and UV-VIS spectrometer, including an inset picture of the laser treated sample (b).^[238]

The XPS survey spectra showed, in addition to the iron signal, substrate impurities (see Figure 68a), a result from increased roughness and pin holes. In the Fe 2p high resolution spectra (see Figure 68b), the distinct quintet of Fe_2O_3 (Fe 2p 3/2) from 709.9 to 713.7 eV could be observed, which corresponded to literature values.^[249] The O 1s high resolution spectra (see Figure 68c) revealed the signals for Fe_2O_3 and Fe-OH around 529.9 eV and 531.6 eV, respectively.^[250] The carbon-oxygen substrate species was seen in both the O 1s and C 1s high resolution spectra, and resulted from increased scattering laser patterned substrate, as they could only be observed on laser treated systems. Again, no chemical modification of the surface was measurable, indicating that the increased photocurrent density (see Figure 67a) must result from the laser induced physical change.

Overall, laser patterning of metal substrates, with the possibility to add an absorber layer (TiO_2 or Fe_2O_3), enhanced the photoelectrochemical water splitting performance because of higher photon harvesting and conversion properties. The surface composition of both laser patterned and untreated samples was nearly identical according to XPS studies, revealing that the boost must be a physical effect. The periodical patterns could also be observed after deposition of the top layers and annealing. They led to increased surface area and in-plane light trapping, ultimately resulting in improved overall absorption and incident photon to current conversion efficiency, proving that the overall PEC efficiency relies on photophysical as well as photochemical processes.

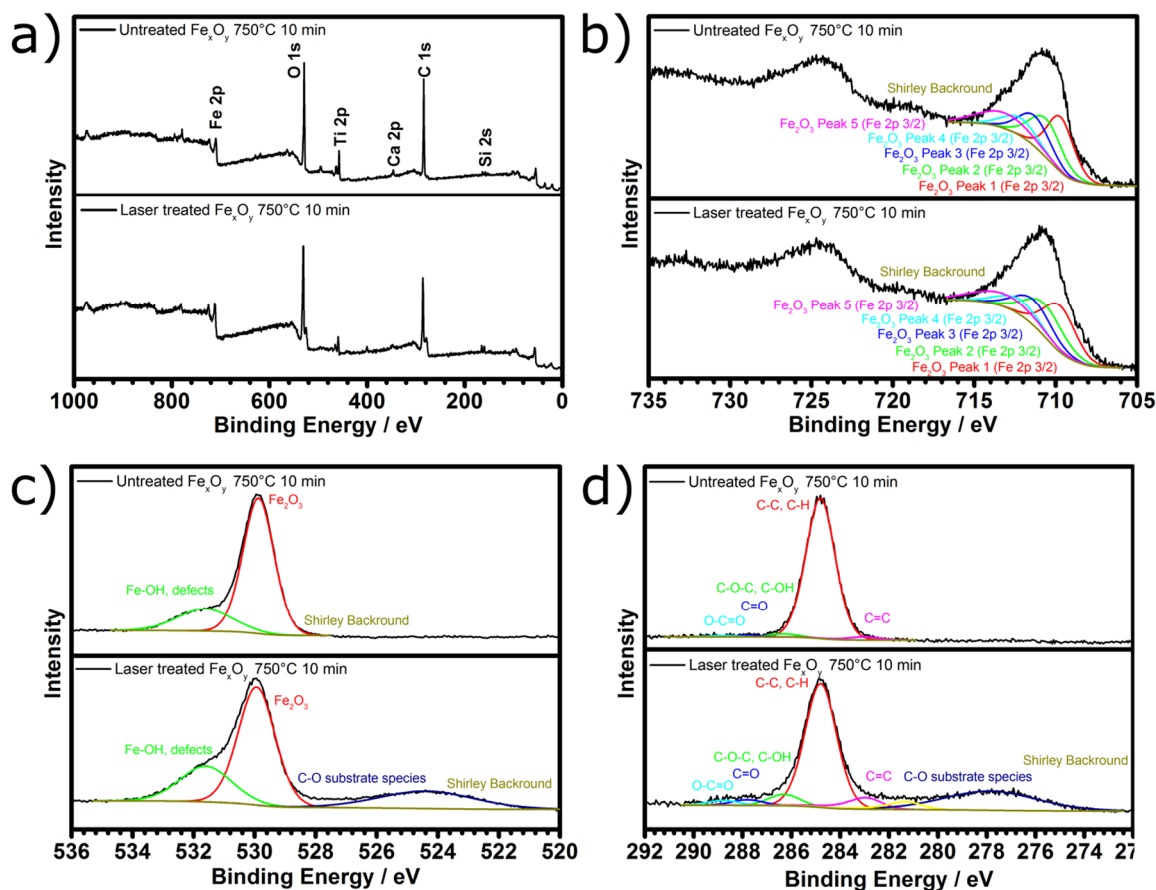


Figure 68: XPS survey (a) and high resolution spectra of the Fe 2p (b), O 1s (c) and C 1s (d), with the top as untreated Fe_xO_y on Ti, and bottom laser treated Fe_xO_y on Ti, both after annealing at 750°C for 10 minutes.^[238]

3.4 Laser Treatment of MAl_2O_4 ($\text{M} = \text{Ni}^{2+}, \text{Co}^{2+}$) Films

3.4.1 Scope and Overview

Laser treatment to induce changes on a chemical level by reducing MAl_2O_4 ($\text{M} = \text{Ni}^{2+}, \text{Co}^{2+}$) films to $\text{M}/\text{Al}_2\text{O}_3$ was studied to identify new methods for obtaining nanocomposite films. A precursor ($\text{M}[\text{Al}(\text{O}^i\text{Pr})_4]_2$) was synthesized by known routes^[251-253] and was used to produce thin films by PE-CVD, which were investigated by XPS before and after laser treatment, amorphous and after annealing. This led to the formation of transition metal clusters embedded in an Al_2O_3 matrix (see Figure 69), known as CERMET (ceramic-metal composite materials) with unique properties.^[254]

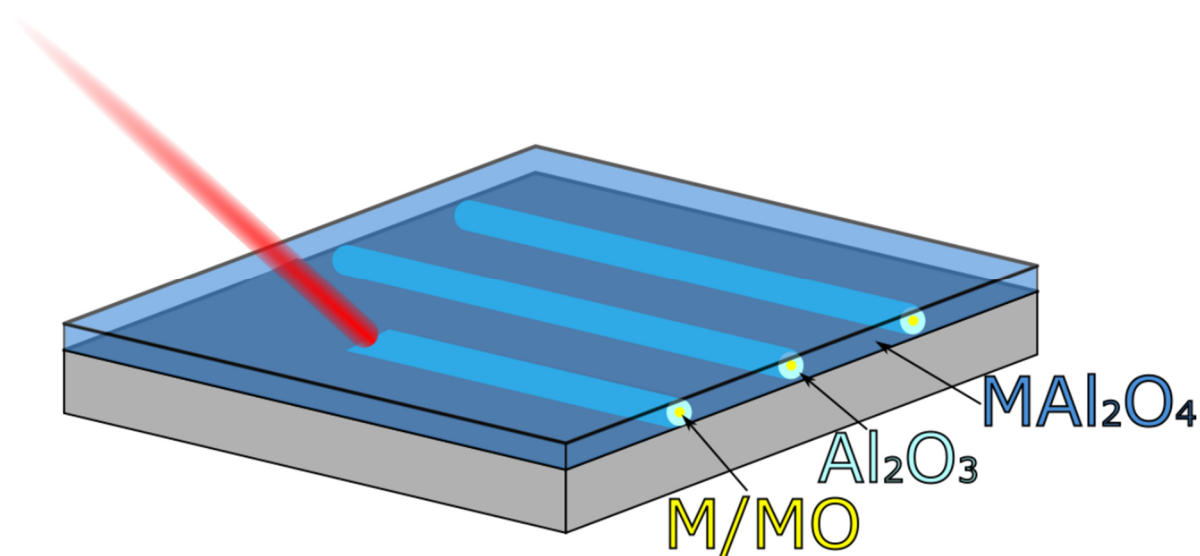


Figure 69: Possible effects of femtosecond laser treatment of MAl_2O_4 ($\text{M} = \text{Ni}^{2+}, \text{Co}^{2+}$) films.

3.4.1.1 State of the Art NiAl_2O_4 and CoAl_2O_4 Materials

The NiAl_2O_4 spinel could be used as catalyst to reform raw bio-oil,^[255] but was more often used as precursor for $\text{Ni}/\text{Al}_2\text{O}_3$ or $\text{NiO}/\text{Al}_2\text{O}_3$ photocatalysts, with different transformation steps, like heating in reductive gas,^[256] its back reaction^[257] and transformation towards the inverse spinel.^[258] Ni^0 , used for the degradation of organic pollutants, could be embedded into an Al_2O_3 lattice to enhance the efficiency and stability during photocatalytic reactions.^[256] The spinel CoAl_2O_4 is a pigment known as cobalt blue,^[259] while Co^0 was often added as co-catalyst for photocatalytic degradation.^[260] $\text{Co}/\text{Al}_2\text{O}_3$ could perform as catalyst for the Fischer-Tropsch reaction,^[261] which enables the transformation of a gas mixture of CO and H_2 into long-chained alkanes, alkenes and alcohols.^[262]

3.4.2 Analysis of $\text{M}[\text{Al}(\text{O}^i\text{Pr})_4]_2$ ($\text{M} = \text{Ni}^{2+}, \text{Co}^{2+}$) Precursor

For the generation of phase pure MAl_2O_4 films, a single-source precursor ($\text{M}[\text{Al}(\text{O}^i\text{Pr})_4]_2$, $\text{M} = \text{Ni}^{2+}, \text{Co}^{2+}$) with the ratio of 0.5 (M:Al) was synthesized through the literature known route (see section 4.5)^[251-253] and resulted in a dark violet liquid after purification (see Figure 70a and b) in both cases.

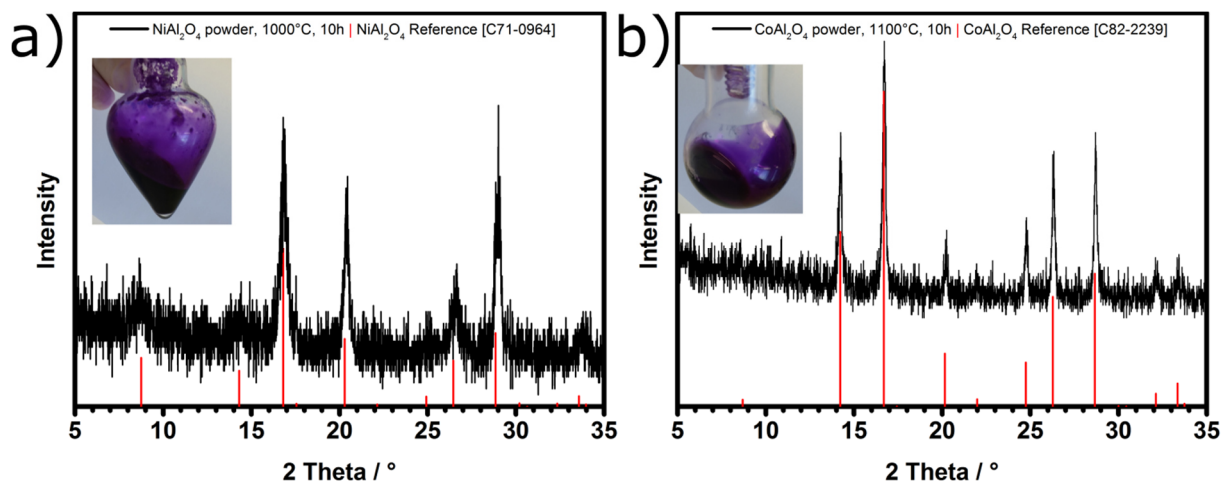


Figure 70: XRD measurement of the NiAl_2O_4 precursor annealed at 1000°C for 10 hours (a) and the CoAl_2O_4 precursor annealed at 1100°C for 10 hours (b), including the respective picture of the purified precursor as inset.

XRD measurements (see Figure 70a and b) revealed phase pure spinel structure in both cases, which proved the proposed precursor M:Al ratio of 0.5, with no different in 1000 or 1100°C annealing temperature. Mass spectroscopic analysis (see section 4.5) revealed the dominant signal as the molecular ion (M^+) peak missing one ($\text{H}_3\text{C}-$) group, most likely due to a shielding effect of the many isopropyl groups. This supported the proposed structure (see Figure 72).

The TGA measurement (see Figure 71a) of the CoAl_2O_4 precursor, performed under nitrogen, showed the loss of solvent at the beginning, followed by the decomposition process. This stopped at roughly 340°C , with a mass loss of approximately $\sim 72\%$, corresponding to the expected loss of $\sim 70\%$ (with $M_{\text{Co-Prec.}} = 585.4 \frac{\text{g}}{\text{mol}}$ and $M_{\text{CoAl}_2\text{O}_4} = 175.88 \frac{\text{g}}{\text{mol}}$). The deviation could be attributed to the additional weight loss through solvent evaporation during the decomposition step. DTA measurement revealed an endothermic signal around 320°C , a result from a reaction using surrounding heat, like a decomposition and evaporation of by-products. No crystallization could be observed as it would have led to exothermic signals in the DTA measurements, most likely due to the limited time at elevated temperatures. EDX analysis of drop coated CoAl_2O_4 , after annealing at 1100°C for 10 hours (see Figure 71b), revealed a M:Al ratio of roughly 0.4, which fit within the deviations of the not calibrated system. The Ti substrate could be seen around 4.45 keV, but had been omitted from the calculation of the ratio.

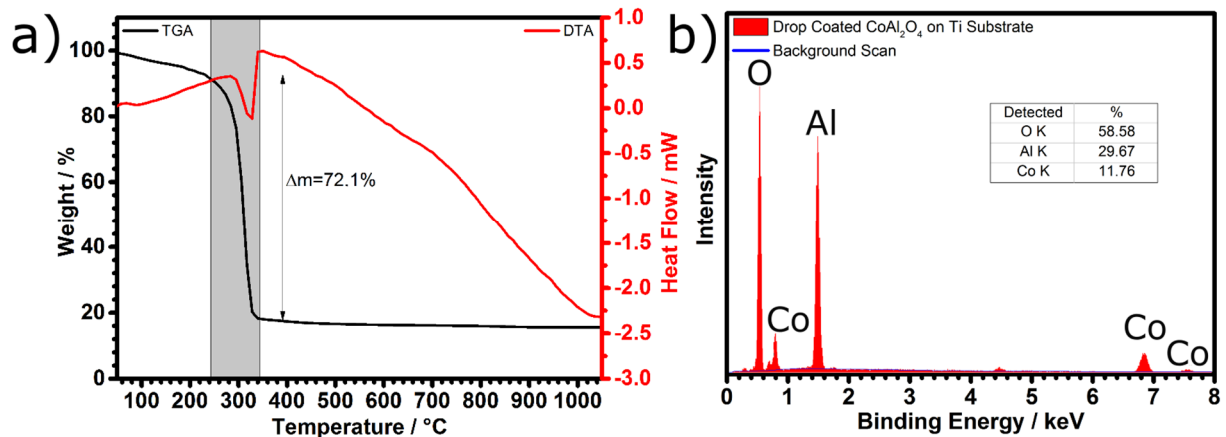


Figure 71: TG- and DTA measurements of the CoAl_2O_4 precursor including the main mass loss during the decomposition and evaporation step (a) and EDX analysis of drop coated annealed CoAl_2O_4 on Ti, with only the Co, Al and O ratios shown (b).

3.4.3 Deposition and Analysis of MAl_2O_4 ($\text{M} = \text{Ni}^{2+}, \text{Co}^{2+}$) Layers

3.4.3.1 PE-CVD Process Development

Many different parameters influence the PE-CVD process, ranging from the different gas flows, temperatures, chamber geometry, substrate positions, inlet systems, plasma gases and power, most of them were fixed in accordance to other standardized processes. An uneven chamber geometry, with a smaller rotatable reaction electrode and the chamber walls as counter electrode, was used for all depositions. The plasma power was set to 100 W, with the reaction gas being a mixture of 20 sccm O_2 and a varied amount of Ar carrier gas. While the precursor temperature was optimized, the substrates remained unheated. Their position was either direct next to the inlet or the neighboring wall (see Figure 89a), only those on the wall had very homogeneous coatings and were investigated further. The inlet system was a self-made T-shaped metallic cylinder with two openings and room for a precursor reservoir, in order to allow high precursor temperatures in addition to carrier gas. This was necessary as glass cracked at the metal-glass connection with high temperatures. This temperature, the carrier gas flow and deposition time were most influential on the layer growth and were varied through the development of a standardized deposition process. The heat range was between 100 to 150°C, as the purification step during the synthesis (see section 4.5) and the TG/DTA measurements (see Figure 71a) revealed the evaporation and decomposition regimes at different pressures. The duration was preferred too long than too short in order to prevent any precursor remaining in the inlet system. Even without any precursor left, the pure plasma did not negatively affect the deposited film. The carrier gas flow helped transporting the precursor from the container to the chamber, and ultimately worked together with the temperature to provide the optimal

precursor flow. If it was too high, the precursor might not decompose fast enough and result in inhomogeneous films or condensed powder on the substrate. If the flow was too low, most of the precursor would be decomposed before reaching the substrates. For this reason, the precursor temperature during the optimized process would be steadily increased until reaching 150°C .

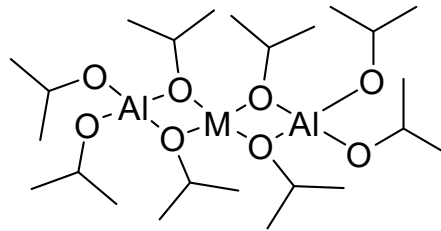


Figure 72: Sketch of the $M[Al(O^iPr)_4]_2$ ($M = Ni^{2+}$ or Co^{2+}) precursor used in PE-CVD processes.

3.4.3.2 Amorphous and Annealed $NiAl_2O_4$ on Ti

The untreated $NiAl_2O_4$ thin films were investigated towards their morphology, on both the macroscopic and microscopic level, including their chemical composition, amorphous and after annealing. The laser treated systems, including their photocatalytic performance, had been discussed in section 3.4.4.2.

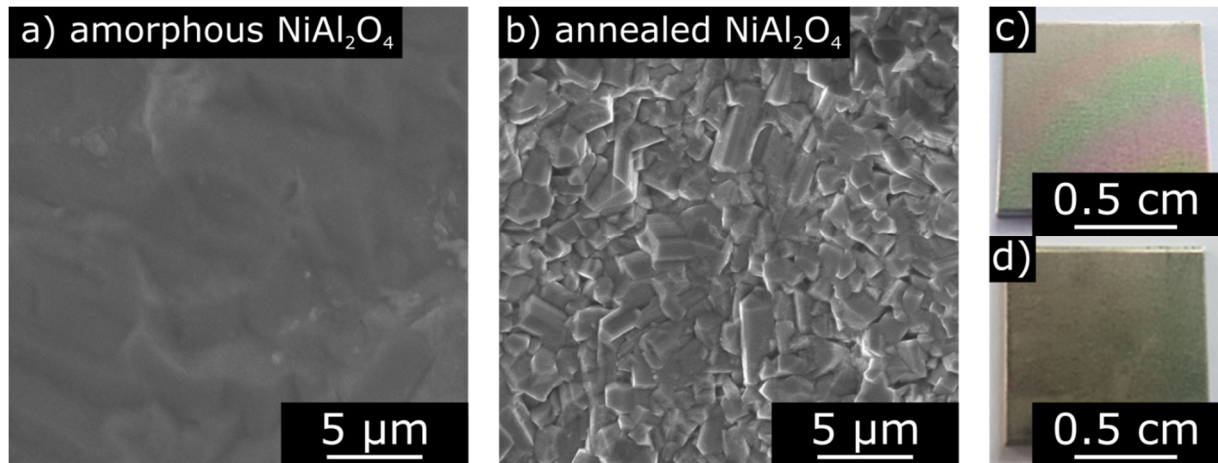


Figure 73: In plane SEM images of untreated $NiAl_2O_4$ on Ti before (a) and after annealing (b), and their corresponding pictures before (c) and after annealing (d).

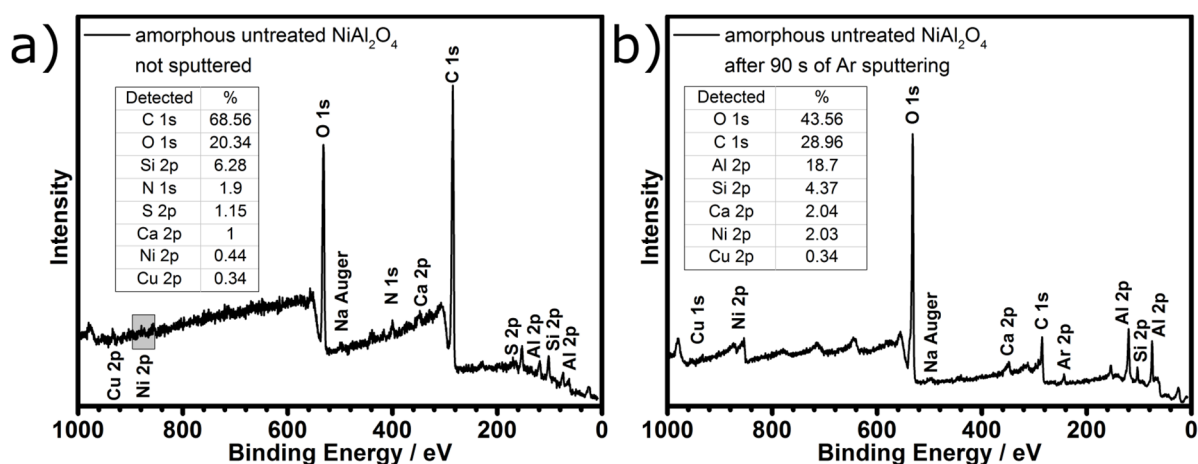


Figure 74: XPS survey spectra of amorphous untreated NiAl_2O_4 on Ti before (a) and after 90 s of Ar sputtering (b).

In plane SEM images of the amorphous NiAl_2O_4 sample (see Figure 73a) showed limited particle formed, while the morphology of the substrate was retained. Annealing resulted in big crystallites (see Figure 73d). Additionally, the small color gradient of the amorphous sample (see Figure 73b), which came from small differences in thickness due to the size and roughness of the substrate, disappeared after annealing (see Figure 73c). That indicates a more homogenous film after densification. Even though the layers were too thin for XRD measurements, the formation of crystalline materials was already proven by previous experiments (see Figure 70a).

The XPS survey spectra of amorphous untreated NiAl_2O_4 without sputtering (see Figure 74a) revealed many surface contaminations like example carbon,^[105] which was adventitious and as remains from the PE-CVD deposition.^[215-218] The small amount of nitrogen, silicon and calcium could be substrate signals, as seen in later measurements (see Figure 83). No titanium signal could be observed. The copper and sulfur were external contaminations, as they only randomly appeared during all XPS analysis in this research. As the amount of nickel and aluminum was very low (see Figure 74b), the systems needed to be sputtered to allow high resolution Ni 2p analysis (see Figure 75). This also resulted in decreased contamination, especially carbon.

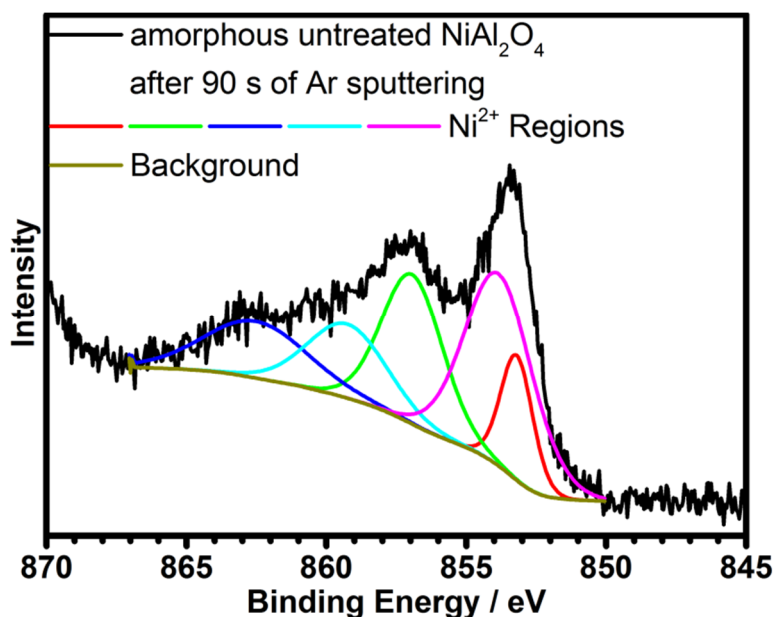


Figure 75: High resolution Ni 2p XPS spectra of amorphous untreated NiAl_2O_4 on Ti after 90 s of Ar sputtering.

The high resolution XPS spectra of the Ni 2p signal (see Figure 75) showed clear Ni^{2+} regions. Due to the amorphous nature of the sample, the fit had to be performed manually, and was a mixture of several literature-known materials. NiO was used as common nickel oxide, while both NiCr_2O_4 and NiFe_2O_4 , the bimetallic nickel oxides in the spinel structure.^[263] No reduction through the argon sputtering could be observed, as Ni^0 would lead to a shoulder around 852.6 eV.^[264]

The photocatalytical performances were discussed in section 3.4.4.2, including the comparison of these samples to their laser treated variation.

3.4.3.3 Amorphous and Annealed CoAl_2O_4 on Ti

In plane SEM images of CoAl_2O_4 samples without annealing (see Figure 76a) showed no particle formation while the morphology of the substrate was retained. Annealing led to many small particles (see Figure 76d). Additionally, the dark brown color of the sample without annealing (see Figure 76b), a result from the high amount of carbon impurities from the PE-CVD deposition,^[215-218] turned into a greenish blue color after annealing (see Figure 76c), which corresponded to a thin film of the cobalt blue spinel on the substrate background. Even though the layers were too thin to result in any XRD signals, previous experiments already proved that under these heat treatment conditions crystalline material would be formed (see Figure 70b).

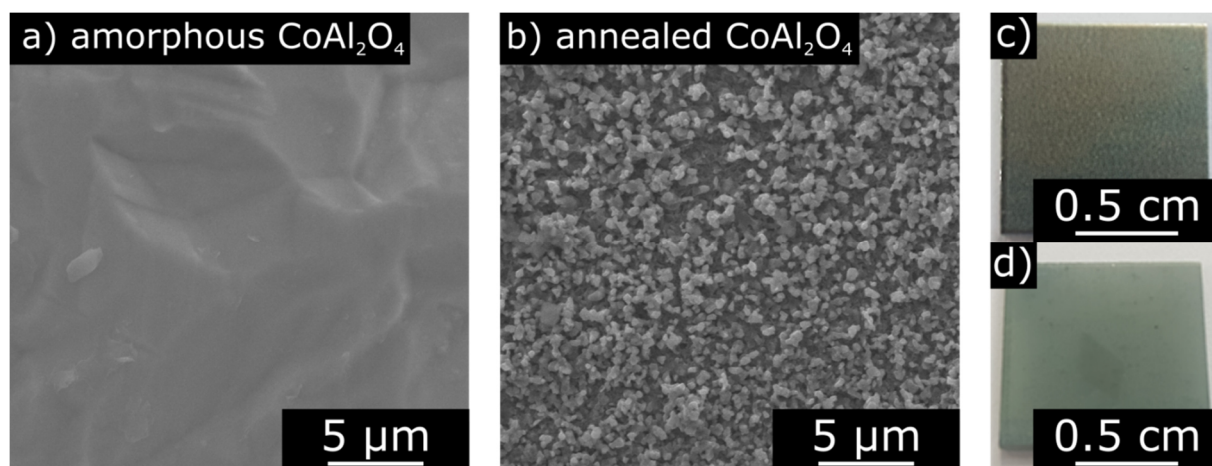


Figure 76: In plane SEM images of untreated CoAl_2O_4 on Ti before (a) and after annealing (b), and their corresponding pictures before (c) and after annealing (d).

EDX measurements (see Figure 77) of a PE-CVD coated, amorphous CoAl_2O_4 film on silicon substrate (Si signal: 1.7 eV) revealed a M:Al ($\text{M} = \text{Ni}^{2+}, \text{Co}^{2+}$) ratio of ~ 0.54 (Co signal: ~ 0.8 and ~ 6.9 eV; Al signal: ~ 1.5 eV), which corresponds to the expected value. During the deposition process, many remnants of the decomposed precursor had been integrated into the lattice in the form of M-CH_3 ,^[215-218] leading to high carbon content.^[105] Additionally, the penetration depth of around 1 μm resulted in the Si substrate signals being measured.^[265]

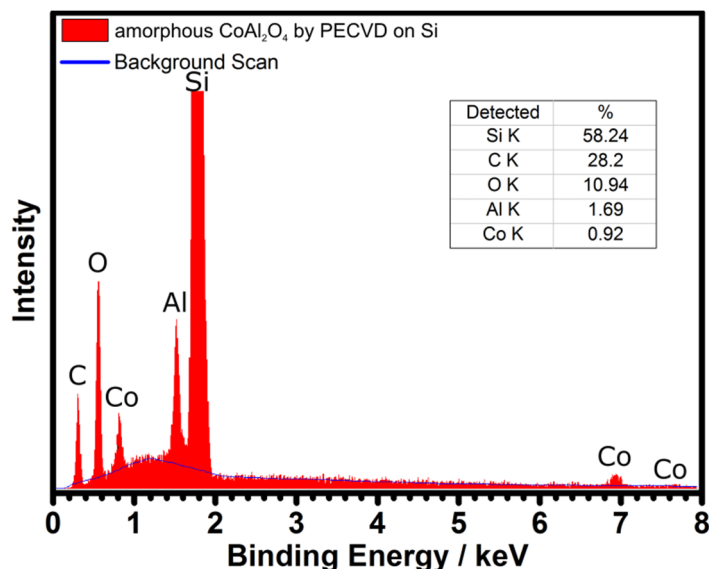


Figure 77: EDX analysis of an amorphous CoAl_2O_4 thin film by PE-CVD on a Si substrate.

The XPS survey spectra of the annealed untreated CoAl_2O_4 film without sputtering (see Figure 78a), revealed high carbon content due to adventitious carbon, which was strongly reduced through sputtering. This means the CoAl_2O_4 film was not free of pin holes or cracks after annealing. Even though a very small aluminum signal could be obtained, the cobalt content on the surface was too low to be detected, with only a small peak around ~ 780 eV, the position of the Co 2p signal.^[250] This problem remained after sputtering, making high resolution analysis impossible. Nevertheless, it led to the reduced carbon content and indicated that nitrogen and

silicon are part of the substrate (see Figure 78b). The argon signal was commonly observed after sputtering, as it partially remains inside the chamber.

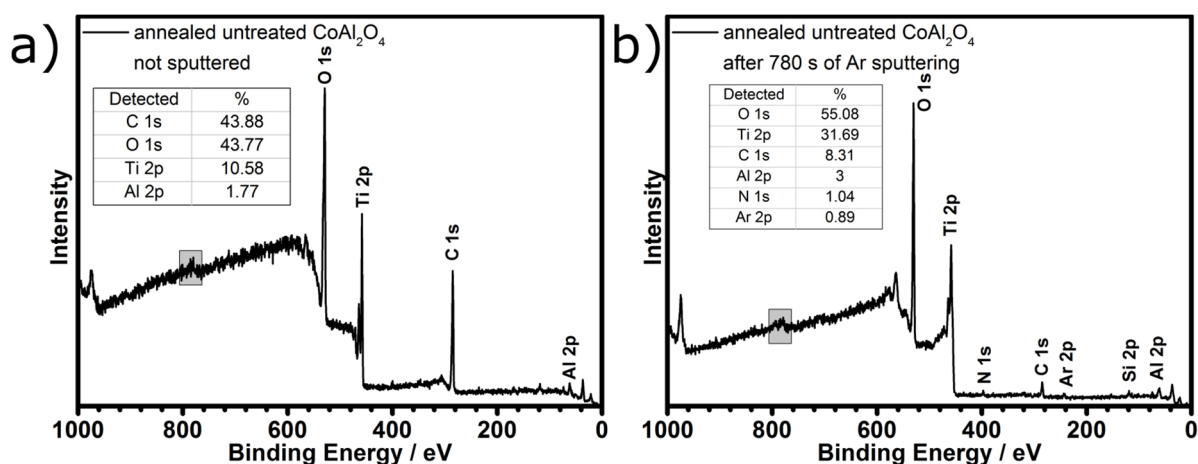


Figure 78: XPS survey spectra of annealed untreated CoAl_2O_4 on Ti before (a) and after 780 s of Ar sputtering (b).

3.4.4 Photocatalytic Degradation of Methylene Blue

The photocatalytic degradation was performed with methylene blue (MB) as organic dye in water by measuring its absorption peak at 664 nm in the UV-VIS spectra (see Figure 79), after fixed durations. This procedure is commonly used in literature.^[266, 267] These values were normalized to allow a proper comparison of different systems. First, the reference systems were measured, followed by the untreated and laser treated MAl_2O_4 ($\text{M} = \text{Ni}^{2+}, \text{Co}^{2+}$) films, which were either without or after annealing.

3.4.4.1 Dye Degradation and Reproducibility

The degradation of methylene blue was measured every 60 minutes for a total of 6 hours, while no additives like H_2O_2 were used. This allowed to only analyze the degradation potential of the fabricated MAl_2O_4 ($\text{M} = \text{Ni}^{2+}, \text{Co}^{2+}$) systems.

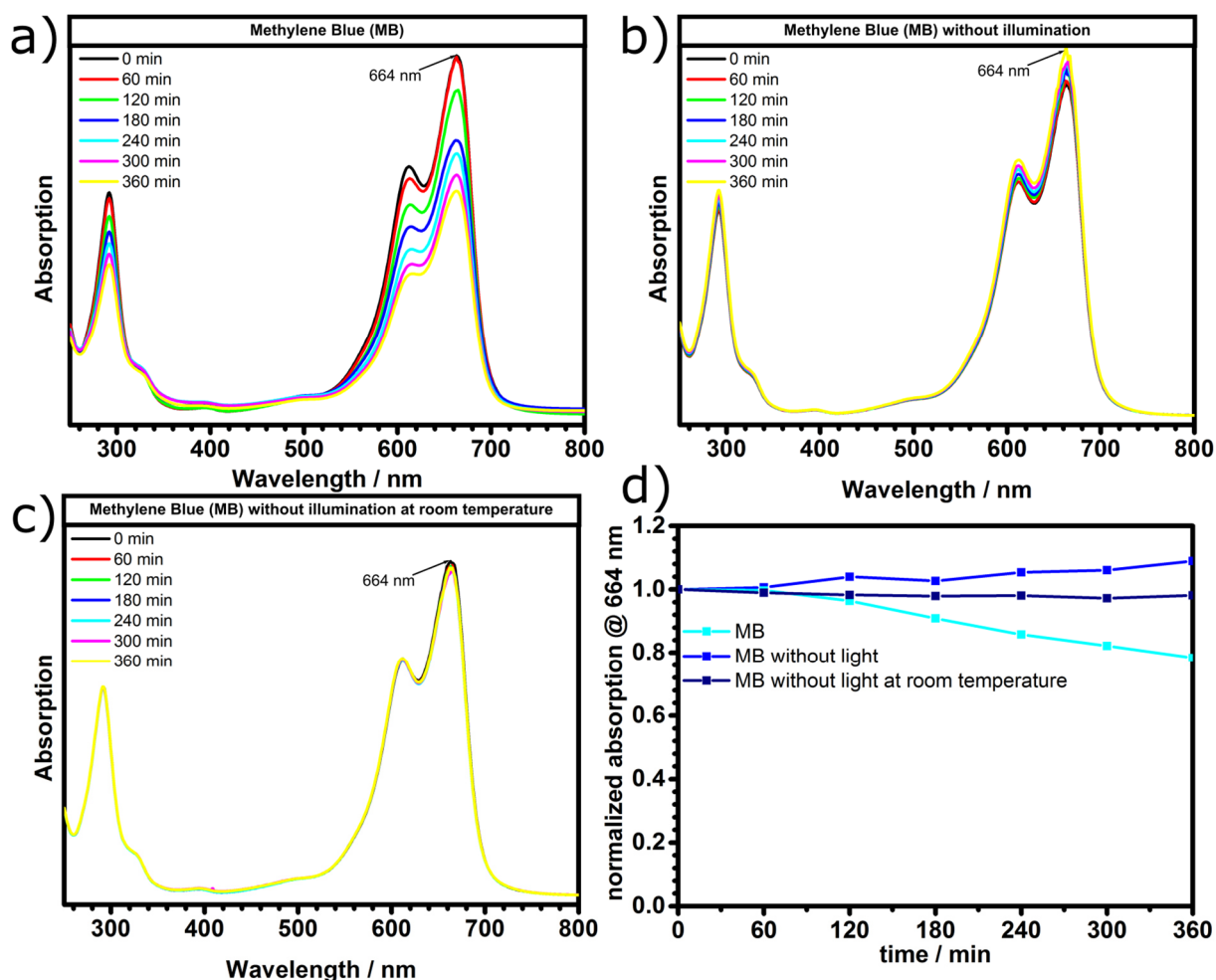


Figure 79: UV-VIS spectra of methylene blue (MB) during photocatalytic decomposition experiments (a), without illumination but still at elevated temperatures (b) and without illumination as well as at room temperature (c), with their normalized changes in absorption displayed over time (d).

The pure dye solution was investigated to distinguish between the photodegradation of the dye itself and the fabricated materials in further experiments. For this, MB was analyzed under experimental conditions (see Figure 79a), which showed a slow but constant decomposition of around 20% after 6 hours. Without illumination (see Figure 79b), the absorption increased by around 10%, as the lamp increased the temperature of the solution, leading to evaporation of the water and increased dye concentration. Without any illumination and at room temperature (see Figure 79c), a measurement deviation maximum of 2% in any direction was observed, as no decomposition or evaporation took place.

In the next step, the degradation of MB was compared to the Ti substrates, which were used as basis for the catalytic system during further experiments, either without (see Figure 80a) or after annealing (see Figure 80b). The bare titanium substrate only blocked the incoming light while taking no part in the degradation process itself. Instead, it reduced the total traveling distance of the light through the MB solution. This limited the un-catalyzed decomposition of around 10%. Annealing the Ti substrate resulted in a very thin crystalline TiO_2 film, a known

photocatalyst and showed increased photodegradation of around 33%. This was lower than reported in literature,^[268] which had increased active surface through the use of nanoparticles. TiO_2 is the gold standard for photocatalytic degradation measurements, yet the thin films produced were not as good as literature values^[172] due to being grown from Ti substrates through thermal annealing. The system was not optimized as it only served as reference.

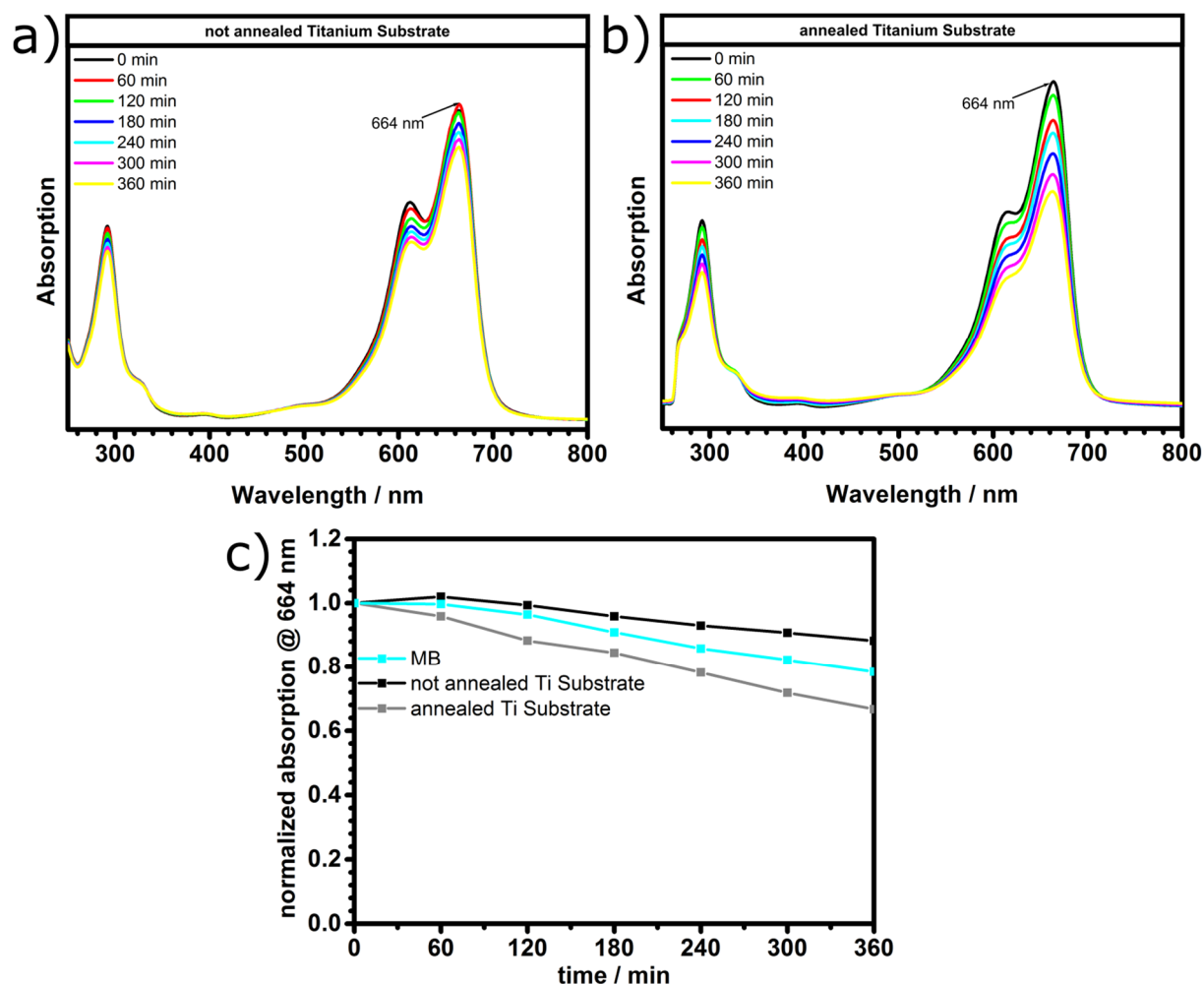


Figure 80: UV-VIS spectra of the Ti substrates during photocatalytic decomposition experiments before (a) and after annealing at 1100°C for 10 hours (b), with their normalized changes in absorption displayed over time (c).

The reproducibility of the measurements was investigated by using three different, amorphous laser treated CoAl_2O_4 thin films (see Figure 81a-c). Even though the samples exhibited no activity (see section 3.4.4.3 Figure 88), they still revealed small deviation in the measurements, similar to the MB measurement at room temperature (see Figure 79c). Additionally, it could be observed that sometimes after the first 60 minutes of illumination, the dye concentration slightly became higher instead of decreasing. This phenomenon was observed in many different measurements and could be a result of a higher initial room temperature on the measurement day, causing increased evaporation during the first hour or a slow equilibration of the concentration in the stock solution. The latter was reduced as much as possible, as the stock solution was always stirred over night before the measurements were performed the next day,

and during the experiment, a magnetic stirring bar was used to get homogenous distributed concentration inside the system (see section 4.4).

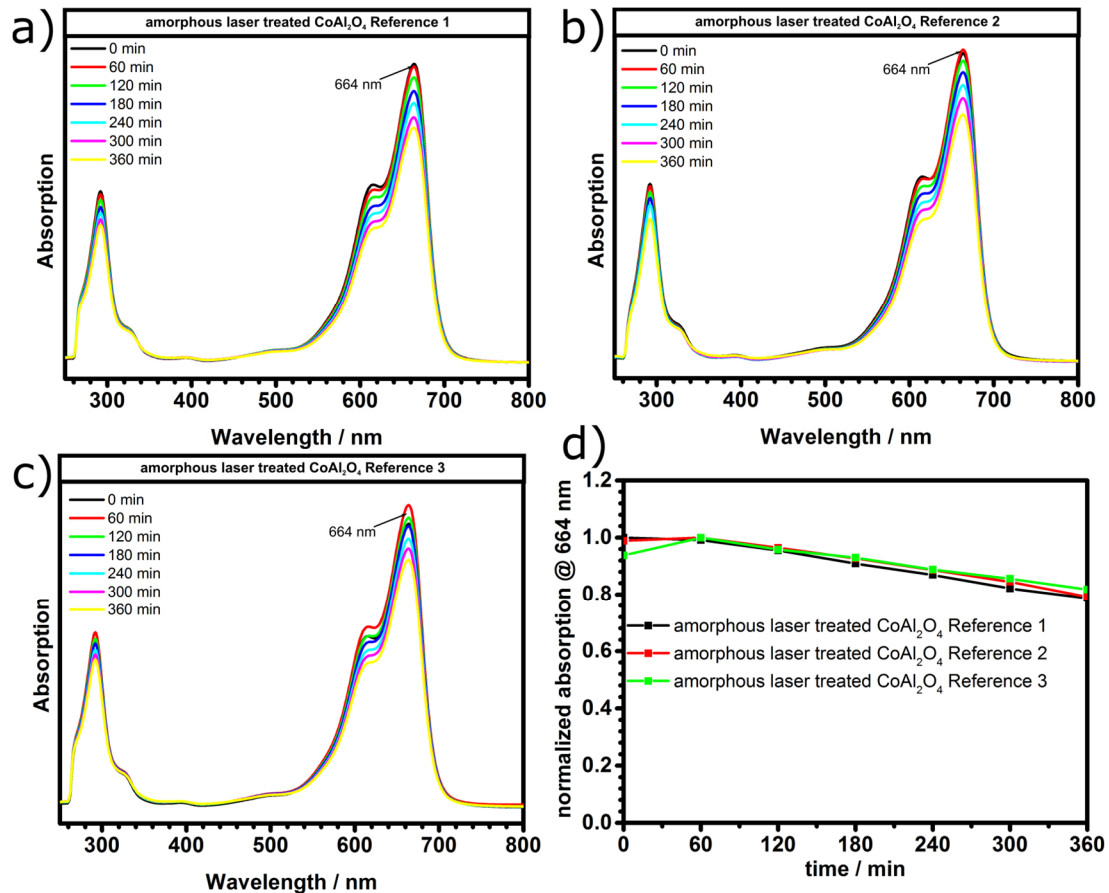


Figure 81: UV-VIS spectra of amorphous laser treated CoAl_2O_4 on Ti during photocatalytic decomposition experiments, three times with identical parameters (a-c) and with their normalized changes in absorption displayed over time (d).

3.4.4.2 Performance of Laser Treated NiAl_2O_4 on Ti

The effect of femtosecond laser treatment on NiAl_2O_4 thin films were investigated towards their morphology on both the macroscopic and microscopic level and their composition after laser treatment. Untreated samples had been discussed in section 3.4.3.2.

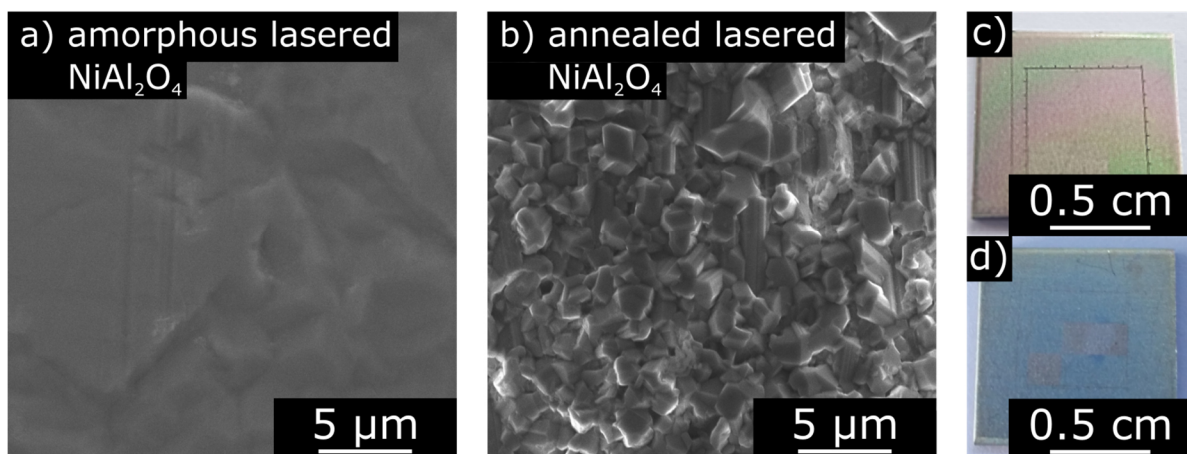


Figure 82: In plane SEM images of the amorphous laser treated NiAl_2O_4 on Ti (a) and annealed laser treated NiAl_2O_4 on Ti (b) and their corresponding pictures before (c) and after annealing (d).

In plane SEM images of the laser treated NiAl_2O_4 without annealing (see Figure 82a) revealed a film with the morphology of the substrate retained with no laser induced physical structures on the surface meaning the modifications remained on a chemical level. On a macroscopic scale, the sample exhibited a small gradient in the substrate color (see Figure 82b), which was not present after annealing (see Figure 82c). Additionally, big crystallites molten together to form a film, which was revealed in the SEM images (see Figure 82d) with a bigger surface area compared to the flat thin film.

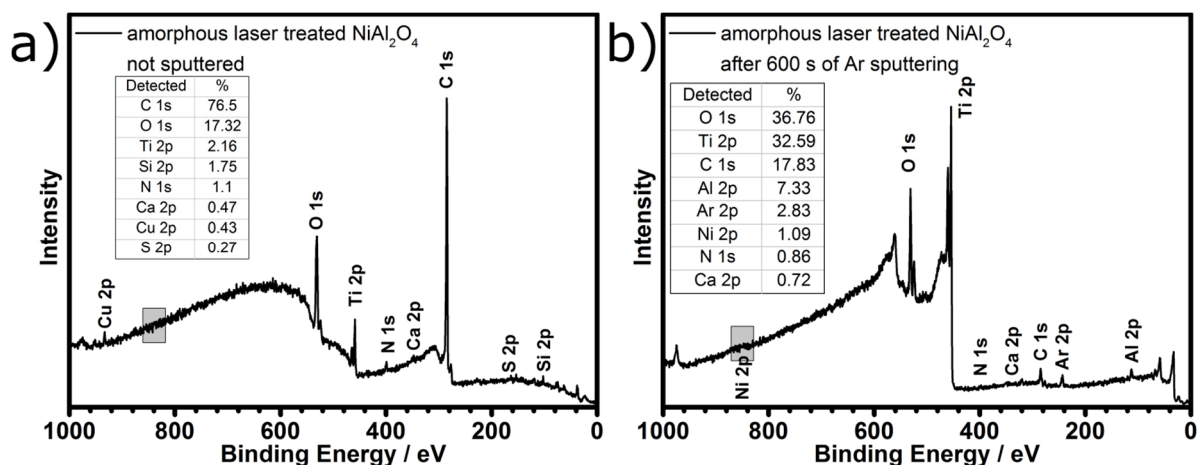


Figure 83: XPS survey spectra of laser treated NiAl_2O_4 on Ti before (a) and after 600 s of Ar sputtering (b).

The XPS survey spectra of the amorphous laser treated NiAl_2O_4 without sputtering (see Figure 83a) revealed high carbon content due to adventitious carbon and precursor remnants in the film.^[215-218] Additional signals were from the titanium substrate, calcium and nitrogen. The detection of the substrate by XPS after laser treatment was also observed in previous measurements (see section 3.3.3.2 Figure 65). Another explanation could be that the laser treatment led to partial ablation or densification of the film, partially revealing the titanium to the X-ray beam as the surface spectra were measured over a big area. Both sulphur and copper were external contaminations, while both aluminum and nickel could only be observed after sputtering (see Figure 83b) and remained below the threshold for high resolution measurements. Nevertheless, it decreased the carbon signal while those of the substrate increased in addition to the argon signal.

The amorphous NiAl_2O_4 layer showed no photoactivity (see Figure 84a). This was expected, as previous XPS analysis showed the amorphous layers consisting of Ni^{2+} (see Figure 75), which might only work as co-catalyst according to literature.^[269] By laser treating amorphous NiAl_2O_4 , the activity drastically increased (see Figure 84b), with approximately 61% of MB decomposed after 6 hours. Even though no high resolution XPS spectra of the Ni 2p signal from

the laser treated films could be measured in the case of nickel, the laser induced reduction of the metal from M^{+2} to M^0 was proved in section 3.4.4.3 (see Figure 87), where the Co^{2+} of $CoAl_2O_4$ was reduced to Co^0 . Previous reports had shown that Ni^0 clusters inside an Al_2O_3 matrix, which itself remained inactive, was a viable photocatalytic system.^[256] The annealed laser treated system (see Figure 84c) showed less activity in comparison with only approximately 37% of MB decomposed after 6 hours, again through the laser induced reduction. The annealing step before the treatment process crystallized the film in spinel structure. The resulting big crystallites (see Figure 82d) might prevent contact of the dye with the Ni^0 clusters or the crystalline $NiAl_2O_4$, which was not reduced, prevented the decomposition while acting as recombination centers. Also, fully crystalline layers might be more resistant to laser reduction than the amorphous film.

By annealing after the laser treatment (see Figure 84d), the system lost all of its photocatalytic activity. The activity, no matter if amorphous or after annealing, must have resulted from the laser treatment process, as no untreated material showed any activity. This also supported the theory of laser induced Ni^0 acting as catalytic centers, with thermal oxidation to Ni^{2+} reverted the system towards no activity. The amorphous laser treated sample was measured without illumination (see Figure 84e) and proved the activity as a result of photoabsorption and not inherent decomposition capabilities of the material.

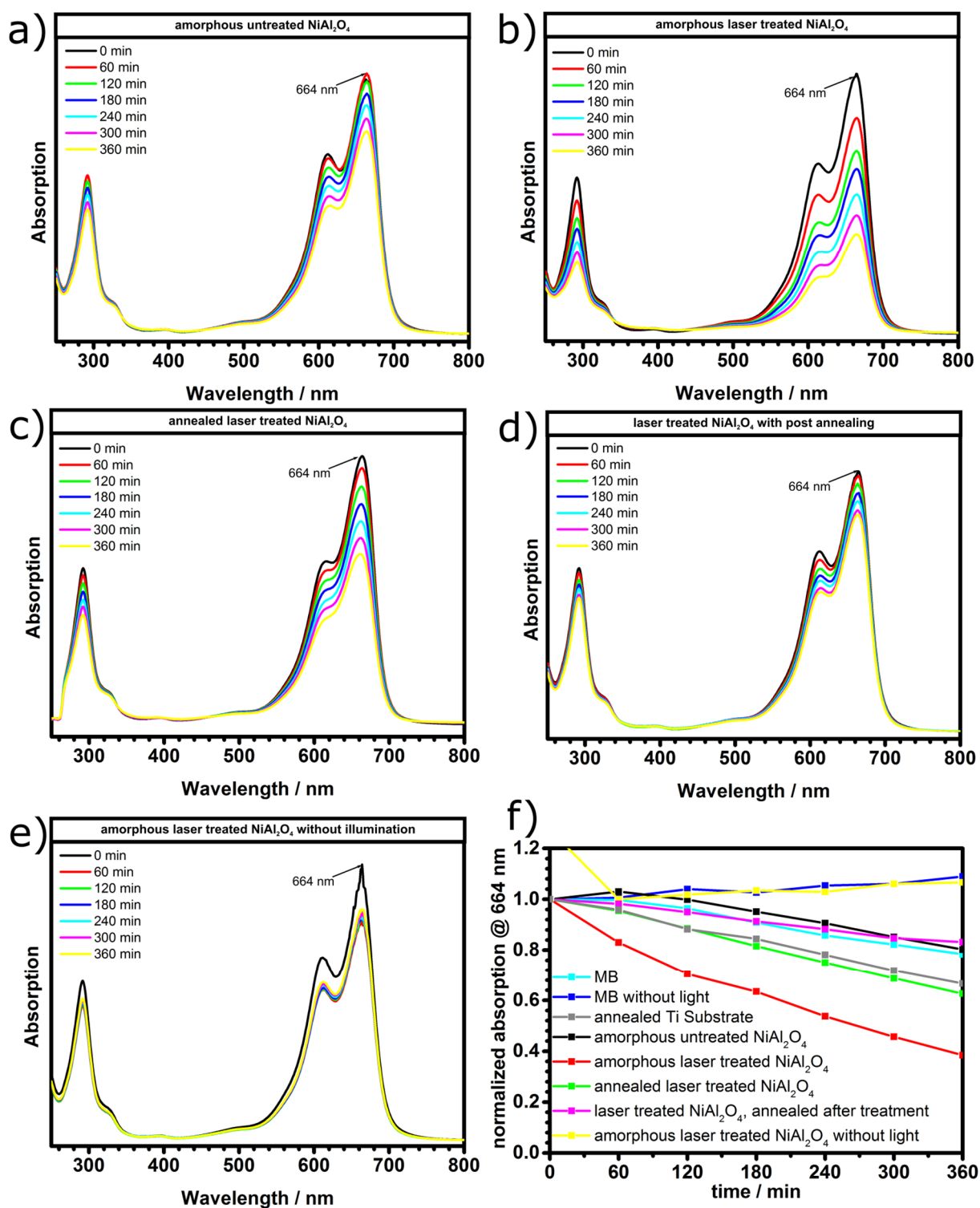


Figure 84: UV-VIS spectra of amorphous untreated NiAl_2O_4 on Ti during photocatalytic decomposition experiments (a), the amorphous laser treated NiAl_2O_4 on Ti (b), the annealed laser treated NiAl_2O_4 on Ti (c), the laser treated NiAl_2O_4 on Ti annealing after the laser treatment (d), the amorphous laser treated NiAl_2O_4 on Ti without illumination (e) and their normalized changes in absorption displayed over time (f).

3.4.4.3 Performance of Laser Treated CoAl_2O_4 on Ti

The effect of femtosecond laser treatment on the CoAl_2O_4 thin films was investigated towards their morphology on both the macroscopic and microscopic level, and their composition after laser treatment, including Co 2p high resolution XPS spectra. Untreated samples had been discussed in section 3.4.3.3.

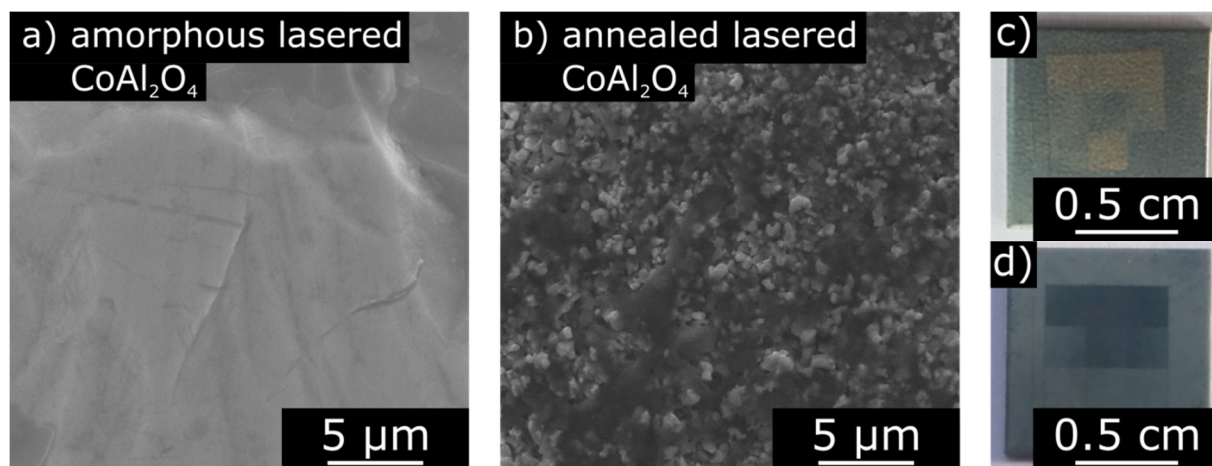


Figure 85: In plane SEM images of the amorphous laser treated CoAl_2O_4 on Ti (a) and annealed laser treated CoAl_2O_4 on Ti (b), and their corresponding pictures before (c) and after annealing (d).

In plane SEM image of the annealed laser treated CoAl_2O_4 sample (see Figure 85a) showed no microscopic effect of the laser treatment except increased amount of cracks. On the macroscopic level however, an effect could be seen as a change of color (see Figure 85b). This was either from partial ablation and thinning of the film, or changes on a chemical level. After annealing, the laser treated areas became darker (see Figure 85c), a possible effect of increased structuring, which could also be observed on a microscopic level (see Figure 85d).

The XPS survey spectra of the annealed laser treated CoAl_2O_4 film without sputtering (see Figure 86a) revealed some adventitious carbon, with small cobalt and aluminum signals next to the titanium signal from the substrate. Treated samples often exhibited increased substrate signals, as seen before (see Figure 68). Through sputtering, the substrate impurities in the form of nitrogen and calcium increased. In addition to the argon signal, the stronger Co 2p allowed for high resolution measurement (see Figure 87).

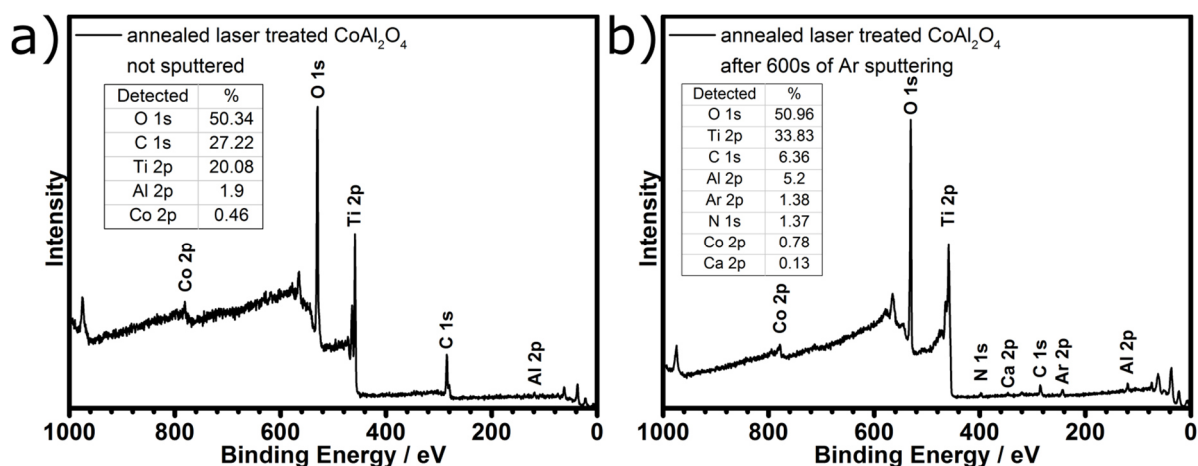


Figure 86: XPS survey spectra of annealed laser treated CoAl_2O_4 on Ti before (a) and after 600 s of Ar sputtering (b).

The high resolution analysis of the Co 2p signal after sputtering (see Figure 87) revealed two distinct cobalt species. The expected Co^{2+} species, which resulted from annealing film at high temperatures and a reduced Co^0 species, fit according to the literature values.^[250] This reduction must have been through the laser treatment, as argon sputtering did not affect the oxidation state in previous analysis (see section 3.4.3.2 Figure 75). This proved that laser pulse absorption could result in a reduced metal embedded in the Al_2O_3 lattice, coexisting with the CoAl_2O_4 film, without a significant physical impact.

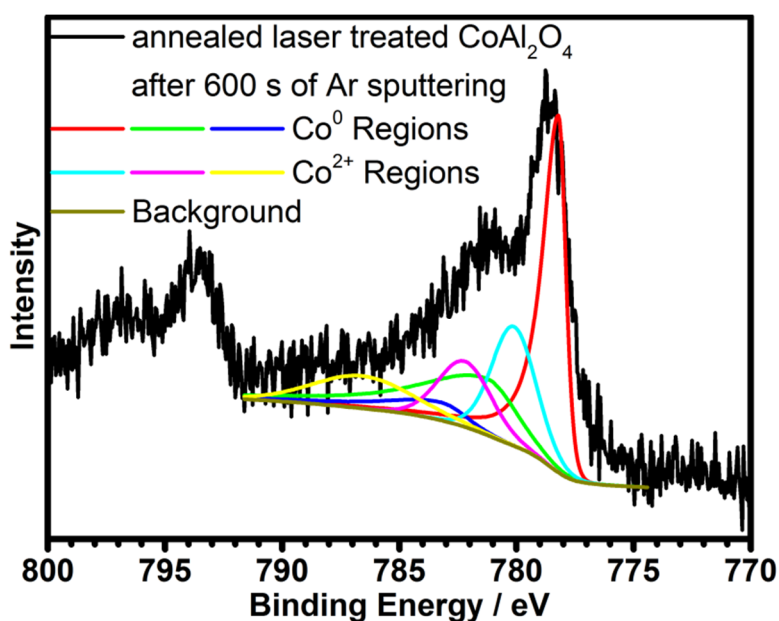


Figure 87: High resolution Co 2p XPS spectra of annealed laser treated CoAl_2O_4 on Ti after 600 s of Ar sputtering.

While femtosecond laser induced reduction was used in previous reports,^[270] the mechanism is still not fully understood. Nonlinear absorption^[271] and the environment^[272] seem to be important factors influencing the process. In water, solvated electrons (e^-) are generated, who act as reducing agents, with proposed reactions as followed:^[273]



For laser treatment in ambient conditions, the electron necessary for the reduction could be a result from the air at the treated area turning into a plasma.^[274, 275] For example, argon plasma can result in reduction of metal ions.^[276] This effect also supports the increased photocatalytic performance for laser treated $NiAl_2O_4$ thin films (see section 3.4.4.2 Figure 84f), where no high resolution spectra could be measured.

The photocatalytic performance of both amorphous and annealed untreated $CoAl_2O_4$ showed no photoactivity (see Figure 88a and c). This was expected, as both amorphous and crystalline $CoAl_2O_4$ were not commonly used in literature. The $NiAl_2O_4$ thin films also exhibited no intrinsic activity (see Figure 81a and d). yet after treatment, no matter if amorphous (see Figure 88b) or after annealing (see Figure 88d), there was no photocatalytic activity. Even after the reduction of Co^{2+} to Co^0 , as seen in XPS high resolution analysis (see Figure 87). Cobalt was commonly used as co-catalyst, like cobalt oxide/iron oxide composites^[260] or cobalt doped TiO_2 ^[277] and sometimes as pure nano cobalt oxide for hydrogen production, which is still inferior to the cheap iron oxide material.^[278] It has to be noted that only very few literature research articles showed any photocatalytic degradation of MB with $CoAl_2O_4$ nanostructures under UV irradiation^[279] and often omitted an absorption spectra of the UV region, the range used to excite the sample or provided no reference to the degradation analysis. Nevertheless, pure UV excitation of the bare and laser treated $CoAl_2O_4$ had not been investigated in this research, as the characteristic absorption peak of this material is at much higher wavelengths.^[280]

To summarize, precursors in the form of $M[Al(O^iPr)_4]_2$ ($M = Ni^{2+}, Co^{2+}$) were synthesized and investigated towards their thermal decomposition, elemental ratios and crystallinity after annealing. MAl_2O_4 ($M = Ni^{2+}, Co^{2+}$) thin films, produced using them in PE-CVD processes, were analyzed on a macro- and microscopic level in addition to their composition. Femtosecond laser treatment of these layers led to a reduction of the M^{2+} to M^0 and in case of $NiAl_2O_4$ resulted

in superior photocatalytic performance by degradation of methylene blue, while the CoAl_2O_4 showed no activity at all.

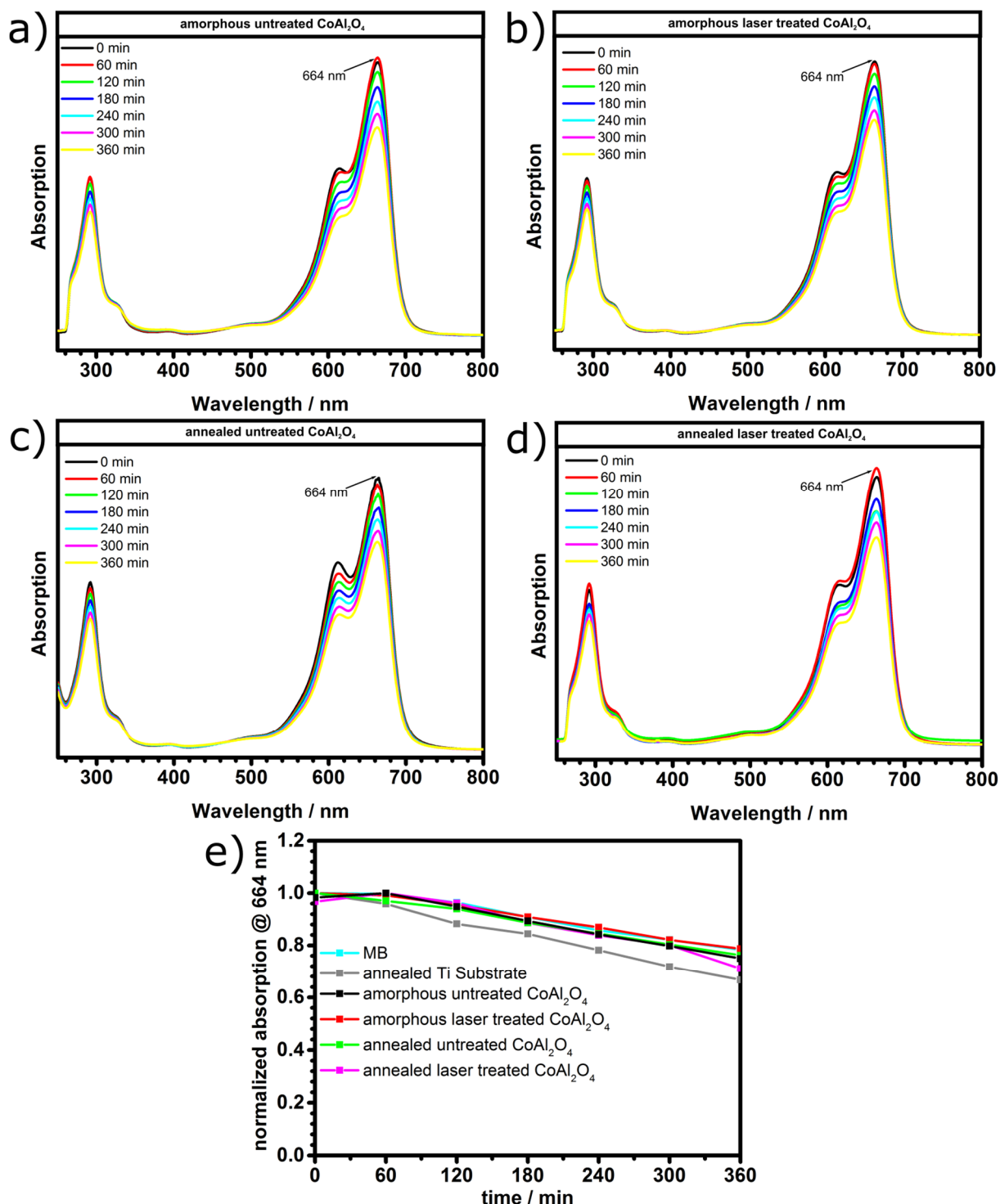


Figure 88: UV-VIS spectra of amorphous untreated CoAl_2O_4 on Ti during photocatalytic decomposition experiments (a), the amorphous laser treated CoAl_2O_4 on Ti (b), the annealed untreated CoAl_2O_4 on Ti (c), the annealed laser treated CoAl_2O_4 on Ti (d) and their normalized changes in absorption displayed over time (e).

4 Experimental Part

4.1 Substrates and Annealing

Substrates: Metal substrates used include unpolished aluminum or titanium plates (grade 4 quality by *Zapp Materials Engineering GmbH*, see Table 9) and quartz were used as transparent substrate. Additionally, silicon (001) was used for analytical purposes.

Table 9: Ti substrate impurities according to the vendor.^[281]

	Fe	C	N	O	H
Ti (grade 4)	0.5	0.08	0.05	0.4	0.015

Annealing: All samples were annealed in a tube furnace (**REST-E 230/3** by *Carbolite Gero*) at different temperatures and durations with a heat rate of 10°C per minute. The samples were positioned as close to the middle as possible, to minimize temperature deviation.

4.2 Deposition Methods

PE-CVD: All substrates were pretreated for 3 minutes with 20 sccm argon with an RF power of 50 W. Standardized plasma enhanced chemical vapor depositions used either Titanium-tetraisopropoxide ($[\text{Ti}(\text{O}^i\text{Pr})_4]$ by *Sigma Aldrich*), heated up to 80°C for a duration of 15 minutes, or Iron-pentacarbonyl ($[\text{Fe}(\text{CO})_5]$ by *Acros Organics*) for duration of 10 minutes at room temperature. Both used precursors were filled in glass flasks, and 20 sccm Oxygen with a RF power of 100 W in the plasma vacuum chamber (Type **DOMINO** by *Plasma Electronic GmbH*, see Figure 89). These precursors were used in excess to make sure there would a deposition through the whole process duration. After reaching the pressure of 1 Pa in the chamber, oxygen gas is added, resulting in roughly 2 Pa total pressure plasma ignition and opening of the precursor valve. The pressure during the deposition was kept around 2.6 Pa in case of TiO_x and 2.4 Pa in case of Fe_xO_y thin films.

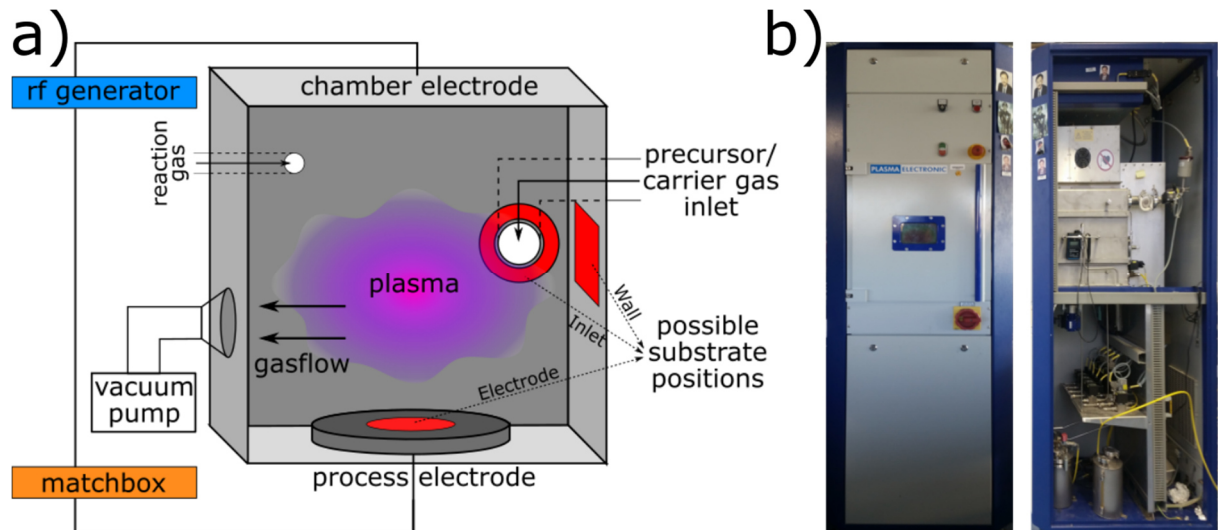


Figure 89: Scheme of the PE-CVD chamber used for the experiments (a), with possible substrate positions marked in red, and picture of the front/right side of the machine used (b).

The MAI_2O_4 was filled in a special precursor container, shaped like a T and made out of metal, to allow high precursor temperatures and the use of carrier gas. During the deposition, a precursor temperature between 100°C and 180°C was used, while the deposition time was kept between 180 and 300 minutes. 20 sccm Oxygen and an RF power of 100 W was exclusively used, while argon carrier gas varied from 2 to 4 Pa. The optimized standard process became as follows: Roughly 500 - 700 mg of precursor was used, and the deposition started at a pressure of 2 Pa (including the 20 sccm oxygen) with a precursor temperature of 100°C for a duration of 20 minutes. The total pressure including carrier gas was kept at 6 Pa. The precursor was then slowly heated over the course of 80 minutes to a temperature of 120°C , and kept at this temperature for an additional 80 minutes. As last step, the temperature was raised over 20 minutes to 140°C , and kept for 40 minutes. The total deposition time was around 240 minutes.

4.3 Laser Treatment Experiments

The setup of the laser system is schematically shown in section 3.1 Figure 26. In order to perform experiments with a broader parameter range, two different femtosecond lasers were investigated. **Tangerine** by *Amplitude Systems* uses a pulse duration $\tau_p \approx 280$ fs, a repetition rate of $f = 2000$ kHz, focusing optic of $f_{\text{optic}} \approx 63$ mm and incident beam diameter of $d_{\text{beam}} = 2.6$ mm with a resulting spot of $d_{\text{spot}} = 33$ μm , and central wavelength $\lambda = 1030$ nm, while **Spitfire Ace** by *Spectra Physics* uses a pulse duration of $\tau_p \approx 100$ fs with a line width of $\Delta\lambda = 60$ nm, a repetition rate of $f = 5$ kHz, focusing optic of $f_{\text{optic}} \approx 100$ mm and incident beam diameter of $d_{\text{beam}} = 10$ mm with a resulting spot of $d_{\text{spot}} = 10$ μm , and central wavelength

$\lambda = 800$ nm. During the process, the linear-polarized laser beam first passes through a half-wavelength plate ($\lambda/2$ -wave plate) and a polarizing beam splitter, where the intensity is adjusted. Afterwards, the beam is guided to the galvanometer scanner (**ScanCube 7/10** by *ScanLAB*), which is used to raster the laser spot and focus it on the sample surface, and the spot size was chosen to be $d \gtrsim 10$ μm , unless otherwise specified. Processes were performed in air at room temperature. The total processed area ranges from 5×5 mm^2 to 10×10 mm^2 in a line-by-line scan, and the distance between laser spots in each line was $\Delta x = 0.2$ μm . By using short pulse length and low repetition rate only minor thermal effects were observed. In all processes of the laser treated metal substrates (see section 3.3), a continuous pulse energy gradient was applied over the processed field. The parameters not specified here will be displayed in the corresponding section of the results and discussion chapter. The laser treatment of TiO_x and Fe_xO_y on Al, Ti or quartz substrates or quartz (see section 3 and 3.2) used a high-overlapping rate, with a scanning speed of $v = 280$ $\mu\text{m}/\text{s}$, which means that each line was exposed to approximately $N = df/v \approx 70000$ pulses, with a time interval of $\delta t_l = f^{-1} = 0.5$ μs between them. The area was treated with 1000 lines per millimeter, with a line length of $L = 1$ cm. This means after $\delta t_l = L/v \approx 36$ s a line was written with approximately 70000 pulses. In total, each site is exposed to approximately ten such laser-heating cycles. A gradient in pulse energy was used, increasing from $E_{\min} = 60$ nJ to $E_{\max} = 200$ nJ per pulse, which corresponds to the average laser power from $P_{\min} = 120$ mW to $P_{\max} = 400$ mW.

For the decomposition of the MAl_2O_4 thin films (see section 3.4.4), the samples were structured with a 3×3 field of varying intensity, ranging from ~ 0.5 to ~ 9 mW average power. In this case, annealed samples were treated with nine intensities, 0.5, 0.75, 1, 1.5, 2, 3, 5, 7 and 9 mW, while amorphous samples were treated with 0.5, 1, 2, 4, 5, 6, 7, 8 and 9 mW, due to the thicker layer of amorphous films.

4.4 Characterization Methods

SEM/EDX: The scanning electron microscope (**Nova Nano SEM 430** by *FEI*) used to analyze the morphology was also equipped with an energy dispersive x-ray spectrometer (**Apollo X** by *FEI*), which allows to determine the elemental composition of thin films. EDX analysis were performed without a proper calibration.

TGA/DTA: The thermogravimeter (**STARE-system** by *Mettler-Toledo*) was used to analyze the decomposition and phase transformation with a **TGA/DTA1** unit and a **GC100** gas controller to provide the nitrogen atmosphere. Al₂O₃ was used as inert container for these processes.

XRD: X-ray diffraction (**STOE STADI MP** by *STOE*) analysis was performed using Mo-K α radiation ($\lambda = 0.71 \text{ \AA}$) and a linear PSD detector in reflection geometry to determine the crystallinity and phase. The data evaluation program was **WinXPOW** by *STOE*.

FIB/STEM: Focused ion beam treatment and scanning transmission electron microscopy (**Helios NanoLab 600** by *FEI*) were performed to analyze the cross sections of thin films.

AFM: Topography measurements were done by atomic force microscopy (**XE-100** by *Park Systems*) using non-contact mode with a cantilever (**PPP-NCHR** by *Nanosensors*), where region measurements were used to determine the roughness, while line scans were used to analyze the depth of the ripples.

EBSD: Electron backscattering diffraction analysis were performed in a scanning electron microscope (**LEO 1560VP SEM** by *Zeiss*) with a special detector (**DigiView 4 EBSD detector** by *Zeiss*).

CA: Contact angle measurements were performed (**DSA100** by *Krüss*) to observe the changes hydrophobicity of the surfaces with 2 μl drops and calculation the average over a minimum of five measurements per area.

UV-VIS: Absorption measurements were performed in direct and in diffusive reflection (**UV-3600 Plus** by *Shimadzu*) for reflecting surfaces in case of metal substrates, while materials on transparent substrates like FTO or quartz were measured in transmission (**Lambda 950** by *Perkin Elmer*).

XPS: Elemental composition measurements of surfaces were done by x-ray photoelectron spectroscopy (**ESCA M-Probe** by *Surface Science Instruments*), irradiated with Al-K α rays ($\lambda = 8.33 \text{ \AA}$). Survey scans were recorded with a detector pass energy of 158.9 eV, while high-

resolution spectra used a pass energy of 22.9 eV. All spectra were referenced to adventitious carbon at 284.8 eV. The analysis was performed using **CasaXPS** by *Casa Software Ltd.*

Gas-Sensing: Chemo-resistive gas sensing experiments were performed with a customized system which consists of four electronic mass-flow controllers by *Aero*, a sensor chamber and a heatable contact stage. Two source meters (**K2400/K2401** by *Keithley*) were used for heat control and resistance measurement, while a self-developed software (using **LabVIEW** by *National Instruments*) controlled the electrical measurement and gas flow concentrations. The total flow during all measurements was kept at 1000 sccm, while synthetic air was used as main compound. The samples were investigated towards reductive gas (H_2) at room temperature, with flow rates ranging from 25 to 200 sccm. The sample consisted of sputtered stripes of Al covered by a PE-CVD TiO_x standard process (see section 4.2) and final laser treatment. Four fs pulses with each ~ 1.5 mW per spot perpendicular in the middle of the aluminum stripe were used. The goal was to cut the strip into two separated parts, and forcing the current during the gas measurement through the top metal oxide layer (see Figure 49a). The disconnection was measured by multi meter.

PEC: The photoelectrochemical water splitting experiments were done in a three electrode setup, with 1M NaOH (pH = 13.6) as electrolyte, platinum wire as counter electrode, a saturated calomel electrode (SCE) and the samples as working electrodes with an active area of ~ 0.64 cm². For illumination, a 150 W xenon lamp (by *Oriel*) with a Schott KG-3 filter was used, which was calibrated to approximately 1 Sun (AM 1.5 global, see Figure 90). The exception is the optimization in section 3.3.2, where the lamp had a fixed focus, but was not calibrated. The performance was measured using linear sweep voltammetry with a scan rate of 10 mV/s in a potential range of -1 to 1 V vs. SCE using a potentiostat (**VersaStat 4** by *Ametek*), comparing light and dark measurements. The potential was then recalculated to the reversible hydrogen electrode (RHE) for better comparison with literature values.

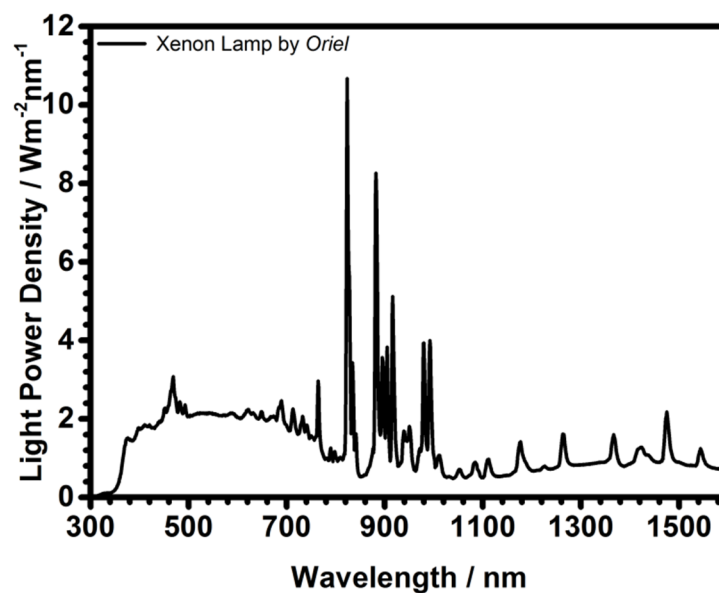


Figure 90: Light power density of the xenon lamp used for PEC water splitting and photocatalytic degradation experiments.

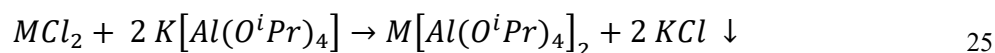
Photocatalysis: The photocatalytic activity of the bimetallic materials was investigated using 0.25 ml of a 1% w/v (10 g/l) solution of methylene blue (MB by *ABCR*) and diluting it with 249.75 ml DI water to produce a stock solution of 0.001% w/v (10 mg/l), which was covered with Al foil to prevent degradation. The measurement setup consisted of small beakers with magnetic stirring bars filled with 20 ml of the MB stock solution. The substrates were fixed inside the beaker, fully submerged in the solution, while illuminated by a 150 W xenon lamp (by *Oriel*) with a Schott KG-3 filter and calibrated to approximately 1 Sun (AM 1.5 global, see Figure 90). Every 60 minutes a UV-VIS spectra was measured and the peak of methylene blue at 664 nm was used to measure the degradation over time. Every degradation experiment was performed in a closed off black box.

Software: For the plotting of data points **OriginPro 9** by *OriginLab Corporation* was used, while **Inkscape 0.92** by *Free Software Foundation* was used for schemes and illustrations. The coloring of images was done with **GIMP 2.10.6** by the *GIMP development team*. If any additional software (other than those provided by the companies of the analytical machines) was used, it is mentioned in the respective sections.

4.5 Precursor Synthesis

Preparation of $M[Al(O^iPr)_4]_2$

The precursors were synthesized according to the literature known procedure (equation 25, with $M = Co^{2+}$ or Ni^{2+}).^[252] In the first step, the potassium aluminum isopropoxide (0.015 mol, 1.5 mg) was synthesized by dissolving potassium (0.015 mol, 0.6 g) in dry isopropanol (30 ml), adding aluminum isopropoxide (0.015 mol, 3.1 g) and stirring until fully dissolved.



Cobalt(II)-chloride (0.008 mol, 1 g) or nickel(II)-chloride (0.008 mol, 1 g) was added and the resulting mixture was stirred at elevated temperatures of around 70°C overnight. The viscous intermediate was distilled under vacuum beginning at 120°C and completing at 140°C. The product was obtained as a dark violet liquid ($M = Co^{2+}$: 0.007 mol, 3.97 g, 585.36 g/mol; $M = Ni^{2+}$: 0.007 mol, 4.03 g, 585.6 g/mol).

EI-MS: (70 eV, 42°C, $M = Ni^{2+}$): $m/z = 569 [M-CH_3]^+$ (94%), $466 [M-CH_3;-C_3H_7;-OC_3H_7]^+$ (28%), $423 [M-CH_3;-Al(OC_3H_7)_2]^+$ (32%), $409 [M-(CH_3)_2;-Al(OC_3H_7)_2]^+$ (44%)

XRD: After heat treatment of ~1000°C for ~10h, phase pure MAI_2O_4 compounds can be observed (see Figure 70).

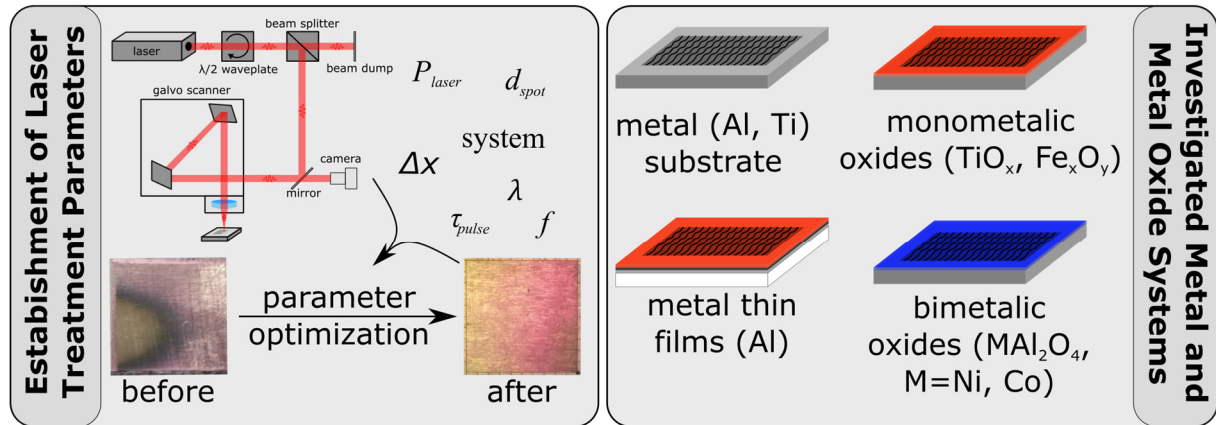
5 Summary and Outlook

The journey from the concept of combining expertise in laser physics with chemical and material knowledge to create ordered/disordered systems ultimately led to optimized, ultrafast laser treatment processes. They were able to improve a plethora of different systems and materials for many applications (see Figure 91). Disordering can be understood as the breaking of periodic potential and was for example achieved through decomposing bimetallic oxide films, creating metal/metal oxide areas. On the other hand, ordering could be induced by laser crystallizing amorphous metal oxides. These modifications can be traced back to changes on a chemical and/or physical level, which was directly related to the laser treatment (see section 3.2). Phenomena including increased surface roughness and hydrophobicity through periodic structures, which increased with processing power, or enhanced light absorption through electronic changes and in-plane light trapping were observed. To enable this, femtosecond laser pulses were mandatory, featuring to minimal photothermal effects, reducing damage to the materials and allowing treated samples to be integrated as devices.

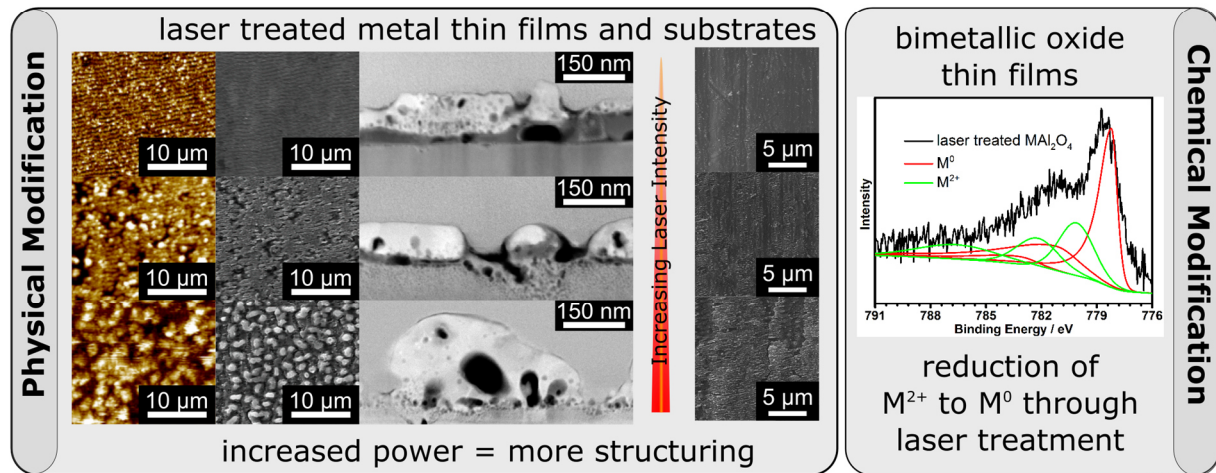
Structuring of metal oxide systems like $\text{Fe}_x\text{O}_y/\text{Al}/\text{TiO}_x$ on quartz led to precise amorphous/crystalline junctions. In addition to this, tailored surface morphology, with high laser power causing Fe_xO_y particle formation on structured TiO_x bottom layer, could be obtained. By decreasing the intensity, reduced ripples and craters on the Fe_xO_y top film were achieved. The overall absorption was increased through these physical changes, improving in-plane light trapping through the laser induced periodic surface structures (LIPSS). These laser processes were additionally used to fabricate room temperature titanium oxide gas sensors on a quartz substrate. The optical improvements were used to enhance metal substrates through periodical patterns as base for photoelectrochemical cells (see section 3.3). The superior performance was independent of the investigated systems, which included the bare Ti substrates, and with added TiO_2 or Fe_2O_3 absorber layers. This also led to higher absorption, photon conversion and ultimately photoelectrochemical performance, nearly doubling in some cases. Since a heat treatment step was necessary to form crystalline materials to perform as PEC electrode, the parameters like the temperature and time were carefully chosen. High values would lead to rutile formation from substrate oxidation, acting as blocking layer, while low values would result in a lack of crystallinity. The laser structuring of metal substrates could be used in many systems, as it was top layer independent, boosting light harvesting performances for applications like water splitting, photocatalytic degradation or in solar cells, which could be further continued by treatment of TCOs. Another application would be alternating crystalline

and amorphous areas, which can be achieved by striped laser patterns. The amorphous domains increase the absorption cross-section due to more dangling bonds and improved electron diffusion processes, while the crystalline stripes enhance the charge transport properties through additional mid-gap states shown in latest simulations.^[115]

Research Approach



Laser Induced Modifications



Unique and Enhanced Properties

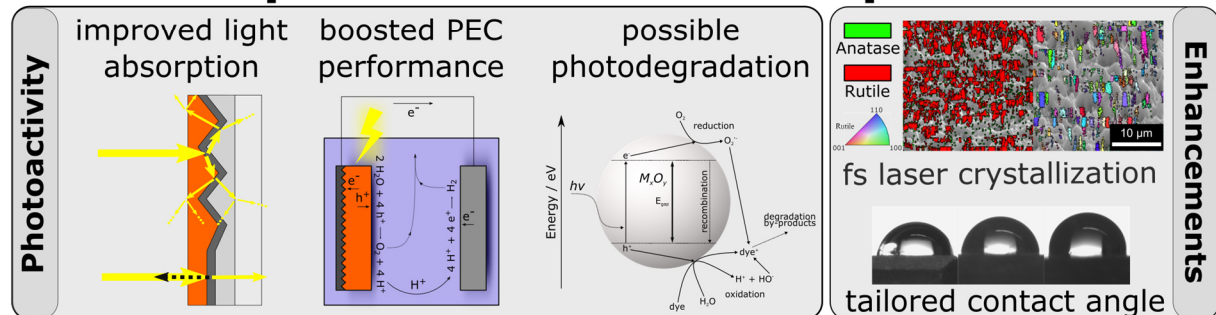


Figure 91: Overview and summary of the process development, systems investigated, the analysis and resulting properties with potential applications through femtosecond laser treatment presented in this work.

The chemical modifications possible through the laser treatment were shown on MAl_2O_4 ($M = Ni^{2+}, Co^{2+}$) thin films (see section 3.4). These were produced by PE-CVD with a synthesized bimetallic precursor ($M[Al(O^iPr)_4]_2$). Laser induced reduction of the films has been investigated by XPS, for both amorphous and crystalline phases. SEM studies revealed that the physical effect of the treatment remained very low. The photocatalytic degradation of methylene blue was investigated, showing that only the treated and thus laser reduced $NiAl_2O_4$ films exhibited any activity, a result from Ni^0 clusters embedded in the Al_2O_3 lattice. While this product was known for its catalytic properties, it was never produced through precise methods like femtosecond laser treatment. While the treated $CoAl_2O_4$ variant showed expectedly no activity, they could potentially be used as a new way to produce Co doped Al_2O_3 , with possible application as Fischer-Tropsch catalyst. The chemical disordering of metal oxides was universal and material independent, opening up hundreds of M doped M'_xO_y materials through this method, resulting in evenly and precise distributed dopants, while the thin films can be easily produced by evaporation of bimetallic alkoxide precursors using thin film deposition processes.

To summarize, the combination of laser processing and different metal and metal oxide systems resulted in a lot of unique and improved properties, which led to performance boosts in many areas with several different applications.

With the knowledge gained in this research, development of optimized and reproducible laser processes, with respect to the desired effects on a physical and chemical level, are achievable for systems and materials not presented here. The industrial viability is very high, as all steps, from precursor synthesis and deposition processes, to the laser treatment, can be easily scaled up, with many different properties tunable on large areas with high reproducibility.

6 References

- [1] R. Baños, F. Manzano-Agugliaro, F. G. Montoya, C. Gil, A. Alcayde, J. Gómez, *Renewable and Sustainable Energy Reviews* **2011**, *15*, 1753-1766.
- [2] H. Zhang, D. Chen, B. Xu, E. Patelli, S. Tolo, *Mechanical Systems and Signal Processing* **2018**, *100*, 524-533.
- [3] M. I. H. Ansari, A. Qurashi, M. K. Nazeeruddin, *Journal of Photochemistry and Photobiology C: Photochemistry Reviews* **2018**, *35*, 1-24.
- [4] D. Ravelli, D. Dondi, M. Fagnoni, A. Albini, *Chemical Society Reviews* **2009**, *38*, 1999-2011.
- [5] G. Crabtree, M. S. Dresselhaus, M. V. Buchanan, *Physics Today* **2004**, *57*, 39-44.
- [6] K. Mazloomi, C. Gomes, *Renewable and Sustainable Energy Reviews* **2012**, *16*, 3024-3033.
- [7] A. Pérez-Tomás, A. Mingorance, D. Tanenbaum, M. Lira-Cantú, in *The Future of Semiconductor Oxides in Next-Generation Solar Cells*, Elsevier, **2018**, pp. 267-356.
- [8] N. K. Awad, E. A. Ashour, N. K. Allam, *Journal of Renewable and Sustainable Energy* **2014**, *6*, 022702.
- [9] H. Palneedi, J. H. Park, D. Maurya, M. Peddigari, G. T. Hwang, V. Annapureddy, J. W. Kim, J. J. Choi, B. D. Hahn, S. Priya, K. J. Lee, J. Ryu, *Advanced Materials* **2018**, *30*, e1705148.
- [10] F. Fraggelakis, G. Mincuzzi, I. Manek-Hönninger, J. Lopez, R. Kling, *RSC Advances* **2018**, *8*, 16082-16087.
- [11] J. Brillet, M. Cornuz, F. L. Formal, J.-H. Yum, M. Grätzel, K. Sivula, *Journal of Materials Research* **2011**, *25*, 17-24.
- [12] S. Linic, P. Christopher, D. B. Ingram, *Nature Materials* **2011**, *10*, 911.
- [13] O. Guillon, *Advanced Ceramics for Energy Conversion and Storage*, Elsevier, Amsterdam, **2019**.
- [14] X. Li, J. Yu, M. Jaroniec, *Chemical Society Reviews* **2016**, *45*, 2603-2636.
- [15] J. Y. Kim, G. Magesh, D. H. Youn, J.-W. Jang, J. Kubota, K. Domen, J. S. Lee, *Scientific Reports* **2013**, *3*, 2681.
- [16] P. Dias, T. Lopes, L. Andrade, A. Mendes, *Journal of Power Sources* **2014**, *272*, 567-580.
- [17] C. Zhang, Q. Wu, X. Ke, J. Wang, X. Jin, S. Xue, *International Journal of Hydrogen Energy* **2014**, *39*, 14604-14612.
- [18] J.-C. Chou, M.-H. Yang, J.-W. Liao, C.-Y. Lee, J.-Y. Gan, *Materials Chemistry and Physics* **2014**, *143*, 1417-1422.
- [19] S. Xie, M. Li, W. Wei, T. Zhai, P. Fang, R. Qiu, X. Lu, Y. Tong, *Nano Energy* **2014**, *10*, 313-321.
- [20] C. Cheng, W. Ren, H. Zhang, *Nano Energy* **2014**, *5*, 132-138.
- [21] A. Jelinska, K. Bienkowski, M. Jadwiszczak, M. Pisarek, M. Strawski, D. Kurzydowski, R. Solarska, J. Augustynski, *ACS Catalysis* **2018**, *8*, 10573-10580.
- [22] Y. Liu, J. Li, W. Li, Y. Yang, Y. Li, Q. Chen, *The Journal of Physical Chemistry C* **2015**, *119*, 14834-14842.
- [23] Y. Pihosh, I. Turkevych, K. Mawatari, T. Asai, T. Hisatomi, J. Uemura, M. Tosa, K. Shimamura, J. Kubota, K. Domen, T. Kitamori, *Small* **2014**, *10*, 3692-3699.
- [24] B.-S. Wang, R.-Y. Li, Z.-Y. Zhang, W. Xing, X.-L. Wu, G.-A. Cheng, R.-T. Zheng, *Catalysis Today* **2019**, *321-322*, 100-106.
- [25] C. Wang, Y. Feng, L. Cai, X. Yang, J. He, W. Yan, Q. Liu, Z. Sun, F. Hu, Z. Xie, T. Yao, S. Wei, *Journal of Power Sources* **2014**, *269*, 24-30.
- [26] M. Meng, X. Wu, X. Zhu, X. Zhu, P. K. Chu, *ACS Applied Materials & Interfaces* **2014**, *6*, 4081-4088.

- [27] H. Li, C. Chen, X. Huang, Y. Leng, M. Hou, X. Xiao, J. Bao, J. You, W. Zhang, Y. Wang, J. Song, Y. Wang, Q. Liu, G. A. Hope, *Journal of Power Sources* **2014**, *247*, 915-919.
- [28] ASTM G173-03(2012), Standard Tables for Reference Solar Spectral Irradiances: Direct Normal and Hemispherical on 37° Tilted Surface, ASTM International, West Conshohocken, PA, 2012, www.astm.org, **30.09.2019**
- [29] K. Sivula, F. Le Formal, M. Gratzel, *ChemSusChem* **2011**, *4*, 432-449.
- [30] Y. W. Phuan, M. N. Chong, T. Zhu, S.-T. Yong, E. S. Chan, *Materials Research Bulletin* **2015**, *69*, 71-77.
- [31] K. Sivula, F. Le Formal, M. Grätzel, *ChemSusChem* **2011**, *4*, 432-449.
- [32] A. B. Murphy, P. R. F. Barnes, L. K. Randeniya, I. C. Plumb, I. E. Grey, M. D. Horne, J. A. Glasscock, *International Journal of Hydrogen Energy* **2006**, *31*, 1999-2017.
- [33] Z. Chen, T. F. Jaramillo, T. G. Deutsch, A. Kleiman-Shwarsstein, A. J. Forman, N. Gaillard, R. Garland, K. Takane, C. Heske, M. Sunkara, E. W. McFarland, K. Domen, E. L. Miller, J. A. Turner, H. N. Dinh, *Journal of Materials Research* **2011**, *25*, 3-16.
- [34] L. Li, P. Liang, C. Liu, H. Zhang, N. Mitsuzaki, Z. Chen, *International Journal of Hydrogen Energy* **2019**, *44*, 4208-4217.
- [35] J. Deng, J. Zhong, A. Pu, D. Zhang, M. Li, X. Sun, S.-T. Lee, *Journal of Applied Physics* **2012**, *112*, 084312.
- [36] Y. Ling, G. Wang, D. A. Wheeler, J. Z. Zhang, Y. Li, *Nano Letters* **2011**, *11*, 2119-2125.
- [37] A. Kaouk, T.-P. Ruoko, M. Pyeon, Y. Gönüllü, K. Kaunisto, H. Lemmetyinen, S. Mathur, *The Journal of Physical Chemistry C* **2016**, *120*, 28345-28353.
- [38] H. K. Dunn, J. M. Feckl, A. Müller, D. Fattakhova-Rohlfing, S. G. Morehead, J. Roos, L. M. Peter, C. Scheu, T. Bein, *Physical Chemistry Chemical Physics* **2014**, *16*, 24610-24620.
- [39] S. Park, H. J. Kim, C. W. Lee, H. J. Song, S. S. Shin, S. W. Seo, H. K. Park, S. Lee, D.-W. Kim, K. S. Hong, *International Journal of Hydrogen Energy* **2014**, *39*, 16459-16467.
- [40] J. Wang, B. Feng, J. Su, L. Guo, *ACS Applied Materials & Interfaces* **2016**, *8*, 23143-23150.
- [41] M. Pyeon, M. Wang, Y. Gönüllü, A. Kaouk, S. Jäckle, S. Christiansen, T. Hwang, K. Moon, S. Mathur, *MRS Communications* **2016**, *6*, 442-448.
- [42] M. Pyeon, V. Rauch, D. Stadler, M. Gürsoy, M. Deo, Y. Gönüllü, T. Fischer, T. Hwang, S. Mathur, *Advanced Engineering Materials* **2019**, *21*, 1900195.
- [43] M. Wang, M. Pyeon, Y. Gönüllü, A. Kaouk, S. Shen, L. Guo, S. Mathur, *Nanoscale* **2015**, *7*, 10094-10100.
- [44] S. Chen, J. Li, J. Bai, L. Xia, Y. Zhang, L. Li, Q. Xu, B. Zhou, *Applied Catalysis B: Environmental* **2018**, *237*, 175-184.
- [45] F. R. W. G. Wyckoff, E. D. Crittenden, in *Zeitschrift für Kristallographie - Crystalline Materials, Vol. 63*, **1926**, p. 144.
- [46] H. S. C. O'Neill, W. A. Dollase, *Physics and Chemistry of Minerals* **1994**, *20*, 541-555.
- [47] E. N. Maslen, V. A. Streltsov, N. R. Streltsova, N. Ishizawa, *Acta Crystallographica Section B* **1994**, *50*, 435-441.
- [48] M. Ni, M. K. H. Leung, D. Y. C. Leung, K. Sumathy, *Renewable and Sustainable Energy Reviews* **2007**, *11*, 401-425.
- [49] D. H. Hanaor, C. Sorrell, *Journal of Materials Science* **2011**, *46*, 855-874.
- [50] Y. Yamada, Y. Kanemitsu, *Applied Physics Letters* **2012**, *101*, 133907.
- [51] M. Fathy, H. Hamad, A. E. H. Kashyout, *RSC Advances* **2016**, *6*, 7310-7316.
- [52] M. Altomare, K. Lee, M. S. Killian, E. Selli, P. Schmuki, *Chemistry – A European Journal* **2013**, *19*, 5841-5844.

- [53] C. Wang, Z. Chen, H. Jin, C. Cao, J. Li, Z. Mi, *Journal of Materials Chemistry A* **2014**, 2, 17820-17827.
- [54] M. M. Islam, T. Bredow, *The Journal of Physical Chemistry C* **2015**, 119, 5534-5541.
- [55] M. M. Islam, T. Bredow, A. Gerson, *ChemPhysChem* **2011**, 12, 3467-3473.
- [56] S. Sato, *Chemical Physics Letters* **1986**, 123, 126-128.
- [57] Y. Su, S. Chen, X. Quan, H. Zhao, Y. Zhang, *Applied Surface Science* **2008**, 255, 2167-2172.
- [58] S. Piskunov, O. Lisovski, J. Begens, D. Bocharov, Y. F. Zhukovskii, M. Wessel, E. Spohr, *The Journal of Physical Chemistry C* **2015**, 119, 18686-18696.
- [59] A. Sasinska, D. Bialuschewski, M. M. Islam, T. Singh, M. Deo, S. Mathur, *The Journal of Physical Chemistry C* **2017**, 121, 15538-15548.
- [60] R. Asahi, T. Morikawa, T. Ohwaki, K. Aoki, Y. Taga, *Science* **2001**, 293, 269.
- [61] X. Chen, L. Liu, P. Y. Yu, S. S. Mao, *Science* **2011**, 331, 746.
- [62] X. Chen, L. Liu, Z. Liu, M. A. Marcus, W.-C. Wang, N. A. Oyler, M. E. Grass, B. Mao, P.-A. Glans, P. Y. Yu, J. Guo, S. S. Mao, *Scientific Reports* **2013**, 3, 1510.
- [63] D. J. Mowbray, J. I. Martinez, J. M. García Lastra, K. S. Thygesen, K. W. Jacobsen, *The Journal of Physical Chemistry C* **2009**, 113, 12301-12308.
- [64] S. Hoang, S. P. Berglund, N. T. Hahn, A. J. Bard, C. B. Mullins, *Journal of the American Chemical Society* **2012**, 134, 3659-3662.
- [65] Y. Shen, T. Xiong, T. Li, K. Yang, *Applied Catalysis B: Environmental* **2008**, 83, 177-185.
- [66] H. Choi, D. Shin, B. C. Yeo, T. Song, S. S. Han, N. Park, S. Kim, *ACS Catalysis* **2016**, 6, 2745-2753.
- [67] E. P. Meagher, G. A. Lager, *Canadian Mineralogist* **1979**, 17, 77-85.
- [68] M. Horn, F. Schwebdtfeger C, P. Meagher E, in *Zeitschrift für Kristallographie - Crystalline Materials, Vol. 136*, **1972**, p. 273.
- [69] W. H. Baur, A. A. Khan, *Acta Crystallographica Section B: Structural Science, Crystal Engineering and Materials* *SV* **27** **1972**, 2133-2139.
- [70] W. Li, P. Da, Y. Zhang, Y. Wang, X. Lin, X. Gong, G. Zheng, *ACS Nano* **2014**, 8, 11770-11777.
- [71] Q. Mi, A. Zhanaidarova, B. S. Brunschwig, H. B. Gray, N. S. Lewis, *Energy & Environmental Science* **2012**, 5, 5694.
- [72] Y. Pihosh, I. Turkevych, K. Mawatari, J. Uemura, Y. Kazoe, S. Kosar, K. Makita, T. Sugaya, T. Matsui, D. Fujita, M. Tosa, M. Kondo, T. Kitamori, *Scientific Reports* **2015**, 5, 11141.
- [73] B. Urasinska-Wojcik, T. A. Vincent, M. F. Chowdhury, J. W. Gardner, *Sensors and Actuators B: Chemical* **2017**, 239, 1051-1059.
- [74] R. B. Goldner, T. E. Haas, G. Seward, K. K. Wong, P. Norton, G. Foley, G. Berera, G. Wei, S. Schulz, R. Chapman, *Solid State Ionics* **1988**, 28-30, 1715-1721.
- [75] J. M. Berak, M. J. Sienko, *Journal of Solid State Chemistry* **1970**, 2, 109-133.
- [76] B. O. Loopstra, H. M. Rietveld, *Acta Crystallographica Section B* **1969**, 25, 1420-1421.
- [77] L. S. Palatnik, O. A. Obol'yaninova, M. N. Naboka, N. T. Gladkikh, *Inorganic Materials (USSR) (English Translation)* **1973**, 9, 718-720.
- [78] A. Wolcott, W. A. Smith, T. R. Kuykendall, Y. Zhao, J. Z. Zhang, *Advanced Functional Materials* **2009**, 19, 1849-1856.
- [79] X. Zhang, Y. Liu, Z. Kang, *ACS Applied Materials & Interfaces* **2014**, 6, 4480-4489.
- [80] V. Rogé, C. Guignard, G. Lamblin, F. Laporte, I. Fechete, F. Garin, A. Dinia, D. Lenoble, *Catalysis Today* **2018**, 306, 215-222.
- [81] L. Liao, H. B. Lu, M. Shuai, J. C. Li, Y. L. Liu, C. Liu, Z. X. Shen, T. Yu, *Nanotechnology* **2008**, 19, 175501.

- [82] X. Zhang, Y. Li, J. Zhao, S. Wang, Y. Li, H. Dai, X. Sun, *Journal of Power Sources* **2014**, *269*, 466-472.
- [83] Y. Li, X. Zhang, S. Jiang, H. Dai, X. Sun, Y. Li, *Solar Energy Materials and Solar Cells* **2015**, *132*, 40-46.
- [84] S. Arooj, T. Xu, X. Hou, Y. Wang, J. Tong, R. Chu, B. Liu, *RSC Advances* **2018**, *8*, 11828-11833.
- [85] J. Mu, B. Chen, M. Zhang, Z. Guo, P. Zhang, Z. Zhang, Y. Sun, C. Shao, Y. Liu, *ACS Applied Materials & Interfaces* **2012**, *4*, 424-430.
- [86] M. G. Mali, H. Yoon, H. Kim, B. Joshi, S. S. Al-Deyab, S. S. Yoon, *ChemPhysChem* **2015**, *16*, 3450-3457.
- [87] Y. Sun, C. J. Murphy, K. R. Reyes-Gil, E. A. Reyes-Garcia, J. P. Lilly, D. Raftery, *International Journal of Hydrogen Energy* **2008**, *33*, 5967-5974.
- [88] D. V. Shinde, D. Y. Ahn, V. V. Jadhav, D. Y. Lee, N. K. Shrestha, J. K. Lee, H. Y. Lee, R. S. Mane, S.-H. Han, *Journal of Materials Chemistry A* **2014**, *2*, 5490-5498.
- [89] C. Chen, J. Moir, N. Soheilnia, B. Mahler, L. Hoch, K. Liao, V. Hoepfner, P. O'Brien, C. Qian, L. He, G. A. Ozin, *Nanoscale* **2015**, *7*, 3683-3693.
- [90] K. R. Reyes-Gil, Y. Sun, E. Reyes-García, D. Raftery, *The Journal of Physical Chemistry C* **2009**, *113*, 12558-12570.
- [91] Y. Li, J. Xu, J. Chao, D. Chen, S. Ouyang, J. Ye, G. Shen, *Journal of Materials Chemistry* **2011**, *21*, 12852.
- [92] S. B. Qadri, H. Kim, *Journal of Applied Physics* **2002**, *92*, 227-229.
- [93] M. Marezio, *Acta Crystallographica* **1966**, *20*, 723-728.
- [94] J. M. Quero, F. Perdignes, C. Aracil, in *Smart Sensors and Mems*, Woodhead Publishing, **2014**, pp. 281-304.
- [95] S. Mathur, in *Chemical Physics of Thin Film Deposition Processes for Micro- and Nano-Technologies*, Springer Netherlands, Dordrecht, **2002**, pp. 91-118.
- [96] C. C. Piras, S. Fernández-Prieto, W. M. De Borggraeve, *Nanoscale Advances* **2019**, *1*, 937-947.
- [97] A. Kay, I. Cesar, M. Grätzel, *Journal of the American Chemical Society* **2006**, *128*, 15714-15721.
- [98] L. Fu, H. Yu, C. Zhang, Z. Shao, B. Yi, *Electrochimica Acta* **2014**, *136*, 363-369.
- [99] R. Rajendran, Z. Yaakob, M. Pudukudy, M. S. A. Rahaman, K. Sopian, *Journal of Alloys and Compounds* **2014**, *608*, 207-212.
- [100] Z. Fu, T. Jiang, Z. Liu, D. Wang, L. Wang, T. Xie, *Electrochimica Acta* **2014**, *129*, 358-363.
- [101] X. Guo, L. Wang, Y. Tan, *Nano Energy* **2015**, *16*, 320-328.
- [102] S. Kment, Z. Hubicka, J. Krysa, J. Olejnicek, M. Cada, I. Gregora, M. Zlamal, M. Brunclikova, Z. Remes, N. Liu, L. Wang, R. Kirchgeorg, C. Y. Lee, P. Schmuki, *Catalysis Today* **2014**, *230*, 8-14.
- [103] S. K. Mohapatra, S. E. John, S. Banerjee, M. Misra, *Chemistry of Materials* **2009**, *21*, 3048-3055.
- [104] J.-T. Wang, in *Modern Inorganic Synthetic Chemistry*, Elsevier, Amsterdam, **2011**, pp. 151-171.
- [105] F. Maury, *J. Phys. IV France* **1995**, *05*, C5-449-463.
- [106] K. L. Choy, *Progress in Materials Science* **2003**, *48*, 57-170.
- [107] D. Depla, S. Mahieu, J. E. Greene, in *Handbook of Deposition Technologies for Films and Coatings (Third Edition)*, William Andrew Publishing, Boston, **2010**, pp. 253-296.
- [108] Y. Hatakeyama, K. Onishi, K. Nishikawa, *RSC Advances* **2011**, *1*, 1815-1821.
- [109] C. W. Pinion, J. D. Christesen, J. F. Cahoon, *Journal of Materials Chemistry C* **2016**, *4*, 3890-3897.

- [110] A. Mettenbörger, V. Merod, A. P. Singh, H. Lemmetyinen, S. Mathur, *Plasma-Assisted Chemical Vapor Deposition of Fe: TiO₂ Films for Photoelectrochemical Hydrogen Production*, *Nanostructured Materials and Nanotechnology V*, **2012**.
- [111] S. R. Droes, T. T. Kodas, M. J. Hampden-Smith, in *Carbide, Nitride and Boride Materials Synthesis and Processing*, Springer Netherlands, Dordrecht, **1997**, pp. 579-603.
- [112] S. Bell Martin, B. K. Teo Kenneth, G. Lacerda Rodrigo, W. I. Milne, B. Hash David, M. Meyyappan, in *Pure and Applied Chemistry, Vol. 78*, **2006**, p. 1117.
- [113] K. J. Kanarik, T. Lill, E. A. Hudson, S. Sriraman, S. Tan, J. Marks, V. Vahedi, R. A. Gottscho, *Journal of Vacuum Science & Technology A* **2015**, *33*, 020802.
- [114] C. Fang, Y. Cao, D. Wu, A. Li, *Progress in Natural Science: Materials International* **2018**, *28*, 667-675.
- [115] H. Han, H. Choi, S. Mhin, Y.-R. Hong, K. M. Kim, J. Kwon, G. Ali, K. Y. Chung, M. Je, H. N. Umh, D.-H. Lim, K. Davey, S.-Z. Qiao, U. Paik, T. Song, *Energy & Environmental Science* **2019**, 2443-2454.
- [116] M. Ibadurrohman, K. Hellgardt, *ACS Applied Materials & Interfaces* **2015**, *7*, 9088-9097.
- [117] P. Dias, A. Vilanova, T. Lopes, L. Andrade, A. Mendes, *Nano Energy* **2016**, *23*, 70-79.
- [118] W. Li, J. Li, X. Wang, J. Ma, Q. Chen, *International Journal of Hydrogen Energy* **2010**, *35*, 13137-13145.
- [119] S. Wu, H. Huang, M. Shang, C. Du, Y. Wu, W. Song, *Biosensors and Bioelectronics* **2017**, *92*, 646-653.
- [120] M. Li, X. Tu, Y. Su, J. Lu, J. Hu, B. Cai, Z. Zhou, Z. Yang, Y. Zhang, *Nanoscale* **2018**, *10*, 1153-1161.
- [121] M. Zhou, X. W. Lou, Y. Xie, *Nano Today* **2013**, *8*, 598-618.
- [122] M. G. Walter, E. L. Warren, J. R. McKone, S. W. Boettcher, Q. Mi, E. A. Santori, N. S. Lewis, *Chemical Reviews* **2010**, *110*, 6446-6473.
- [123] I. S. Cho, J. Choi, K. Zhang, S. J. Kim, M. J. Jeong, L. Cai, T. Park, X. Zheng, J. H. Park, *Nano Letters* **2015**, *15*, 5709-5715.
- [124] J. Su, L. Guo, S. Yoriya, C. A. Grimes, *Crystal Growth & Design* **2010**, *10*, 856-861.
- [125] Y. Wu, B. Yang, B. Zong, H. Sun, Z. Shen, Y. Feng, *Journal of Materials Chemistry* **2004**, *14*, 469-477.
- [126] S. Chen, S. S. Thind, A. Chen, *Electrochemistry Communications* **2016**, *63*, 10-17.
- [127] C. K. Ngaw, V. B. Wang, Z. Liu, Y. Zhou, S. Kjelleberg, Q. Zhang, T. T. Y. Tan, S. C. J. Loo, *npj Biofilms and Microbiomes* **2015**, *1*, 15020.
- [128] A. Wolcott, W. A. Smith, T. R. Kuykendall, Y. Zhao, J. Z. Zhang, *Small* **2009**, *5*, 104-111.
- [129] P. R. Deshmukh, Y. Sohn, W. G. Shin, *Journal of Alloys and Compounds* **2017**, *711*, 573-580.
- [130] Y. O. Kim, K.-S. Ahn, S. H. Kang, *Materials Letters* **2015**, *151*, 28-30.
- [131] N. Liu, S. P. Albu, K. Lee, S. So, P. Schmuki, *Electrochimica Acta* **2012**, *82*, 98-102.
- [132] S. Rai, A. Ikram, S. Sahai, S. Dass, R. Shrivastav, V. R. Satsangi, *International Journal of Hydrogen Energy* **2017**, *42*, 3994-4006.
- [133] S. Grigorescu, B. Bärhausen, L. Wang, A. Mazare, J. E. Yoo, R. Hahn, P. Schmuki, *Electrochemistry Communications* **2015**, *51*, 85-88.
- [134] B. D. Chernomordik, H. B. Russell, U. Cvelbar, J. B. Jasinski, V. Kumar, T. Deutsch, M. K. Sunkara, *Nanotechnology* **2012**, *23*, 194009.
- [135] H. M. Chen, C. K. Chen, Y.-C. Chang, C.-W. Tsai, R.-S. Liu, S.-F. Hu, W.-S. Chang, K.-H. Chen, *Angewandte Chemie* **2010**, *122*, 6102-6105.
- [136] W. Sheng, B. Sun, T. Shi, X. Tan, Z. Peng, G. Liao, *ACS Nano* **2014**, *8*, 7163-7169.

- [137] M. Allieta, M. Marelli, F. Malara, C. L. Bianchi, S. Santangelo, C. Triolo, S. Patane, A. M. Ferretti, Š. Kment, A. Ponti, A. Naldoni, *Catalysis Today* **2018**.
- [138] X. Zhang, Y. Lin, D. He, J. Zhang, Z. Fan, T. Xie, *Chemical Physics Letters* **2011**, *504*, 71-75.
- [139] S. Guo, S. Han, H. Mao, S. Dong, C. Wu, L. Jia, B. Chi, J. Pu, J. Li, *Journal of Power Sources* **2014**, *245*, 979-985.
- [140] T. Grewe, H. Tüysüz, *ACS Applied Materials & Interfaces* **2015**, *7*, 23153-23162.
- [141] J. S. Hoppius, D. Bialuschewski, S. Mathur, A. Ostendorf, E. L. Gurevich, *Applied Physics Letters* **2018**, *113*, 0719041-0719044.
- [142] M. Law, L. E. Greene, A. Radenovic, T. Kuykendall, J. Liphardt, P. Yang, *The Journal of Physical Chemistry B* **2006**, *110*, 22652-22663.
- [143] X. Pan, M.-Q. Yang, X. Fu, N. Zhang, Y.-J. Xu, *Nanoscale* **2013**, *5*, 3601-3614.
- [144] J. Leduc, Y. Goenuellue, P. Ghamgosar, S. You, J. Mouzon, H. Choi, A. Vomiero, M. Grosch, S. Mathur, *ACS Applied Nano Materials* **2019**, *2*, 334-342.
- [145] R. Saito, Y. Miseki, K. Sayama, *Chemical Communications* **2012**, *48*, 3833-3835.
- [146] R. Saito, Y. Miseki, K. Sayama, *Journal of Photochemistry and Photobiology A: Chemistry* **2013**, *258*, 51-60.
- [147] H. Tan, Z. Zhao, M. Niu, C. Mao, D. Cao, D. Cheng, P. Feng, Z. Sun, *Nanoscale* **2014**, *6*, 10216-10223.
- [148] H.-i. Kim, D. Monllor-Satoca, W. Kim, W. Choi, *Energy & Environmental Science* **2015**, *8*, 247-257.
- [149] W. He, Y. Yang, L. Wang, J. Yang, X. Xiang, D. Yan, F. Li, *ChemSusChem* **2015**, *8*, 1568-1576.
- [150] K. Sun, Y. Jing, C. Li, X. Zhang, R. Aguinaldo, A. Kargar, K. Madsen, K. Banu, Y. Zhou, Y. Bando, Z. Liu, D. Wang, *Nanoscale* **2012**, *4*, 1515-1521.
- [151] S. S. Kale, R. S. Mane, T. Ganesh, B. N. Pawar, S.-H. Han, *Current Applied Physics* **2009**, *9*, 384-389.
- [152] S. Chaguetmi, N. Sobti, P. Decorse, L. Mouton, S. Nowak, F. Mammeri, S. Achour, S. Ammar, *RSC Advances* **2016**, *6*, 114843-114851.
- [153] Q. Xiang, J. Yu, M. Jaroniec, *The Journal of Physical Chemistry C* **2011**, *115*, 7355-7363.
- [154] Y. Hou, F. Zuo, A. Dagg, P. Feng, *Nano Letters* **2012**, *12*, 6464-6473.
- [155] K. Zhang, W. Kim, M. Ma, X. Shi, J. H. Park, *Journal of Materials Chemistry A* **2015**, *3*, 4803-4810.
- [156] S. M. Sze, K. K. Ng, *Physics of Semiconductor Devices*, Wiley, **2007**.
- [157] B. Hu, F. Cai, T. Chen, M. Fan, C. Song, X. Yan, W. Shi, *ACS Applied Materials & Interfaces* **2015**, *7*, 18247-18256.
- [158] K. Sivula, *The Journal of Physical Chemistry Letters* **2013**, *4*, 1624-1633.
- [159] C. Jiang, S. J. A. Moniz, A. Wang, T. Zhang, J. Tang, *Chemical Society Reviews* **2017**, *46*, 4645-4660.
- [160] S. Crawford, E. Thimsen, P. Biswas, *Journal of the Electrochemical Society* **2009**, *156*, H346-H351.
- [161] Z. Chen, H. Dinh, E. Miller, *Photoelectrochemical Water Splitting: Standards, Experimental Methods, and Protocols*, Springer, **2013**.
- [162] L. J. Minggu, W. R. Wan Daud, M. B. Kassim, *International Journal of Hydrogen Energy* **2010**, *35*, 5233-5244.
- [163] T. Bosserez, J. Rongé, J. van Humbeeck, S. Haussener, J. Martens, *Oil & Gas Science and Technology – Revue d'IFP Energies nouvelles* **2015**, *70*, 877-889.
- [164] T. Lopes, P. Dias, L. Andrade, A. Mendes, *Solar Energy Materials and Solar Cells* **2014**, *128*, 399-410.

- [165] E. A. Hernández-Pagán, N. M. Vargas-Barbosa, T. Wang, Y. Zhao, E. S. Smotkin, T. E. Mallouk, *Energy & Environmental Science* **2012**, *5*, 7582-7589.
- [166] Kumar A, Pandey G, *Material Sci & Eng Int J* **2017**, *1*, 106-114.
- [167] A. Ajmal, I. Majeed, R. N. Malik, H. Idriss, M. A. Nadeem, *RSC Advances* **2014**, *4*, 37003-37026.
- [168] M. N. Chong, B. Jin, C. W. K. Chow, C. Saint, *Water Research* **2010**, *44*, 2997-3027.
- [169] S. C. Yan, Z. S. Li, Z. G. Zou, *Langmuir* **2010**, *26*, 3894-3901.
- [170] J. Qin, X. Zhang, C. Yang, M. Cao, M. Ma, R. Liu, *Applied Surface Science* **2017**, *392*, 196-203.
- [171] N. Q. T. Ton, T. N. T. Le, S. Kim, V. A. Dao, J. Yi, T. H. T. Vu, *Journal of Nanoscience and Nanotechnology* **2020**, *20*, 2214-2222.
- [172] Y. Cong, J. Zhang, F. Chen, M. Anpo, *The Journal of Physical Chemistry C* **2007**, *111*, 6976-6982.
- [173] L. Gnanasekaran, R. Hemamalini, S. Rajendran, J. Qin, M. L. Yola, N. Atar, F. Gracia, *Journal of Molecular Liquids* **2019**, *287*, 110967.
- [174] M. Huang, C. Xu, Z. Wu, Y. Huang, J. Lin, J. Wu, *Dyes and Pigments* **2008**, *77*, 327-334.
- [175] M. Batzill, U. Diebold, *Progress in Surface Science* **2005**, *79*, 47-154.
- [176] A. Dey, *Materials Science and Engineering: B* **2018**, *229*, 206-217.
- [177] N. Barsan, D. Koziej, U. Weimar, *Sensors and Actuators B: Chemical* **2007**, *121*, 18-35.
- [178] K. Zakrzewska, M. Radecka, *Nanoscale Research Letters* **2017**, *12*, 89.
- [179] Z. M. Seeley, A. Bandyopadhyay, S. Bose, *Materials Science and Engineering: B* **2009**, *164*, 38-43.
- [180] O. K. Tan, W. Cao, W. Zhu, J. W. Chai, J. S. Pan, *Sensors and Actuators B: Chemical* **2003**, *93*, 396-401.
- [181] B. Comert, N. Akin, M. Donmez, S. Saglam, S. Ozcelik, *IEEE Sensors Journal* **2016**, *16*, 8890-8896.
- [182] N. D. Cuong, T. T. Hoa, D. Q. Khieu, N. D. Hoa, N. Van Hieu, *Current Applied Physics* **2012**, *12*, 1355-1360.
- [183] H. Yang, X. Zhang, J. Li, W. Li, G. Xi, Y. Yan, H. Bai, *Microporous and Mesoporous Materials* **2014**, *200*, 140-144.
- [184] L. Sun, W. Fang, Y. Yang, H. Yu, T. Wang, X. Dong, G. Liu, J. Wang, W. Yu, K. Shi, *RSC Advances* **2017**, *7*, 33419-33425.
- [185] Y. Wang, G. Duan, Y. Zhu, H. Zhang, Z. Xu, Z. Dai, W. Cai, *Sensors and Actuators B: Chemical* **2016**, *228*, 74-84.
- [186] D. S. Dhawale, D. P. Dubal, A. M. More, T. P. Gujar, C. D. Lokhande, *Sensors and Actuators B: Chemical* **2010**, *147*, 488-494.
- [187] S. Bhatia, N. Verma, R. K. Bedi, *Results in Physics* **2017**, *7*, 801-806.
- [188] R. C. Ewing, T. Beirau, U. Bismayer, W. D. Nix, G. A. Schneider, L. A. Groat, *American Mineralogist* **2016**, *101*, 399-406.
- [189] D. D. Sarma, *Journal of Electron Spectroscopy and Related Phenomena* **1996**, *78*, 37-42.
- [190] M. Birnbaum, *Journal of Applied Physics* **1965**, *36*, 3688-3689.
- [191] J. E. Sipe, J. F. Young, J. S. Preston, H. M. van Driel, *Physical Review B* **1983**, *27*, 1141-1154.
- [192] S. A. Akhmanov, I. E. y. Vladimir, I. K. Nikolai, V. N. Seminogov, *Soviet Physics Uspekhi* **1985**, *28*, 1084.
- [193] F. Costache, M. Henyk, J. Reif, *Applied Surface Science* **2002**, *186*, 352-357.
- [194] E. L. Gurevich, *Applied Surface Science* **2016**, *374*, 56-60.

- [195] E. L. Gurevich, Y. Levy, S. V. Gurevich, N. M. Bulgakova, *Physical Review B* **2017**, *95*, 054305.
- [196] S. Maragkaki, T. J. Y. Derrien, Y. Levy, N. M. Bulgakova, A. Ostendorf, E. L. Gurevich, *Applied Surface Science* **2017**, *417*, 88-92.
- [197] A. Žemaitis, M. Gaidys, M. Brikas, P. Gečys, G. Račiukaitis, M. Gedvilas, *Scientific Reports* **2018**, *8*, 17376.
- [198] N. V. Tkachenko, in *Optical Spectroscopy*, Elsevier Science, Amsterdam, **2006**, pp. 49-55.
- [199] J. F. Ready, in *Industrial Applications of Lasers (Second Edition)*, Academic Press, San Diego, **1997**, pp. 47-52, 66-70.
- [200] Tangerine: Femtosecond laser for research & development in micro processing and scientific applications by Amplitude Systems, www.amplitude-laser.com, **30.09.2019**
- [201] Tangor: Powerful, full-featured and versatile femtosecond laser by Amplitude Systems, www.amplitude-laser.com, **30.09.2019**
- [202] Spitfire Ace: Industry leading power, maximum stability by Spectra Physics, www.spectra-physics.com, **30.09.2019**
- [203] Solstice Ace: High-energy, industrial one-box, ultrafast amplifiers by Spectra Physics, www.spectra-physics.com, **30.09.2019**
- [204] Monaco 1035: Industrial Femtosecond Laser by Coherent, www.coherent.com, **30.09.2019**
- [205] Femtosecond Laser Micromachining Workstation FemtoFAB by Workshop of Photonics, www.wophotonics.com, **30.09.2019**
- [206] A. K. Dubey, V. Yadava, *International Journal of Machine Tools and Manufacture* **2008**, *48*, 609-628.
- [207] A. Lasagni, F. Mücklich, M. R. Nejati, R. Clasen, *Advanced Engineering Materials* **2006**, *8*, 580-584.
- [208] S. K. Sundaram, E. Mazur, *Nature Materials* **2002**, *1*, 217-224.
- [209] H. Palneedi, D. Maurya, G.-Y. Kim, V. Annapureddy, M.-S. Noh, C.-Y. Kang, J.-W. Kim, J.-J. Choi, S.-Y. Choi, S.-Y. Chung, S.-J. L. Kang, S. Priya, J. Ryu, *Advanced Materials* **2017**, *29*, 1605688.
- [210] T. Shinonaga, M. Tsukamoto, M. Takahashi, M. Fujita, N. Abe, *Applied Physics A* **2013**, *112*, 57-60.
- [211] Industrial Laser Solutions For Manufacturing, *Femtosecond laser processing of metal and plastics in the medical device industry*, <http://www.industrial-lasers.com/articles/print/volume-29/issue-5/features/femtosecond-laser-processing-of-metal-and-plastics-in-the-medical-device-industry.html>, Zugriff: **30.09.2015**.
- [212] M. Alyobi, R. Cobley, *International Journal of Research in Science; Vol 3 No 2 (2017): International Journal of Research in Science* **2017**.
- [213] S. P. Koiry, P. Jha, P. Veerender, C. Sridevi, A. K. Debnath, A. K. Chauhan, K. P. Muthe, S. C. Gadkari, *Journal of the Electrochemical Society* **2017**, *164*, E1-E4.
- [214] H. Tolner, B. Feldman, D. McLean, C. Cording, *Transparent conductive oxides for display applications, Vol. 24*, **2008**.
- [215] K. Teshima, Y. Inoue, H. Sugimura, O. Takai, *Thin Solid Films* **2001**, *390*, 88-92.
- [216] H. Wojcik, M. Junige, W. Bartha, M. Albert, V. Neumann, U. Merkel, A. Peeva, J. Gluch, S. Menzel, F. Munnik, R. Liske, D. Utess, I. Richter, C. Klein, H. J. Engelmann, P. Ho, C. Hossbach, C. Wenzel, *Journal of the Electrochemical Society* **2011**, *159*, H166-H176.
- [217] Y. S. Kim, J. H. Lee, T. T. T. Pham, J. T. Lim, G. Y. Yeom, *J. Korean Phy. Soc.* **2008**, *53*, 892-896.

- [218] L. A. Mochalov, A. S. Lobanov, A. V. Nezhdanov, M. A. Kudryashov, A. I. Mashin, A. N. Stepanov, A. I. Korytin, A. V. Vorotyntsev, V. M. Vorotyntsev, *Optical Materials Express* **2016**, *6*, 3759-3765.
- [219] J. Sun, B. Bhushan, J. Tong, *RSC Advances* **2013**, *3*, 14862-14889.
- [220] X. Wu, H. Chen, *Journal of Physics C: Solid State Physics* **1986**, *19*, 5957-5974.
- [221] Y. M. Mos, A. C. Vermeulen, C. J. N. Buisman, J. Weijma, *Geomicrobiology Journal* **2018**, *35*, 511-517.
- [222] H. Wang, J. Houard, L. Arnoldi, A. Hideur, E. P. Silaeva, B. Deconihout, A. Vella, *Ultramicroscopy* **2016**, *160*, 18-22.
- [223] C. Cheng, A. Amini, C. Zhu, Z. Xu, H. Song, N. Wang, *Scientific Reports* **2014**, *4*, 4181.
- [224] R. Kitamura, L. Pilon, M. Jonasz, *Applied Optics* **2007**, *46*, 8118-8133.
- [225] A. B. D. Cassie, S. Baxter, *Transactions of the Faraday Society* **1944**, *40*, 546-551.
- [226] M. Kubiak, W. Piekarska, S. Stano, *International Journal of Heat and Mass Transfer* **2015**, *83*, 679-689.
- [227] Y. Pan, M. Yang, Y. Li, Z. Wang, C. Zhang, Y. Zhao, J. Yao, Q. Wu, J. Xu, *Scientific Reports* **2016**, *6*, 19571.
- [228] M. Zamfirescu, M. Ulmeanu, F. Jipa, O. Cretu, A. Moldovan, G. Epurescu, M. Dinescu, R. Dabu, *Journal of Laser Micro/Nanoengineering* **2009**, *4*, 7-10.
- [229] R. J. Peláez, C. N. Afonso, J. Bulíř, M. Novotný, J. Lančok, K. Piksová, *Nanotechnology* **2013**, *24*, 095301.
- [230] J. P. W. Treacy, H. Hussain, X. Torrelles, D. C. Grinter, G. Cabailh, O. Bikondoa, C. Nicklin, S. Selcuk, A. Selloni, R. Lindsay, G. Thornton, *Physical Review B* **2017**, *95*, 075416.
- [231] D. T. Cromer, K. Herrington, *Journal of the American Chemical Society* **1955**, *77*, 4708-4709.
- [232] D. Bialuschewski, J. S. Hoppius, R. Frohnhoven, M. Deo, Y. Gönüllü, T. Fischer, E. L. Gurevich, S. Mathur, *Advanced Engineering Materials* **2018**, *20*, 1800167.
- [233] Q. Liu, H. Lu, Z. Shi, F. Wu, J. Guo, K. Deng, L. Li, *ACS Applied Materials & Interfaces* **2014**, *6*, 17200-17207.
- [234] E. Stratakis, V. Zorba, M. Barberoglou, C. Fotakis, G. A. Shafeev, *Applied Surface Science* **2009**, *255*, 5346-5350.
- [235] S. Rtimi, C. Pulgarin, V. A. Nadtochenko, F. E. Gostev, I. V. Shelaev, J. Kiwi, *Scientific Reports* **2016**, *6*, 30113.
- [236] H. Dotan, O. Kfir, E. Sharlin, O. Blank, M. Gross, I. Dumchin, G. Ankonina, A. Rothschild, *Nature Materials* **2013**, *12*, 158-164.
- [237] M. Radecka, K. Zakrzewska, M. Rękas, *Sensors and Actuators B: Chemical* **1998**, *47*, 194-204.
- [238] D. Bialuschewski, J. S. Hoppius, R. Frohnhoven, M. Deo, Y. Gönüllü, T. Fischer, E. L. Gurevich, S. Mathur, *Advanced Engineering Materials* **2018**, *20*, 18001671-18001678.
- [239] T. Atefeh, R. Davood, *Semiconductor Science and Technology* **2016**, *31*, 125012.
- [240] K. Maeda, *Catalysis Science & Technology* **2014**, *4*, 1949-1953.
- [241] M. Pyeon, T.-P. Ruoko, J. Leduc, Y. Gönüllü, M. Deo, N. V. Tkachenko, S. Mathur, *Journal of Materials Research* **2018**, *33*, 455-466.
- [242] H.-J. Ahn, M.-J. Kwak, J.-S. Lee, K.-Y. Yoon, J.-H. Jang, *Journal of Materials Chemistry A* **2014**, *2*, 19999-20003.
- [243] K. Sugioka, Y. Cheng, *Light: Science & Application* **2014**, *3*, e149.
- [244] A. Sasinska, D. Bialuschewski, M. M. Islam, T. Singh, M. Deo, S. Mathur, *J. Phys. Chem. C* **2017**, 15538-15548.
- [245] N. Q. Le, C. E. Ekuma, B. I. Dunlap, D. Gunlycke, *The Journal of Physical Chemistry C* **2018**, *122*, 2832-2839.

- [246] D. Barreca, A. Gasparotto, C. Maccato, C. Maragno, E. Tondello, *Surface Science Spectra* **2007**, *14*, 27-33.
- [247] J. Liu, Q. Zhang, J. Yang, H. Ma, M. O. Tade, S. Wang, J. Liu, *Chemical Communications* **2014**, *50*, 13971-13974.
- [248] Z. Wang, C. Yang, T. Lin, H. Yin, P. Chen, D. Wan, F. Xu, F. Huang, J. Lin, X. Xie, M. Jiang, *Advanced Functional Materials* **2013**, *23*, 5444-5450.
- [249] Z. Xu, H. Wang, Y. Wen, W. Li, C. Sun, Y. He, Z. Shi, L. Pei, Y. Chen, S. Yan, Z. Zou, *ACS Applied Materials & Interfaces* **2018**, *10*, 3624-3633.
- [250] M. C. Biesinger, B. P. Payne, A. P. Grosvenor, L. W. M. Lau, A. R. Gerson, R. S. C. Smart, *Applied Surface Science* **2011**, *257*, 2717-2730.
- [251] S. Mathur, M. Veith, M. Haas, H. Shen, N. Lecerf, V. Huch, S. Huefner, R. Haberkorn, H. P. Beck, M. Jilavi, *ChemInform* **2001**, *32*.
- [252] J. V. Singh, N. C. Jain, R. C. Mehrotra, *Synthesis and Reactivity in Inorganic and Metal-Organic Chemistry* **1979**, *9*, 79-88.
- [253] S. Mathur, M. Veith, T. Ruegamer, E. Hemmer, H. Shen, *Chemistry of Materials* **2004**, *16*, 1304-1312.
- [254] T. Enomoto, in *CIRP Encyclopedia of Production Engineering*, Springer Berlin Heidelberg, Berlin, Heidelberg, **2014**, pp. 152-157.
- [255] A. Remiro, A. Arandia, L. Oar-Arteta, J. Bilbao, A. G. Gayubo, *Applied Catalysis B: Environmental* **2018**, *237*, 353-365.
- [256] N. Sahli, C. Petit, A. C. Roger, A. Kiennemann, S. Libs, M. M. Bettahar, *Catalysis Today* **2006**, *113*, 187-193.
- [257] J. Zygmuntowicz, P. Wicińska, A. Miazga, K. Konopka, *Journal of Thermal Analysis and Calorimetry* **2016**, *125*, 1079-1086.
- [258] I. Halevy, D. Dragoi, E. Stndag, A. F. Yue, E. H. Arredondo, J. Hu, M. S. Somayazulu, *Journal of Physics: Condensed Matter* **2002**, *14*, 10511-10516.
- [259] J.-H. Kim, B.-R. Son, D.-H. Yoon, K.-T. Hwang, H.-G. Noh, W.-S. Cho, U.-S. Kim, *Ceramics International* **2012**, *38*, 5707-5712.
- [260] S. A. B. Asif, S. B. Khan, A. M. Asiri, *Nanoscale Research Letters* **2014**, *9*, 510.
- [261] F. Dumond, E. Marceau, M. Che, *The Journal of Physical Chemistry C* **2007**, *111*, 4780-4789.
- [262] B. H. Davis, *Catalysis Today* **2002**, *71*, 249-300.
- [263] M. C. Biesinger, B. P. Payne, L. W. M. Lau, A. Gerson, R. S. C. Smart, *Surface and Interface Analysis* **2009**, *41*, 324-332.
- [264] A. P. Grosvenor, M. C. Biesinger, R. S. C. Smart, N. S. McIntyre, *Surface Science* **2006**, *600*, 1771-1779.
- [265] S. Rades, V.-D. Hodoroaba, T. Salge, T. Wirth, M. P. Lobera, R. H. Labrador, K. Natte, T. Behnke, T. Gross, W. E. S. Unger, *RSC Advances* **2014**, *4*, 49577-49587.
- [266] A. M. Tayeb, D. S. Hussein, *American Journal of Nanomaterials* **2015**, *3*, 57-63.
- [267] R. Zuo, G. Du, W. Zhang, L. Liu, Y. Liu, L. Mei, Z. Li, *Advances in Materials Science and Engineering* **2014**, *2014*, 1-7.
- [268] A. Gautam, A. Kshirsagar, R. Biswas, S. Banerjee, P. K. Khanna, *RSC Advances* **2016**, *6*, 2746-2759.
- [269] Y. Wang, J. Zhao, X. Xiong, S. Liu, Y. Xu, *Applied Catalysis B: Environmental* **2019**, *258*, 117903.
- [270] Y. Zhang, L. Guo, S. Wei, Y. He, H. Xia, Q. Chen, H.-B. Sun, F.-S. Xiao, *Nano Today* **2010**, *5*, 15-20.
- [271] S. Kang, C. C. Evans, S. Shukla, O. Reshef, E. Mazur, *Optics & Laser Technology* **2018**, *103*, 340-345.
- [272] D. D'Angelo, S. Filice, M. Miritello, C. Bongiorno, E. Fazio, F. Neri, G. Compagnini, S. Scalese, *Physical Chemistry Chemical Physics* **2018**, *20*, 10292-10301.

-
- [273] N. Nakashima, K.-i. Yamanaka, M. Saeki, H. Ohba, S. Taniguchi, T. Yatsunami, *Journal of Photochemistry and Photobiology A: Chemistry* **2016**, 319-320, 70-77.
- [274] M. E. Shaheen, J. E. Gagnon, B. J. Fryer, *Laser Physics Letters* **2015**, 12, 066103.
- [275] A. A. Ilyin, S. S. Golik, K. A. Shmirko, *Spectrochimica Acta Part B: Atomic Spectroscopy* **2015**, 112, 16-22.
- [276] B. A. van Hassel, A. J. Burggraaf, *Applied Physics A* **1991**, 52, 410-417.
- [277] J. Liang, C. Hao, K. Yu, Y. Li, *Nanomaterials and Nanotechnology* **2016**, 6, 1847980416680808.
- [278] P. A. Mangrulkar, M. M. Joshi, S. N. Tijare, V. Polshettiwar, N. K. Labhsetwar, S. S. Rayalu, *International Journal of Hydrogen Energy* **2012**, 37, 10462-10466.
- [279] T. Gholami, M. Salavati-Niasari, S. Varshoy, *International Journal of Hydrogen Energy* **2016**, 41, 9418-9426.
- [280] F. Meyer, R. Hempelmann, S. Mathur, M. Veith, *Journal of Materials Chemistry* **1999**, 9, 1755-1763.
- [281] Zapp Materials Engineering GmbH, Titanium Grade 1-4 Datasheet, <https://www.zapp.com/us/products/plate-sheet/nickel-cobalt-titanium/data-sheets-stock-lists.html>, **30.09.2019**

7 Appendix

7.1 Erklärung

Hiermit erkläre ich, dass die von mir vorgelegte Dissertation selbstständig angefertigt wurde, und alle verwendeten Quellen und Hilfsmittel mit Verweisen im Text korrekt zitiert und Berechtigungen aus Journalen eingeholt wurden, sofern der Inhalt ohne Änderung verwendet wurde. Diese Dissertation hat noch keiner anderen Fakultäten oder Universitäten zur Prüfungen vorgelegen. Mit Ausnahme der erwähnten Teilpublikationen (Abschnitt 7.2) wurde diese Arbeit noch nicht veröffentlicht, und wird auch vor dem Abschluss des Promotionsverfahrens nicht vorgenommen. Mir, dem Autor ist das Bestimmungsprotokoll der Promotionsordnung bekannt.

(Danny Bialuschewski)

7.2 Publikationsliste

A. Sasinska, D. Bialuschewski, M. M. Islam, T. Singh, M. Deo, S. Mathur, "Experimental and Theoretical Insights into Influence of Hydrogen and Nitrogen Plasma on the Water Splitting Performance of ALD Grown TiO₂ Thin Films", *J. Phys. Chem. C* **2017**, *121*, 15538-15548.

D. Bialuschewski, J. S. Hoppius, R. Frohnhoven, M. Deo, Y. Gönüllü, T. Fischer, E. L. Gurevich, S. Mathur, "Laser-Textured Metal Substrates as Photoanodes for Enhanced PEC Water Splitting Reactions.", *Adv. Eng. Mat.* **2018**, *20*, 18001671-18001678.

J. S. Hoppius, D. Bialuschewski, S. Mathur, A. Ostendorf, E. L. Gurevich, "Femtosecond laser crystallization of amorphous titanium oxide thin films", *Appl. Phys. Lett.* **2018**, *113*, 0719041-0719044.

Participation in the book "Advanced Ceramics for Energy Conversion and Storage" by O. Guillon *Elsevier*, Amsterdam, **2019**, with the chapter "Functional metal oxide ceramics as electron transport media in photovoltaics and photo-electrocatalysis" by D. Bialuschewski, A. Möllmann, T. Fischer, Y. Tachibana, S. Mathur.

7.3 Curriculum Vitae

Persönliche Daten	
Name:	Danny Bialuschewski
Geburtsdatum:	21.12.1988
Adresse:	Luxemburger Str. 174, 50937 Köln
Email:	D.Bialuschewski@gmx.de
Staatsangehörigkeit:	deutsch
Bildungsweg	
10/2013 – 09/2015	Master-Studium im Fach Chemie an der Universität zu Köln. Thema der Masterarbeit: "Lasergestützte Strukturierung von mittels PE-CVD hergestellten TiO ₂ -Oberflächen", Note: 1,1
10/2010 – 11/2013	Bachelor-Studium im Fach Chemie an der Universität zu Köln. Thema der Bachelorarbeit: "Asymmetrische Paternò-Büchi-Reaktion mit TADDOL-Derivaten", Note: 1,5
10/1999 – 06/2008	Abitur, Christian-Rauch-Schule (Bad Arolsen), Leistungskurse: Mathematik, Englisch
DFG Projekte	
2015-2018	Forscher für das DFG Programm SPP1839 "Tailored Disorder"
Auslandserfahrungen	
01/2019 – 02/2019	Wissenschaftliche Arbeit im Laserlabor von Professor Doktor Yasuhiro Tachibana, Royal Melbourne Institute of Technology, Melbourne, Australien. Finanziert durch den DAAD.
11/2015 – 12/2015	Wissenschaftliche Arbeit in der Forschungsgruppe von Federico Rosei, Institut national de la recherche scientifique, Montreal, Canada. Finanziert durch EU, FP7.
Konferenzbeiträge	
21 – 25/05/2019	ENHANCE 2019: Posterbeitrag
27/01 – 01/02/2019	ICACC 2019: Posterbeitrag
25 – 30/11/2018	MRS Fall Meeting 2018: Präsentation vorbereitet
05 – 08/07/2017	AMAES VI: Posterbeitrag
27 – 29/09/2016	MSE 2016: Präsentation
31/08 – 03/09/2016	AMAES V: Posterbeitrag und Präsentation
06 – 08/04/2016	Manfred-Eigen-Meeting 2016: Posterbeitrag